Soliton Dynamics in Liquid-core Optical Fibers

DISSERTATION

for the acquisition
of the academic title
Doctor rerum naturalium (Dr. rer. nat.)

submitted to the council of the
Faculty of Physics and Astronomy

of the

FRIEDRICH-SCHILLER-
UNIVERSITÄT
JENA

by Dipl. Phys. Mario Chemnitz
born in Lutherstadt Wittenberg, Germany, on 21st Oct 1986.

REVIEWERS:

1. Prof. Dr. Markus A. Schmidt, Friedrich-Schiller-University Jena, Germany
2. Prof. Dr. Alexander Szameit, University Rostock, Germany
3. Prof. Dr. Arnaud Mussot, University Lille, France

DAY OF THE DISPUTATION: 25. February 2019

"Every particular in nature, a leaf, a drop, a crystal, a moment of time is related to the whole, and partakes of the perfection of the whole."

— Ralph Waldo Emerson

Dedicated to my love Margarethe and my little Lorelin.

ABSTRACT

Solitons are self-maintaining wave patterns occurring in many dynamic systems in nature. In optics, the rich dynamics of non-dispersing temporal solitons enable the generation of supercontinuum spectra covering wide wavelength ranges from the visible ultraviolet to the near-infrared and beyond. Such nonlinear multi-color light sources are indispensable for next-generation sensing and imaging technologies. Particularly optical fibers proved to be superiorly effective for nonlinear light generation integrated in a robust platform. However, commercial nonlinear fiber sources are based on silica as fiber material, which is limited in its bandwidth, nonlinearity, and wavelength tuneability. Hence, recent efforts in nonlinear fiber optics try to overcome these limitations by exploring new fiber designs and new core materials with enhanced nonlinear properties, such as soft-glasses and gases. Also liquids possess wider transmission windows and higher nonlinearities than silica, while exhibiting unique nonlinear responses due to the long-lasting molecular motions in a light field. First experimental demonstrations reveal the potential of liquid-core optical fibers for broadband light generation. However, soliton dynamics, as most effective broadening mechanisms, are largely unexplored in these systems.

This thesis theoretically and experimentally explores these dynamics in liquid-core fibers. Following a rigorous empirical approach, hybrid soliton-like states are proposed as potential solution of those systems. Key benchmarks, such as optical phase relations and a modified soliton number, are found and confirmed as tool to classify noninstantaneous nonlinear systems by means of their capabilities for hosting hybrid solitons. This thesis further elaborates realistic material models which allows to identify soliton regimes in easily producible step-index liquid-core fiber designs. Finally hybrid soliton-like states are shown to emerge in simulated supercontinuum spectra for these experimentally addressable fiber and laser parameters. Thereupon, soliton-mediated supercontinuum generation is demonstrated experimentally in liquid-core fibers using state-of-the-art thulium fiber lasers. In correlation with numerical simulations, the unusual broadening and coherence behavior of the measured spectra is shown to originate from dominant noninstantaneous nonlinear effects in liquids, and thus delivers the first positive indications for the hypothesis of novel hybrid soliton dynamics. The study closes with the experimental demonstration of external soliton control via temperature, static pressure, and liquid composition, overall highlighting liquid-core fibers as a dynamic platform for broadband and tuneable nonlinear light generation with a plethora of unprecedented nonlinear effects and scientific potential.

ZUSAMMENFASSUNG

Solitonen sind selbsterhaltende Wellenmuster, die in vielen dynamischen Systemen in der Natur auftreten. In der Optik ermöglichen die reichhaltigen Dynamiken von nichtverbreiternden zeitlichen Solitonen die Generation von Superkontinuumsspektren über weite Wellenlängenbereiche vom Sichtbaren bis ins Nah-Infrarote und darüber hinaus. Solche nichtlinearen mehrfarbigen Lichtquellen sind für Sensor- und Bildgebungstechnologien der nächsten Generation unverzichtbar. Insbesondere für die nichtlineare Lichterzeugung in integrierten, robusten Systemen erwiesen sich optische Fasern als überragend. Kommerzielle nichtlineare Faserquellen basieren jedoch auf Siliciumdioxid als Fasermaterial, welches in seiner Bandbreite, Nichtlinearität und Wellenlängenabstimmbarkeit begrenzt ist. Die jüngsten Bemühungen im Bereich der nichtlinearen Faseroptik versuchen deshalb, diese Einschränkungen zu überwinden, indem neue Faserdesigns und neue Kernmaterialien mit verbesserten nichtlinearen Eigenschaften, wie Weichgläsern und Gasen, untersucht werden. Auch Flüssigkeiten haben breitere Transmissionsfenster und höhere Nichtlinearitäten als Siliciumdioxid, während sie aufgrund der langanhaltenden molekularen Bewegungen in einem Lichtfeld einzigartige nichtlineare Reaktionen zeigen. Erste experimentelle Demonstrationen zeigen das Potenzial von Flüssigkern-Glasfasern für die Breitbandlichterzeugung. Die Solitondynamiken als effektivste Verbreitungsmechanismen sind aber in diesen Systemen noch weitgehend unerforscht.

Diese Dissertation untersucht diese Dynamiken in Flüssigkernfasern theoretisch und experimentell. Einem streng empirischen Ansatz folgend werden hybride solitonähnliche Zustände als mögliche Lösung dieser Systeme vorgeschlagen. Wichtige Kenngrößen, wie optische Phasenbeziehungen und eine modifizierte Solitonzahl, werden als Werkzeuge zur Klassifizierung nichtinstantaner, nichtlinearer Systeme hinsichtlich ihrer Fähigkeiten zur Beherbergung von Hybrid-Solitonen gefunden und bestätigt. In dieser Arbeit werden außerdem realistische Materialmodelle erarbeitet, die die Identifizierung von Soliton-Regimen in einfach herstellbaren Flüssigkern-Fasern mit Stufenindex Design ermöglichen. Schließlich wird gezeigt, dass hybride solitonähnliche Zustände in simulierten Superkontinuumspektren für diese experimentell adressierbaren Faser- und Laserparameter auftreten. Daraufhin wird die Soliton-gestützte Superkontinuumserzeugung experimentell in Flüssigkernfasern unter Verwendung von modernsten Thuliumfaserlasern demonstriert. Im Zusammenhang mit numerischen Simulationen wird hervorgehoben, dass das ungewöhnliche Verbreitungs- und Kohärenzverhalten der gemessenen Spektren von dominanten, nichtinstantanen, nichtlinearen Effekten in Flüssigkeiten herrührt und somit die ersten positiven Hinweise für die Hypothese neuartiger Hybrid-Soliton-Dynamiken liefert. Die Studie schließt mit der experimentellen Demonstration der externen Soliton-Kontrolle über Temperatur, statischen Druck und flüssige Zusammensetzung. Dabei werden Flüssigkernfasern als dynamische Plattform für breitbandige und abstimmbare nichtlineare Lichterzeugung mit einer Fülle von beispiellosen nichtlinearen Effekten und wissenschaftlichem Potenzial hervorgehoben.

HYPOTHESES

This work investigates the following hypotheses (H):

1. Highly-refractive liquids filled in silica capillaries allow optical waveguiding in the near- and mid-infrared, forming a step-index liquid-core fibers.

2. Step-index liquid-core fibers feature anomalous dispersion regimes at wavelengths addressable with state-of-the-art fiber lasers, thus providing an experimental platform for exciting optical solitons.

3. The highly noninstantaneous nonlinear response of certain liquids enables the formation of noninstantaneous solitons, so-called linearons.

4. Soliton-mediated supercontinuum spectra contain characteristic signatures of modified soliton dynamics.

5. The modified soliton dynamics within noninstantaneous liquid-core fibers can be understood as result of the emergence of hybrid nonlinear soliton-like states.

6. Step-index liquid-core fibers offer an experimental platform for soliton-mediated supercontinuum generation.

7. The fiber dispersion of liquid-core fibers can be adjusted by applying temperature and pressure on the liquid core as well as changing its composition.

8. The supercontinuum generation process, in particular the soliton fission onset and the emission of non-solitonic radiation, can be controlled via external thermodynamic controls and the core composition.

ACRONYMS

ADD anomalous dispersion domain

CBP coherence-bandwidth product

CS_2 carbon disulfide

CCl_4 carbon tetrachloride

C_2Cl_4 tetrachloroethylene

$CHCl_3$ chloroform

IOR index of refraction

FOM figure of merit

FWM four-wave mixing

GVD group velocity dispersion

GNSE generalized nonlinear Schrödinger equation

HNSE hybrid nonlinear Schrödinger equation

HSW hybrid solitary wave

HSS hybrid soliton state

IKP instantaneous Kerr phase

LCF liquid-core fiber

NDD normal dispersion domain

NIR near-infrared

NIP noninstantaneous phase

NRF nonlinear response function

NRI nonlinear refractive index

NSE nonlinear Schrödinger equation

NISE noninstantaneous Schrödinger equation

NSE nonlinear Schrödinger equation

NSR non-solitonic radiation

MI modulation instabilities

MIR mid-infrared

OFM opto-fluidic mount

POC piezo-optic coefficient

SC supercontinuum

SCG supercontinuum generation

SMC single-mode criterion

SPM self-phase modulation

SFS self-frequency shift

TOC thermo-optic coefficient

TOD third-order dispersion

VIS visible

VUV visible ultraviolet

XPM cross-phase modulation

ZDW zero-dispersion wavelength

T_{HP}	pulse width at half maximum power, also known FWHM width
P_0	peak power
P_s	soliton peak power
$\mathcal{E}_p$	pulse energy
ω_0	(angular) operation frequency
λ_0	operation (pump) wavelength
λ_{ZD}	zero-dispersion wavelength
n	refractive index
n_2	nonlinear refractive index
$\varnothing_{\mathrm{co}}$	core diameter
α	absorption coefficient
β	propagation constant
β_2	second-order dispersion parameter
γ	nonlinear parameter
A_{eff}	effective mode area
NA	numerical aperture
V	(guidance) V-parameter
D	dispersion parameter
f_m	molecular fraction
f_m^{equil}	equilibrium fraction
L_{D}	dispersion length
L_{NL}	nonlinear length
L_{fiss}	fission length
N	(classical) soliton number
N_{eff}	effective soliton number
R_0	maximum of the nonlinear response
$\lvert g_{mn}^{(1)} \rvert$	first-order degree of coherence

CONTENTS

1 INTRODUCTION

About the fundamental role of solitons in nature

The existence of our world in a universe that, before anything else, distributes energy seems like a miracle. Fermi, Pasta, Ulam, and Tsingou unintentionally delivered a possible explanation, when they reported on some peculiar oscillations of mechanical bodies in a lattice connected by springs, in 1955. To their surprise, certain initial displacements of the bodies did not result in random distributions of oscillations, as commonly expected for dynamic systems, but evolved into recurrent wave forms, that traveled along the lattice without changing their shape or amplitude [1]. In fact, they rediscovered a fundamental phenomenon, which was observed earlier in 1834 by Sir Scott Russell on horseback, who reported on non-spreading water waves in a channel near Edinburgh [2]. These non-dispersing *solitary* waves, despite being observed in two completely different systems, were found to belong to a general class of solutions of special nonlinear systems. This class was later termed **solitons**.

Solitons, in the widest sense of self-stabilizing wave packets, play a fundamental role in nature. They can be found in various areas of science, including aero- and hydrodynamics (e.g. cyclones or giant ocean waves [3]), optics (e.g. non-dispersing pulses [4]), astrophysics (e.g. self-gravitating objects [5], or matter-wave solitons [6]), and biology (e.g. acoustic pulses in nerves [7]). Whenever the evolution of a wave in time and space is governed by a nonlinear feedback of the wave itself, solitary solutions come in reach. They exist through a balanced interplay between linear and (self-induced) nonlinear wave effects. For instance, the spring lattice states reported by Fermi *et al.* propagated in balance of the nonlinear displacement forces of the springs, tearing the system towards the maximum amplitude, and the energy dispersion, pushing the system towards an equal distribution of oscillation frequencies. The discovery by Fermi *et al.* contributed substantially to a new field of research that became popular under the term *chaos theory*, which focuses on the predictable behavior of dynamic nonlinear systems. It unifies the findings from multiple fields in science, which describe the sudden formation of self-maintaining structures (e.g., wave forms and particle clusters) out of chaotic initial conditions. However, the rich dynamics of chaotic systems is hard to study. Many nonlinear systems (e.g., relativistic systems) are multi-dimensional and possess many degrees of freedom which are not experimentally accessible. The physics of these systems becomes partly accessible by practical platforms, which exhibit soliton formation and interactions and therefore prove to follow similar theoretical concepts. Such platforms can emulate a multiverse of physical effects and promise new insights in many areas of science.

Hybrid material fibers as platform to study soliton dynamics

In 1973, Hasegawa and Tappert identified optical fibers as ideal platform to investigate electromagnetic solitons in the form of non-dispersing optical pulses [8]. The system parameters dispersion and nonlinearity are largely adjustable via the fiber geometry. For

instance, the reduction of the core size leads to a stronger mode confinement and larger field intensities which enhance the nonlinear coupling to the electrons of the material over meters and kilometers of fiber. Since the first experimental confirmation of optical solitons in standard silica fibers in 1987/88 [9, 10], many different types of solitons were theoretically predicted and experimentally observed in loss- and dispersion-managed optical fiber systems. They emerged into multiple fields of optics and led to technological advances, e.g., in optical data communications [11] and mode-locked laser engineering [12, 13, 14]. Furthermore, the dynamics of optical solitons were found to emulate many physical effects known from other areas of physics. Some prominent examples include (1) the emission of Cherenkov radiation [15], known as the electromagnetic exhaust from relativistic particles, (2) the spontaneous formation of giant (rogue) waves in hydrodynamics, [16, 17, 18], or (3) the physics at event horizons of black holes [19].

In parallel, the invention of micro-structured optical fibers in the 1990's provided a powerful means of controlling the optical mode dispersion landscape, which significantly boosted the exploration of complex soliton dynamics. This quickly led to the discovery of ultrabroad spectral broadening, so-called **supercontinuum generation (SCG)**, which found application in many areas, e.g., in nonlinear imaging [20], spectroscopy [21, 22], optical metrology [23, 24], and telecommunications [25, 26]. Most notably, the resonant filtering of coherent supercontinuum (SC) spectra in an optical cavity led to the discovery of broadband *optical frequency combs*, through which Glauber, Hall, and Hänsch won the Nobel prize in physics in 2005. Nowadays, SCG in silica fibers is well understood as result of complex soliton dynamics and greatly reviewed (e.g., [27, 28, 29]). These insights allow to investigate the behavior of a *soliton though the prism of an optical SC* [28] – a methodology utilized in this work.

Both SC fiber lasers and frequency combs from the visible (VIS) to near-infrared (NIR) wavelength domain are now commercialized and experience a growing market in sensing and microscopy. Recent application requirements in spectroscopy and imaging are pushing for widening the SC bandwidth towards both the visible ultraviolet (VUV) and the mid-infrared (MIR), increasing the achievable output power, and improving the pulse-to-pulse spectral stability (i.e. temporal *coherence*). These demands drive the transmission and nonlinear properties of silica to its physical limits, and currently limit the further advancement of soliton-mediated SC sources in science and industry as possible key technology for next-generation sensing devices.

The incorporation of uncommon optical materials, such as composite glasses, semiconductors [30], gases, or liquids, into **hybrid material fibers** [31, 32] provide a promising way to overcome the current limitations in SCG. Recent break-throughs in terms of spectral bandwidth and outreach of SCG into the MIR were realized using low-melting compound glasses as core material, so-called *soft-glasses*, containing heavy metals (e.g., lead glasses), fluorides (e.g., ZBLAN), or chalcogenides (e.g., S, Se, or Te). Nonlinear optical processes in soft-glass fibers largely benefit from their transparency in the NIR to MIR, as well as from the huge nonlinearities of those materials (one to three orders of mag-

nitude larger than silica [33]). Substantial SCG in the MIR was realized in chalcogenide step-index fibers (setting the current record bandwidth of 1–13 µm [34]), as well as suspended core fibers (e.g., [35, 36]). Suspended core fluoride fibers even addressed the VUV domain [37]. Today, the challenges in fiber drawing and handling of those materials are about to be overcome, and first soft-glass-fiber SC sources were commercialized for sensing applications at low- to medium optical power levels. However, specific drawbacks such as strong absorptions in the VIS, low thermal stability, mechanical brittleness, and missing biocompatibility of arsenic compositions slow down the advent of those fibers for specific applications such as broadband MIR endoscopes and fiber sensor systems, motivating further research into alternative MIR fiber materials.

In the high power regime, gas-filled hollow-core fibers have established tremendous technological advances in ultrafast pulse generation, as well as novel scientific insights in soliton dynamics [38]. Due to the low number of atoms or molecules in the core, gas-filled fibers feature large damage thresholds, low material dispersion, large transmission windows spanning from the ultraviolet to the MIR, and pressure tunable optical properties. These properties, together with the strong electric field confinement in microstructured hollow-core fibers, have led to numerous ground-breaking results, such as the nonlinear compression of high energy pulses (i.e., µJ to mJ level) up to terawatts of peak power and pulse widths in the order of few optical cycles [39, 40, 41], ultrabroadband SCG spanning from the deep ultraviolet to the NIR (e.g., [40, 42, 43]), and pressure-tunable femtosecond pulse generation in the VUV with energy conversion efficiencies up to 5% [44, 45]. Most uniquely, the nonlinear response (i.e., the temporal variation of the intensity-induced refractive index change of the core material) is distinctly different in single-atomic (noble) gases (e.g., Ar, Xe), with entirely instantaneous contributions from the electrons, than in molecular gases (e.g., H_2, SF_6), with additional noninstantaneous contributions from molecular resonances, known as *stimulated Raman scattering*. The absence of Raman scattering in noble gases enabled the unmistakable identification of ionization-induced modulation instabilities of few-cylce pulses [46] and frequency coupling mechanism to the MIR [47], whereas the coherently driven molecular resonances in Raman-active gases triggered further energy transfer towards the deep ultraviolet [42]. These few (and by far not comprehensive) examples in this research field demonstrate the large variety of accessible optical parameters of gas-core fibers, which makes them a superior platform to study soliton dynamics while opening a new realm of physics with a rich pool of unprecedented optical effects.

In addition to the extremely successful soft-glass and gas-filled fibers, the application capabilities of **liquid-core fibers (LCFs)** have also been explored over the years, with the first experiments on LCF transmission dating back to the 1970's [48, 49]. Early material studies identified *heavy organics* (such as carbon chlorides, bromides, or sulfides) as suitable core materials for liquid-core light guidance, due to their large refractive index (required for wave guiding by total internal reflection), as well as comparable transmission and nonlinear properties to soft-glasses. Moreover, the considerable temperature sens-

itivity of the refractive index, as well as the variety of molecular nonlinearities among different liquids, promise similar tuneability capabilities to gas-core fibers. However, a lack in linear and nonlinear material property models has inhibited further technological leaps in developing liquid-core fiber devices for a long time. In the last decade, models for both the refractive index dispersion [50, 51] and nonlinearity [52, 53] were refined for few selected liquids (e.g., water, benzenes, and few heavy organics) to meet the precision requirements of optical devices. The elaboration of those models triggered a series of application-oriented optofluidic fiber devices, including all-fiber optical phase modulators [54], fiber-integrated dye lasers [55], high-sensitivity refractive index and temperature sensors (e.g., [56, 57, 58]), photo-chemical reactors and monitoring systems (e.g., [59, 60, 61]), and high-power MIR light guides for clinical lasers [62]. Also, meaningful dispersion studies provided the basis for demonstrating various nonlinear effects in LCFs, including cascaded stimulated Raman scattering (e.g., [63, 64, 65]), self-phase modulation [66], and SCG. The most successful demonstrations of SCG utilized carbon disulfide (CS_2)-core step-index fibers pumped in the normal dispersion domain (NDD) and proved this liquid suitable for efficient broadband light generation from the VIS towards the MIR (i.e., beyond 2.4 µm wavelength) [67, 68].

However, despite those pioneering experiments, nonlinear liquid-core light sources are still in their infancy, since the underlying nonlinear mechanisms in the liquids are not entirely understood. Large fractions of the nonlinearity of certain liquids, such as CS_2, originate from the unique slow molecular motions induced by the optical excitation field. Depending on the liquid, the duration of the nonlinear feedback can vary between few hundred femtoseconds and multiple picoseconds, a time scale not achievable by the Raman response of glass-type or gas-type fibers. The impact of these *noninstantaneous* nonlinearities on nonlinear broadening processes, and in particular on the soliton dynamics, is largely unexplored. First approaches by Pricking *et al.* use brute-force numerical simulations over large parameter sets in order to identified the impact of the molecular nonlinear contributions on the maximally achievable spectral bandwidth and the required fiber length [69]. Apart from that, the rigorously analytical work by Conti *et al.* predicts a new type of soliton in such fiber systems [70]. The correlation between these two theoretical predictions is unclear to date. Experimentally, the soliton regime in the anomalous dispersion domain (ADD) has not been studied extensively in liquid-core systems. Only two liquid systems were reported, in which the ADD was accessed using micro-structured fibers selectively filled with carbon tetrachloride (CCl_4) [71] or water [72, 73]. Novel observations in the soliton dynamics were inhibited due to the ordinary glass-like nonlinear response of CCl_4, or strong absorption of water on the soliton side of the spectrum. Thus, the impact of the highly noninstantaneous nonlinearities of liquids on the soliton dynamics remains an open question with uncertain implications to the technological and scientific potential of LCFs. The work presented in this thesis addresses these outstanding questions.

Merit and structure of this thesis

The chapters (ch.) and sections (sec.) of this thesis successively investigate eight main hypotheses (H). After a short introduction into the theoretical fundamentals of step-index fiber modes, nonlinear pulse propagation, and soliton fission in ch. 2, linear and nonlinear optical properties of selected heavy organic liquids are discussed in ch. 3 in order to identify suitable liquids that allow optical wave guiding when incorporated inside silica capillaries (hypothesis H1). The common dispersion models known from literature will be extended and used to design easily producible silica-cladding LCFs for unexplored ADD that allow to access the soliton regime with commercial laser sources (H2). Chapter 3 also introduces the unique long-lasting (i.e., noninstantaneous) nonlinear response of liquids, which is then used in ch. 4 to test whether realistic LCF systems can support noninstantaneous soliton states, as introduced by Conti *et al.* (H3). Multiple perturbations on the theoretical solution will be discussed using semi-analytical and numerical methods, and important benchmarks are defined, which allow to classify the soliton propagation characteristic into two categories: classical and hybrid soliton propagation. However, due to the large losses in the chosen operation regime, the fundamental single-soliton propagation cannot be addressed experimentally in this work. Instead, the impact of the molecular nonlinear response on the complex soliton fission characteristics (supercontinuum regime) in LCFs will be in the focus. Thus, in ch. 5, SC simulations are used to prove the emergence of modified solitary states within SC spectra out of realistic LCFs. Important spectral observables (i.e., bandwidth, broadening onset energy, dispersive wave location, and coherence) will be identified, which indicate the dominance of noninstantaneous nonlinearities during the fission process (H4). The findings are consistent with the expectations from the soliton theory, elaborated in ch. 4, and corroborate the assumption, that the spectral broadening behaviour in LCFs, under defined conditions, originates from the fission of modified (hybrid) solitary states (H5).

In the experimental part in ch. 6, multiple LCF systems will be shown to enable octave-spanning soliton-mediated SCG in the NIR wavelength domain (H6). The experiments present the first clean observation of soliton fission in highly noninstantaneous nonlinear LCFs. The measured spectra are analyzed in light of the spectral observables for dominant noninstantaneous nonlinearity in order to uncover LCF systems, which potentially support hybrid solitary states and carry their spectral signatures in the measured SC spectra. Finally, ch. 7 presents three proof-of-concept experiments to elaborate on the scope of external control over the soliton dynamics of LCFs by applying temperature, static pressure or other core compositions (H7). Moreover, the findings will clarify the impact of thermodynamic controls and core composition on the bandwidth and onset energy of SCG in such fibers (H8). The conclusions of the individual chapters are cohesively summarized in ch. 8, and the application potential of the deduced findings will be presented in form of an outlook.

2.1 Fundamental wave equation of optics

This chapter introduces briefly the theoretical concepts of linear and nonlinear light propagation in optical fibers. The concept of optical fiber modes will be explained and used to deduce a nonlinear pulse propagation equation, in a rigorous and non-common way. Finally, the nonlinear optical effects being most relevant for this thesis, such as supercontinuum generation as a result of soliton fission and modulation instabilities, will be outlined briefly.

In contrast to other types of waves in nature, light does not require a medium to propagate. However, as an oscillatory electromagnetic field, it interacts with the charges (i.e., electrons and nuclei) in media and induces transient dipole moments, which act back on the optical wave and imprint material-specific phase and amplitude modifications to the optical wave. In general, the spatio-temporal propagation of an optical wave through an optical medium (without free charges or magnetic polarizations, i.e., dielectric optical materials) can be expressed by the four **fundamental equations of electrodynamics**

$$\nabla \times \boldsymbol{\mathcal{E}} = -\mu_0 \partial_t \boldsymbol{\mathcal{H}} \tag{1}$$

$$\nabla \times \boldsymbol{\mathcal{H}} = \varepsilon_0 \partial_t \boldsymbol{\mathcal{E}} + \partial_t \boldsymbol{\mathcal{P}} \tag{2}$$

$$\varepsilon_0 \nabla \boldsymbol{\mathcal{E}} = -\nabla \boldsymbol{\mathcal{P}} \tag{3}$$

$$\nabla \boldsymbol{\mathcal{H}} = 0\,, \tag{4}$$

with the electric field $\boldsymbol{\mathcal{E}}$, the magnetic field $\boldsymbol{\mathcal{H}}$, the macroscopic polarization $\boldsymbol{\mathcal{P}}$, and the electric and magnetic constants, ε_0 and μ_0. Combining Eqs. (1)-(2) yields the fundamental wave equation of electrodynamics of an optical field $\boldsymbol{\mathcal{E}}$ traveling in a *homogeneous* dielectric medium

$$\nabla^2 \boldsymbol{\mathcal{E}} - c_0^{-2} \partial_t^2 \boldsymbol{\mathcal{E}} = \mu_0 \partial_t^2 \boldsymbol{\mathcal{P}}\,, \tag{5}$$

with c_0 being the speed of light. The macroscopic polarization field $\boldsymbol{\mathcal{P}}$ of the electronic environment of atoms or molecules in the medium is induced by the electromagnetic radiation field, and follows the fundamental principles of causality, i.e., *where never was a field, there cannot be a polarization*. In case of a locally responding medium, the field-dependence of the polarization may be expressed as Taylor expansion in the frequency (ω) space

$$\tilde{\boldsymbol{\mathcal{P}}}(\omega) = \underbrace{\varepsilon_0 \hat{\chi}^{(1)}(\omega;\omega')\tilde{\boldsymbol{\mathcal{E}}}(\omega')}_{\text{linear } \tilde{\boldsymbol{\mathcal{P}}}_{\mathrm{L}}} + \underbrace{\varepsilon_0 \hat{\chi}^{(2)} \tilde{\boldsymbol{\mathcal{E}}}\tilde{\boldsymbol{\mathcal{E}}} + \varepsilon_0 \hat{\chi}^{(3)} \tilde{\boldsymbol{\mathcal{E}}}\tilde{\boldsymbol{\mathcal{E}}}\tilde{\boldsymbol{\mathcal{E}}} + \dots}_{\text{nonlinear } \tilde{\boldsymbol{\mathcal{P}}}_{\mathrm{NL}}}\,. \tag{6}$$

Thus, in first order approximation, the induced polarization of a medium linearly follows the electric field with the dielectric response tensor $\varepsilon_0 \hat{\chi}^{(1)}$ as proportionality constant. Considering very strong electric fields, the electron clouds of the atomic units of the medium are deflected so strongly from their usual harmonic motion, that the non-

linear terms in $\boldsymbol{\mathcal{E}}$ are required to accurately describe the induced polarization. Here, the fields couple with high dimensional susceptibility tensors, e.g., $\hat{\chi}^{(2)}$ or $\hat{\chi}^{(3)}$, to the nonlinear material response. It shall be noted that, due to the centre-inversion symmetry of the molecules, second-order effects can safely be neglected in most optical waveguide materials, (i.e., amorphous material where $\hat{\chi}^{(2)} = 0$), and third-order effects play the dominant role. This regime of third-order *nonlinear optics* is in the focus of this dissertation.

To approach a solution of Eq. (5), any arbitrary temporal light field, as well as the corresponding induced polarization field, can be expressed as superposition of monochromatic (i.e., single frequency) components - an operation that is mathematically expressed with the Fourier transform $\mathcal{F}\{\cdot\}$ of the fields

$$\boldsymbol{\mathcal{E}}(\mathbf{r},t) = \mathcal{F}\{\tilde{\boldsymbol{\mathcal{E}}}(\mathbf{r},\omega)\} = \int_{-\infty}^{\infty} \mathrm{d}\omega\ \tilde{\boldsymbol{\mathcal{E}}}(\mathbf{r},\omega)\exp(-\mathrm{i}\omega t), \tag{7}$$

$$\boldsymbol{\mathcal{P}}(\mathbf{r},t) = \mathcal{F}\{\tilde{\boldsymbol{\mathcal{P}}}(\mathbf{r},\omega)\} = \int_{-\infty}^{\infty} \mathrm{d}\omega\ \tilde{\boldsymbol{\mathcal{P}}}(\mathbf{r},\omega)\exp(-\mathrm{i}\omega t)\ . \tag{8}$$

For each of the frequency components $\tilde{\boldsymbol{\mathcal{E}}}(\mathbf{r},\omega)$ and $\tilde{\boldsymbol{\mathcal{P}}}(\mathbf{r},\omega)$, the wave equation (5) can be written in the frequency domain while the nonlinear contributions of the polarization can be isolated as source term on the right-hand side using Eq. (6)

$$\nabla^2\tilde{\boldsymbol{\mathcal{E}}} + \hat{\varepsilon}\omega^2 c_0^{-2}\tilde{\boldsymbol{\mathcal{E}}} = -\mu_0\omega^2\tilde{\boldsymbol{\mathcal{P}}}_{\mathrm{NL}}\ , \tag{9}$$

with the **dielectric function** $\hat{\varepsilon}(\omega) = 1 + \hat{\chi}^{(1)}(\omega)$.

Considering nonlinear optical effects first to be negligible (i.e., $\tilde{\boldsymbol{\mathcal{P}}}_{\mathrm{NL}} \approx 0$ at weak irradiance), Eq. (9) is identical to the **Helmholtz equation**

$$\nabla^2\tilde{\boldsymbol{\mathcal{E}}} + \hat{\varepsilon}\omega^2 c_0^{-2}\tilde{\boldsymbol{\mathcal{E}}} = 0\ , \tag{10}$$

whose trivial solutions are monochromatic plane waves, which follow a linear dispersion relation $|k| = \sqrt{\varepsilon(\omega)}\omega/c_0$ [74]. The proportionality constant of the dispersion relation is commonly known as the complex **index of refraction (IOR)** $\bar{n}(\omega) = \sqrt{\varepsilon(\omega)} = n(\omega) + \mathrm{i}\kappa(\omega)$. The IOR is a fundamental optical material property and hosts the full information about optical loss (or gain; given in κ) and optical diffraction and refraction (given in n) of a medium.

In the following, the Helmholtz equation is solved for cylindrical waveguide geometries, which will then be used in section 2.2 to introduce one approach to solve the nonlinear wave equation (9) in direction of a propagating fiber mode.

2.1.1 Optical modes of cylindrical fibers

Only few optical systems allow a rigorous analytic treatment to find a solution of the Helmholtz equation (10). One of those systems, and the most relevant in this work, is the step-index fiber with circular geometry. The most common implementation consists of a single core with radius R and IOR n_{co} embedded in a cladding with lower IOR

$n_{cl} < n_{co}$ (q.v. Fig. 1). Thus, light can be guided along the symmetry axis of the fiber by total internal reflection. Any guided wave of a fiber can be described by a set of optical eigenmodes. The derivation of the corresponding eigenmode solution of this waveguide type is comprehensively reviewed in the literature [75, 76] and shall just briefly be sketched out in the following.

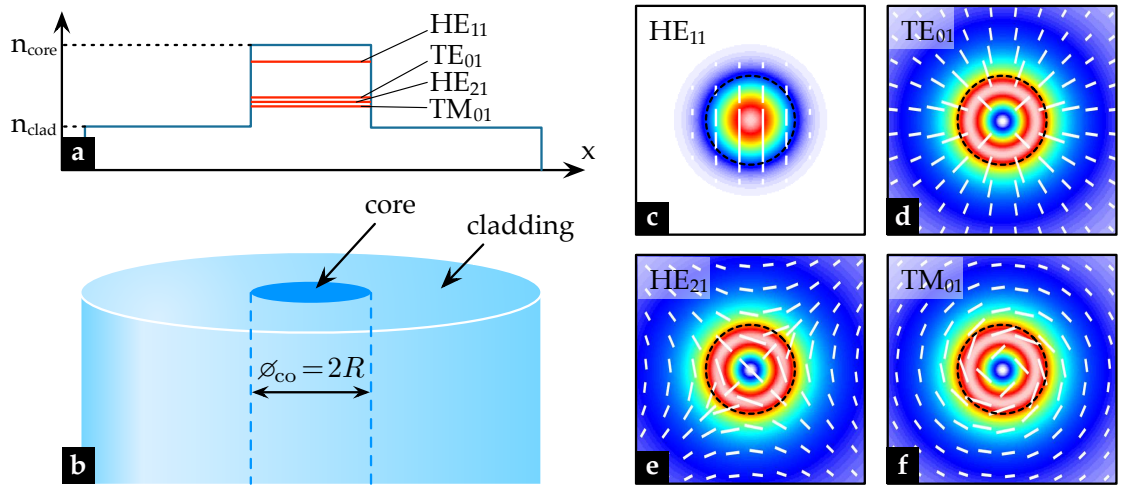

Fig. 1: **Optical modes of step-index fibers.** a) IOR profile and b) illustration of a step-index optical fiber. c-f) Intensity and polarization distributions of the first four optical modes for an index contrast of $\Delta n = 0.05$ and $\lambda/R = 1$. The dashed circle indicates the fiber core.

The optical modes can be found by solving the Helmholtz equation (10) in cylindrical coordinates section-wise, i.e. for each domain with a homogeneous IOR separately. The cylindrical waveguide geometry implies a preferential propagation direction, which allows to express the modal field in the separable form $\tilde{\boldsymbol{\mathcal{E}}}_j(x,y,z) = \tilde{\mathbf{E}}_j(r_\perp)\exp(\mathrm{i}\beta_j z)$ (and the same for the magnetic field $\tilde{\boldsymbol{\mathcal{H}}}_j(x,y,z)$)). Using this ansatz, the Helmholtz equation in cylinder coordinates (i.e., radius ϱ, angle φ and length z) can be expressed as a Bessel differential equation

$$\nabla_\perp^2\tilde{\boldsymbol{\mathcal{E}}} + (n_i^2k_0^2 - \beta^2)\tilde{\boldsymbol{\mathcal{E}}} = \partial_\rho^2\tilde{\boldsymbol{\mathcal{E}}} + \rho^{-1}\partial_\rho\tilde{\boldsymbol{\mathcal{E}}} + \varrho^{-2}\partial_\varphi^2\tilde{\boldsymbol{\mathcal{E}}} + (n_i^2k_0^2 - \beta^2)\tilde{\boldsymbol{\mathcal{E}}} = 0 \tag{11}$$

for each i$^{\text{th}}$ region with constant IOR n_i. Since both electric and magnetic field, i.e. $\tilde{\boldsymbol{\mathcal{E}}}$ and $\tilde{\boldsymbol{\mathcal{H}}}$ must satisfy the four equations (1)-(4), only two out of six components are independent. Thus, it is sufficient to solve Eq. (11) for the longitudinal field components E_z and H_z. This is possible with the general ansatz $E_{z,\mathrm{co}} = \sum_{\nu=-\infty}^{\infty} A_\nu J_\nu(p\varrho)\exp(\mathrm{i}\nu\varphi)$ in the core domain (i.e., $\varrho < R$) and $E_{z,\mathrm{cl}} = \sum_{\nu=-\infty}^{\infty} C_\nu K_\nu(q\varrho)\exp(\mathrm{i}\nu\varphi)$ in the cladding domain with the corresponding Bessel functions, J_ν and K_ν, the relative propagation constants $p = \sqrt{k_{\mathrm{co}}^2 - \beta^2}$ and $q = \sqrt{\beta^2 - k_{\mathrm{cl}}^2}$ (with $k_{\mathrm{co/cl}} = n_{\mathrm{co/cl}}k_0$, where $k_0 = \omega/c_0$ is the vacuum wave number), and the undetermined coefficients A_ν and C_ν. Applying the same ansatz for the magnetic field H_z yields two further sets of coefficients, B_ν and D_ν, overall ending up with pairs of four unknowns per mode order ν. Using the fundamental boundary conditions of electrodynamics, i.e., tangential field components (here $E_z, H_z, E_\varphi, H_\varphi$) are continuous at interfaces (i.e., at $\varrho = R$), all four unknown coefficients can be determined by satisfying the *Dirichlet* condition (i.e., $f_{\mathrm{co}}(\varrho = R) \equiv f_{\mathrm{cl}}(\varrho = R)$ with f being either one

of the field components E_z, H_z, E_φ, and H_φ). This yields four equations which can be expressed in matrix form, whereas the characteristic function of the coefficient matrix (i.e., by demanding the determinant of the matrix to be zero) yields a compact **transcendental dispersion relation** [76, 75]

$$\left[\frac{\partial_\rho J_\nu(pR)}{pJ_\nu(pR)} + \frac{\partial_\rho K_\nu(qR)}{qK_\nu(qR)}\right]\left[\frac{k_1^2\partial_\rho J_\nu(pR)}{pJ_\nu(pR)} + \frac{k_2^2\partial_\rho K_\nu(qR)}{qK_\nu(qR)}\right] = \left(\frac{\beta\nu}{R}\right)^2\left(\frac{1}{p^2}+\frac{1}{q^2}\right)^2. \quad (12)$$

For a given fiber (i.e., $n_{\mathrm{co}}, n_{\mathrm{cl}}, R$) and mode (i.e., ν, λ) the μ^{th} roots of this function over β denote for the eigenvalue of the propagating mode, and thus the modal propagation constant $\beta_{\nu\mu}$. For simplicity, in this work, appropriate optical materials are assumed to the greatest extent transparent, and fiber modes to be bound, which limits β to a real codomain within $k_{\mathrm{co}} > \beta > k_{\mathrm{cl}}$. Finding the root of Eq. (12) is a numerical practice.

2.1.2 Linear fiber mode properties in brief

Depending on the inner (core) diameter ($\varnothing_{\mathrm{co}}$) and the **numerical aperture (*NA*)** of the fiber, i.e., $NA = \sqrt{n_{\mathrm{co}}^2 - n_{\mathrm{cl}}^2}$, the fiber supports from one to multiple modes. Modes are distinguished in their propagation constant β (i.e., here $\beta = \beta_{nm}$) , their field distribution, and their polarization. The mode with the largest **effective mode index** $n_{\mathrm{eff}} = \beta/k_0$ is called the fundamental mode. Different to ridge or slab waveguides, the fundamental fiber mode is a hybrid electric (HE) mode (i.e., all electric field components are non-zero) with mode order $n = 1$ and mode number $m = 1$. The HE_{11} mode features a Gauss-like intensity distribution with the largest field overlap with the core domain compared to all other fiber modes (cf. intensity patterns in Fig. 1c-f). Also in contrast to higher-order modes, the HE_{11} has no cut-off frequency (i.e., a minimum frequency below which the mode is not bound anymore). However, it shall be noted, that in practice microbends and other fabrication imperfections introduce high losses due to scattering, which limits single-mode operation on the low frequency side.

Thus, a practical parameter to estimate the quality of the guide becomes necessary, which can be found in the so-called **V-parameter** [75]

$$V = k_0 \cdot R \cdot NA\ . \quad (13)$$

A fiber operates in the *single-mode regime* as long as the **single-mode criterion (SMC)** $V < 2.405$ is fulfilled. Scattering losses limit the parameter range additionally to $V > V_{\mathrm{crit}}$, whereas the critical limit has to be determined empirically for each fiber type. The V-parameter can also be used to estimate the number of modes M supported in the fiber using the empiric relation $M \approx V^2/2$.

Further, the linear propagation characteristics of both optical waves and pulses in any given fiber mode is described by the frequency-dependent propagation parameter β. To

expose this information $\beta(\omega)$ can be expanded in a Taylor series around a given central frequency ω_0

$$\beta(\omega) \approx \beta_0 + \beta_1(\omega - \omega_0) + \tfrac{1}{2}\beta_2(\omega - \omega_0)^2 + \mathcal{O}(\omega^3) \quad \text{with} \quad \beta_j = \left.\frac{\mathrm{d}^j\beta}{\mathrm{d}\omega^j}\right|_{\omega_0} . \tag{14}$$

According to the bandwidth of the pulse more terms have to be added in the series. The coefficients of the individual terms play a specific role in the propagation of an optical pulse. Whereas β_0 describes the fast carrier oscillation of the pulse (i.e., the central wave number), β_1 is the inverse of the **group velocity** of the pulse (i.e., $v_g = \mathrm{d}\omega/\mathrm{d}\beta$), and β_2 is the **group velocity dispersion** (often used in units of fs^2/m). The group velocity dispersion describes the relative difference between the group velocities of higher and lower frequency components of a spectrally broadband optical pulse, and, thus, is a measure of how strong a pulse disperses along propagation. In detail, the broadening of a pulse with duration T_{HP} over a propagation length L can be estimated with $\beta_2 L/T_{\mathrm{HP}}$ (in units of fs). Third and fourth order dispersions (i.e., β_3 and β_4) might also play a role if the pulse width is in the order of sub-picoseconds.

In practice, the dispersion is often expressed in terms of the technical **dispersion parameter**

$$D = -\frac{\lambda}{c_0}\frac{\mathrm{d}^2 n_{\mathrm{eff}}}{\mathrm{d}\lambda^2} = \frac{2\pi c_0}{\lambda^2}\frac{\mathrm{d}^2\beta}{\mathrm{d}\omega} , \tag{15}$$

with wavelength $\lambda = 2\pi c_0/\omega$. D is usually given in units of ps/(nm·km), which corresponds to temporal pulse spreading per bandwidth and propagation length. This parameter is denoted as **group velocity dispersion (GVD)** throughout this work to investigate fiber designs, whereas all values of D are given units of fs/(nm·cm) to account for the pulse widths and fiber lengths usually used in the experiments. The fiber dispersion is distinguished in **normal dispersion domain (NDD)** (i.e., $D < 0$) and **anomalous dispersion domain (ADD)** (i.e., $D > 0$). The wavelength, where the dispersion changes from ADD to NDD or vice versa, is denoted as **zero-dispersion wavelength (ZDW)**. It is an important benchmark of nonlinear fiber designs, as explained in sec. 2.3.1.

2.2 Nonlinear pulse propagation in optical fibers

2.2.1 Intensity-dependent refractive index

The strong confinement of optical fiber modes along meter- to kilometer-long propagation lengths significantly boosts the relevance of optical nonlinear effects. One way to understand the generation of new frequencies via nonlinear light-matter interactions, is to think of an refractive index grating (with period length $n(\omega)k_0$) inscribed by the field intensity, at which the field refracts causing an energy transfer to field components at distant wavelengths. This index modulation can particularly be understood by introducing a practical quantity, namely the nonlinear refractive index.

This is possible by simplifying the general nonlinear polarization $\tilde{\mathcal{P}}_{\mathrm{NL}}$ in Eq. (6). A first practical assumption is to consider only linear polarized electric fields and isotropic (or weakly anisotropic), and lossless, nonlinear media, resulting in identical polarization of all involved fields, i.e., $\tilde{\boldsymbol{\mathcal{E}}}/|\tilde{\boldsymbol{\mathcal{E}}}| = \tilde{\mathcal{P}}_{\mathrm{NL}}/|\tilde{\mathcal{P}}_{\mathrm{NL}}|$. The assumption further allows to drastically reduce the 21 nonzero elements of the third-order susceptibility tensor $\hat{\chi}^{(3)}$ to a single independent component [77, 78], which is straightforwardly denoted as $\chi^{(3)}_{\mathrm{eff}} = \chi^{(3)}_{xxxx}$ in the common literature (e.g., [79]). Under those assumptions, the general nonlinear polarization field can be simplified in the frequency domain to [78]

$$\tilde{\mathcal{P}}_{\mathrm{NL}}(\omega) = \varepsilon_0 C^{(3)} \chi^{(3)}_{\mathrm{eff}}(\omega;\omega',\omega'',\omega''')\tilde{\mathcal{E}}(\omega')\tilde{\mathcal{E}}(\omega'')\tilde{\mathcal{E}}(\omega''') \,. \tag{16}$$

The permutation factor is $C^{(3)} = 3$, if third-harmonic effects are neglected and only self-induced nonlinear effects are assumed (i.e., $P_{NL}(\omega = \omega + \omega - \omega) \propto \tilde{\mathcal{E}}\tilde{\mathcal{E}}\tilde{\mathcal{E}}^*$). In general, the material response $\chi^{(3)}$ can be assumed as linear combination of different nonlinear contributions, such as instantaneous electronic motions and noninstantaneous nuclear effects (e.g., stimulated Raman scattering, or molecular reorientation). This general treatment is reviewed in appendix B. For now, only electronic effects, as major source of nonlinearity in most optical glasses, shall be considered, which allows to express Eq. (16) in its most simple form

$$\tilde{\mathcal{P}}_{\mathrm{NL}}(\omega) = 3\varepsilon_0 \chi^{(3)}_{\mathrm{eff}}(\omega)\tilde{\mathcal{E}}(\omega)\tilde{\mathcal{E}}^*(\omega)\tilde{\mathcal{E}}(\omega) \,. \tag{17}$$

Inserting Eq. (17) into Eq. (9), allows to define a field-dependent IOR, based on the definition of the dielectric function from sec. 2.1

$$n^2(\omega,\mathcal{E}) = 1 + \chi_{\mathrm{eff}}(\omega,\mathcal{E}) = 1 + \chi^{(1)} + 3\chi^{(3)}_{\mathrm{eff}}|\mathcal{E}|^2 \,. \tag{18}$$

In first-order approximation $n(\omega,\mathcal{E})$ can be expressed in terms of linear perturbation Δn, i.e., $n(\omega,\mathcal{E})^2 = (n_0(\omega) + \Delta n(\omega,I))^2 \approx n_0^2 + 2n_0\Delta n$. Finally, combined with the definition of the intensity $I(\omega) = 2n_0\varepsilon_0 c_0|\mathcal{E}(\omega)|^2$, the **nonlinear refractive index (NRI)** n_2 (in units of m^2/W) can be found [78]

$$\Delta n(\omega,I) = \frac{3\chi^{(3)}_{\mathrm{eff}}}{2n_0}|\mathcal{E}|^2 = \frac{3\chi^{(3)}}{4n_0^2\varepsilon_0 c_0} I(\omega) \equiv n_2 I \quad \Longrightarrow \quad n_2 = \frac{3\chi^{(3)}_{\mathrm{eff}}}{4n_0^2\varepsilon_0 c_0} \,. \tag{19}$$

The corresponding phase term $\Delta n k_0 = k_0 n_2 I$ can be seen as an additional momentum acting on certain frequency components of the pulse causing an energy transfer. The NRI is widely used in experimental work to evaluate the nonlinearity of different materials. It will be applied in a modified form to slowly responding nonlinear liquids in sec. 3.3.1.

2.2.2 Nonlinear Schrödinger equation

The nonlinear pulse dynamic in optical fibers can become quite complex, and requires a rigorous model involving all relevant effects. However, to solve the general vectorial

nonlinear wave equation in Eq. (9) is a nontrivial and computational resource consuming task. Thus, many simplified nonlinear propagation equations were used in literature (e.g., a very good overview is given in the review [80]), each owing their own benefits and limitations. Within the framework of this work, the nonlinear Schrödinger equation in the generalized form was chosen to investigate pulse propagation in the special fiber systems numerically. To understand its limitations and to form the theoretical background for specialized versions introduced later the derivation of the this widely used amplitude equation shall be outlined in the following. Note that, different to many publications, the derivation does not follow the approach by Agrawal presented in his book [79], but the more general derivation presented by Mamyshev and Chernikov [81]. Alternative mathematically rigorous derivations can be found, e.g., in the works by Kolesik and Moloney [82] and the review by Courairon *et al.* [80].

The solution of the linear wave equation (11) can be used to simplify the nonlinear wave equation (9). Therefore, the monochromatic field ansatz is extended to

$$\tilde{\boldsymbol{\mathcal{E}}} = \mathbf{e}_0 \tilde{F}(r_\perp;\omega)\tilde{U}(z;\omega)\exp(\mathrm{i}\beta_j(\omega)z)\ , \tag{20}$$

where $\beta_j = n_{j,\mathrm{eff}}(\omega,\tilde{\boldsymbol{\mathcal{E}}})\omega/c_0$ is the propagation constant of the j^{th} perturbed fiber mode in the nonlinear system. Heuristically, the ansatz separates a slowly varying envelope $\tilde{U}$ from the fast carrier wave oscillating with ω. The real transversal field pattern $\tilde{F}$ is real.

Inserting the perturbation ansatz from Eq. (20) into Eq. (9) and splitting of the Laplace operator into its transversal and perpendicular parts (i.e., $\nabla^2 = \nabla_\perp^2 + \partial_z^2$) yields

$$\tilde{U}\underbrace{\left[\nabla_\perp^2\tilde{F} + n_i^2 k_0^2\tilde{F} - \beta_j^2\tilde{F}\right]}_{\text{Eq. (11)}\,\Rightarrow\,0} + \underbrace{\tilde{F}\partial_z^2\tilde{U}}_{\text{SVEA}\,\Rightarrow\,0} + 2\mathrm{i}\beta_j\tilde{F}\partial_z\tilde{U} = -\mu_0\omega^2\tilde{P}_{\mathrm{NL}}(\tilde{F},\tilde{U})\mathrm{e}^{-\mathrm{i}\beta_j z} \tag{21}$$

The first term is the eigenmode problem and becomes zero in waveguides assuming the nonlinear perturbation of the propagation constant $\bar{\beta}_j$ to be weak. Note that the latter is intrinsically given by the ansatz in Eq. (20) already, since the transversal field is assumed real and propagation invariant, i.e., $\tilde{F} \neq f(z)$. Further, we assume that the field envelope $\tilde{U}(\omega,z)$ varies only slowly along the propagation along z, so that $\partial_z^2\tilde{U} \ll \beta_j\partial_z\tilde{U}$. This allows neglecting the second z-derivative in Eq. (21), commonly known as *slowly varying envelope approximation* (SVEA). Both assumptions allow to simplify Eq. (21) to

$$\tilde{F}\partial_z\tilde{U} = \mathrm{i}\frac{3\mu_0\omega^2}{2\beta_j(\omega)}\tilde{P}_{\mathrm{NL}}(\tilde{F},\tilde{U})\mathrm{e}^{-\mathrm{i}\beta_j(\omega)z}\ . \tag{22}$$

Indeed, Eq. (22) confirms the nonlinear polarization as source of the slow field variation along the propagation. The general nonlinear polarization $\tilde{P}_{\mathrm{NL}}$ is derived in detail for

an isotropic noninstantaneous medium in appendix B. Using the expression in Eq. (83) from there, $\tilde{P}_{\mathrm{NL}}$ in the propagation equation can be expressed in $\tilde{U}$

$$\begin{aligned}\tilde{F}\partial_z\tilde{U} = \mathrm{i}\frac{3k_0}{2n_{\mathrm{eff},j}(\omega)}\int \mathrm{d}\omega' \int \mathrm{d}\omega''[\tilde{F}\tilde{U}](\omega')[\tilde{F}\tilde{U}]^*(\omega'+\omega''-\omega) \\ \times [\tilde{F}\tilde{U}](\omega'')\chi^{(3)}(\omega-\omega')\mathrm{e}^{\mathrm{i}\Delta\beta z}\,,\end{aligned} \tag{23}$$

with the phase mismatch $\Delta\beta = \beta_j(\omega') + \beta_j(\omega'') - \beta_j(\omega'+\omega''-\omega) - \beta_j(\omega)$. We normalize Eq. (23) to the power by (1) multiplying $\tilde{F}$ from the left side, (2) integrating over the transversal coordinates $r_\perp$, and (3) dividing the equation by $\int \mathrm{d}^2 r_\perp \tilde{F}^2$. Thus, Eq. (23)

$$\begin{aligned}\partial_z\tilde{U} = \mathrm{i}\frac{3k_0}{2n_{\mathrm{eff},j}(\omega)}\int \mathrm{d}\omega' \int \mathrm{d}\omega'' G(\omega,\omega',\omega'')\tilde{U}(\omega') \\ \times \tilde{U}^*(\omega'+\omega''-\omega)\tilde{U}(\omega'')\chi^{(3)}(\omega-\omega')\mathrm{e}^{\mathrm{i}\Delta\beta z}\,,\end{aligned} \tag{24}$$

with the mode field overlap

$$G(\omega,\omega',\omega'') = \frac{\int \mathrm{d}^2 r_\perp \tilde{F}(r_\perp;\omega)\tilde{F}(r_\perp;\omega')\tilde{F}(r_\perp;\omega'+\omega''-\omega)\tilde{F}(r_\perp;\omega'')}{\int \mathrm{d}^2 r_\perp \tilde{F}^2(r_\perp;\omega)}\,. \tag{25}$$

In practice, it is useful normalize $\tilde{U}$ to the power of the field $P = \int \mathrm{d}^2 r_\perp I = 2n_{\mathrm{eff},j}\varepsilon_0 c_0 \times \int F^2 \mathrm{d}^2 r_\perp |U|^2$. This yields the normalized amplitude $\tilde{A}'(z;\Delta\omega) = \sqrt{2n_{\mathrm{eff},j}\varepsilon_0 c_0 \int \mathrm{d}^2 r_\perp F^2} \times \tilde{U}\exp(i[\beta_j(\omega) - \beta_{j,0} - \beta_{j,1}\Delta\omega]z)$ with $\Delta\omega = \omega - \omega_0$. The phase of this substituent is chosen such that it incorporates the full fiber dispersion minus the fast carrier oscillation (associated with $\beta_{j,0}$) and the group velocity of the pulse (associated with $\beta_{j,1}$). The latter corresponds to the common transformation in time domain to a reference frame moving with the pulse at the group velocity $v_g = \beta_{j,1}^{-1}$ [81, 79].

The normalization changes G to $G' = G/\int \mathrm{d}^2 r_\perp \tilde{F}^2$. To the first order, G' can be approximated with $G'(\omega,\omega',\omega'') \approx [A_{\mathrm{eff}}(\omega)A_{\mathrm{eff}}(\omega')A_{\mathrm{eff}}(\omega'')A_{\mathrm{eff}}(\omega'+\omega''-\omega)]^{-1/4}$ [83], which introduces the **effective mode area** $A_{\mathrm{eff}} = (\int \mathrm{d}^2 r_\perp \tilde{F}^2)^2 / \int \mathrm{d}^2 r_\perp \tilde{F}^4$. The linear separation in G' now justifies a further renormalization of the field amplitude to $\tilde{A} = \tilde{A}'/A_{\mathrm{eff}}^{1/4}$, so that $\tilde{A}$ is in units of intensity W/m. Finally, we obtain the so-called **generalized nonlinear Schrödinger equation (GNSE)** [81]

$$\begin{aligned}&\partial_z\tilde{A}(z;\omega) - \mathrm{i}\left[\beta_j(\omega) - \beta_{j,0} - \beta_{j,1}\Delta\omega\right]\tilde{A} \overset{\text{Eq. (14)}}{=} \partial_z\tilde{A} - \mathrm{i}\sum_{k\geq 2}\frac{1}{k!}\beta_{j,k}\Delta\omega^k\tilde{A} \\ &= \mathrm{i}\frac{3k_0}{4n_{\mathrm{eff},j}^2\varepsilon_0 c_0\sqrt[4]{A_{\mathrm{eff}}}}\int \mathrm{d}\omega' \int \mathrm{d}\omega''\tilde{A}(\omega')\tilde{A}^*(\omega'+\omega''-\omega)\tilde{A}(\omega'')\chi^{(3)}(\omega-\omega') \\ &= \mathrm{i}\bar{\gamma}(\omega)\mathcal{F}^{-1}\left\{A(z;t)\left[R * |A|^2\right]\right\}\,,\end{aligned} \tag{26}$$

with the modified **nonlinear gain parameter** $\bar{\gamma} = k_0 n_2 / A_{\mathrm{eff}}^{1/4}$, the convolution operator $[*]$, and the **nonlinear response function (NRF)** $R(t)$ (normalized to $\int \mathrm{d}t R = 1$ and

introduced with Eq. (82) in appendix B). The last step in Eq. (26) also incorporated the definition of the NRI in Eq. (19).

Equation (26) is the most physical representation of the different GNSEs known from literature and used throughout this thesis. It features the full dispersion of the propagation parameter $\beta_j(\omega)$ and the nonlinearity $\bar{\gamma}(\omega)$. Broadband loss (or gain) can straightforwardly be included adding the term $\frac{1}{2}\alpha(\omega)\tilde{A}$ on the left-hand side. Most notably, the renormalization to the field $\tilde{A}$ incorporates the frequency dependent mode area in the temporal convolution, since the temporal envelope is now $A(z;t) = \mathcal{F}\{\tilde{A}(z;\omega)/\sqrt[4]{A_{\text{eff}}}\}$. This normalization is often forgotten in the recent literature, but was explicitly proposed as correction, e.g., by Laegsgaard [83].

From Eq. (26) the more prominent version of the GNSE can be derive by applying the following operations:

1. Assume the effective mode areas to be frequency independent, i.e., $[A_{\text{eff}}(\omega)A_{\text{eff}}(\omega')A_{\text{eff}}(\omega'')A_{\text{eff}}(\omega'+\omega''-\omega)]^{1/4} \approx A_{\text{eff}}(\omega_0)$, whereas the $A_{\text{eff}}^{-1/4}$ factors from the field normalization can be combined to the common nonlinear gain parameter $\gamma(\omega) = k_0 n_2 / A_{\text{eff}}$,

2. Expand the nonlinear parameter in a Taylor series, i.e., $\gamma(\Delta\omega) \approx \gamma_0 + \gamma_1\Delta\omega$, with $\gamma_k = \partial_\omega^k \gamma(\omega)|_{\omega_0}$,

3. Transform Eq. (26) into the time domain.

These changes result in the GNSE commonly known from literature (cf. Eq. (2.3.36) in [79])

$$\partial_z A(z;t) + \frac{\alpha}{2}A - \sum_{k\geq 2} \mathrm{i}^{k+1}\beta_{j,k}\partial_t^k A = \mathrm{i}\gamma_0\left(1 + \mathrm{i}\frac{\gamma_1}{\gamma_0}\partial_t\right)\left(A(z,t)\left[R * |A|^2\right]\right) . \tag{27}$$

At this point, further simplifications can be made on Eq. (27) to achieve different model systems, which are useful to study specific nonlinear effects in optical fibers. The most relevant for this work, is the **specialized nonlinear Schrödinger equation (NSE)**

$$\partial_z A(z;t) + \mathrm{i}\tfrac{1}{2}\beta_{j,2}\partial_t^2 A = \mathrm{i}\gamma_0|A|^2 A , \tag{28}$$

which allows to find optical solitons as introduced in sec. 2.3.3.1. The specialized NSE can be obtained assuming a lossless (i.e., $\alpha = 0$), second-order dispersive (i.e., $\beta_{j,k} = 0$ for $k > 2$) fiber with non-dispersive nonlinear gain (i.e., $\gamma_1 = 0$), and instantaneous nonlinear response (i.e., $R(t) = \delta(t)$).

2.2.3 Nonlinear gain parameter of step-index fibers

With the GNSE the nonlinear gain parameter γ was introduced, which combined the material-specific NRI n_2 with the mode-specific effective mode area A_{eff}. It has been shown in the scope of this work [84] and others [85], that the standard definition of A_{eff} deviates strongly from the accurate vectorial mode area. A powerful alternative is

obtained using the identity between the Poynting vector S_z and the intensity $I \propto |\tilde{F}^2|$, which yields [86]

$$\gamma = \frac{k_0 n_2}{A_{\text{eff}}} = \frac{k_0 n_2 \int \mathrm{d}^2 r_\perp \tilde{F}^4}{(\int \mathrm{d}^2 r_\perp \tilde{F}^2)^2} = k_0 \frac{\int_A n_2 S_z^2 \,\mathrm{d}\mathbf{r}}{(\int_A S_z \,\mathrm{d}\mathbf{r})^2} \,. \tag{29}$$

The analytic expression of the Poynting vector S_z is known for step-index fiber modes (q.v. Eq. (77 in appendix B) and was used in this work to deduce a semi-analytical form for γ [84]

$$\gamma = \frac{2\pi}{\lambda} \frac{n_2^{\text{co}} N^{\text{co}} + n_2^{\text{cl}} N^{\text{cl}}}{(D^{\text{co}} + D^{\text{cl}})^2} = A \cdot n_2^{\text{co}} + B \cdot n_2^{\text{cl}} \tag{30}$$

$$\begin{aligned} \text{with} \quad N = 2\pi \int_\star^\star \mathrm{d}\varrho \; \varrho \Big[& {C_1}^2 G_{m-1}^4(r) + {C_2}^2 G_{m+1}^4(r) \\ & + \left(\tfrac{1}{2}{C_3}^2 + 2C_1C_2\right) G_{m-1}^2(r) G_{m+1}^2(r) \Big] \,, \end{aligned} \tag{31}$$

$$D = 2\pi \int_\star^\star \mathrm{d}\varrho \; \varrho (C_1 \, G_{m-1}^2(r) \; + \; C_2 \, G_{m+1}^2(r)). \tag{32}$$

Thus, γ splits in a core and cladding contribution, i.e., A and B, assuming a constant NRI in each region. The star symbols indicate that the radial integration range for N and D changes depending on the considered region. Within the core, indicated by index co, the range is $[0, R]$, whereby in the cladding, indicated by index cl, it is $[R, \infty]$. Also, the C_i constants and the generalized Bessel functions G_m vary for each region, accordingly to the definitions in Tab. 6 in appendix B. While the integrals of the D coefficients are fully solvable for both core and cladding, this is not the case for the integrals of N. But it breaks down to a single radial integral only, which can be calculated significantly faster than the area integral. It shall be noted, that, although the cladding contribution B can be neglected in case of well-confined modes in fibers with a highly nonlinear core [84], each calculation of γ within this work incorporates both core and cladding contribution for completeness.

2.2.4 Numerical solution of the Schrödinger equation

The nonlinear character of the NSEs requires sophisticated methods to approach a solution. Analytical solutions can be found only under very strong assumptions and, e.g., using inverse scattering methods [87]. For practical applications, however, the solution of a non-ideal input pulse (e.g., featuring frequency chirps and asymmetric pulse profiles) propagating in a fiber with unusual dispersion landscape and losses is often more relevant. Thus, several numerical algorithms have been developed to solve Eq. (26) efficiently. Numerical models offer the great benefit to study the modification of the solution by adding or neglecting specific terms of the underlying complex equation, or by changing the input conditions. One of these algorithms has been implemented in the scope of this work and is introduced in the following.

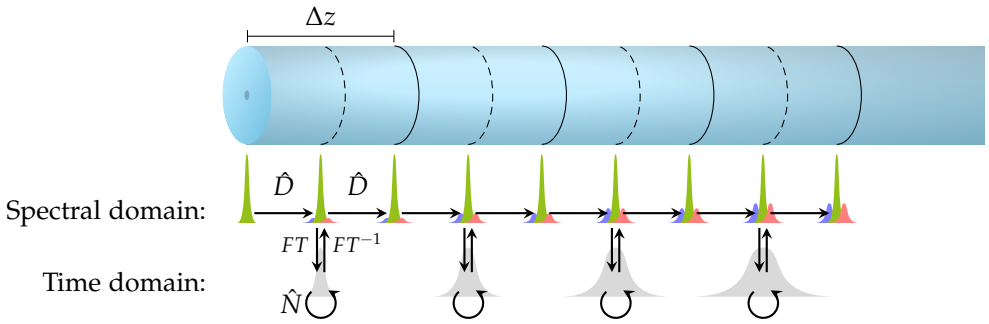

Fig. 2: **Split-step Fourier algorithm.** Schematics to visualize the simulation of the propagation of optical pulses in fibers. The propagation length L is divided in small calculation steps h. For each step the nonlinear equation is solved alternately in time and in frequency domain.

As indicated in Eq. (26), the nonlinear part of the GNSE is solved more efficiently in the time domain, whereas the linear part (i.e., loss and dispersion terms) can straightforwardly be solved in the frequency domain. Such a procedure can indeed be implemented using the so-called *split-step algorithm*, that builds on the split up of the GNSE in a dispersion ($\hat{D}$) and a nonlinear operator ($\hat{N}$), whereas the first is operated in the frequency domain and the latter in the time domain, i.e.,

$$\partial_z A = (\hat{D} + \hat{N})A \begin{cases} \partial_z \tilde{A} = \hat{D}\tilde{A} & \text{in frequency domain,} \\ \partial_z A = \hat{N}(A) & \text{in time domain.} \end{cases} \tag{33}$$

The solution of a propagation step is depicted in Fig. 2 and formally given by

$$\tilde{A}(z+h;\omega) = \mathrm{e}^{\frac{h}{2}\hat{D}}\mathcal{F}^{-1}\left\{\int_z^{z+h} \hat{N}\left(\mathcal{F}\left\{\mathrm{e}^{\frac{h}{2}\hat{D}}\tilde{A}(z;\omega)\right\}\right)\mathrm{d}z\right\} . \tag{34}$$

Further details on the numerical implementation of the algorithm are given in the appendix B. Here, also the parameters of all simulations shown in the main part of this thesis are listed in Tab. 8. Therefore, the general dispersion $\beta(\omega)$ and nonlinear gain $\gamma(\omega)$ are expanded in a low-order Taylor series, just to provide an estimate of the used system parameters.

Note that **optical shot noise** was included, when needed, by adding one photon per mode with random phase noise ϕ_{rand} to the input pulse. The corresponding noise field can be expressed as $\tilde{A}'_{\text{noise}}(\omega) = \sqrt{\hbar\omega\Omega}\exp(\mathrm{i}\phi_{\text{random}})$ with the spectral resolution of the numerical grid Ω and the random phase ϕ_{rand}. The physical meaning of this model is that every laser (gain medium) emits at least one photon in frequency channels offside of the pump spectrum due to parasitic optical, thermal, vibrational, or optomechanical transitions – an assumption that surely overestimates the noise bandwidth, but possibly underestimates the noise amplitude in vicinity of the pump frequency.

2.3 Relevant nonlinear effects for supercontinuum generation

2.3.1 Overview of third-order nonlinear effects in fibers

Optical fibers support a multitude of nonlinear effects, which can become dominant depending on the width, wavelength, and peak power of the input pulse. Fig. 3 shows a coarse overview of parameter domains of the most dominant nonlinear effects in fibers, ignoring, however, the respective peak power demands for the individual processes. The operation domains strongly depend on dispersion and pulse widths, whereby the latter can be roughly distinguished in a quasi-continuous wave regime (i.e., pulse widths $>$ 10 ps) and an ultrafast (i.e., sub-picosecond) pulse regime. Since only few highly tuneable laser systems allow to adjust both pulse width and center wavelength, the dispersion landscape of conventional silica fibers is fix, which usually allows only limited access to other spectral conversion regimes with one system.

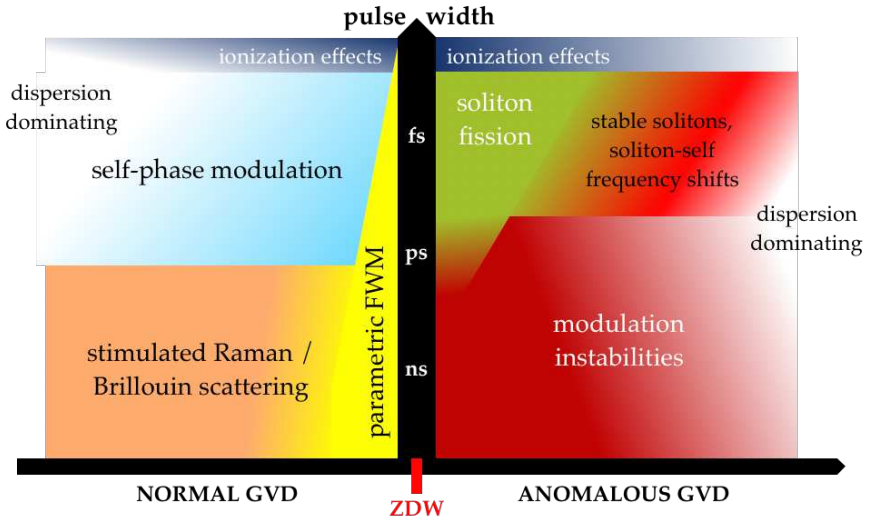

Fig. 3: **Operation domains of dominating nonlinear effects in optical fibers.** The operation domains are defined by the input pulse width and the dispersion of the fiber. The wavelength of vanishing dispersion is denoted as zero-dispersion wavelength (ZDW).

Each nonlinear operation domain offers the possibility of generating ultrabroad spectra, so-called supercontinuum (SC), given a suitable input power. However, the respective SC come with very specific properties and power demands. Soliton-mediated spectral broadening in the ultrafast pulse regime is well known to feature multiple octaves of bandwidths, due to the rich underlying soliton dynamics, as well as a close-to-perfect temporal coherence [27]. Hence, soliton-mediated SC generation is in the focus of the current efforts in nonlinear optical sciences. However, solitons are largely unexplored in highly noninstantaneous media, such as liquids, and might offer a plethora of research opportunities and advances in SC light sources. This work focuses on the anomalous dispersion regime and sub-picosecond pulses to investigate soliton dynamics at the boundary to modulation instabilities.

In the next sections, the effect of the individual nonlinear terms of the NSE will be discussed and an heuristic understanding of optical solitons will be given, as well as of their dynamics. The simulations results in Fig. 4 are used to illustrate the impact of the

various terms of the NSE on pulse propagation. The individual panels of Fig. 4 show the pulse evolution, the input and output pulse, and the spectrogram of the output pulse (i.e., the spectral content along the pulse). The simulation gives also access to the differential phase of the pulse, which is calculated from the field $A(t, z_i) = a_i(t, z_i)e^{i\phi_i(t,z_i)}$ at position z_i via $\partial_z\varphi(t, z_i) = (\phi_i - \phi_{i-1})/(z_i - z_{i-1})$. Throughout the thesis the differential phase is denoted as *phase* for simplicity.

2.3.2 Self-phase modulation

The effect of **self-phase modulation (SPM)**, also denoted as *nonlinear dispersion*, is a direct consequence of the nonlinear Kerr effect. To illustrate the SPM effect on the pulse propagation, one may consider the dispersion-less form of the NSE (28), that is $\partial_z A(z;t) = i\gamma_0|A|^2A$. Here, the weakly nonlinear field ansatz $A(z;t) = \sqrt{P_0(0;t)}\exp(i\phi_{NL}(z;t))$ results in the nonlinear phase $\phi_{NL}(z;t) = \gamma_0 P_0(t)z$. Thus, as consequence of the peak power, the pulse experiences a power-dependent phase shift. This phase shift varies along the pulse and causes the creation of new frequencies. This can be shown straightforwardly by calculating the instantaneous frequency of the pulse at delay τ and a propagation length L, which is $\delta\omega = -\partial_\tau\phi_{NL}(L;\tau) = -\gamma_0 L\partial_\tau P(\tau)$.

From this small apprentice piece, it can be seen that the frequency shifts accordingly to the slope of the instantaneous pulse power. As consequence, the pulse transfers energy to spectral side bands $\omega_0 \pm \delta\omega$ (q.v. Fig. 4d), which broadens the pulse spectrum and modulates the temporal phase, often referred to as *frequency chirp* (q.v. Fig. 4e).

2.3.3 Optical solitons

2.3.3.1 *Fundamental properties*

Solitons, as a solution of the NSE in Eq. (28), and their unique properties are well studied in numerous works in mathematics, physics and, particularily, in fiber optics [88, 89, 4, 90, 91, 92, 15, 93, 94, 95, 96, 28], and are well summarized in the common literature (e.g., [97, 98]). Due to the vast scope of these studies, only the very basic properties of these states can be summarized in this section.

In an instantaneous nonlinear and lossless medium, the nonlinear dispersion (i.e., SPM) can be compensated by second-order dispersion (i.e., GVD) during propagation. In that case, the dispersive pulse chirp is perfectly compensated, which results in a flat phase (q.v. Fig. 4h), and an **optical temporal soliton** forms. One of the most striking features for applications in laser engineering and telecommunications is the intrinsic non-dispersive propagation of solitons (q.v. Fig. 4i). A soliton preserves its shape in time and spectrum during propagation, which is visualized by a localization in the spectrogram in Fig. 4g. In order to excite such a state in common optical fibers, the dispersion ought to be anomalous to form solitons to compensate the nonlinear dispersion, since most materials feature a positive effective nonlinearity (i.e., $n_2 > 0$). For instance, the phase curvature of anomalous GVD in Fig. 4b is opposite to the phase curvature of SPM in Fig. 4e. Moreover, the

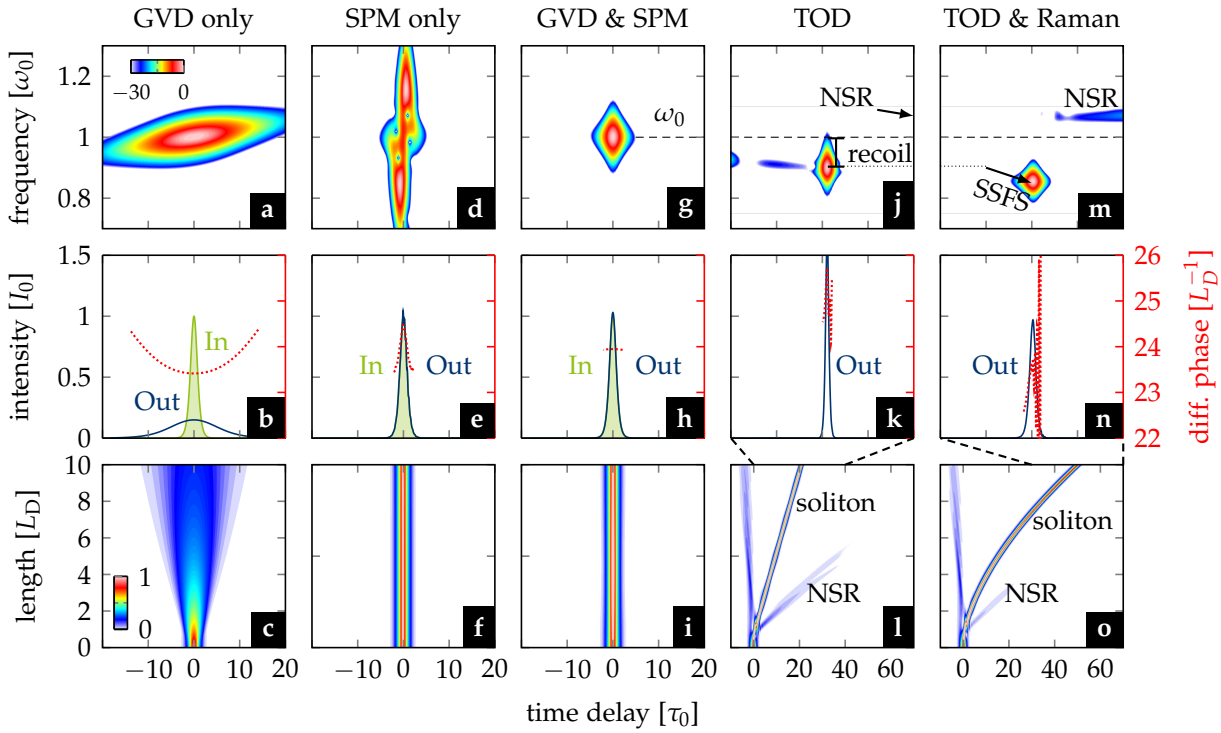

Fig. 4: Pulse propagation in several linear and nonlinear systems. (a,d,g,j,m) Spectrogram, (b,e,h,k,n) input/output pulse shape and the differential phase $\partial\phi/\partial z$, and (c,f,i,l,o) evolution of a 50 fs pulse along 10 L_D. The chosen soliton numbers are (a-i) $N = 1$, and (j-o) $N = 2$.

nonlinear dispersion depends on the pulse shape, and, in order to perfectly compensate the GVD, ideal fundamental solitons need to belong to the single-parameter family

$$a(Z,T) = N\,\mathrm{sech}(NT)\exp(\mathrm{i}N^2Z/2)\ . \tag{35}$$

Eq. (35) fulfills the renormalized NSE, which can be obtained by applying the normalizations $T = t/T_0$, $L_D = T_0^2/|\beta_2|$, $Z = z/L_D$, and $a = A/\sqrt{P_0}$ to Eq. (28)

$$\mathrm{i}\partial_Z a(Z;T) + \frac{1}{2}\partial_T^2 a = -N^2|a|^2 a \tag{36}$$

$$\text{with } N^2 = \frac{L_D}{L_{NL}} = \frac{\gamma_0 P_0 T_0^2}{|\beta_2|}. \tag{37}$$

The (classical) **soliton number** N plays an essential role in evaluating nonlinear systems, as we will see further on. It links the most essential parameters of the optical pulse and the fiber system, namely the pulse width T_0 (according to a half-power (FWHM) width of $T_{HP} = 2\ln(1+\sqrt{2})T_0$), the peak power P_0, the second-order dispersion β_2, and the nonlinear gain parameter γ_0. The latter includes the total NRI of the system. In theory, input pulses for $N > 1.5$ form solitons of higher order. Those solitons can be expressed as superposition of fundamental (i.e., $N = 1$) solitons, and their propagation is characterized by a periodic broadening and narrowing of the pulse width (and the spectrum, respectively), which is known as *soliton breathing* [98]. However, in practice, higher-order solitons are hard to excite, since realistic fibers deviate from the ideal model

in dispersion and nonlinearity. Those deviations act as perturbation on the higher-order soliton propagation causing characteristic effects, which are briefly described in q.v. sec. 2.3.3.2, 2.3.3.3 and 2.3.4.

The normalization of Eq. (36) introduces two further helpful quantities, which are the **dispersion length** $L_D = T_0^2/|\beta_2|$ and the **nonlinear length** $L_{NL} = (\gamma_0 P_0)^{-1}$. The length scales can be used to estimate whether dispersive (for $L \geq L_D$) or nonlinear effects (for $L \geq L_{NL}$) dominate the pulse propagation in a fiber of length L. If the fiber length is longer than or comparable to both lengths (i.e., $L \geq [L_D, L_{NL}]$), an interplay of both dispersion and nonlinearity leads to a characteristically different pulse propagation, which may evoke the formation of solitons.

Finally, it is important to note that most realistic fiber systems underlie deviations from the ideal model described with Eq. (36), which includes losses, mode field dispersion (often forgotten), higher order dispersion, or nonlinear scattering effects. In some cases, those deviations can be handled as perturbations on the soliton, which modify its properties (q.v. sec. 2.3.3.2 and 2.3.3.3). In other cases, those perturbations are too strong and the soliton, although potentially created in the fiber, decays after a certain propagation length, which in turn conflicts with the self-maintaining character of a soliton. Moreover, in some narrower definitions, solitons are solutions of integrable mathematical equations and have to withstand collisions with other solitons of the same type, which is not always easy to proof. Thus, throughout this work, the term soliton is used in the wider framework of a **solitary wave**, which is characterized by a self-similar pulse shape (in time and spectrum) over a limited propagation length. In particular, the use of the term soliton does not imply the mathematical integrability of the governing NSE, which is used as soliton condition in theory.

2.3.3.2 *Impact of third-order dispersion*

The effect of third-order dispersion (TOD) can straightforwardly be added to Eq. (36) with the term $\delta_3 \partial_T^3 a$ with $\delta = \beta_3/(6|\beta_2|T_0)$. This term can be understood as perturbation on the ideal β_2 soliton, which has been extensively studied theoretically (e.g., [99, 100, 4, 101, 102, 103, 104]) and utilized in many experiments in fibers [105, 106, 42, 107] and ridge waveguides [108, 109, 110]. In proximity to the ZDW, the soliton spectrum may overlap with perfectly phase-matched resonance frequencies of linear waves to which the soliton transfers energy. The efficiency of this process depends on the spectral seed energy (i.e., spectral overlap), and the group-velocity mismatch between soliton and the phase-locked radiated wave. The process shows similarities to the emission of radiation from an accelerated charged particle in relativistic physics, the linear wave emitted from a soliton is often called *(Vavilov–)Cherenkov radiation*, but also known as **non-solitonic radiations (NSRs)**, or *dispersive waves*. If the perturbation is strong enough, TOD can lead to a split-up of the pulse into maximum N consecutive fundamental solitons, which is known as *soliton fission* and is briefly described in sec. 2.3.4.

The coupling between NSR and solitons is well studied theoretically in many works (e.g. by Gordon [90], Akhmediev *et al.* [15], Herrmann *et al.* [111], Biancalana *et al.* [93], or Efimov *et al.* [112]). Those studies reveal a **phase matching condition** (resonance condition), that links a fundamental optical soliton to its radiated NSR, given by

$$\Delta\beta \approx \beta(\omega) - \beta_s - (\omega - \omega_s)\beta_{1,s} - \tfrac{1}{2}\gamma_0 P_0 \equiv 0 \,. \tag{38}$$

The condition compares the flat phase of a soliton (i.e., $\beta_s + \frac{1}{2}\gamma_0 P_0$) with the general dispersion of a linear wave (i.e., $\beta(\omega)$) in the moving frame of the soliton (i.e., $(\omega - \omega_s)\beta_{1,s}$), which accounts for the group velocity match. Condition (38) can be used to calculate the frequency of the radiated NSR in case the soliton frequency is given, or vice versa. However, it shall be noted that the exhaust of energy to NSR causes the soliton to shift deeper into the ADD. This shift is called the *soliton recoil* (q.v. Fig. 4j) and can heuristically be explained by momentum conservation between the radiated field and the soliton [15, 93]. The recoil modifies the soliton net phase (cf. red curve in Fig. 4k) and, thus, causes a temporal shift. However, this shift depends on a multitude of parameters (e.g., amplitudes and frequencies of each field involved) and is hard to take into account when determining the frequencies of solitons and NSR from a measured spectrum.

Optical trapping of NSR and further nonlinear energy exchange between solitons and NSR (as well as other linear waves) is possible via four-wave mixing under certain conditions and may lead to a continuous red-shift of the soliton frequency and a blue-shift of the NSR [113, 114, 112, 95].

Note that, despite the reasonable understanding of NSR generation, the theoretical description lacks in a discrete description of the wave mixing mechanics and proper energy conservation laws. Thus, NSR generation is still object of recent investigations. Alternative descriptions of this effects include spectral coupling between nonlinear radiation modes [115], or cascaded four wave mixing through the spectral valley between soliton and NSR [116].

2.3.3.3 *Impact of short-term noninstantaneous nonlinearities*

Short-term noninstantaneous nonlinear effects in the NSE were studied in the framework of stimulated Raman scattering in silica fibers. The temporal response (and the spectral gain, respectively) of the Raman effect in silica is well measured and modelled [117, 118, 119]. The Raman effect is mostly included in the NSE by the quasi-instantaneous approximation of the general convolution term in Eq. (27). Therefore, the **response function** R is assumed to be

$$R(t) = (1 - f_R)\delta(t) + f_R h_R(t) \,, \tag{39}$$

with the Dirac delta function $\delta(t)$ representing the instantaneous electronic nonlinear effect, the Raman fraction $f_R \approx 0.18$, and the characteristic Raman response of silica h_R [119]. When the pulse width is assumed to be much longer than the response time

(i.e., $T_0 \gg T_R = 32\,\mathrm{fs}$), the field intensity can be expanded in a Taylor series (i.e., $|A(z;t-t')|^2 \approx |A(z;t)|^2 + t'\partial_t|A(z;t)|^2$) and the convolution integral can be approximated with

$$\int_{-\infty}^{\infty} \mathrm{d}\tau\, h_R(\tau) * |A(z;t-\tau)|^2 \approx |A|^2 + T_R \partial_t |A|^2 \,, \tag{40}$$

with the response time $T_R = f_R \int_0^\infty \mathrm{d}t h_R(t)$. It is possible to find a modified soliton solution of the NSE (36) extended by the (renormalized) Raman term from Eq. (40) [89, 120]. The Raman term leads to a linear frequency red-shift of solitons over propagation, also known as soliton **self-frequency shift (SFS)** [121] or intrapulse (i.e., self-induced) Raman scattering. The strength of red-shift increases for decreasing pulse width, or increasing spectral overlap between pulse spectrum and Raman gain spectrum, respectively. Moreover, the soliton adiabatically adjusts its pulse width when shifting into domains of higher or lower dispersion to maintain its fundamental soliton condition $N = 1$.

SFS serves as formidable mechanism to tune the frequency of soliton-governed light sources [14], whereas it has detrimental effects for the channel stability of soliton telecommunication networks [11]. It also has been found, that the SFS can be cancelled by TOD, where the radiation pressure of an emitted NSR can de- or accelerate the soliton in its Raman driven motion [93]. Notably, the consecutive stabilized state of this manifold perturbed system can still be described as soliton [120], which is in perfect balance between higher-order dispersion, dispersive nonlinearity, and noninstantaneous effects, indeed forming a separate family of meta-stable states.

2.3.4 Soliton-mediated supercontinuum generation

2.3.4.1 *Key properties of supercontinua*

The complex interplay of multiple nonlinear optical effects, such as SPM, four-wave mixing, soliton fission, and stimulated Raman scattering can generate broadband *supercontinuum (SC)* spectra. Those spectra feature key properties, such as bandwidth, spectral density, and temporal coherence, which strongly depend on the governing nonlinear mechanics. In general, the complex nonlinear interactions depend manifold on the fiber dispersion and the nonlinear gain. Thus, it is not straightforward to predict or estimate the bandwidth or even the spectral envelope of a nonlinear supercontinuum (SC) source. However, quantifying the spectral properties gives insights into the nonlinear dynamics of the broadening process and potentially allows to optimize it.

The most obvious benchmark of a SC, is the **spectral bandwidth**, which is often measured in terahertz or *octaves*. Octaves count the amount of frequency doublings that are needed to go from the low-frequency edge of the spectrum to the high-frequency edge (e.g., a spectral extent from ω_1 to $\omega_2 = 3\omega_1$ spans 1.5 octaves). The bandwidth is typically measured between the most outlying edges of a *continous* spectrum. The minimum spectral contrast forming the edge threshold (i.e., the minimum spectral power density, relative to the maximum spectral power density, considered to be within the bandwidth), should always be noted with the bandwidth. Typical bandwidths are given at

20 dB to 30 dB spectral contrast, and sometimes reach across gaps of vanishing spectral power density (i.e., discontinuous spectra). In practice, a pulse with a flat-top spectrum covering at least one octave of bandwidth can be compressed to a single-cycle electric oscillation field.

The **power density** $S(\lambda) = \partial P/\partial\lambda$ (in units $\mathrm{W\,nm^{-1}}$ or $\mathrm{dBm\,nm^{-1}}$) is a further quantity of SC with practical relevance. It denotes the power of the SC source being available after filtering, which is relevant for a multitude of applications, e.g., in spectroscopy. It further adds to the *brightness* (or luminous flux in units of lumen) of the laser source.

A further parameter is the pulse-to-pulse stability of a SC spectrum. Each broadband emission process underlies a certain vulnerability to noise. Noise may lead to spectral fluctuations over time, which can be quantified by the **first-order degree of coherence** [27, 122]

$$|g_{mn}^{(1)}|(\lambda) = \left| \frac{\langle \tilde{A}_m^*(\lambda)\tilde{A}_n(\lambda)\rangle}{\sqrt{\langle|\tilde{A}_m(\lambda)|^2\rangle\langle|\tilde{A}_n(\lambda)|^2\rangle}} \right|, \tag{41}$$

where $\tilde{A}(\lambda)$ denotes the electric fields in the frequency domain, m and n denote the indices of the individual spectra ($m \neq n$), and the angle brackets refer to an ensemble average. $|g_{mn}^{(1)}|(\lambda)$ reaches unity if the spectral component at λ is perfectly stable over time, so to say, temporally coherent. It is also common to give the **average coherence** $\langle|g_{mn}^{(1)}|\rangle = \int |g_{mn}^{(1)}(\lambda)||\tilde{A}(\lambda)|^2 \mathrm{d}\lambda / \int |\tilde{A}(\lambda)|^2 \mathrm{d}\lambda$. A full description of the SC stability requires the investigation of higher-order degrees of coherence [122], too, which was not done in the scope of this work due to the complexity of the procedure.

The coherence properties of multiple nonlinear processes have been investigated [123, 124, 125, 126]. The observations generally allow to say that dominant nonlinear processes in the quasi-continous wave regime (cf. Fig. 3 for $T_0 > 1\,\mathrm{ps}$) do not provide noise-stable spectra, whereas ultrafast nonlinear processes ($T_0 < 200\,\mathrm{fs}$) can be driven coherently within certain parameter regimes. In particular, SPM-driven spectral broadening in all-normal dispersive micro-structured fibers was demonstrated to possess close to perfect coherence across the entire spectrum [126], which allowed stable spectral broadening of a narrow-band input pulse and its compression to a transform-limited sub-two cycle optical field [127]. This concept is opposed by ultrafast soliton fission in anomalous dispersive fibers, which provides much larger bandwidths, but is limited in spectral continuity and coherence. The following sections provide the fundamental concepts of soliton-mediated SCG.

2.3.4.2 *Coherent soliton fission*

Soliton fission appears at high peak powers in classical Kerr systems as a result of perturbations on the soliton propagation by TOD or Raman scattering. As a consequence, higher-order solitons ($N > 1$) fall apart into a series of fundamental solitons ($N = 1$) each experiencing different frequency shifts and potentially generating NSR in the NDD.

This complex process is known as **soliton fission** and is well described in a series of theoretical works [4, 128] and practical reviews [102, 27, 129, 130, 28, 29].

Soliton fission features a series of characteristic spectral signatures, which shall be outlined with the sample calculation in Fig. 5a-c. The simulation shows a classical soliton fission process occurring in a commercial step-index fiber (SMF28) pumped with a 50 fs pulse at 1.35 µm wavelength ($N \approx 10$). The simulation is based on solving the general GNSE in Eq. (26), including a multimodal fit model for the Raman response [118]. The spectral pulse evolution in Fig. 5b,c shows three characteristic stages: Initially, the dominant nonlinear SPM phase leads to nonlinear self-compression in the time domain causing a significant spectral broadening. The broadening is interrupted after a characteristic propagation length (here at ≈ 2 cm) by the generation of NSR that triggers the recoil of an initial fundamental soliton (i.e., with $N = 1$). Along further propagation, more fundamental solitons shear off sequentially from the pulse center accompanied by NSR, until the residual power of the pump pulse is to low to reach the soliton condition $N = 1$. The individual solitons undergo SFS, reach other dispersion domains, and adapt in pulse shape and group velocity. The quasi-linear NSR broadens in time but remains invariant in spectrum, until it might collide with a soliton. At collision, soliton and NSR interact via four-wave mixing, which further increases the spectral distance of the two partners [95, 96]. Both, SFS and soliton-NSR interactions stop as soon as the required soliton- and phase matching conditions are not fulfilled anymore.

The characteristic length at which the first soliton is expelled can be estimated using the empirical rule [27]

$$L_{\text{fiss}} = L_{\text{D}}/N = \sqrt{L_{\text{D}} L_{\text{NL}}} = \frac{T_0}{\sqrt{|\beta_0|\gamma_0 P_0}} \,. \tag{42}$$

For the example in Fig. 5b, the fission length calculates to $L_{\text{fiss}} = 1.9$ cm, which matches well to the simulation. It is further possible and useful to estimate the peak power $P_{s,j}$ and the pulse width $\tau_{s,j}$ of the j^{th} soliton expelled from the pulse with [4, 27]

$$P_{s,j} = P_0(2N - 2j + 1)^2/N^2, \qquad \tau_{s,j} = T_0/(2N - 2j + 1) \,. \tag{43}$$

Eqs. (43) show that the initial soliton upon fission is the shortest in pulse width and the largest in peak power of the entire series. It shall further be noted that adding a frequency chirp on the pulse affects the initial SPM stage, which might accelerate or delay the fission process (i.e., the fission length decreases) and modify the spectral position of the NSR. Choosing the chirp appropriately can lead to a further spectral bandwidth extent [131].

Due to the distinct separation of the solitons, each spectral signal can be identified in the time domain, too (cf. labels in Fig. 5a-c). Thus, the profound knowledge about soliton dynamics in optical fibers allows to draw conclusions about the soliton interactions by just looking *through the prism of a supercontinuum* [28]. Numerical simulations are decisive to supplement the drawn conclusions. For instance, Fig. 5a compares a simulated spectrum with a measured spectrum, produced with a 50 fs pulse launched into a 5 m long

SMF28. The spectral features on the long and the short wavelength side match considerably well. Thus, it is fair to interpret the measured results based on the corresponding temporal soliton dynamics observed in the simulations.

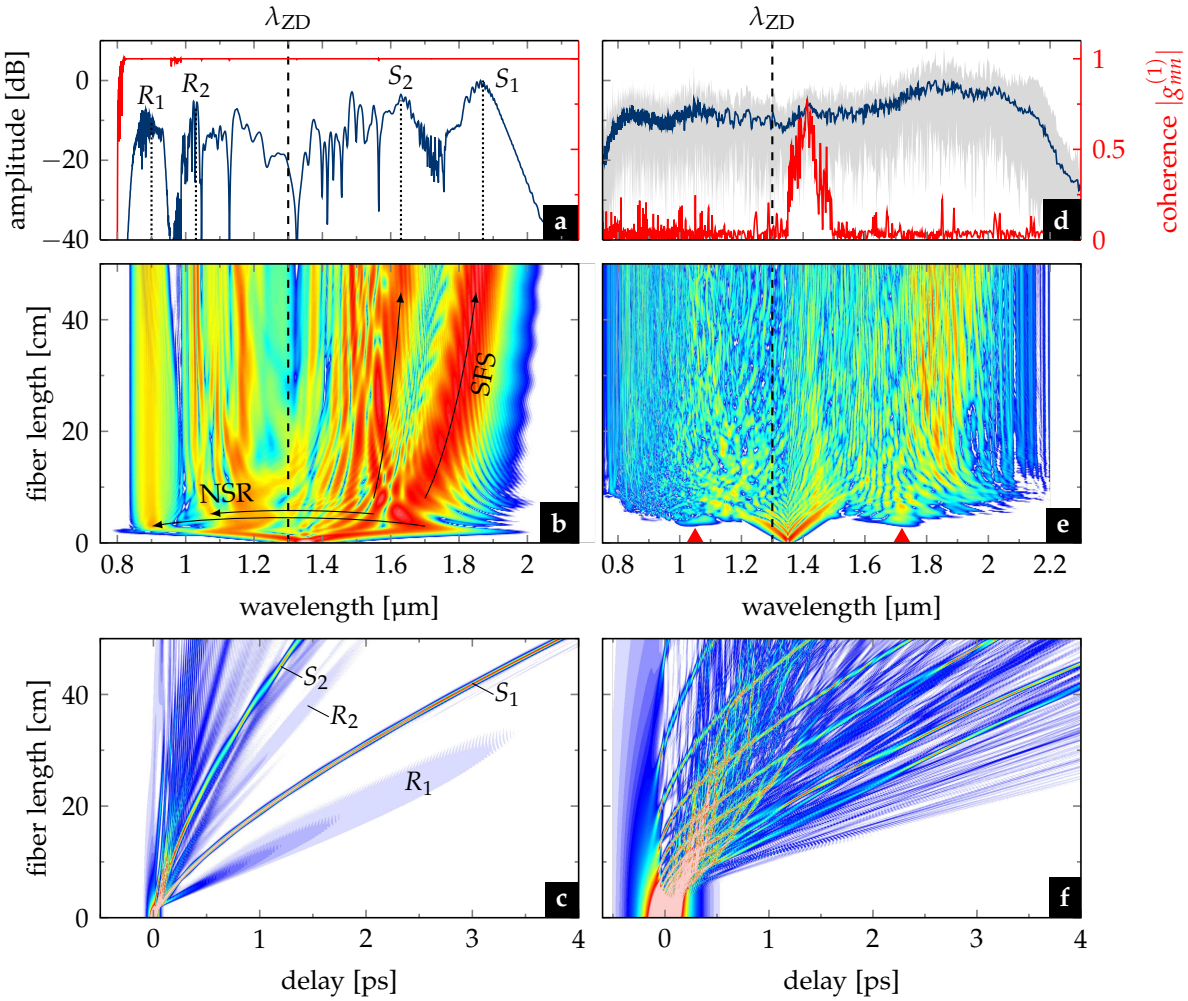

Fig. 5: **Soliton fission versus modulation instabilities.** a,d) Output spectrum and coherence of a standard SMF28 fiber pumped with (a-c) 50 fs and (d-f) 300 fs pulse width and 350 kW peak power in the ADD. b,e) Corresponding spectral and c,f) temporal evolutions of the pulse. in panels (a-c) the first two solitons (S) and NSRs (R) are labeled. In panel (e) the modulation instabilities (MI) onset features are marked with red triangles. The soliton number of the systems is (a-c)$N \approx 10$ and (d-f) $N \approx 60$. Input noise, Raman, and loss are included in the simulations.

Finally, it is worth noting that fission-based SCs feature a high degree of coherence (q.v. Fig. 5a) as long as the initial broadening mechanism is dominated by coherent SPM. In silica fibers this is the case for pulses that fulfill $N \ll 16$ and in particular for $N \leq 10$ with pulse widths $T_0 < 100\,\text{fs}$ [27]. For larger N, minimal phase and amplitude noise of the input pulse is incoherently amplified causing temporal jitter and fluctuations in the spectral positions of the fundamental solitons at the fission point. This decoherence process is known as **modulation instabilities (MI)** and places the main limitation on the scalability of pulse power and width to enhance the brightness or bandwidth of a SC source.

2.3.4.3 *Noise-driven modulation instabilities*

MI arise from the parametric amplification of optical shot noise (i.e., phase and amplitude noise of the input pulse) in spectral side bands. This parametric process originated from perfectly **phase-matched four-wave mixing** [27, 29] following the conditions

$$2\beta_p - \beta_i - \beta_s + 2\gamma_0 P_0 \equiv 0 \qquad \text{and} \qquad 2\omega_p = \omega_i + \omega_s \,, \tag{44}$$

where the indices correspond to the pump (p), the signal (s) and the idler (i) wave. In the degenerate case shown in Eq. (44), the signal and idler sidebands appear symmetrically around the pump frequency. In the ADD, the frequency splitting is mainly controlled by the small nonlinear phase term $2\gamma_0 P_0$. Thus, the highly resonant domains are in close proximity of the pump, and host a huge parametric amplification gain being affected by the smallest fluctuations, such as photon noise.

The spectral broadening of ultrashort pulses with $N > 10$, and in particular $T_0 > 100\,\text{fs}$, is mostly dominated by MI due to the large parametric gain, which increases with input power [27], and the missing coherent seed signal of the side bands provided by SPM. Contrariwise, the process is inhibited by the significantly stronger SPM broadening of shorter pulses, which quickly provides the spectral overlap with the parametric gain and coherently seeds (and saturates) the parametric amplification.

The spectral characteristic of MI-driven SCG is distinctly different from soliton fission, as exemplarily shown for a 300 fs pulse ($N \approx 60$) in Fig. 5d-f: The initial SPM stage is interrupted by emerging spectral side lobes (q.v. red labels in Fig. 5f) symmetric around the pump. This length is often denoted as the fission point, too. In fact, along further propagation the side lobes are amplified and cascade, which quickly forms temporal modulations. These modulations individually evolve to uncorrelated solitons, which may occasionally emit NSR or undergo SFS. This random *soliton burst* decreases the spectral coherence drastically, as shown in Fig. 5d. This decrease in pulse-to-pulse stability gives rise to very flat spectra in the average of several hundred to thousand measurements (q.v. Fig. 5d). Hence, flat-top spectra obtained by pumping in the ADD do not necessarily turn out useful for certain applications where shot-by-shot spectral stability is required.

3.1 Overview of promising liquid candidates

This chapter is denoted to identify suitable liquids for optical waveguiding and soliton propagation, focussing on the formidable optical properties of heavy organic solvents. The work will extend the common models for the IOR dispersion known from literature by additional terms, to account for the dispersive molecular resonances in the MIR wavelength domain. This will be done on basis of IOR data published over the last 80 years. In particular, the data base of CS_2 will allow to build an original thermodynamical dispersion model involving the thermo- and piezo-optical effects. Further, absorption measurements of bulk liquids will be presented to get an estimate for the transmission properties of the potential fiber-core liquids. The current state-of-the-art nonlinear response models of liquids will then be reviewed, which was applied in this work to deduce a response model for tetrachloroethylene (C_2Cl_4) – a highly transparent solvent largely overlooked by the optofluidic community today. Finally, the elaborated material models will be used to investigate the dispersion and the nonlinear gain of liquid-infiltrated silica capillaries in order to identified accessible ADDs, providing the opportunities to study soliton dynamics in those LCFs. The results of this study are partly published in [132, 133].

Nonlinear optics in liquids is a vast field with a long history. The variety of liquids suitable for optics in the VIS to NIR seems large. However, demands on chemical, physical and in particular optical properties exclude a big part of liquid candidates already. This work focuses on liquid carbonates, sometimes referred to as organic solvents, with simple molecular structure, which fulfill the following criteria:

DATA AVAILABILITY Studying nonlinear light generation requires extensive knowledge of dispersion, absorption and nonlinearity of the material over a large bandwidth. There are many potentially transparent and nonlinear liquids (e.g., inorganic solvents such as Ge-/Si-Cl_4) for which this data basis is not provided.

HIGH TRANSPARENCY IN THE NIR Effective light guidance along centimeters of an optical fiber requires low losses, which is generally not given in long organic molecules with many CH, CO, or OH bonds. Thus, long-chained alkanes, alcohols, aromates, esters, and oils (such as the well characterized Cargille™ oils [134]) were not considered despite their reasonably good transparency in the VIS.

SUITABLE IOR FOR SILICA FIBERS Liquids, such as short-chained alkanes, alkohols and some polar solvents (e.g., acetone, water), were excluded from this work, because their IOR is lower than silica, and they do not allow light guidance in silica capillaries. This also excludes the interesting class of liquid flourides (e.g., perfluorohexane C_6F_{14}, hexafluorobenzene C_6F_6), despite their promising transparency in the NIR.

LOW TOXICITY Health and safety concerns play an important role in the work with many solvents such as aromates (i.e., benzene and benzene derivates), which are considered to be genetically harmful and carcinogenic. Thus, potentially highly nonlinear and transparent solvents such as bromides (e.g., bromoform $CHBr_3$), iodides (e.g., methyl iodide CH_3I), or arsenides (e.g., carbon diselenide CSe_2, arsenic trichloride $AsCl_3$) were excluded from this study. Nevertheless, all investigated solvents belong to the health hazard category 3 (NFPA 704 norm), which means that short-time exposure could cause serious temporary or moderate residual injury. Experimental precautions (e.g., small dead volumes, sealed sample mounts etc.) were taken to ensure the acceptable safety limits constituted by law.

HANDLING AND COSTS Liquid handling and their costs play a minor but notable role. For instance, large vapor pressures or high viscosity reduced the applicability of the solvents chloroform and nitrobenzene. Also the costs of, e.g., deuterated liquids with 1-10 EUR/mg limited accessible amounts and, thus, the scale of experiments.

Table 1 summarizes the most important physical properties, including the toxicity levels, of the most common liquids used in nonlinear optics. The optical properties of few of those candidates are studied in detail in the next sections.

Table 1: **Parameter overview of selected solvents.** Halides are colored in yellow, aromatic compounds in light blue. Viscosity and vapor pressure are given for 20-25 °C. The toxicity level of the solvent is represented by the maximum workplace concentration (MWC) in air in terms of short-term exposure (STE) and time-weighted average over 8 hours (TWA) taken from either the german list of "Arbeitsplatzgrenzwerte" (TRGS 900; indicated by an asterisk *) or the european commission directive (2009/161/EU; 2017/164/EU). The label *s* at some MWC values stand for easy resorption by the skin and the label *c* for a proved carcinogenic effect.

liquid	viscosity [mPa·s]	melting point [°C]	boiling point [°C]	vapor pressure [kPa]	MWC (STE) $[\frac{mg}{m^3}]$	MWC (TWA) $[\frac{mg}{m^3}]$
CS_2	0.363	−112	46	48.1	n.a.	15 (30*, s)
$CHCl_3$	0.563	−64	61	25.9	n.a.	10 (2.5*, s)
$CHBr_3$	1.857	8	148	0.7	n.a.	15* (s)
CCl_4	0.958	−23	77	11.9	32	6.4 (3.2*, s)
C_2Cl_4	0.890	−19	121	1.9	275	138 (s)
C_6H_6	0.608	6	80	10.0	n.a.	3.3 (s, c)
C_7H_8	0.590	−95	111	2.8	382	192 (s)
$C_6H_5NO_2$	1.863	6	211	0.0(3)	n.a.	1 (5*, s)

3.2 Linear optical properties of liquids

3.2.1 The complex refractive index

The complex IOR $\bar{n}(\omega) = \sqrt{\varepsilon(\omega)} = n(\omega) + i\kappa(\omega)$ describes the amplitude and phase evolution of an optical wave propagating through a medium. It is a technically practical redefinition of the optical susceptibility $\chi^{(1)}$, that describes the response of bound electrons to an electromagnetic wave acting back on the wave itself.

The dielectric function can be linked to the intrinsic electronic motions in an electric field. Assuming multiple electronic resonances the generalized *Lorentz-Drude model* can be found to be [135]

$$\varepsilon(\omega) = 1 + \chi(\infty) + \sum_m \chi_m(\omega) = \varepsilon(\infty) + \omega_p \sum_m \frac{f_m}{\omega_m^2 - \omega^2 + \mathrm{i}\omega\Gamma_m} \,, \tag{45}$$

with the experimentally unaccessible resonances combined in the constant $\varepsilon(\infty) = 1 + \chi(\infty)$, the individual oscillator strengths f_m, the resonance frequencies ω_m and the attenuation constants Γ_m. In the lossless case (i.e., $\Gamma_m = 0$), Eq. (45) can be transferred to the empiric model for the real part of the IOR found by Sellmeier in 1871 [136]

$$n^2(\lambda) = \varepsilon(\lambda) = A + \sum_m \frac{B_m \lambda^2}{\lambda^2 - C_m^2} \,, \tag{46}$$

with the individual Sellmeier coefficients $A = \varepsilon(\infty)$, $B_m = \omega_p \omega_m^{-2} f_m$, and $C_m = \lambda_m$, and the vacuum wavelength λ (in µm). Each term represents the phase change near an absorption resonance with strength B_m at spectral location C_m. The **Sellmeier equation** has been serving as powerful fit model for IOR data in numerous work [137, 77, 50, 51].

It shall be noted, that another common model is often used in experimental work [50, 51, 138], too, called the **Cauchy equation**. This model is based on a Taylor series of the IOR respective to the wavelength λ (in µm)

$$n^2(\lambda) = A_{-1}\lambda^2 + A_0 + A_1\lambda^{-2} + A_2\lambda^{-4} + \ldots = \sum_{n=-1}^{N} A_n \lambda^{-2n} \,, \tag{47}$$

with the expansion coefficients A_n. The Cauchy equation is especially practical in data fit algorithms. However, it misses a physical-phenomenological origin and, thus, does not necessarily follow natural dispersion slopes. This is different in case of the resonance-based Sellmeier equation, which allows physical relevant extrapolations and higher order derivations of the refractive index. Hence, all refractive index fits and dispersion studies in this work are based on Sellmeier equations, beside few designated exceptions. The dispersion properties of several selected liquids is discussed in sec. 3.2.3.

In fact, it is possible to derive a fit model for the absorption from the Lorentz-Drude model, too. However, modeling the absorption spectrum becomes increasingly complicated with increasing number of resonances and exceeds the scope of this work. In the following section, the absorption properties of selected liquids is discussed by means of the absorption coefficient α. This absorption coefficient is a technical redefinition of the imaginary part of the refractive index, that is given by $\alpha = -20\log(\mathrm{e})k_0\kappa$ in units of dB/m. Similar to the dispersion parameter D, α enables direct comparability of the here-presented LCFs with commercial fibers and allows to quickly estimate the output power P_{out} after a propagation length L following the definition $\alpha L \equiv -10\log(P_{\mathrm{out}}/P_{\mathrm{in}})$.

3.2.2 Absorption

3.2.2.1 *General overview*

Classical optical devices underly efficiency and bandwidth limits imposed by the absorption of their incorporated materials. The need of integrated optical sources and waveguides for the NIR and MIR triggered a lot research in glass chemistry with a strong focus on flouride (F) and chalcogenite (S, Se, Te) compound glasses. Those novel glass types are called *soft-glasses* due to their low melting temperatures of a few hundred degree Celsius. They enable a low-loss operation up to 5 µm wavelength (e.g. for ZrF_4-BaF_2-LaF_3-AlF_3-NaF composition, also called ZBLAN glass, or for ZnTe glass) and even beyond in case of some special chalcogenite compounds (e.g. As_2S_3) [139]. The optical transmission limits of some prominent examples of this material class are compared with fused silica (SiO_2) in Fig. 6.

Many materials of the same chemical class are in liquid phase and largely unexplored for optical applications. The transmission of such liquids is not well quantified to date, although they promise similar transmission benefits as their amorphous partners. However, their loss characteristics is fundamentally different to solids or amorphous materials. The electronic and molecular optical transitions of liquid molecules are less broadened due to much weaker phonon lattice coupling to the thermal background than in solids or amorphous materials. Thus, absorption lines in simple (i.e., short-chained) binary molecular liquids generally appear sparse and narrow, opening many optical operation regimes from the VIS to presumably the MIR.

For instance, a larger range of halides (i.e. binary compounts containing F, Cl, Br, I) is reported in literature with remarkably broad transmission windows from the VIS to the MIR as indicated in Fig. 6. In particular the predicted transmission of tetrachloroethylene (C_2Cl_4) even exceeds the bandwidth of some arsenic chalcogenides, which are the current record holders in terms of MIR transparency.

However, the data for the liquids in Fig. 6 should be taken with care since they are mainly based on a single measurement from which a 1 dB/m absorption threshold was estimated. This data base (esp. Ref. [140]) is hard to confirm. Despite the long period of active research in the field of optofluidics quantitative models for the absorption coefficient are barely available across the optical domain. Only few work exists were transmission along centimeters of propagation through highly transparent liquids was measured, so that absorption values in application-relevant units (e.g., $\mathrm{dB\,cm^{-1}}$) can actually be given [51, 141]. Moreover, most loss studies exclude the domain between 1.7 and 3 µm due to sensitivity limits of the used spectrometers or spectrophotometers. The lack of quantitative data, especially in the NIR, leaves large uncertainties in the applicability of liquids as core material for optical fibers.

In the scope of this work, the transmission limits in the VIS to the NIR of the liquid candidates in Tab. 1 are studied, with special focus on the *erbium* and *thulium* laser operation ranges around 1.55 µm and 2 µm wavelength. In the following, absorption analysis

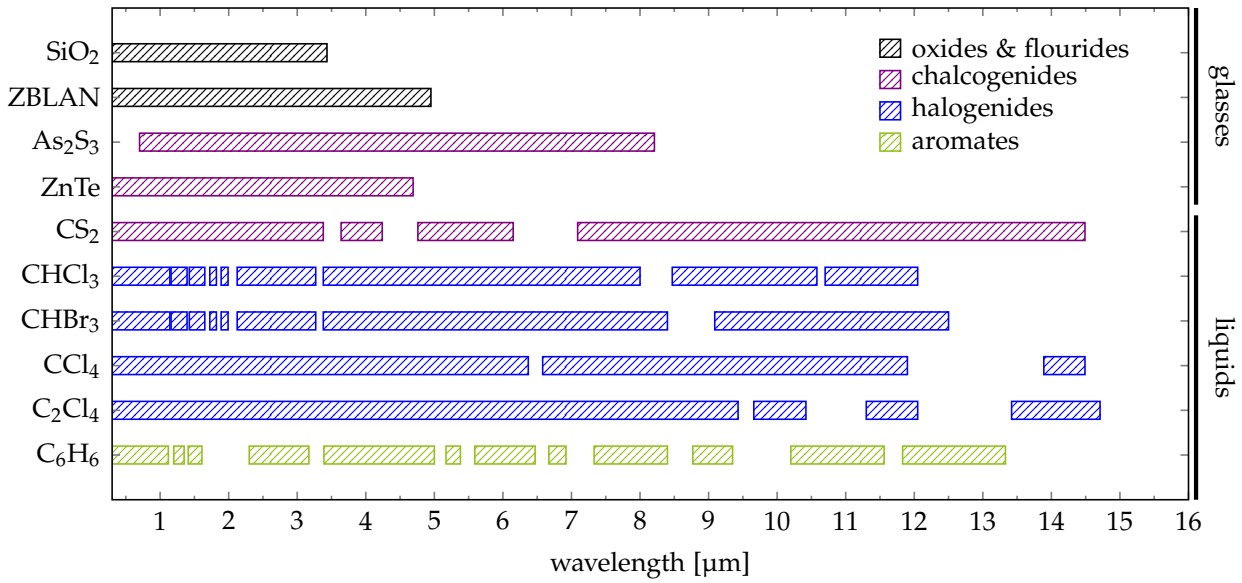

Fig. 6: **Overview of transmission windows of selected glasses and liquids.** The bars indicate domains with less than 1 dB cm^{-1} loss. Data above 3 µm are taken from [140] (liquids) and [139] (glasses), data below 2.2 µm are taken from own measurements and [141, 51] (liquids), and [142] (As_2S_3). The regions between 2.2 µm and 3 µm are assumed to be transparent on basis of multiple data sources [143, 144, 145].

of the two main classes of liquids of this work are presented: (a) low-loss chalcogenide and halide liquids (i.e. CS_2, CCl_4, C_2Cl_4, chloroform ($CHCl_3$)), and (b) selected benzene derivates (i.e., C_7H_8, $C_6H_5NO_2$).

3.2.2.2 *Low-loss chalcogenide and halide liquids*

The absorption of CS_2 and C_2Cl_4 was measured in this work, similar to Ref. [51], using a 1 m long tube closed on both sides by a sealed 1 mm thick silica window. The transmitted spectrum of the tube was measured using a broadband fiber laser (NKT SuperK) as input source and a fiber-coupled grating spectrometer (National Instruments, Spectro320) at the output side. The setup is explained in detail in appendix A. The data were corrected by the wavelength-dependent reflection coefficients and a beam divergence correction function.

The results in Fig. 7a,c reveal that both liquids are highly transparent within the VIS to the NIR domain. They offer potentially similar transparency than the data of CCl_4 in Fig. 7d, measured by Kedenburg *et al.* with a two orders of magnitude lower noise limit. Spectral fluctuations of the supercontinuum source and flow-induced perturbations limited the sensing sensitivity in the measurements here to approximately 2 dB/m.

The tremendous impact of CH bonds becomes obvious when we compare the absorption spectrum of CCl_4 and $CHCl_3$ in Fig. 7b,d. The overtones of the CH-stretching and the CH-deformation modes dominates the spectrum and drastically reduces the transmission properties of $CHCl_3$ in the NIR domain. The use of $CHCl_3$ for LCF design is therefore largely limited. This limit can be overcome using the deuterated counterparts of the liquid.

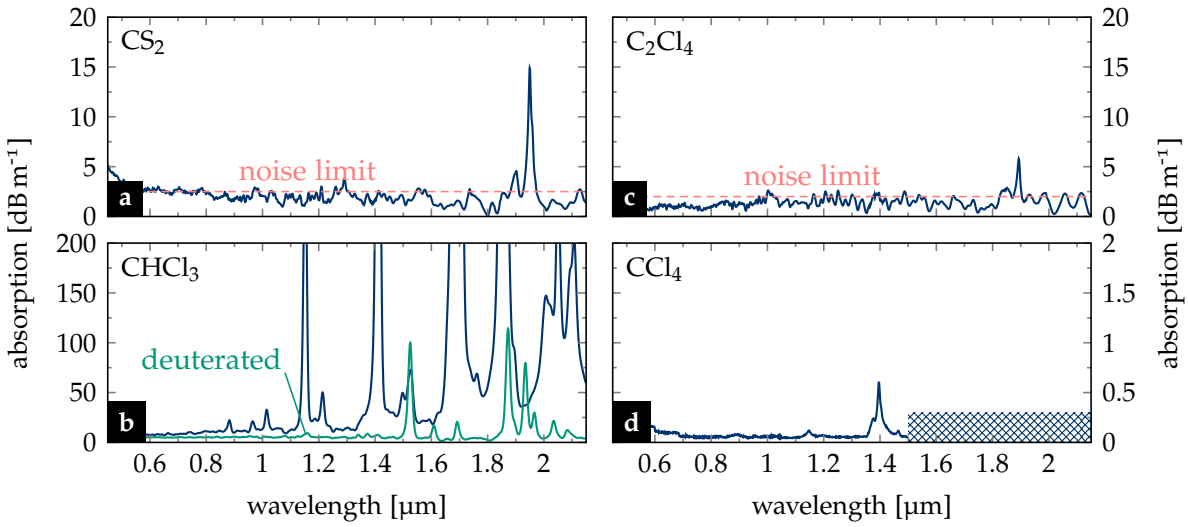

Fig. 7: **Absorption spectra of carbon disulfide and halide liquids.** a) Carbon disulfide, b) chloroform (and its deuterated counterpart), c) tetrachloroethylene, and d) carbon tetrachloride from [51]. The crosshatched domain in (d) was not measured in the data source.

3.2.2.3 *Absorption engineering using deuterated compounds*

Deuteration is the chemical process that replaces a covalently bonded hydrogen atom by a deuterium atom (i.e., heavy hydrogen) in a molecule. In a phenomenological picture the increase of oscillator mass detunes the molecular resonance system and shifts all vibrational resonances towards smaller resonance frequencies (i.e., red-shift of the resonance wavelengths). Thus, the dominant resonances in the NIR domain are shifted further towards the MIR which reduces the losses in the NIR significantly, as shown in Fig. 7b for $CHCl_3$ and in Fig. 8 for C_7H_8 and $C_6H_5NO_2$.

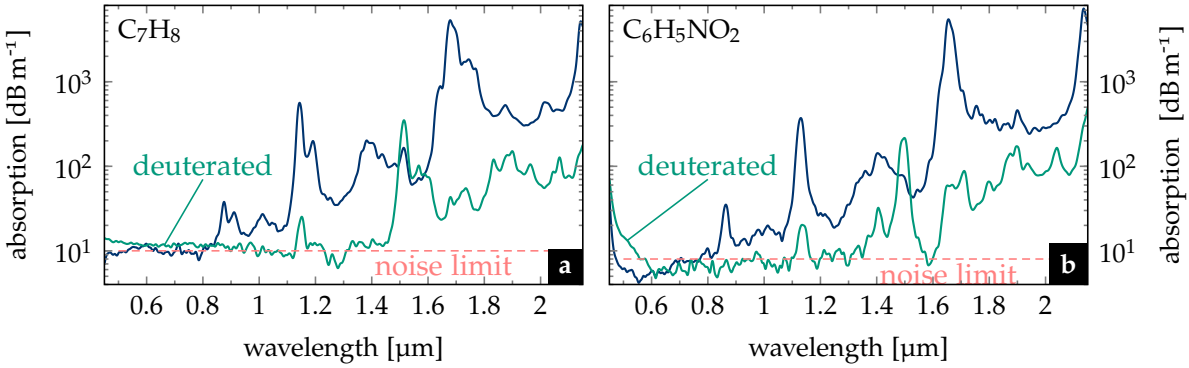

Fig. 8: **Absorption spectra of benzene derivates.** a) Toluene (and its deuterated counterpart), and b) nitrobenzene (and its deuterated counterpart). The data were recorded in a collaborative work, in-house, and published in [141].

Despite a significant reduction of the losses compared to their non-deuterated counterparts, the deuterated benzene derivates still possess large losses in the NIR, that makes them unusable as pure core materials. Deuterated $CHCl_3$, however, can indeed be considered as core material for LCF design. Corresponding fiber designs can be based on the refractive index models of the non-deuterated compounds, since their IOR changes with deuteration less than 2×10^{-3} (at 1064 nm [146]), and can therefore be neglected in first approximation. Amongst all investigated liquids, the most promising candidates for

fiber designs are CS_2, CCl_4, C_2Cl_4, and deuterated chloroform, whose refraction properties are studied in the following. For completeness, the refractive properties of benzene and its derivates can be found in appendix A.

3.2.3 Refraction

3.2.3.1 *Neat liquids*

The dispersion design of LCFs requires precise knowledge about the refractive index dispersion of the liquids used. The refractive index dispersion of liquids was investigated over the past 80 years with a strong emphasis on carbon disulfide, and organic solvents such as chloroform and benzene [147, 148, 149]. However, the existing dispersion models in the literature are insufficient for accurate waveguide dispersion design and need extensions to enable operating in the NIR regime and beyond.

Most dispersion models for liquids known from literature are either based on Cauchy's equation [51, 50] or an over-simplistic 1-term Sellmeier equation [51]. Both models do not account for the strong molecular absorptions in the MIR wavelength domain (e.g., CS_2 resonance at 6.6 µm) and are insufficient for a physically meaningful extrapolation of the IOR beyond the NIR. As a consequence, these models provide an incomplete description of the spectral distribution of the GVD. For instance, in case of CS_2 both literature models deviate from the measured IOR data beyond 2 µm in Fig. 9a, with the consequence of largely different ZDWs in Fig. 9b.

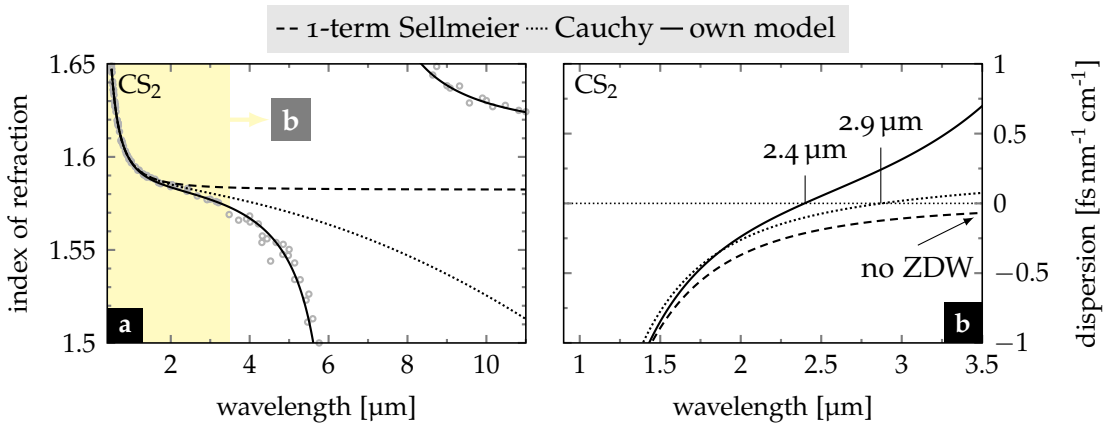

Fig. 9: **Dispersion of carbon disulfide.** a) Refractive index, and b) dispersion parameter D of CS_2 accordingly to a one-term Sellmeier model, the Cauchy model (both taken from [51]), and the new two-term Sellmeier fit from this work based on various IOR data at 20 °C [147, 150, 148, 149, 50, 51]. The labels in (b) denote the ZDW.

In this work, a large set of published IOR data was re-analyzed to obtain new models for the wavelength dispersion of the IOR of four highly transparent solvents. A two- to three-term Sellmeier equation (i.e., Eq. (46) with maximum number of terms $N \in \{2,3\}$) was chosen as model function to fit the data. The Sellmeier parameters obtained by the best fits are listed in Tab. 4 in appendix A. The overall good data match between the data and the model fits in Fig. 9a, confirms how well the new models include the first strong molecular resonance in the MIR, e.g. at 6.6 µm for CS_2, and at 12.8 µm for C_2Cl_4. Moreover, the resonance frequency and amplitude of the first model term differ only

slightly from those reported by Kedenburg *et al.* for CS_2, $CHCl_3$, and CCl_4 [51]. Note that no model existed for C_2Cl_4 previous to this work.

The second Sellmeier term has a strong impact on the position of the ZDW of CS_2, which was absent in case of the 1-term Sellmeier model and can now be found at $\lambda_{ZD} = 2.4\,\mu m$ (cf. Fig. 9b). Also, the ZDW from the 2-term Sellmeier is smaller than in case of the Cauchy equation, where $\lambda_{ZD} = 2.9\,\mu m$. Similar trends in the ZDW position between new and previous dispersion models were observed in case of the other liquids considered here (cf. Fig. 10b). The new models enable accurate fiber design (q.v. sec. 3.4), as well as simulations of broadband SCG across the entire NIR domain (q.v. ch. 5).

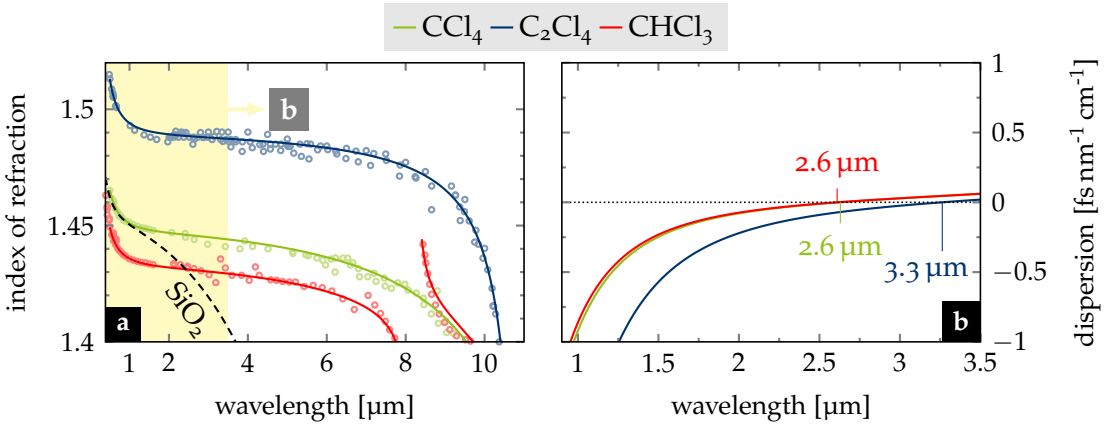

Fig. 10: **Dispersion of halide liquids.** a) Refractive index, and b) dispersion parameter D of $CHCl_3$, CCl_4, and C_2Cl_4 based on new fits of various IOR data ($CHCl_3$ from [148, 50, 51], CCl_4 from [147, 148, 151, 51, 152], C_2Cl_4 from [148, 153, 154]). The labels in (b) denote the ZDW.

3.2.3.2 *Thermodynamic dispersion model*

The IOR of all materials is strongly dependent on the electron configuration of the atoms and molecules of the material, which again is influenced by the thermodynamic environment (i.e., temperature and pressure). As a consequence, the IOR depends on temperature and pressure known as thermo-optic and piezo-optic effect.

Liquids feature two to three orders of magnitude stronger dependency of their IOR on temperature than glasses. Also, against the common belief that liquids are incompressible the IOR depends on the local pressure (or density) which can be controlled by the environment to a certain extent. Both dependencies can be described in first approximation with a simple linear perturbation term [152]

$$n(\lambda, T, p) = n_0(\lambda) + \left.\frac{\partial n}{\partial T}\right|_{T_0,p_0} \Delta T + \left.\frac{\partial n}{\partial p}\right|_{T_0,p_0} \Delta p \tag{48}$$

with $\partial n/\partial p|_{T_0,p_0}$ as piezo-optic coefficient and $\partial n/\partial T|_{T_0,p_0}$ as thermo-optic coefficient at room temperature $T_0 = 293\,K$ and atmospheric pressure $p_0 = 10^5\,Pa$. Tab. 4 in appendix A includes the thermo-optic coefficient (TOC) and the piezo-optic coefficient (POC) values of the four selected solvents, whereas the values were taken partially from own measurements [58] and literature [152].

The TOC and POC are mostly treated monochromatically and constant in first approximation – both assumptions limit the application field to the narrow temperature and wavelength windows. Broadband nonlinear and, in particular, phase-matched processes depend on higher-order derivatives of the IOR (e.g., group velocity or group velocity dispersion), which are not affected by constant offsets of the IOR. Thus, the impact of temperature and pressure on the IOR dispersion is not covered correctly by the linear TOC and POC model in Eq. (48).

In fact, the bandwidth and positions of the optical transitions, inherently influencing the material dispersion via the Kramers-Kronig relation [74], depend on temperature and pressure. The change of an optical transition with temperature (or pressure) might be significantly stronger in the vicinity of the resonance than far away from it. Thus, the change of the material dispersion with temperature, i.e. the TOC, must be assumed wavelength dependent. A similar dependence should apply to the POC. For silica, it is known that such a dependence can be expressed accurately via temperature dependent Sellmeier coefficients [155, 156].

The spectral distribution of the TOC has only been determined for a few selected solvents [157, 158, 159, 138], but the physical models assumed here do not justify an extension of the validity domain beyond the visible. Hence, these models are unsuitable for broadband design studies.

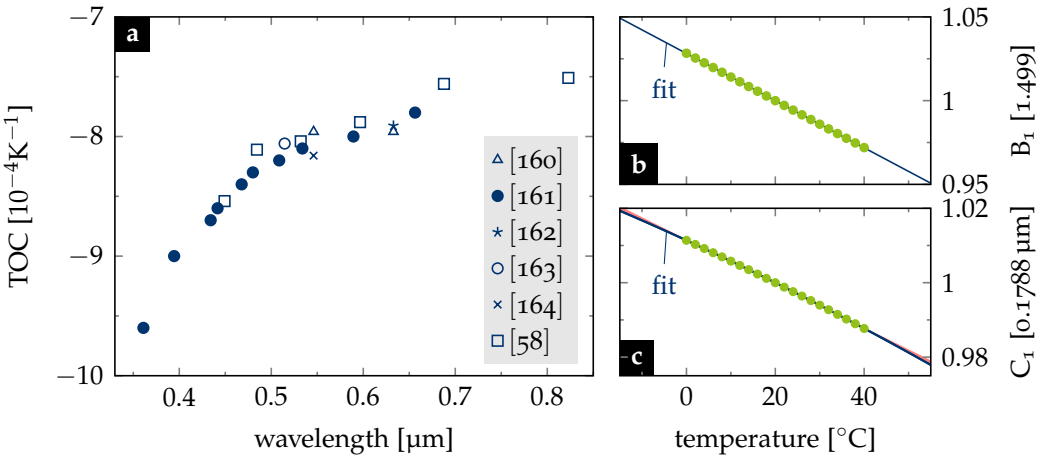

Fig. 11: **Dispersion of the TOC.** a) Measured TOC data CS_2 from collaborative work with Pumpe *et al.* [58], various sources [160, 161, 162, 163, 164], excluding two points in the VUV. b-c) Temperature dependence of (b) amplitude coefficient B_1 and (c) resonance coefficient C_1 of the first Sellmeier term (i.e. UV-term) used to describe the refractive index dispersion of CS_2. The red domain in (c) highlights the deviation of a linear to a parabolic fit model. (b) and (c) were reprinted from the supplementary material of [133]. ©2018, OSA.

In this work, the wavelength dependence of TOC (and POC) were investigated for selected solvents based on broadband TOC data measured in collaborative work with Pumpe *et al.* [58]. In particular, the data of CS_2, shown in Fig. 11a allowed to construct a temperature-dependent IOR dispersion model in the following way: (1) The IOR of CS_2 $n_0(\lambda_k)$ is determined using the Sellmeier model known for room temperature (cf. Tab. 4 in appendix A) at wavelengths λ_k where the TOC is known. (2) The new values of the IOR $n(\lambda_k, T_l)$ were calculated for a selected temperature T_l using the linear thermo-optical

relation in Eq. (48). (3) Finally, all $n(\lambda_k, T_l)$ were fitted with a new Sellmeier equation to gain individual coefficients B_l and C_l for the chosen temperature T_l.

This process is repeated for multiple temperatures T_l between 0 °C and 40 °C whereby each temperature yields a new set of Sellmeier coefficients $[B_l, C_l]$. Finally, the temperature dependence of the B_l and C_l parameters is fitted by low-order polynomial functions. Figure 11 b,c shows the determined parameter sets $[B_l, C_l]$ per temperature and the corresponding polynomial fits. The polynomial functions $[B(T), C(T)]$ allow a reasonable extrapolation beyond the measured temperature domain of the TOC.

However, the TOC data set is limited to the VIS domain, whereas the second Sellmeier term (i.e., the MIR resonance) had to be assumed constant. This is, however, justified by the generally weaker impact of the infrared resonances on the total IOR (i.e., $B_2 \ll B_1$).

In principle, the procedure can be applied to the POC, too. However, the POC is only known for three wavelengths, which is too sparse for a trustworthy fit. The weak wavelength dependence of the known POC values justifies to use the common linear approximation from Eq. (48). Thus, the final expression for the pressure and temperature dependent IOR dispersion of CS_2 follows the thermodynamic Sellmeier equation:

$$n(\lambda, T) = \left(1 + \frac{B_1(T)\lambda^2}{\lambda^2 - C_1^2(T)} + \frac{B_2\lambda^2}{\lambda^2 - C_2^2}\right)^{1/2} + \left.\frac{\partial n}{\partial p}\right|_{p_0,T_0} (p - p_0) \,. \tag{49}$$

The related Sellmeier coefficients in Tab. 2 allow to accurately describe the impact of temperature and pressure on the dispersion of CS_2 from ultraviolet to NIR wavelength.

Table 2: **Sellmeier coefficients of carbon disulfide.** $T_0 = 293.15\,\mathrm{K}$.

B_1(T [K])	$2.16081106 - 0.619064845(T/T_0)$
B_2	0.08953092
C_1(T [K]) [µm]	$0.19209961 + 0.00606716(T/T_0) - 0.01736701(T/T_0)^2$
C_2 [µm]	6.59194611

In general, both TOC and POC are temperature and pressure dependent on their own [58]. Those effects have been neglected in the extended dispersion model of CS_2, since the currently available data matrix does not allow to include this effect in the fitting algorithm.

3.2.3.3 *Dispersion engineering using liquid mixtures*

One clear advantage of liquids is their miscibility, which allows adjusting the optical properties of the corresponding liquid mixture. The miscibility of two liquids compounds depends on multiple parameters but most prominently on their permanent dipole moment. One general mixing rule is that liquids with similar dipole moment do mix well, as soon as no other forces (e.g., hydrogen-bridge bonds) hinder them [165].

Assuming perfect miscibility, the IOR of a multi-component mixture changes as response to the new composition of the molecular ensemble. There are multiple models to calculate the IOR of the composition (a compact overview can be found in [165, 166]),

which all work similarly well in case of liquid compounds with similar molecular mass. The most general model is based on the assumption of a linear combination of the individual molecular polarizabilities. This model is known as *Lorentz-Lorenz model* [167, 168]

$$\frac{n_m^2 - 1}{n_m^2 + 2} = \sum_{k=1}^{N} \frac{V_k}{V} \frac{n_k^2 - 1}{n_k^2 + 2} \tag{50}$$

with the volume of the individual liquids V_k and the volume of the final mixture V. The Lorentz-Lorenz model remains also valid for liquid compounds with entirely different molecular masses. It is not entirely clear, whether the refractive index in Eq. (50) can be assumed weakly imaginary, so that the rule could be extended to include the absorption, as proposed recently, e.g. by Baranovič [169]. In this work, the absorption coefficient (as well as the NRI) of a mixture was approximated using a linear combination of the individual liquid parameters, described by the *Argo-Biot relation* $x_m = \sum_k V_k / V x_k$ [166].

3.3 Nonlinear optical properties of selected liquids

3.3.1 The general nonlinear response

As described in sec. 2.2, the transient nonlinear polarization can be expressed in the NRI and the nonlinear optical response (i.e., the NRF) $R(\tau)$ of a material. In rather static molecule networks, such as solids and amorphous materials, the nonlinear optical response originates mainly from the electrons, and to small parts (ca. 18%) from ultrafast molecular vibrational (i.e., Raman) modes. In silica, the response time of the Raman response is about 32 fs. Thus, the nonlinear response of silica can be assumed (quasi-)instantaneous.

In liquids, the relatively slow molecular motions, caused by the induced dipole moment trying to follow the incident field polarization, contribute to the nonlinear response. For more than four decades the nonlinear optical response of liquids is continously investigated in the light of their unique noninstantaneous response (e.g., [170, 171, 172, 173]. First in 2014, an accurate multi-term model for the NRF of CS_2 was developed by Reichert *et al.* [174], which enabled the calculation of the NRI in dependence of pulse width, field polarization, and wavelength. Follow-up work was published shortly after by Zhao *et al.* [53] and Miguez *et al.*[175]. This work utilizes the quantitative model by Reichert *et al.* to estimate the effective nonlinearity $n_{2,\mathrm{eff}}$ of selected liquids, forming the essential backbone of the numerical models in the following.

The NRI of liquids, and noninstantaneous nonlinear media in general, is calculated by

$$n_{2,\mathrm{eff}} = n_{2,\mathrm{el}} + n_{2,\mathrm{m}} = n_{2,\mathrm{el}} + \frac{\int I(t) \int \bar{R}(t-\tau) I(\tau) \mathrm{d}\tau \mathrm{d}t}{\int I^2(t) \mathrm{d}t}\,, \tag{51}$$

where $n_{2,\mathrm{el}}$ is the electronic NRI, $n_{2,\mathrm{m}}$ is the NRI associated with the molecular nonlinearities, and $\bar{R}(t)$ is the natural (unnormalized) NRF of the liquid response model by Reichert *et al.* [174]. Eq. (51) incorporates the general molecular dynamics induced by an

excitation pulse with intensity distribution $I(t)$. In consequence, $n_{2,\text{eff}}$ strongly depends on the pulse width and shape.

The NRF model as introduced by Reichert et al. [174] considers the total nonlinear response as a sum over individual response terms for each nonlinear process:

$$\bar{R}(t) = \sum_k n_{2,k} r_k(t) \ , \tag{52}$$

with summation over the symbolic index k denoting one of the three molecular processes diffusive reorientation (d), collision (c), or libration (l). The authors give a model function $r_k(t)$ for each of the three relevant nonlinear mechanisms, which are reproduced in appendix A. Each response term r_k is normalized to $\int r_k(t)\mathrm{d}t = 1$ and weighted by a process specific NRI $n_{2,k}$. Fig. 12a shows all response terms and their superposition exemplarily for CS_2, as well as pictograms illustrating the physical origins of the underlying nonlinear mechanisms (see appendix A for a detailed description of each effect).

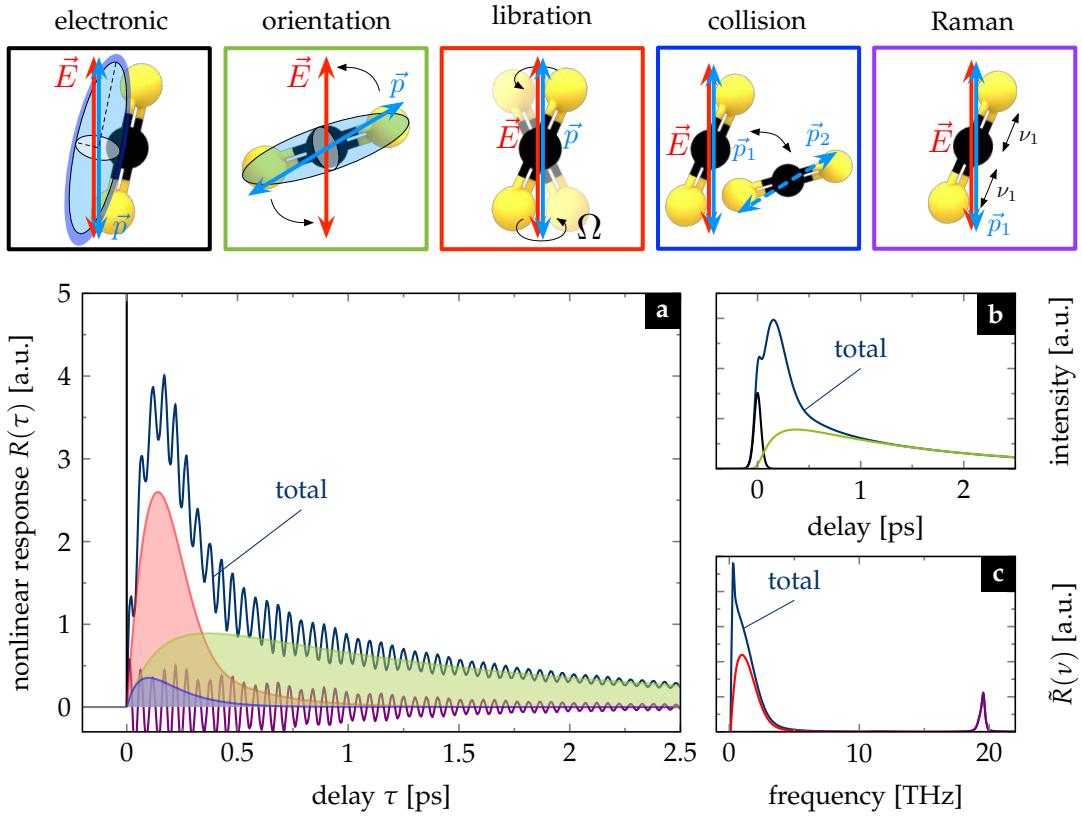

Fig. 12: Nonlinear mechanisms of liquids exemplarily for CS_2. a) Individual nonlinear contributions and the total nonlinear response (in dark blue). The color of the curves refers to the frame color of the individual light-molecule interactions illustrated on top. b) Convolution of a 60 fs pulse with the total nonlinear response as well as the electronic response (black), and the reorientation response (green). c) Spectrum of the convolution signal in (b) compared to the spectrum of libration response (red) and Raman response (purple).

It should be noted, that the Reichert model does not include other sources of nonlinearity such as electro- or thermostriction. These effects require comparably large pulse energies, and can therefore safely be neglected in this study. This is different to Raman effects, which might coherently be excited by the ultrashort pulses created in the nonlin-

ear LCFs, given that the pulse spectrum overlaps with Raman resonances of the liquids. Stimulated Raman scattering was added to the Reichert model in this work, based on linear Raman scattering measurements of selected solvents and silica (reference). The model extension is described and discussed in appendix A.

3.3.2 Overview of the nonlinear response of selected liquids

Because of their different molecular shape, the dominating nonlinear processes and, thus, the individual nonlinear response is fundamentally different for all liquids. Just recently, the model by Reichert *et al.* was extended for a larger set of liquids [53, 175]. Fig. 13 shows the nonlinear response of selected solvents, and the resulting $n_{2,\mathrm{eff}}$ in dependence of the pulse width of a sech-pulse. Also, the pulse-width dependence of the **molecular fraction** f_m is presented – a key quantity, which describes the molecular contribution to the total NRI and is discussed in detail in ch. 4.

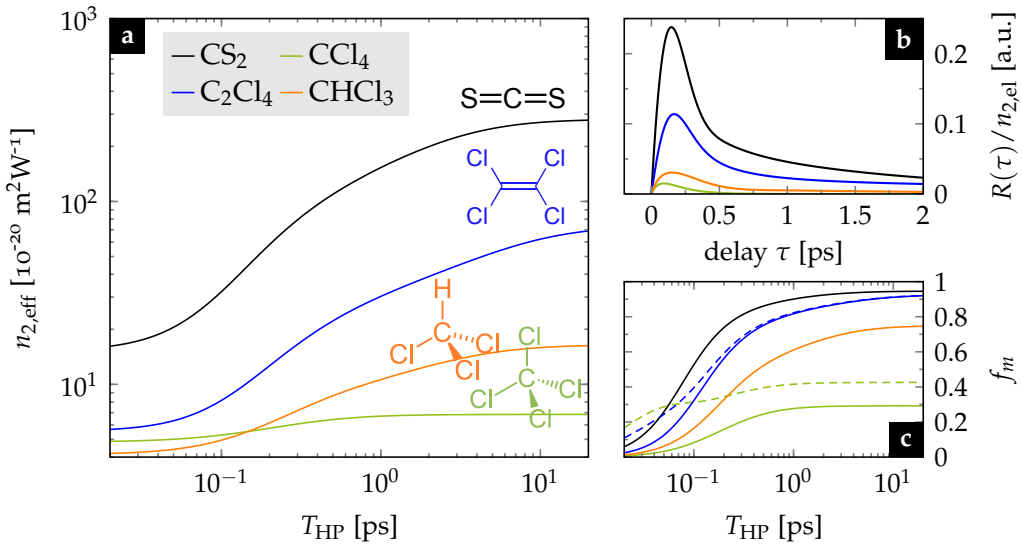

Fig. 13: Overview of the nonlinear optical responses of selected liquids. a) The effective NRI over half-power pulse width. b) The NRF (without Raman term) normalized to the electronic NRI. The model parameters are listed in Tab. 5 in appendix A. c) The molecular fraction over half-power pulse width. The legend in (a) applies to all curves in each panel. The dotted curves in (c) include the Raman terms in the NRF.

The decay times of the response functions in Fig. 13b are characteristic for the molecular shapes of the liquids. For instance, CCl_4 features a quasi-isotropic molecular shape and its nonlinearity is dominated by instantaneous electronic excitations with small contributions from intermolecular dipole-dipole interactions and intramolecular vibrational Raman oscillations. Its NRF does not feature reorientation or libration components (i.e., $n_{2,\mathrm{d}} = 0$ and $n_{2,\mathrm{l}} = 0$ [176]), but shows a rather fast dynamic. The response of CCl_4 can therefore be seen as quasi-instantaneous due its small molecular contribution (e.g., $f_\mathrm{m} = 0.18$, i.e., 18% for a pulse width of 300 fs). In consequence, the effective NRI of CCl_4 varies only weakly between pulses of different width.

In contrast, C_2Cl_4, for example, is a prolate molecule such as CS_2, which causes an intensity dependent anisotropy based on molecular reorientation in a linearly polarized light field. The resulting response in Fig. 13b shows that C_2Cl_4 has a highly non-

instantaneous temporal response (e.g., with a comparably large molecular contribution of $f_m = 67\%$ in case of a 300 fs excitation pulse), that is comparable to the highly non-instantaneous CS_2. Thus, the effective NRI of C_2Cl_4 increases drastically for increasing pulse width, as shown in Fig. 13a. It shall be noted, that no quantitative nonlinear model existed for C_2Cl_4 prior to this work. The model by Reichert *et al.* was applied to pump-probe data measured for trichloroethylene by Thantu & Schley [177] and in-house NRI measurements for C_2Cl_4 (q.v. appendix A). Thus, the model can only be seen as rough estimate, and requires further confirmation via pump-probe experiments.

3.4 Nonlinear liquid-core fiber design

3.4.1 Overview of the optical properties of the fundamental fiber mode

The elaborated material models from the previous sections can now be applied to investigate the linear and nonlinear optical properties of liquid-core silica-cladding step-index fibers. The transcendental dispersion relation in Eq. (12) is used to calculate the effective IOR n_{eff} for the fundamental HE_{11} mode of a LCF for a given core diameter $\varnothing_{co}$, pump wavelength λ_0, and core material. From the effective IOR the dispersion parameter D is calculated to identify the dispersion domains. The dispersion varies considerably over $\varnothing_{co}$, as exemplarily shown in Fig. 14a for CS_2-core LCFs with increasing diameter. Since the ZDW decides over the predominant nonlinear effects on a propagating pulse (q.v. sec. 2.3.1), this quantity is a key parameter in nonlinear fiber design.

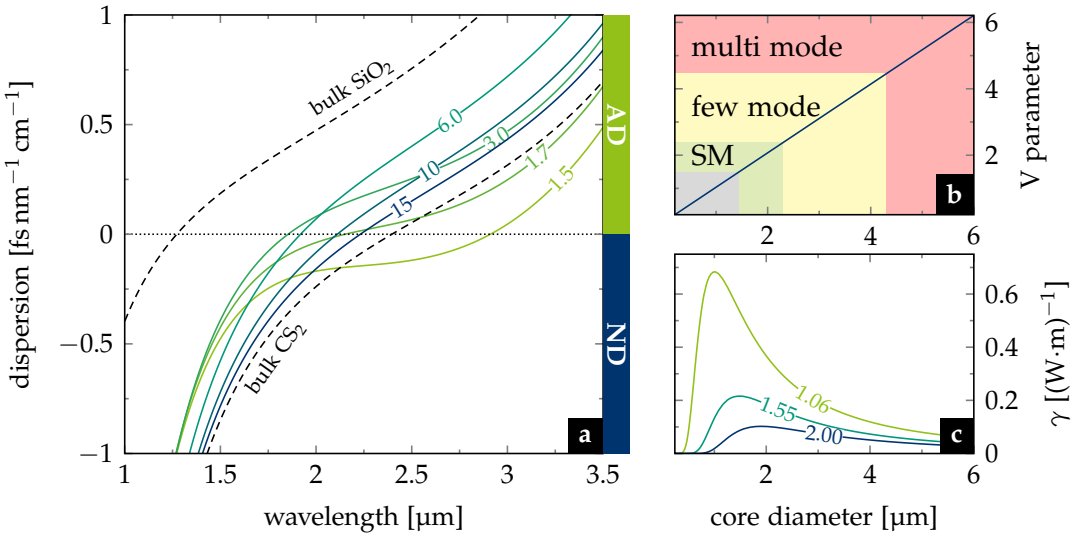

Fig. 14: **Fundamental mode properties of CS_2-core LCFs** a) Dispersion parameter D of the fundamental HE_{11} mode of a CS_2/silica step-index fiber. The number on the curves denote the $\varnothing_{co}$. b) V-parameter and c) nonlinear gain parameter over $\varnothing_{co}$. SM in (b) is the single-mode domain for $\lambda_0 = 2\,\mu m$. The numbers in (b) refer to λ_0.

In fiber design, the V-parameter (q.v. Eq. (13)) defines the range of acceptable core diameters for a given wavelength. It should be chosen such that $V > V_{crit}$ to avoid scattering losses, and below the SMC to avoid the higher-order mode regime, which limits efficient light coupling to a single selected mode (i.e., preferentially the fundamental mode). In particular, the latter constraint reduces the design range for high-index liquids consider-

ably (q.v. Fig. 14b). In case of free-space coupling, the few-mode regime above the SMC (q.v. Fig. 14b) can also be considered as possible operation regime, since efficient coupling to selected modes is still possible by careful beam alignment. Moreover, V_{crit} was empirically found to be approximately 1.5 for LCFs in this work. Thus, the V-parameter range of the LCFs considered in this work is $1.5 < V \lesssim 4.5$.

A further essential parameter addressing the nonlinear properties of the fiber mode, is the nonlinear parameter γ from Eq. (30) (q.v. Fig. 14c), which, ought to be large and low-dispersive, to ensure strong nonlinear coupling across a broad bandwidth. Overall, the large amount of fiber benchmarks (i.e., D, V, γ) in combination with the many degrees of freedom in the LCF design parameters (i.e., core material, $\varnothing_{\mathrm{co}}$, λ_0) demands a systematic presentation of the key parameters in a new format, as introduced in the following.

3.4.2 Design maps for nonlinear fibers

The relevant fiber and mode quantities (i.e., D, V, γ) feature important isolines in the multi-parameter space spanned by the operation wavelength λ_0 and the core diameter $\varnothing_{\mathrm{co}}$. These isolines are for example the ZDW, the SMC, or the maximum nonlinear parameter $\gamma^{\lambda}_{\mathrm{max}} = \max(\gamma(R)|_{\lambda})$. Fig. 15 shows these isolines for selected LCFs and glass fibers together with the logarithmic nonlinear parameter $\gamma(\lambda, R)$. Due to the relevance of this presentation for nonlinear fiber design, it is further denoted as **nonlinear design map**.

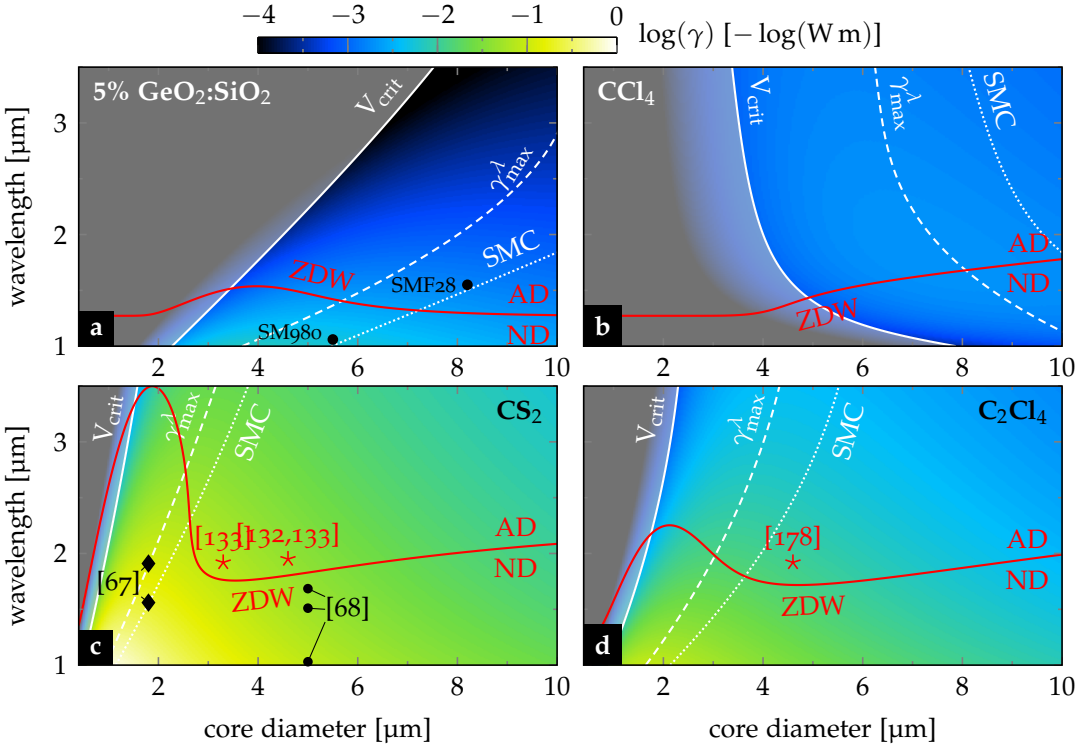

Fig. 15: **Nonlinear design maps of selected fibers.** a-d) The color plots show the logarithmic nonlinear parameter as function over $\varnothing_{\mathrm{co}}$ and λ_0 for multiple silica-cladding fibers. The core material is denoted in the panels. The contour lines incorporate the ZDW, the SMC, the maximum nonlinear parameter per wavelength $\gamma^{\lambda}_{\mathrm{max}}$, and $V_{\mathrm{crit}} = 1.5$. The nonlinear parameter of the liquids includes the total NRI accordingly to Eq. (51) assuming a sech pulse with $T_{\mathrm{HP}} = 300\,\mathrm{fs}$. The black marks label system configurations experimentally tested by other groups, the red marks the configurations investigated in this work.

The nonlinear design maps in Fig. 15 give intuitive impressions of the design possibilities of step-index LCFs, compared to standard step-index GeO_2-doped silica fibers. In case of the standard glass fiber geometry, the low core index enables single-mode operation for large core diameters easily accessible by large-scale fiber drawing facilities. The large core diameters keep the nonlinear parameter low, which is desirable for error-free telecommunication purposes. The ZDW varies only weakly over $\varnothing_{co}$.

Compared to silica fibers, CCl_4-core LCFs allow single-mode operation for even larger core diameters (i.e., $\varnothing_{co} > 8\,\mu m$; q.v. Fig. 15b) at even lower nonlinearity. The monotonic increase of the ZDW with increasing $\varnothing_{co}$ provides broad access to the NDD for the most common fiber laser lines (i.e., $\lambda_0 < 2\,\mu m$). For smaller core diameters (i.e., $\varnothing_{co} < 8\,\mu m$) light guidance becomes critical. Thus, the design capabilities of pure CCl_4 fibers are limited, which can be overcome by an admixture of a high-index liquid.

In contrast, high-index LCFs filled with CS_2 or C_2Cl_4 commonly show robust guidance, whereby the SMC is located at comparably small core diameters (q.v. Fig. 15c,d). Notably, the SMC gives a good approximation for the design parameters exhibiting maximum nonlinearity in those fibers – a finding that was published in the scope of this thesis [84]. The nonlinear maps of CS_2 and C_2Cl_4 reveal a local minimum of the ZDW at comparably large core diameters in the few-mode regime (e.g., 3-5 µm in case of CS_2 fibers in Fig.15c). This ZDW minimum benefits from a comparably large nonlinear gain and grants access to the ADD at operation wavelengths about 2 µm.

In conclusion of this chapter, the new material dispersion models developed in this work allow accurate optical system design in the NIR domain towards the MIR domain. The large variety of liquids allows to widely select the IOR, the effective NRI, and the NRF appropriately to the given pulse shape and to the demands of the experiment. The parameter range can be further enlarged by incorporating miscibility and thermodynamic optical detuning of liquids. Absorption manifests the primary limit of operation in this wavelength domain. However, especially hydrogen-less carbon chlorides and CS_2 feature a remarkably high transparency (i.e., below 0.025 dB/cm loss) across large parts of the VIS to the NIR, offering a wide application potential for optical waveguiding. Incorporated into silica capillaries, those liquids form step-index LCFs and grant access to the ADD at easy-to-couple core diameters and operation wavelengths readily provided by thulium-doped fiber lasers. They therefore offer a platform to study optical solitons. However, the effect of the shown noninstantaneous nonlinearities of the liquids on soliton formation is poorly understood and requires proper theoretical groundwork. The following section provides the first steps to a modified soliton theory, which accounts for the liquid nonlinearities.

4 MODIFIED SOLITONS IN PARTLY NONINSTANTANEOUS MEDIA

4.1 Linearons – Eigenstates of highly noninstantaneous nonlinear media

In this chapter, the soliton theory introduced by Conti *et al.* is applied to liquid-core systems with realistic nonlinear response. Conti *et al.* followed a rigorous theoretical approach and derived a quasi-linear differential equation from the GNSE assuming an ideal noninstantaneous nonlinearity (i.e., exponential response and $f_m = 1$) [70]. They further found new solitary states, so-called *linearons*, and proposed highly noninstantaneous LCFs as potential platform for proving their existence. Understanding the dynamics of those states is practically relevant since they might emerge, e.g., in SCG and imprint characteristic features in the spectra with advantageous or detrimental implications for applications.

This chapter applies the noninstantaneous formalism by Conti *et al.* to discuss the practical relevance of linearons in realistic liquid systems. Solitary solutions will be found for media with natural nonlinear response, and their susceptibility to perturbations, such as TOD, Kerr nonlinearity, and causality, will be investigated. It will be shown that these states do not persist the most general propagation model (i.e., the GNSE). However, soliton-like states with characteristic spectral and temporal signatures can be identified in media with hybrid nonlinearity, which allow the hypothesis of the existence a new class of solitons in highly noninstantaneous media. The phase relations and model quantities derived herein provide useful tools to define operation domains of those states, and to understand the experimentally accessible soliton fission dynamics in LCFs later in this work.

4.1.1 Noninstantaneous Schrödinger equation

A strong noninstantaneous response allows certain approximations to deduce a problem-specific propagation equation. The derivation starts with the GNSE in the frequency domain from Eq. (26) in sec. 2.2.2. Assuming a fully noninstantaneous medium (i.e., $f_m = 1$), non-dispersive nonlinearity (i.e., $\bar{\gamma}(\omega) = \bar{\gamma}_0$), and no loss (i.e., $\alpha = 0$) yields

$$\partial_z \tilde{A}(z;\omega) - \mathrm{i}\left[\beta(\omega) - \beta_0 - \Delta\omega\beta_1\right]\tilde{A} = \mathrm{i}\bar{\gamma}_0 \mathcal{F}^{-1}\left\{A(z,t)\left[R * |A|^2\right]\right\}, \tag{53}$$

with the field envelope A in time domain (and its Fourier transformed counterpart $\tilde{A} = \mathcal{F}\{A\}$), propagation constant β, nonlinear coefficient $\gamma = k_0 n_{2,\mathrm{m}}/A_{\mathrm{eff}}$ (with molecular NRI $n_{2,\mathrm{m}}$ and effective mode field area A_{eff} from [84]), the frequency shift $\Delta\omega = \omega - \omega_0$ relative to the center/soliton frequency ω_0, and the normalized response function $R(t)$. This equation is transformed to time domain while assuming second order dispersion

only, which means $\beta(\omega)$ is expanded in a Taylor series around the soliton frequency ω_0 to get $\beta(\omega) - \beta_0 - \Delta\omega\beta_1 \approx \Delta\omega^2\beta_2$ and to find

$$\partial_z A + \tfrac{1}{2}\mathrm{i}\beta_2\partial_t^2 A = \mathrm{i}\gamma_0 A(z,t)[R(t) * |A|^2] \,, \tag{54}$$

whereas t is the time scale in the moving frame of the pulse. This equation cannot be solved analytically in general without putting tight constraints on the response function $R(t)$. Most soliton solutions were found and studied for the fully instantaneous case $R(t) \approx \delta(t)$, easily resolving the convolution in Eq. (54) to $R(t) * |A|^2 = |A|^2$ and transforming Eq. (54) into the fully integrable classical NSE as known from literature (cf. sec. 2.2.2).

An analogous mathematical simplification can be done by assuming optical pulses being much shorter than the nonlinear response, i.e., assuming $T_0 \ll T_R$. Conti *et al.* presented this **noninstantaneous approximation** in the mathematically correct form of a Taylor expansion of the slowly varying response

$$\begin{aligned}\int_{-\infty}^{t} R(t-t')|A(t')|^2\mathrm{d}t' &\approx \int_{-\infty}^{t}\Big(R(t) + \partial_t R t' + \mathcal{O}(\partial_t^2 R)\Big)|A(t')|^2\mathrm{d}t' \\ &\overset{\star}{\approx} R(t)\int_{-\infty}^{t}|A(t')|^2\mathrm{d}t' = R(t)\mathcal{E}_p \,.\end{aligned} \tag{55}$$

The step at $\star$ is verified for large response times since the n$^{\text{th}}$ derivative of the response function $R(t)$ is proportional to $1/T_R^n$ and quickly becomes negligible for large T_R. This statement can easily be proven exemplarily for $R(t) = \exp(-t/T_R)/T_R$. From Eq. (55) follows the short form of the approximation $|A|^2 \approx \mathcal{E}_p\delta(t)$ and $R * |A|^2 \approx \mathcal{E}_p R(t)$ with the pulse energy $\mathcal{E}_p = \int |A(t)|^2\mathrm{d}t$. Thus, Eq. (54) simplifies to the quasi-linear Schrödinger equation in the noninstantaneous limit, i.e., the **noninstantaneous Schrödinger equation (NISE)**

$$\partial_z A + \tfrac{1}{2}\mathrm{i}\beta_2\partial_t^2 A = \mathrm{i}\gamma_0\mathcal{E}_p R(t)A(z,t) \,, \tag{56}$$

with γ_0 including the noninstantaneous NRI only (i.e., the electronic nonlinearity is neglected for now). With the normalizations $Z = z/L_R$, $T = t/T_R$, and $a = A/\sqrt{P_0}$, Eq. (56) is brought into a normalized form as first presented by Conti *et al.* [70]

$$\partial_Z a + \tfrac{1}{2}\mathrm{i}\,\mathrm{sgn}(\beta_2)\partial_T^2 a = \mathrm{i}\mathcal{E}_a H(T)a(Z,T) \,, \tag{57}$$

with the normalized pulse energy $\mathcal{E}_a = N_R^2\int |a(T)|^2\mathrm{d}T$, the modified soliton number $N_R^2 = L_R/L_{NL}$, and the renormalized response function $\int H(T)\mathrm{d}T \equiv \int R(t)\mathrm{d}t = 1$. Note that, different to the original work by Conti *et al.* the normalization is based on the system invariant response time $T_R = \int_{-\infty}^{\infty} tR(t)\mathrm{d}t$ since the solution does not yield a characteristic pulse width T_0 (q.v. solution in Eq. (86) in appendix B). This requires the introduction of a hypothetical response length $L_R = T_R^2/|\beta_2|$. For positive nonlinearities

(i.e., $\gamma > 0$), the dispersion β_2 ought to be negative to compensate the nonlinear effects, thus $\mathrm{sgn}(\beta_2) = -1$ is set for all considerations in the following.

Comparing Eq. (56) and Eq. (57) allows to link the normalized parameters introduced and discussed by Conti *et al.* to the parameters of a realistic waveguide system. Thus, the following identities can be found

$$H(T) = T_R R(T_R T) \qquad \text{normalized response (\textit{potential}),} \tag{58}$$

$$\mathcal{E}_a = \gamma_0 L_R \mathcal{E}_p / T_R \qquad \text{energy parameter.} \tag{59}$$

4.1.2 Solution of the noninstantaneous Schrödinger equation

4.1.2.1 *Numerical solutions*

Conti *et al.* found a semi-analytical solution for an ideal exponential response (*potential*), which is reviewed in appendix B. Realistic noninstantaneous systems such as liquid CS_2, however, have a more complex functional form (q.v. sec. 3.3), which does not necessarily allow a analytical treatment to find a solution. Realistic systems in particular differ in having a rise time of the noninstantaneous potential which displaces the maximum of the potential away from the zero-delay (i.e., the time where the nonlinear excitation pulse should have its maximum). Thus, one may ask which implications follow from such modifications of the functional form of $H(T)$. This question will be discussed exemplarily for the noninstantaneous response of CS_2 in the following.

The inhomogeneous linear differential equation Eq. (57) can be expressed as eigenvalue equation using the ansatz $a(Z,T) = a(T)\exp(\mathrm{i}\beta Z)$. To solve the eigenvalue equation (q.v. Eq. (85) in appendix B) for general response functions a numerical eigenvalue solver was implemented. Depending on the targeted eigenvalue, propagation constant β or pulse energy $\mathcal{E}_a$, the problem has to be formulated accordingly in either of the two forms

$$\hat{M}a(T) = \beta a(T) \quad \text{with} \quad \hat{M} = \mathcal{E}_a H(T) - \tfrac{1}{2}\partial_T^2 \quad \text{or} \tag{60}$$

$$\hat{M}a(T) = \mathcal{E}_a \hat{N} a(T) \quad \text{with} \quad \hat{M} = \beta \mathbb{1} - \tfrac{1}{2}\partial_T^2 \quad \text{and} \quad \hat{N} = H(T)\,, \tag{61}$$

where $\mathbb{1}$ is the unity matrix. Both equations can be solved effortless with numerical solvers (e.g., `eigs` function in the programming environment MATLAB). However, the pulse width dependence of the molecular NRI (cf. Eq. 51) implies that a found solution modifies γ_0 (and thus, $\mathcal{E}_a(\gamma_0)$), whereas the NISE needs to be adjusted, and a new solution has to be found in turn. In fact, this dependency results in a nonlinear problem again. Luckily, the NRI, and thus $\mathcal{E}_a(\gamma_0)$, is limited in its codomain, which allows to use an iterative algorithms to find a solution. Within 10 iterations, an invariant solution can be found for a large set of initial parameters (q.v. appendix B).

The first four eigenmodes for both constant β and $\mathcal{E}_a$ in Figs. 16a,b show the linear mode characteristics known from the solutions by Conti *et al.* (q.v. appendix B). Fig. 16c shows the propagation constant β and the $1/\mathrm{e}^2$ pulse width T_{e^2} as function of pulse

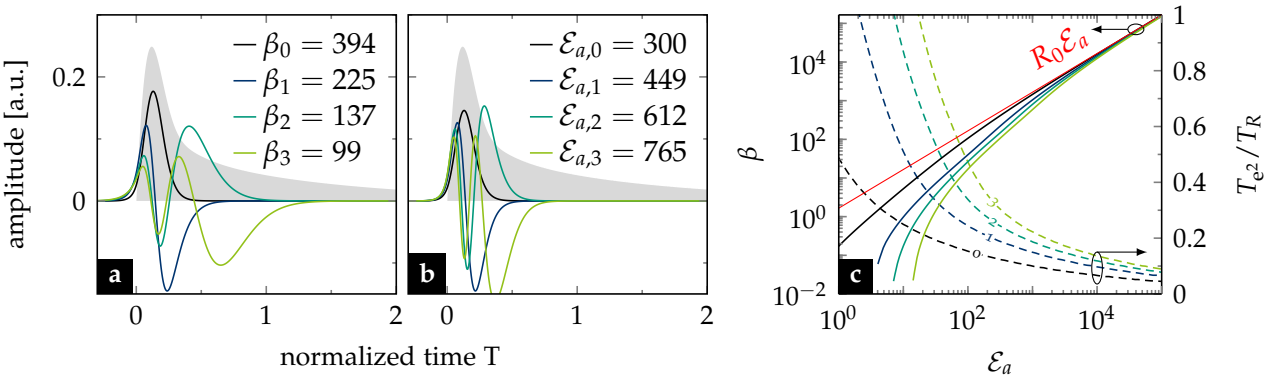

Fig. 16: **Linearon states of a realistic noninstantaneous response.** a) Modes for fixed normalized pulse energy $\mathcal{E} = 300$. The grey-shaded curve is the noninstantaneous nonlinear response of CS_2 with $T_R = 1.26\,\text{ps}$. b) Modes for fixed normalized propagation constant $\beta = 394$. The fundamental solution is defined by the point $[\beta_0 = 394, \mathcal{E}_{a,0} = 300]$ in the phase space. c) Dispersion relation $\beta(\mathcal{E}_a)$ and pulse width as function of pulse energy. The dotted lines indicate the mode cutoffs. The normalized response maximum for CS_2 is $R_0 = 1.65$.

energy. β tends asymptotically towards $\mathcal{E}_a R_0$ for increasing pulse energy (cf. red line in Fig. 16) with $R_0 = \max(R(t))$. The pulse width of the fundamental solution (i.e., $m = 0$) features a pulse width significantly smaller than the response time of the material for all energies considered, generally indicating a reasonable solution.

For practical purposes, it is useful to know that the fundamental solution can be fitted by a Gaussian pulse with $T_{\text{HM}} = \sqrt{\ln 4}\,T_{e^2}$, which was empirically found in this work. The accuracy of the fit increases quickly with increasing pulse energy and is close to perfect for $\mathcal{E}_a \gtrsim 10$.

The solutions were tested using a split-step propagation solver for Eq. (56) that features an initial NRI calculation based on the input pulse. The results (e.g. in Fig. 17a,b) confirm the solitary propagation character of the recursive solution. In the next section, the impact of the most prominent perturbations on the linearon solution during propagation will be investigated, in order to define the characteristics of those *quasi-states* potentially observable in realistic liquid-core fiber systems.

4.2 Hybrid propagation characteristics

4.2.1 Linearon propagation and perturbations

The relevance of the concept of linearons for pulse propagation in a nonlinear noninstantaneous system strongly depends on their susceptibility to perturbations, such as power fluctuations of the input pulse, higher-order dispersion, and, most importantly, the instantaneous electronic nonlinearities, which are unavoidable in realistic systems. In this section, the effect of perturbations on the linearon states will be investigated to better understand what is actually observable in realistic systems, and which part of the discussed properties are purely theoretical. Therefore, the practically relevant hybrid nonlinear Schrödinger equation (HNSE) is introduced, which extends the NISE by higher-order dispersion terms and the Kerr effect.

The HNSE is used to study the three perturbations, which are most essential to discuss the soliton fission experiments later: third-order dispersion (sec. 4.2.3), Kerr nonlinearity (sec. 4.2.4), and non-approximated noninstantaneous interaction (i.e., full nonlinear convolution, sec. 4.2.5). In the scope of this work, the study is limited to the fundamental state (i.e., $m = 0$). The perturbations are investigated using the numerical split-step solver (q.v. sec. 2.2.4) to solve HNSE and GNSE exemplarily for the noninstantaneous nonlinearity of CS_2. Thus, findings are motivated empirically and do not fall under any general validity. However, since the noninstantaneous response functions of all liquids considered in this work are very similar in shape (q.v. Fig. 13b) similar findings may be expected for other liquid-core waveguides. Also, the chosen numerical methodology can handle the full complexity of the equations without being restricted to analytically solvable problems. All simulation parameters are listed in Tab. 8 in appendix B.

4.2.2 Hybrid Schrödinger equation

Waveguides with flat GVD (i.e., no higher order dispersion) are very hard to design and to fabricate. Thus, the extension of the dispersion operator of the NISE (i.e., $\hat{D}^{(2)}(\partial_t) = \frac{1}{2}\mathrm{i}\beta_2\partial_t^2$) by further dispersion terms to $\hat{D}^{(p)}(\partial_t) = \sum_{k\geq 2}^{p} \frac{1}{k!}\mathrm{i}\beta_k\partial_t^k$ is a mandatory step to get closer to realistic fibers. Also, all realistic media contain electrons and, hence, the instantaneous nonlinearity, i.e., the Kerr nonlinearity, can never be switched off entirely. To include the Kerr nonlinearity the nonlinear term of the NISE in Eq. (57) needs to be combined with the Kerr term of the nonlinear Schrödinger equation in Eq. (28). This is straightforwardly possible by introducing the **molecular fraction** $f_m = n_{2,\mathrm{mol}}/(n_{2,\mathrm{el}} + n_{2,\mathrm{mol}})$ to quantify the weight between molecular ($n_{2,\mathrm{mol}}$) and electronic ($n_{2,\mathrm{el}}$) nonlinearities.

Both extensions lead to a new propagation equation, here in physical units, called **hybrid nonlinear Schrödinger equation (HNSE)**

$$\partial_z A + \hat{D}^{(p)}(\partial_t)A = \mathrm{i}\gamma_0\left((1-f_m)|A|^2 + f_m\mathcal{E}_p R(t)\right)A(z,t)\ . \tag{62}$$

Note that the only purpose of the factor f_m is to redistribute the effect of the nonlinear gain parameter γ_0, which contains all nonlinearities of the medium (i.e., electronic and molecular) calculated for the initial state of the pulse. In particular, the important identity $(1-f_m)\gamma_0 = k_0 n_{2,\mathrm{el}}/A_{\mathrm{eff}} = \gamma_{0,\mathrm{el}}$ should be noted. When applying the same normalizations used in Eq. (36) to Eq. (62), the Kerr term yields the (instantaneous) soliton number for hybrid systems, which is further denoted as **effective soliton number**

$$N_{\mathrm{eff}}^2 = (1-f_m)L_{\mathrm{D}}/L_{NL} = \frac{\gamma_{0,\mathrm{el}}P_0T_0^2}{|\beta_2|}\ . \tag{63}$$

In the following, the HNSE is used to study the influence of TOD (i.e., $\hat{D}^{(3)}$) and Kerr effect on the fundamental linearon (i.e., the recursive solution of the unperturbed system with $m = 0$) being launched as input field.

4.2.3 Linearons in third-order dispersive media

Analogously to classical solitons, TOD perturbs the propagation of a linearon causing it to radiate NSR (q.v. sec. 2.3.3.2), as indicated by the spectral trace in the spectrogram Fig. 17c. Simultaneously, the linearon looses energy and needs to adapt its temporal shape leading to a rejection of a part of its front, which becomes obvious in the small difference between the spectrogram of the unperturbed and the perturbed output mode (cf. the field around $T = -5$ in Fig. 17a,c). This process changes the spectro-temporal shape and the phase of the linearon (cf. Fig. 17a-d) depending on the amount of energy transfered to the NSR, but not necessarily a decay of the state (cf. the input and output field in Fig. 17d).

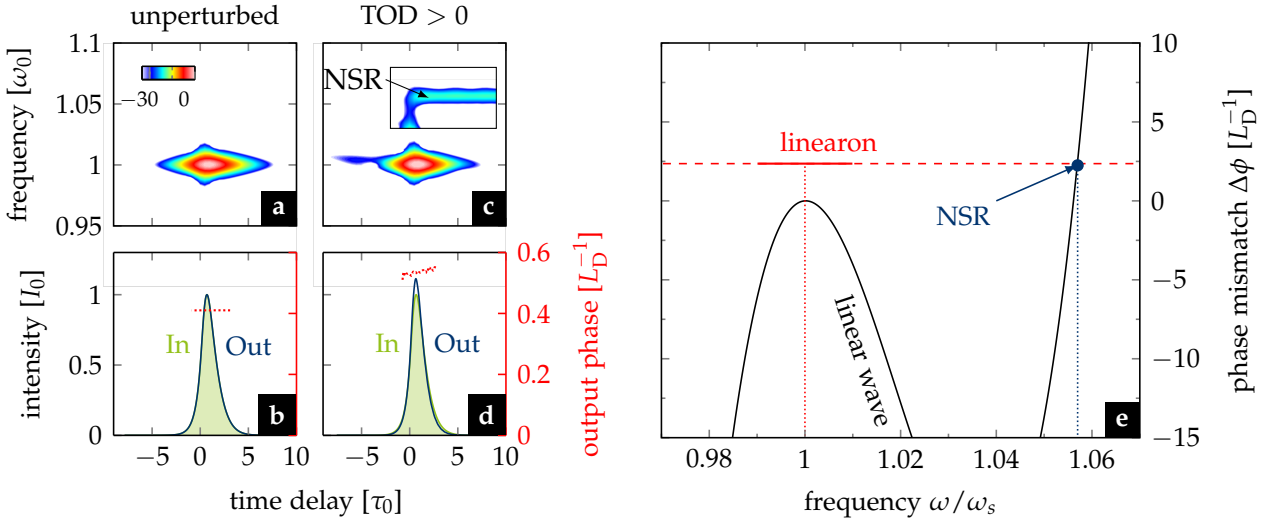

Fig. 17: **Influence of TOD on linearon propagation.** a,c) Spectrogram of the output pulse (log. scale), and b,d) pulse shape and phase of the fundamental linearon before and after $10\,L_D$ propagation in (a-b) an unperturbed system and (c-d) a system perturbed by TOD (both with $f_m = 1$). In the framed domain in (c), solely the contrast is enhanced (color scale from -55 to -35) to visualize the signature of the NSR. e) Phase mismatch between linear (dispersive) waves and a fundamental linearon with approximated phase $R_0\mathcal{E}_a$. The crossing point defines the frequency of perfect phase matching to NSR.

As shown in sec. 2.3.3.2 the generation of NSR is a phase-matched process underlying a strict phase relation. This relation can also be found for linearons in the farthest approximation, analogously to classical solitons, by equalizing the phase of the linear (dispersive) waves $\beta(\omega)$ and the nonlinear phase $\beta_s + R_0\mathcal{E}_a$ and subtracting the group velocity mismatch between both. This yields the **phase matching relation of NSR** radiated by a highly energetic linearon

$$\Delta\beta \approx \beta(\omega) - \beta_s - (\omega - \omega_s)\beta_{1,s} - R_0\mathcal{E}_a = 0\,, \tag{64}$$

with $\beta_s = \beta(\omega_s)$, $\beta_{1,s} = \partial_\omega\beta(\omega_s)$, and $R_0 = \max(R(t))$.

Fig. 17e shows the linear phase-mismatch between linearon and NSR along with the nonlinear phase of the linearon. The crossing point of both curves defines the resonant frequency at $1.0566\omega_s$, which matches well to the value $1.0564\omega_s$ gained by the simula-

tion in Fig. 17c. This proofs, that linearons indeed radiate phase sensitive NSR following a specific nonlinear phase offset that is different to the phase offset of classical solitons. This also highlights the generation of NSR as ideal tool to check the phase properties of a solitary state or a strong quasi-solitary wave featuring a flat phase, which is utilized later in this work.

4.2.4 Linearons in Kerr-perturbed media

The nonlinear response of liquids is inherently hybrid and the instantaneous contribution from the electronic motions cannot be neglected in general. Therefore, it is useful to investigate the linearon stability in a system perturbed by the instantaneous Kerr effect, whereby the molecular fraction f_m in Eq. (62) controls the strength of the perturbation.

To quantify the impact of the respective nonlinear phases, a system with classical soliton number $N \approx 1$ is discussed. The general meaning of this special case is justified since in most high power scenarios in realistic fiber systems the pulse decomposes in many fundamental states (i.e., with $N = 1$) due to perturbations. Thus, the characteristics of those fundamental states play a central role.

Systematic simulations of a hypothetic fiber system with ideal β_2 dispersion and constant nonlinearity γ_0, but increasing weight f_m showed that Kerr nonlinearity does not affect the linearon up to a critical molecular fraction. For instance, phase and pulse shape of a propagating linearon in a system with $f_m = 0.85$ barely change over a propagation of $3L_\mathrm{D}$ (q.v. Fig. 18a,b), whereas the same pulse in a system with $f_m = 0.5$ (q.v. Fig. 18c,d) undergoes a distinct transition from a noninstantaneous spectro-temporal signature to a compressed spectro-temporal signature being significant for classical solitons. The output phase of the latter state is slightly perturbed, but relatively flat.

This transition can be monitored via the mean phase of the output pulse. As shown in Fig. 18e, the simulated phase at $z = 3L_D$ decreases for increasing f_m. This behavior can be described well by a linear combination of the instantaneous Kerr phase (IKP) and the noninstantaneous phase (NIP) contributions via the **hybrid soliton phase** relation

$$\varphi_{NL} = \varphi_{IK}/2 + \varphi_{NI} = \underbrace{(1-f_m)\gamma_0 P_0/2}_{\text{inst. soliton phase}} + \underbrace{f_m \beta / L_\mathrm{R}}_{\text{noninst. soliton phase}} \tag{65}$$

whereas β is the normalized eigenvalue of the recursive fundamental solution. P_0 is the expected peak power of a classical fundamental soliton, calculated using the power-energy relation for sech-pulses (i.e., $P' = 0.88\mathcal{E}_p/T_\mathrm{HW}$), and the peak power enhancement factor for solitary compression (i.e., $P_0 = P'(2N-1)^2/N^2$ from Eq. (43)). Herein, the phase terms φ_{IK} and φ_{NI} are called **instantaneous Kerr phase (IKP)** and **noninstantaneous phase (NIP)**, whereas the IKP is double the classical soliton phase.

In Fig. 18e, both soliton phase and NIP (normalized to L_D for convenience) are shown as function of f_m, whereas their superposition nicely reproduces the slope of the simulated phase. We find a f_m value where both phases are equally strong, which justifies

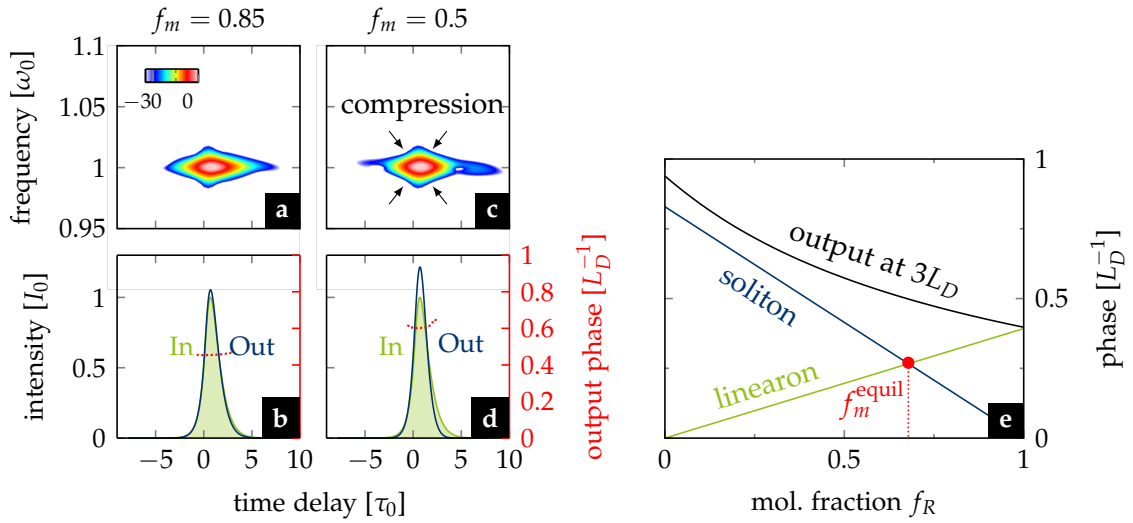

Fig. 18: **Influence of Kerr effect on linearon propagation** a,c) Spectrogram of the output pulse (log. scale), and b,d) pulse shape and phase of the fundamental linearon before and after $10\,L_D$ propagation in (a-b) a system weakly perturbed by the Kerr effect (i.e., $f_m = 0.85$), and (c-d) a system strongly perturbed by the Kerr effect (i.e., $f_m = 0.5$). e) Phase of the simulated output pulse after $3L_D$ propagation as function of the molecular fraction, compared to the ideal soliton phase (reduced by $1 - f_m$) and the linearon phase β. The red mark highlight the equilibrium fraction $f_m^{\text{equil}} = 0.68$, where both phases are equally strong.

the name **equilibrium point** f_m^{equil}. For $f_m < f_m^{\text{equil}}$ the IKP dominates and the solitary characteristics can mainly be described by classical soliton physics described by N_{eff}.

For $f_m > f_m^{\text{equil}}$ the NIP takes over and linearon-like states may form. In the highly energetic limit the hybrid nonlinear phase in Eq. (65) can be approximated with

$$\varphi_{NL} \xrightarrow{\mathcal{E}_p \to \infty} (1 - f_m)\gamma_0 P_0/2 + f_m \gamma_0 \mathcal{E}_p R_0 \,. \tag{66}$$

The expression in Eq. (66) is of general use, since it does not require to solve the NISE to gain the eigenvalue β and, thus, it allows to identify the equilibrium point for a wide set of pulse parameters as shown later. In a realistic medium, however, f_m cannot freely be chosen for a given pulse energy but follows the constraints of the intrinsic pulse width dependence of the NRI (i.e., Eq. (51), also cf. Fig. 13c). This introduces a new material-specific limit that needs to be evaluated for each noninstantaneous system separately.

4.2.5 Linearons in media with realistic hybrid nonlinearity

Getting closer to a realistic system one must give up on the noninstantaneous approximation and handle the nonlinear response by the general convolution with pulse intensity to enforce *causality*. Thus, linearon propagation is investigated here using the GNSE from Eq. (27) instead of the HNSE used before. The discussion is limited to the lossless case of the GNSE with constant γ_0 (i.e., $\gamma_1 = 0$) and β_2 only.

First, a hypothetical system is considered, without electronic contributions (i.e., $f_m = 1$). The linearon looses its solitary character along propagation, as exemplarily depicted in Fig. 19c. This is due to a temporal delay between the approximated nonlinear poten-

tial $\mathcal{E}_p R(t)$, used to calculate the input linearon, and the general nonlinear convolution of the GNSE. This mismatch is independent of the linearon parameters as it is intrinsic for response functions featuring a rise time, which is explained in detail in appendix B (goodness of the solution). Thus, the rise time causes the input state to follow a continuously shifting potential whereby it distributes energy over time and decomposes (q.v. Fig. 19b). Spectrally, this effect causes a continuous self-frequency shift towards lower frequencies. The resulting state features a spectro-temporal signature in Fig. 19a with comet-like shape, i.e., a red-shifted delayed maximum and a train towards earlier times and larger frequencies.

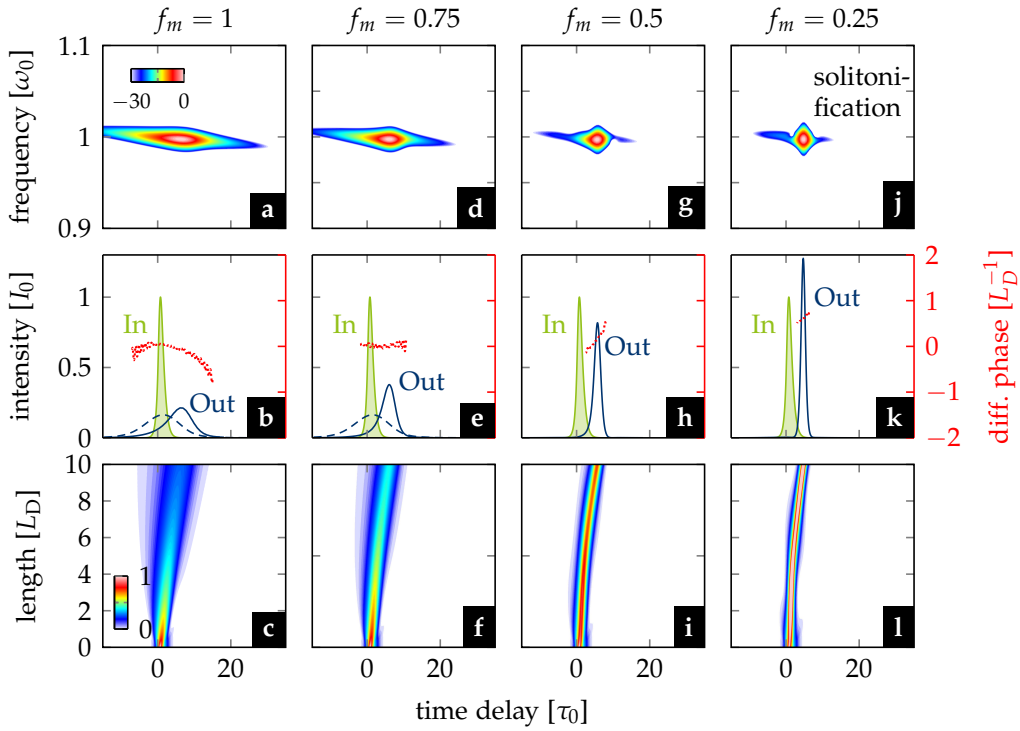

Fig. 19: **Hybrid propagation characterisitics as a result of the interplay between Kerr and noninstantaneous effects in liquid media** a,d,g,f) Spectrogram of the output mode (log. scale), b,e,h,k) input and output intensity and output phase, and c,f,i,l) temporal pulse evolution (lin. scale) of an initial ideal linearon along propagation in four lossless hypothetical systems ($N \approx 1$) with different nonlinear response: a-c) a fully noninstantaneous nonlinear system, and d-l) three hybrid nonlinear systems with decreasing f_m. The dashed curves in (b) and (e) is the output of the same system without nonlinearity for comparison.

In the following, linearon propagation in a system with hybrid nonlinear response is considered, containing both electronic and molecular contributions to a fraction f_m. The condition of the initial linearon is chosen such that $N = 1.3$, and in particular $N_{\text{eff}} < 1$ for $f_m > 0.4$.

The spectro-temporal signature of the pulse after $10L_D$ propagation in Fig. 19a,d,g,j undergoes a notable transition for artificially decreasing f_m. Above a critical f_m (e.g., $f_m \gtrsim 0.5$ in the example in Fig. 19) an intermediate state can be found with a spectro-temporal signature in between the perfectly instantaneous (i.e., $f_m = 0$) and the perfectly noninstantaneous systems (i.e., $f_m = 1$). This set of pulses still features a dispersive

pulse front, but a temporally shorter trailing confinement compared to the noninstantaneous case (cf. Fig. 19e,h with a). Decreasing the molecular fraction below the critical f_m increases the trailing confinement up to a point where the Kerr effect dominates. Here, any input mode is transformed into a classical solitary wave with a compressed spectro-temporal shape (q.v. Fig. 19j) if the fundamental soliton condition $N_{\text{eff}} = 1$ can be fullfilled. This *solitonification* process to classical solitons is exemplarily shown in Fig. 19l. The weak noninstantaneous phase causes a temporal shift as known from intra-pulse Raman scattering (q.v. sec. 2.3.3.3), indicated by a linearly increasing phase (q.v. Fig. 19k), but no further modification of the spectro-temporal signature of the state.

In contrast, output states of systems with large molecular fractions (e.g., $f_m \gtrsim 0.5$ in Fig. 19) do not loose the comet-like spectro-temporal features during propagation (cf. Fig. 19d,g) being a result of the inevitable NIP. Yet, the IKP imposes a less dispersive, quasi-solitary propagation characteristics for increasing f_m (cf. Fig. 19e,h). With notable pulse features from both nonlinear phase contributions (e.g., the comet-like spectrogram with enhanced confinement), those states are referred to as **hybrid solitary waves (HSWs)** in analogy to so-called *solitary waves* as detectable residuals of ideal Kerr solitons in perturbed glass fiber systems.

Most notably, amongst the iteratively tested parameter sets, there are subsets that yield HSWs with relatively flat phase. One of those occasionally found states is exemplarily shown in Fig. 19e. Offset and tilt of the pulse phase remains mainly constant along the last $3L_{\text{D}}$. Smaller phase oscillations (less than 2% deviation from the mean value) potentially originate from non-perfect excitation conditions and cause further weak but continuous energy dispersion of the pulse. However, these special cases indicate the existence of parameter domains, where dispersion, IKP, and NIP might compensate each other to form a quasi-stationary state not underlying temporal or spectral shifts, and, thus, obeying true soliton character. Since those states might be formed by solitonification from an arbitrary input field, similar to the example in Fig. 19f, they are real eigenstates of a hybrid nonlinear system and justify the name **hybrid soliton state (HSS)**. They seem to be unique points in a multi-parameter space spanned by instantaneous and noninstantaneous NRI, NRF, width and energy of the pulse. The complexity of this parameter space requires further systematic studies to identify the underlying characteristics and parameter domains of those states. Hence, the existence of HSSs can only be postulated in the framework of this thesis and not formally verified.

Finally, the hybrid nonlinear phase as introduced in sec. 4.2.4 shall be demonstrated as versatile tool to separate the classical soliton-like regime from the hybrid state regime. Therefore, the propagation of multiple linearon states with $N \approx 1$ to 5 was simulated and the output after $10L_{\text{D}}$ was analysed. For $N > 1.5$ a split-up of the input pulse into fundamental solitary states is observed, i.e., soliton fission occurs (q.v. Fig. 20a). The number of states after fission can be estimated with the effective soliton number N_{eff} from Eq. (63).

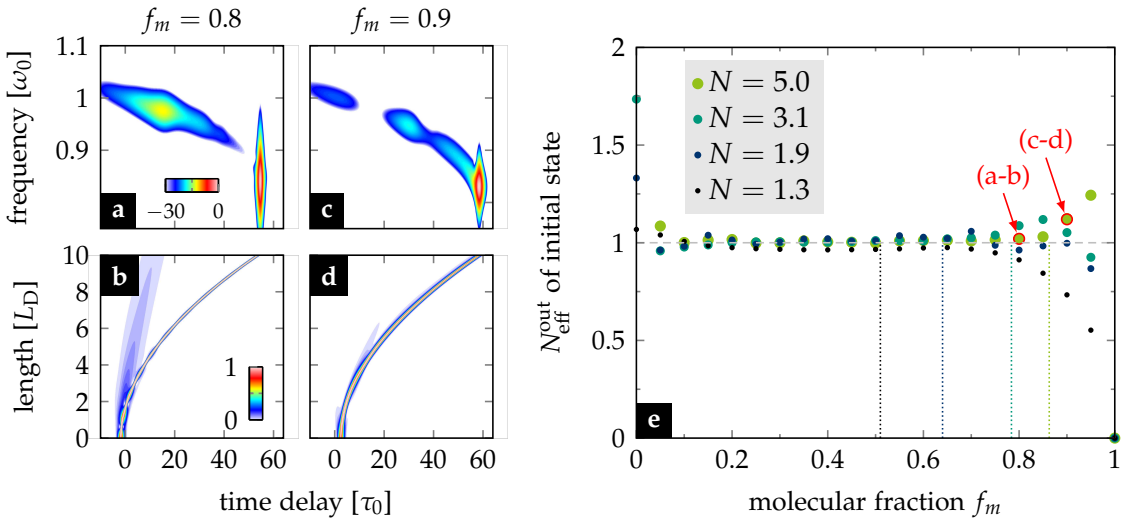

Fig. 20: **Molecular fraction threshold.** a,c) Spectrogram of the output mode (log. scale), and b,d) temporal pulse evolution (lin. scale) of an initial ideal linearon of the unperturbed system (i.e., NISE, $N \approx 5$) along propagation in two perturbed systems (i.e., GNSE with same parameters) with slightly different Kerr perturbation: (a-b) $f_m = 0.8$, $N_{\text{eff}} = 2.2$, (c-d) $f_m = 0.9$, $N_{\text{eff}} = 1.6$. e) The effective soliton number $N_{\text{eff}}^{\text{out}}$ of the strongest soliton calculated at $z = 10L_D$, emerging in systems decreasingly perturbed by the Kerr effect. The dotted lines mark the equilibrium fraction f_m^{equil} of the individual input state, whereas the two individual simulations highlighted in red are shown in (a-d).

To characterize the output state, peak power P_s and pulse width T_s of the strongest output pulse (i.e., the first split-off soliton at fission) were measured at $z = 10L_D$, and used to calculate the current $N_{\text{eff}}^{\text{out}}$ of this pulse. Over a large f_m domain in Fig. 20 e, the output states feature a soliton number $N_{\text{eff}}^{\text{out}} \approx 1$ indicating a classical Kerr soliton behavior. Only for very large fractions above a critical value of f_m, $N_{\text{eff}}^{\text{out}}$ differs from unity indicating a non-classical output. This critical value increases quickly for increasing input pulse energy (i.e., increasing N).

In fact, the equilibrium fraction f_m^{equil} found in sec. 4.2.4 can be used to estimate the critical fraction. Therefore, IKP and NIP are assumed to be equal at the fission point, i.e., $(1 - f_m^{\text{equil}})\gamma_0 P_s/2 \equiv f_m^{\text{equil}} \gamma_0 R_0 \mathcal{E}_p$, yields an expression for the **equilibrium fraction**

$$f_m^{\text{equil}} = \frac{\gamma_0 P_s}{\gamma_0 P_s + 2\gamma_0 \mathcal{E}_p R_0} \,. \tag{67}$$

It is not straightforward to reveal the pulse width dependency of Eq. (67), since $P_s = P_0(2N_{\text{eff}} - 1)^2/N_{\text{eff}}^2$ depends nonlinearly on the pulse width. The complex benchmark parameter f_m^{equil} allows to clearly distinguish the two regimes, $f_m < f_m^{\text{equil}}$ and $f_m > f_m^{\text{equil}}$, in which the spectro-temporal characteristics of the output mode changes notably. For instance, in the system with $N = 5$ and $f_m = 0.8 < f_m^{\text{equil}}$ the spectro-temporal signature of the strongest solitary state (i.e., at $T \approx 55\tau_0$, $\omega \approx 0.85\omega_0$ in Fig. 20a) shows an isolated confinement with a clear symmetry as usual for classical Kerr solitons. This is different in the system with $N = 5$ and $f_m = 0.9 > f_m^{\text{equil}}$, where the signature (i.e., at $T \approx 60\tau_0$, $\omega \approx 0.85\omega_0$ in Fig. 20b) features the characteristic comet-like shape known from the

HSW. This proves the use of the hybrid nonlinear phase to distinguish between IKP- and NIP-dominant regimes.

4.3 Intermediate conclusion

In this chapter, the NISE introduced by Conti *et al.* was utilized to reveal solitary solutions, so-called linearons, in lossless liquid-like media with natural nonlinear response, using a rigorous numerical eigenmode solver. The NISE was extended to the HNSE, which allowed to demonstrate the robustness of the linearon states during propagation in systems perturbed by instantaneous nonlinearity and TOD. The results revealed important phase conditions for NSR generation and solitonification (i.e., soliton formation in a hybrid nonlinear system).

However, linearon states disperse as soon as the approximate noninstantaneous term is replaced by the general convolution term of the GNSE. The convolution leads to a continuously shifting potential, which hinders the launched linearon to reach a steady state while inevitably distributing energy. The temporal drift cannot be overcome by adjusting the input (linearon) parameters, as it is intrinsic for all media possessing a nonlinear response with a rise time, such as liquids. The predicted existence of linearons in realistic LCFs can therefore not be confirmed.

Nonetheless, the hybrid nonlinear phase relation in Eq. (66) and the equilibrium fraction f_m^{equil} found in this chapter allow to predict another non-classical soliton regime. This regime presumably hosts modified solitary states (i.e., HSW) with shared spectro-temporal properties from both sides, classical solitons and noninstantaneous states. However, this study also exposed fundamental limits on measuring HSWs. Large noninstantaneous nonlinearities are required which demands considerably long pulses and highly noninstantaneous liquids. Potential candidates are CS_2 or C_2Cl_4, which provide molecular fractions of $f_m > 0.6$ for pulse widths of 300 fs or more (q.v. sec. 3.3.2), and thus grant access to the NIP-dominated regime. Such long pulses require meter-long propagation lengths (i.e., $L \gg L_D$) in the ADD to undergo the necessary adiabatic transitions of the input pulse to a hybrid state. But, as shown in ch. 3.4, the wavelength domain of the ADD regime is situated relatively far in the NIR, in case of step-index fibers, where losses are more dominant (e.g., q.v. Fig. 14b). Facilitated fiber designs, such as selectively filled micro-structured fibers, might enable access to the ADD in other wavelength domains with lower losses. However, their design and error-free fabrication along meters is very challenging.

In this work, another approach is followed. With the theoretical background obtained in this section, it should be possible to identify measurable observables of HSWs in soliton-mediated supercontinua generated in the more lossy ADD domains of easily accessible step-index LCFs. The definition of these potential observables and the systematic investigation of the impact of highly noninstantaneous nonlinearity on supercontinuum spectra is the central purpose of the next chapter.

5 HYBRID SOLITON DYNAMICS THROUGH THE PRISM OF SUPERCONTINUUM SPECTRA

5.1 Methodology

In the previous chapter, a new hypothesis was formulated, which predicts a new class of solitary waves (i.e., HSW) resulting from a hybrid electronic-molecular nonlinear system. A hybrid nonlinear phase relation appears as key parameter to identify the dominant nonlinearities. In this chapter, the impact of noninstantaneous nonlinearities on soliton-mediated supercontinuum generation (SCG) will be investigated. It will be shown that it is not sufficient to treat noninstantaneous systems as electronic systems with effectively reduced NRI. Instead, SC parameters such as bandwidth, fission onset, and coherence will show distinct dependencies on the molecular contribution. The signature of HSWs will show up in the SC spectra, indicating their relevance in the broadening process. The results of this chapter are partly published in [132].

In the closer scope of this work, we will immediately proceed to high soliton numbers and not investigate the *few soliton* regime. However, the calculations for $N > 1$ shown in sec. 4.2.5 allow the following conclusions:

1. Small contribution of noninstantaneous nonlinearity will cause the fission of solitary waves. For increasing molecular weight f_m (at constant total nonlinearity γ_0), the number of states created at fission is reduced.
2. The nonlinear compression of the pulse causes a successive transition from an potentially NIP-dominated regime to an IKP-dominated pulse regime. The equilibrium fraction f_m^{equil} can be used to estimate the dominating nonlinear phase at the fission point. For increasing soliton number N (i.e., not N_{eff}), f_m^{equil} converges towards unity (q.v. Fig. 20), and, thus, instantaneous effects dominate the fission process. How fast f_m^{equil} increases with N depends on the pulse width.
3. The effective soliton number N_{eff} (q.v. Eq. (63)) is an appropriate quantity to estimate the maximum number of created states after fission.

The findings in this chapter are based on systematic simulations of the nonlinear pulse propagation in the fundamental fiber mode (i.e., HE_{11}) using the full dispersive, lossless GNSE from q.v. Eq. (26). For practical purposes, simulation parameters will be given in realistic units. Pulse and fiber parameters are chosen to be close to experimentally accessible domains of anomalously dispersive CS_2-core silica-cladding fibers (q.v. ch. 3.4). In particular, the laser wavelength is limited to the thulium laser band (i.e., $1.9 - 2.0\,\mu\text{m}$).

The study starts in sec. 5.2 with comparing the SCG process in four selected systems, pumped with a 450 fs sech (noiseless) pulse at 1.95 µm center wavelength. The findings will help to classify the experimental SCG results in sec. 6.2. All four systems feature the same mode dispersion $\beta(\omega)$, and frequency dependence of the effective mode area $A_{\text{eff}}(\omega)$ (q.v. Tab. 8 in appendix B for more details). They are only distinguished in their NRI and molecular fraction f_m, which are chosen to mimic the following four nonlinear systems:

①OVERESTIMATED CASE This is a hypothetical glass-type system with entirely instantaneous nonlinear response, i.e. $f_m = 0$, and NRI as large as the total nonlinearity of a liquid system, i.e. $n_{2,\mathrm{tot}} = n_{2,\mathrm{el}} + n_{2,\mathrm{m}}$. It features a classical soliton number N.

②CONSERVATIVE CASE This is a hypothetical glass-type system with entirely instantaneous nonlinear response, i.e. $f_m = 0$, and NRI reduced to the electronic nonlinearity of a liquid system, i.e. $n_{2,\mathrm{tot}} = n_{2,\mathrm{el}}$. Hence, the system's soliton number N is smaller than in case ①.

③REALISTIC CASE This is a system assumed to be closest to a realistic CS_2 system with hybrid nonlinearity, whereas f_m is calculated pulse width dependent after Eq. 51 (e.g., as herein often used $f_m(450\,\mathrm{fs}) = 0.85$ for CS_2), and NRI as large as the total nonlinearity of a liquid system, i.e. $n_{2,\mathrm{tot}} = n_{2,\mathrm{el}} + n_{2,\mathrm{m}}$. The effective soliton number N_{eff} of this system is equal the soliton number N in case ②.

④UNREALISTIC CASE This is a hypothetical system with entirely noninstantaneous nonlinear response, i.e. $f_m = 1$, and NRI as large as the total nonlinearity of a CS_2 system, i.e. $n_{2,\mathrm{tot}} = n_{2,\mathrm{el}} + n_{2,\mathrm{m}}$. It features the same large soliton number N as case ①.

In sec. 5.3, bandwidth, onset energy, and coherence of the generated SCs are systematically investigated in dependence on the molecular weight f_m, pulse width, and pump wavelength to carefully identify operation regimes, where the noninstantaneous response contributes significantly to the broadening characteristics. Different to the section before, noise is added to the input pulse (q.v. sec. 2.2.4) to trigger noise seeded phenomena like MI (q.v. sec. 2.3.4.3). All data are shown in average of 20 individual runs with random input noise.

Finally, in sec. 5.4, the gathered insights will allow to formulate a theory to explain the impact of a strong noninstantaneous nonlinearity at each stage of the soliton-driven broadening process.

5.2 Hybrid fission characteristics

The broadening process in all four cases is exemplarily shown in Fig. 21 to elucidate the impact of the different non-linear contributions on the soliton fission process. Specific differences in the transition from instantaneous and noninstantaneous dominated systems can be identified.

Both instantaneous systems (i.e., cases ① and ② in Fig. 21a,b and c,d) show conventional soliton fission: after initial pulse compression going along with self-phase modulation up to the ZDW, a burst of solitons is released from the center of the pulse at a fission length of approximately 2 cm, and 5 cm, respectively. In detail, the strongly compressed pulse breaks up turbulently into multiple fundamental solitons on the long wavelength side (domain B), which shed energy towards shorter wavelengths via the generation of NSR (domain A). During further propagation the turbulent soliton burst is going over to deterministic soliton fission where solitons are sequentially sheared off from the outer zones of the pulse (domain C, not yet visible in case ② in Fig. 21c). In the transition of

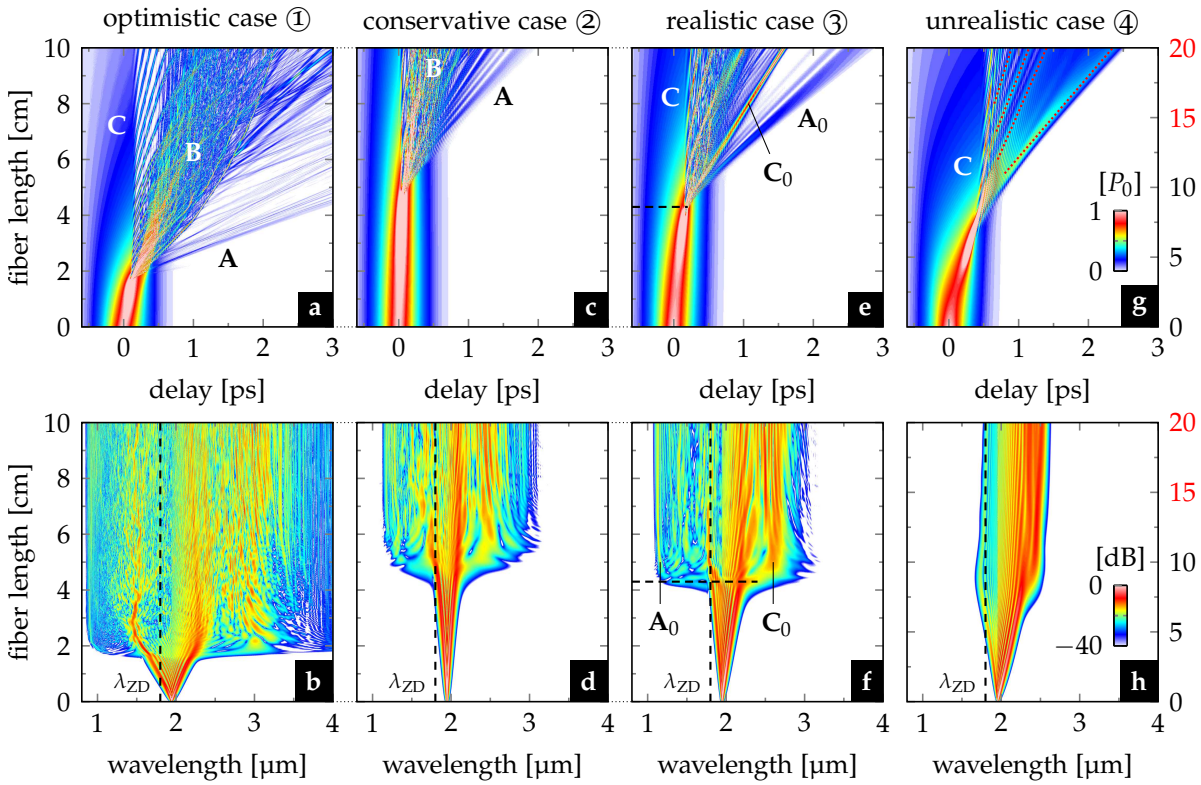

Fig. 21: **Impact of noninstantaneous nonlinearity on the soliton fission process** Comparison of temporal (a,c,e,g; linear scale) and spectral evolutions (b,d,f,h; log. scale) of a high power pulse ($P_0 = 10\,\mathrm{kW}$, $T_{HP} = 450\,\mathrm{fs}$, $\lambda_0 = 1.95\,\mu\mathrm{m}$) in the four nonlinear systems introduced in sec. 5.1 with zero loss and same dispersion, but different nonlinear response. The dynamics after pulse break-up can coarsly be distinguished in (A) radiation of NSR, (B) turbulent soliton bursts, and (C) neat soliton sheer-offs. The specified labels in panels (e,f) mark a sheer-off soliton (C_0) and the correlated NSR wave (A_0), and the vertical dashed line marks the fission length. The dotted red lines in panel (g) mark the direction of few degrading noninstantaneous states after wave breaking. The colorbar is the same for all panels in the respective row.

system ② ($N = 36$) to ① ($N = 92$), it becomes apparent that the achievable bandwidth increases, as well as the fission length decreases, for increasing N. It shall be reminded, that the broadening process also becomes increasingly vulnerable to noise for larger N, causing MI and incoherent broadening (q.v. sec. 2.3.4).

The noninstantaneous system (i.e., case ④ in Fig. 21g,h), shows different dynamics: the pulse initially undergoes self-steeping while forming a shock front up to a critical point where the wave breaks and temporally confined wave packets are created. The initial pulse compression happens over much longer propagation length of 7.5 cm as well compared to the other systems, and only a few well-separated states are formed (q.v. red dotted lines in Fig. 21g). Remarkably, their temporal characteristics reveal confined trailing features and dispersive fronts similar to the degrading noninstantaneous states shown in sec. 4.2.5 (q.v. Fig. 19c). In fact, the neat sequential shear-off of those wave packets has unmistakeable similarities to deterministic soliton fission. The output spectrum of this system features a significantly reduced bandwidth compared to the instantaneous systems ① and ② and no indications of NSR.

The hybrid system (i.e., case ③ in Fig. 21e,f) describes an intermediate situation between the overestimated case ① and the unrealistic case ④ in terms of bandwidth and fission length (i.e., 4.3 cm), that makes it most comparable with the conservative instantaneous case ②. This proves that the effective soliton number N_{eff} is a valuable tool to estimate the fission process of a hybrid nonlinear system, whereas the classical soliton number N, which includes the total NRI, overestimates the SCG capabilities. However, fundamental differences in the fission dynamics can be identified between conservative and realistic case (② and ③) in both time and spectral domain. In time domain, the fission process is rather comparable to deterministic soliton fission (domain C) than to turbulent soliton bursts (domain B) being dominant in case ②. In spectral domain, the spectral broadening sets on earlier than in case ② and progresses faster, which is both explained by an enhanced pulse compression similar to an instantaneous system with higher nonlinearity (e.g., case ①). Also, the initial soliton (i.e., C_0 in Fig. 21f) and its corresponding NSR (i.e., A_0 in Fig. 21f) are spectrally well distinguishable from other spectral components due to their high intensity and fast creation (i.e., temporally set off from consecutive states).

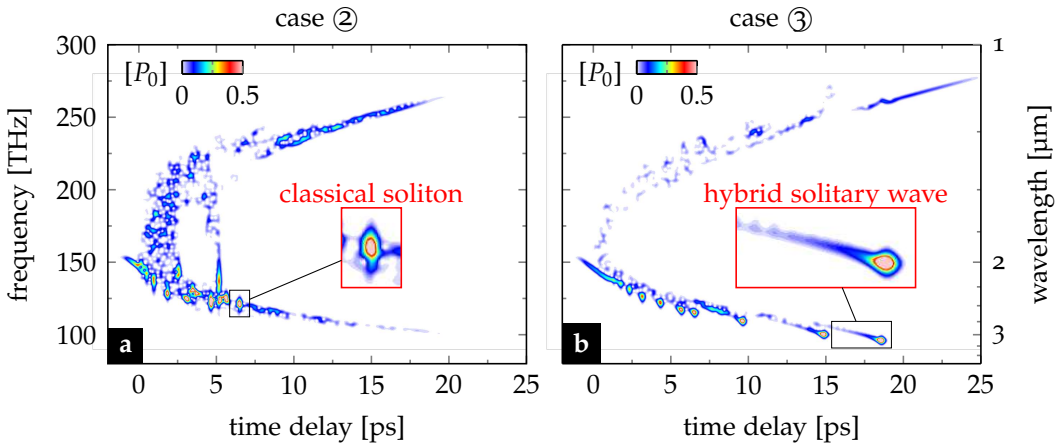

Fig. 22: HSW **emerging in supercontinua.** Spectrogram of a) system ② and b) system ③ (linear scale normalized to initial peak power) assuming lossless propagation over 50 cm.

The notable differences between the system with reduced instantaneous nonlinearity (i.e., case ②) and the realistic system with hybrid nonlinearity (i.e., case ③) indicate a modification of the soliton dynamics as a result of the emergence of HSWs. Moreover, the spectro-temporal visualization in Fig. 22 of the decomposed pulse after 50 cm propagation in system ③ reveals the characteristic comet-like signature of a HSW, as introduced in sec. 4.2.5 (q.v. Fig. 19d or Fig. 20c). It is not straightforward to explain at which state of the fission process HSWs emerge since the soliton features closer to the fission point cannot be resolved clearly in the spectro-temporal visualization. Thus, further benchmarks need to be applied to enlighten the entire fission process.

5.3 Spectral observables of hybrid soliton dynamics

5.3.1 Bandwidth and onset energy

The characteristic differences between the SC systems shown in the previous section motivate to study the dependency of SCG on the molecular fraction f_m in more detail, and to identify observables of a dominant NIP. Here, a series of hybrid nonlinear systems with artificially varied f_m, but equal effective soliton number $N_{\text{eff}} = 17$, is compared to an instantaneous reference system with same soliton number N (i.e., case ② where $N = N_{\text{eff}}$). Practically, this means that different liquid-core systems are analyzed in contrast to a comparable glass-like waveguide. The reader may note, that the soliton number is chosen such to be beyond the empirical coherence limit introduced by Dudley *et al.* (i.e., $N \leq 10$; q.v. sec. 2.3.4).

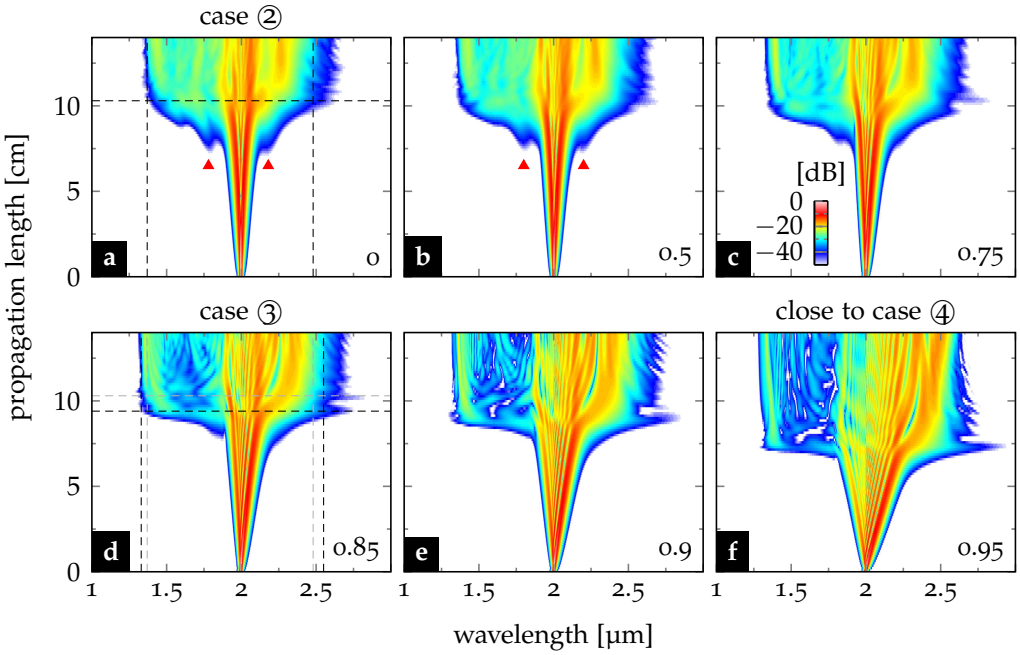

Fig. 23: Impact of the NIP on the supercontinuum bandwidth and onset. Evolutions of the pulse spectrum averaged over 20 shots ($T_{\text{HP}} = 450\,\text{fs}$, $\lambda_0 = 1.95\,\mu\text{m}$, $P_0 = 2.5\,\text{kW}$) each propagating through CS_2-core waveguides with same dispersion and electronic nonlinearity (i.e., same N_{eff}), but differently strong contributions of the noninstantaneous response. The numbers in the lower right corner denote the molecular fraction f_{m}. Simulations are based on the GNSE with initial phase noise.

Fig. 23 shows the averaged spectral evolutions of 20 individual simulation runs with input noise for each selected system with increasing molecular fractions ranging from $f_{\text{m}} = 0$ (i.e., case ②) to $f_{\text{m}} = 0.95$ (i.e., close to case ④). The spectral pulse evolution changes only little for increasing f_m up to $f_{\text{m}} = 0.75$. This domain is dominated by noise-driven soliton bursts, or MI, which is indicated by small spectral modulations symmetric (on the frequency axis) around the central pump frequency at the broadening onset (q.v. red marks in Fig. 23a and b), as well as blurred average spectra as consequence of shot-to-shot spectral fluctuations. Starting from $f_{\text{m}} = 0.75$, the spectral pump modulations start to disappear and the broadened spectra show more spectral features, e.g., distinct NSR

signals. Remarkably, this empirically found threshold of $f_m = 0.75$ is close to identical with the equilibrium fraction $f_{\mathrm{m}}^{\mathrm{equil}} = 0.73$ of the system, where IKP equals NIP.

Thus, for $f_m > f_m^{\mathrm{equil}}$, the impact of the NIP increases, in particular during the SPM-driven broadening prior soliton fission. Here, the NIP causes a notable increase of the broadening and a red-shift of the spectrum (cf. Figs. 23 d-f). The red-shifted components propagate in waveguide regions with higher dispersion leading to a reduction of the fission length (i.e., $L_{\mathrm{fiss}} \propto |\beta_2|^{-1/2}$), which is exemplarily shown in Fig. 23d (dashed lines) for increasing f_m. Moreover, the altered initial soliton wavelength at fission causes a blue-shift of the NSR and potentially increases the soliton recoil, overall leading to a slightly broader bandwidth than in case of MI-driven broadening in system ② (cf. dashed lines in Fig. 23a and d).

In consequence, bandwidth and broadening serve as experimental observables for the NIP impact. The direct method requires a liquid-core fiber and a glass fiber with comparable optical properties, or at least, comparable effective soliton number. Since this is not a trivial requirement, alternatively the accurate correlation of the measured results from a liquid-core system with simulation results of various systems (i.e., case ② or ③) allows to identify the underlying broadening mechanics. However, the latter method is challenging, since the simulations demand detailed knowledge about all pulse parameter, input and output energies, and the linear and nonlinear properties of the waveguide.

5.3.2 Non-solitonic radiation

The emergence of NSR in the simulated spectra provides another tool to get insights in the broadening process, in particular in the early fission process. Depending on the dominating soliton phase, a suitable phase-matching condition should exist to theoretically link the strongest NSR-related feature in the measured spectrum (i.e., the most blue-shifted maxima) to the spectral feature of the first expected soliton (i.e., the most red-shifted maxima). For instance, the so-calculated spectral location of the initial fundamental soliton should coincide with the measured maxima especially well just above the supercontinuum onset, where the soliton is mainly unaffected by self-frequency shifts. Beyond the fission length (i.e., $L > L_{\mathrm{fiss}}$) the initial soliton is frequency shifted due to noninstantaneous effects as shown in Fig. 19, which causes an offset between calculated and measured soliton positions. Also note, that this procedure assumes a negligible frequency offset due to soliton recoil.

The key for this theoretical link is an accurate dispersion model and the correct handling of the nonlinear phase term in the phase-matching. The phase-matching conditions introduced before (cf. Eq. (38) and Eq. (64)) include a characteristic nonlinear phase term φ_{NL} for either instantaneous or noninstantaneous solitary states. Moreover, the solitary states emerging from fission in hybrid nonlinear media may also possess a hybrid nonlinear phase. Thus, for each of the four model systems (i.e., case ①–④) φ_{NL} needs to be

chosen adequately, which requires a generalization of the phase-matching conditions in the following form

$$\Delta\beta \approx \beta(\omega) - \beta_s - (\omega - \omega_s)\beta_{1,s} - \varphi_{\mathrm{NL}} \equiv 0 \tag{68}$$

$$\text{with} \begin{cases} \varphi_{\mathrm{NL}}^{①,②} = \gamma_0 P_s/2 & \text{for system ① and ②} \\ \varphi_{\mathrm{NL}}^{③} = (1-f_m)\gamma_0 P_s/2 + f_m \gamma_0 \mathcal{E}_p R_0 & \text{for system ③} \\ \varphi_{\mathrm{NL}}^{④} = \gamma_0 \mathcal{E}_p R_0 & \text{for system ④} \end{cases}$$

whereas $P_s = P_0(2N_{\mathrm{eff}} - 1)^2/N_{\mathrm{eff}}^2$ can straightforwardly be used to estimate the peak power of the initial soliton upon fission. $\mathcal{E}_p$ is the pulse energy of the input pulse (i.e., assuming maximum phase) and R_0 is the response maximum. In case of the hybrid system ③, the hybrid nonlinear phase from Eq. (66) was pragmatically chosen, since it was successful applied in sec. 4.2.3 and 4.2.5. It shall not be implied that this nonlinear phase has any relevance to a theoretical solution of the hybrid system eventually being found in the future. The reader should note that the difference in $\varphi_{\mathrm{NL}}^{②}$ and $\varphi_{\mathrm{NL}}^{③}$ is solely the NIP term, since γ_0 of system ② is equal to $(1-f_m)\gamma_0$ of system ③.

5.3.3 Temporal coherence

The changing broadening characteristics shown in sec. 5.3.1 indicate a change of the noise stability of the nonlinear system for increasing contribution of the noninstantaneous effects. This noise behavior should become visible in the first-order degree of coherence $|g_{mn}^{(1)}|$ of those systems as introduced in 2.3.4.1.

Fig. 24 shows the evolution of the coherence along propagation for the same systems shown in Fig. 23. In the systems with $f_{\mathrm{m}} < 0.75$, the coherence drops drastically beyond the fission point, which confirms the appearance of MI in Kerr-dominated systems. The average coherence $\langle|g_{mn}^{(1)}|\rangle$ of the output spectra is always smaller than 0.6 in this domain. As shown in sec. 2.3.4.3, MI-driven supercontinua underlie turbulent soliton bursts triggered by the initial phase noise of the input pulse.

For increasing molecular contributions beyond $f_{\mathrm{m}} \approx 0.75$, the hybrid systems are remarkably less susceptible to initial noise. This pulse-to-pulse spectral stability correlates with an improving coherence in Fig. 24d-f across the entire bandwidth after soliton fission. The mean coherence of the output spectrum increases from 0.70 for $f_R = 0.75$ to 1.00 for $f_R = 0.95$. This behavior is remarkable given the relatively high effective soliton number (i.e., $N_{\mathrm{eff}} = 17$) beyond the empirical stability limit (i.e., $N \leq 10$), and clearly distinguishes highly noninstantaneous hybrid systems from quasi-instantaneous systems.

The origin of the reduced susceptibility to noise is associated with the strong impact of the noninstantaneous nonlinearity. The slow molecular response of CS_2 *stiffens* the nonlinear phase against fast temporal fluctuations. The pulse undergoes a phase rectification process during the propagation through the noninstantaneous medium. The phase properties of a certain pulse section are encoded in the induced nonlinear polarization of the slow molecular motions and couple back to all later parts of the pulse. Thus, the

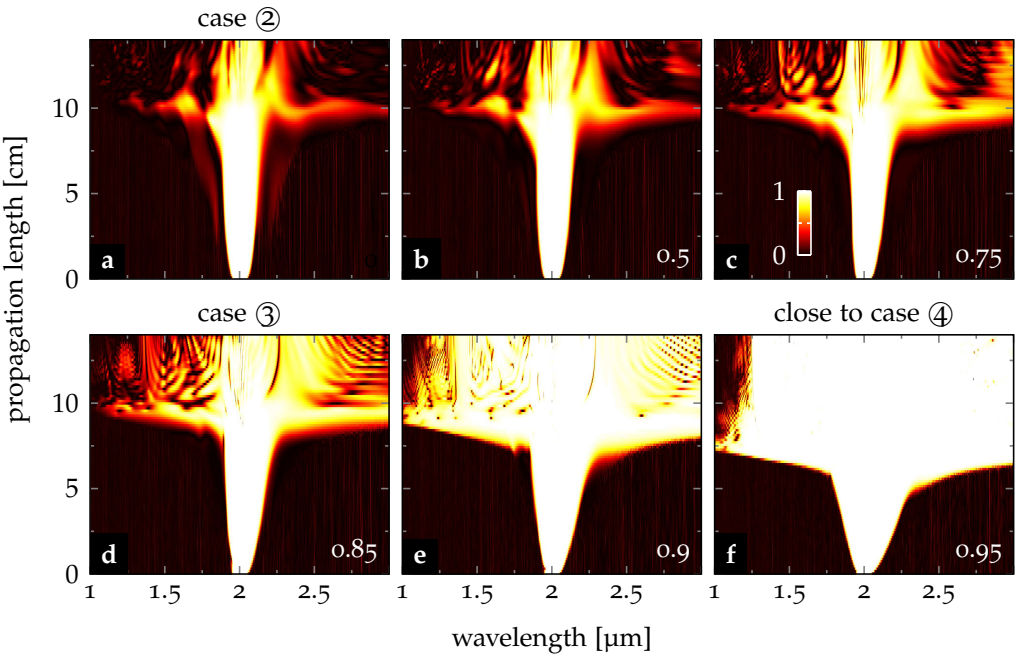

Fig. 24: **Impact of the NIP on the spectral reproducibility.** Evolutions of the spectral distribution of temporal coherence between 20 shots ($T_{HP} = 450\,fs$, $\lambda_0 = 1.95\,\mu m$, $P_0 = 2.5\,kW$) each propagating through CS_2-core waveguides with same dispersion and electronic nonlinearity (i.e., same N_{eff}), but differently strong contributions of the noninstantaneous response. The numbers in the lower right corner denote the molecular fraction f_m. Simulations are based on the GNSE with initial phase noise.

local fluctuations of later pulse sections are quickly averaged with phase contributions of all previous times. Mathematically, this can be seen in the GNSE, where the continuous convolution of the optical pulse with the slow material response can be understood as a moving average filter. This filter adds a smoothened temporal phase to the pulse, instead of accumulating the noisy local phase by the Kerr effect. Overall, this leads to a phase clean-up (i.e., *phase rectification*) along the pulse during propagation and, thus, to coherent soliton fission.

To measure the coherence of the generated supercontinua offers the most direct link to reveal a modification of the soliton dynamics by NIP, and the potential involvement of HSWs. However, also here, the experimental comparison of the targeted hybrid system against a comparable instantaneous system is essential.

5.3.4 Bandwidth-coherence product

In the sections before, the hybrid system was studied for artificially increasing molecular fractions and a single pulse condition. However, the molecular fraction of a natural liquid cannot freely be chosen, but depends on the pulse shape. Thus, entering the NIP-dominant soliton regime of a selected liquid requires careful control over pulse width and operation wavelength. This section provides a laser parameter map exemplarily for a CS_2-core fiber ($\varnothing_{co} = 4.7\mu m$) that identifies operation domains of improved coherence and bandwidth compared to glass fibers.

In accordance with the empirical work by other groups [27, 129], both the conservative case ② and the realistic case ③ were simulated for large sets of pulse widths

and wavelengths. The pump wavelengths were chosen around the fiber's ZDW (i.e., $\lambda_{ZD} = 1.8\,\mu m$), and the pulse widths span two orders of magnitude from 30 fs to 1 ps. In case ③, the parameters γ and f_m were calculated individually for each input pulse using the NRI definition from Eq. (51). The peak power was kept constant at 3 kW. Each parameter set was simulated 20 times, each with random input phase noise, to deduce coherence information. Fig. 25 shows three properties of the simulated output spectra after 20 cm propagation over pulse width and wavelength. These properties are the 20 dB bandwidth of the average spetrum, the average coherence, and the product of both quantities denoted as **coherence-bandwidth product (CBP)**.

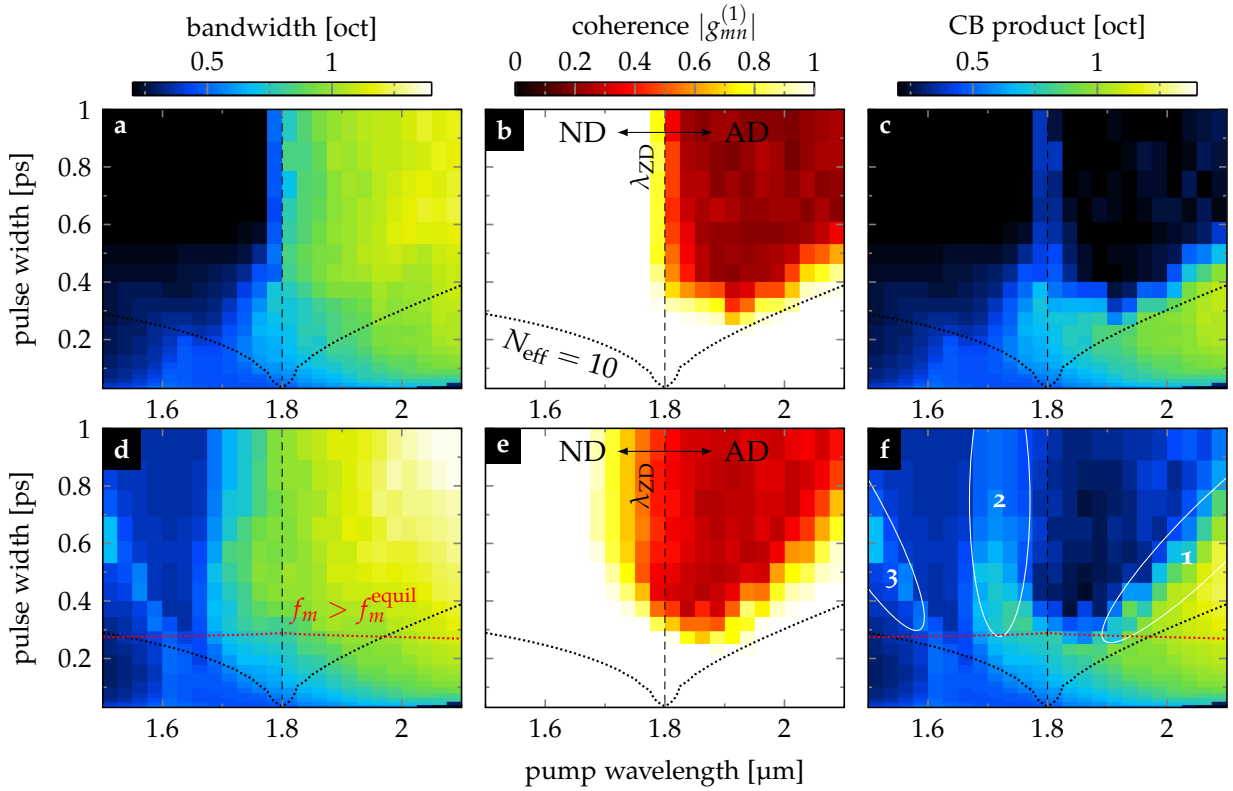

Fig. 25: **Impact of the noninstantaneous nonlinearity on the supercontinuum properties in a wider parameter domain.** An instantaneous (a-c) and a noninstantaneous system (d-f) are compared in terms of (a,d) 20 dB bandwidth (in octaves), (b,e) coherence, and (c,f) the coherence-bandwidth product. The ZDW is located at $\lambda_{ZD} = 1.8\,\mu m$. The dotted lines mark the parameter conditions for which $N_{eff} = 10$ (black) and $f_m = f_m^{equiv}$ (red).

Focusing on the bandwidth first, case ② in Fig. 25a shows the classical behavior of an instantaneous system. Pumping at wavelengths across the ZDW in the ADD leads to a sudden bandwidth increase, which improves for increasing pump wavelength and pulse width. In the realistic systems ③, considerable broadening occurs already in the NDD close to the ZDW (i.e., around 1.7 μm in Fig. 25d). Remarkably, the realistic system features larger bandwidths than the instantaneous one for identical pump parameters as soon as $f_m > f_m^{equil}$ (i.e., here for $T_{HP} > 300\,fs$).

The coherence map, in Fig. 25e reveals that the extended broadening regime of the realistic systems towards the NDD features a similarly low coherence as the major part of the ADD. In fact, the coherence deteriorates in highly noninstantaneous systems if

pumped in the NDD close to the ZDW. In the ADD, however, an improvement of the coherence can be noted in the vicinity of the classical coherence threshold (i.e., $N_{\mathrm{eff}} = 10$ in Fig. 25b). The coherent domain of the realistic systems clearly exceed this threshold, unambiguously confirming the coherence improvement as an accessible phenomena in natural liquid-core waveguides.

Since both benchmarks, bandwidth and coherence, ought to be large in well performing SC sources, the introduction of a combined quantity in form of the product of both appears meaningful. The CBP can be understood as shot-to-shot reproducible bandwidth of the nonlinear system. It allows to clearly distinguish divergent parameter domains between nonlinear systems within a single graphical visualization per system.

The CBP of the realistic system ③ reveals three improved parameter domains compared to the instantaneous systems ②. The first domain is the before-mentioned domain of improved coherence in the ADD close to the classical coherence limit $N_{\mathrm{eff}} = 10$ (q.v. domain 1 in Fig. 25f). A second domain opens in the weak NDD around 1.7 µm (q.v. domain 2 in Fig. 25f), which clearly correlates with the shifted broadening onset towards the ZDW mentioned before. Third, a highly coherent domain with moderate bandwidth can be identified far in the NDD above $N_{\mathrm{eff}} = 10$ (q.v. domain 3 in Fig. 25f). Most notably, all three domains occur in systems with molecular fractions larger than the equilibrium fraction f_m^{equil} (q.v. red line in Fig. 25f), which entirely attributes the observed changes in the CBP to the dominant noninstantaneous effects.

The origin of domain 1 was discussed in earlier sections. Domain 2 and 3 need further explanations, which shall be sketched out here briefly. Domain 2 is a result of the strong spectral red-shift during SPM broadening, leading to efficient energy transfer towards and across the ZDW, which in turn triggers soliton fission or MI. Thus, soliton-mediated broadening can be achieved in hybrid systems at pump wavelengths significantly shorter than the ZDW.

Domain 3 originates from self-seeded four-wave mixing between multiple spectral parts of an SPM-broadened spectrum. First, energy is efficiently transferred close to the ZDW due to the red-shifted SPM, delivering the pump energy for the four-wave mixing process. Weaker spectral components of the SPM spectrum may overlap with phase-matched spectral domains and serve as seed for the parametric process. In time, the pulse forms a shock-front providing the necessary overlap between pump and seed, which finally triggers efficient energy conversion from the pump (i.e., the field components close to the ZDW) to spectrally symmetric side bands. This situation is in absolute balance between (1) the right amount of SPM, to provide enough pump energy at the ZDW, (2) the decelerated temporal pulse spreading and shock-front formation, and (3) the spectral overlap with the phase-matched mixing components. This process might be much more efficient in LCFs due to the NIP-enhanced red-shift of the SPM towards the pump domain close to the ZDW. Also it may allow to transfer a notable part of the pulse energy across the ZDW into the ADD, and may possibly allow for the excitation of fundamental solitons while pumping in the NDD.

5.4 Theory of noninstantaneously dominated supercontinuum generation

The large scale parameter study of the hybrid nonlinear systems allows to form the following conclusion: SCs generated in highly noninstantaneous systems are unambiguously influenced by the slow nonlinearity, and in particular the dominant NIP. In consequence, both bandwidth and coherence (i.e., pulse-to-pulse spectral stability) increase, while the fission length decreases, for increasing molecular fraction f_m. Most impressively, the broadening characteristics for large soliton numbers undergoes a transition, starting with noise-driven modulation instabilities at small f_m to coherent soliton fission at large f_m. An empirical critical molecular fraction, beyond which the noninstantaneous effects become non-negligible, was found to be $f_m = 0.75$, which matches well with the theoretical equilibrium fraction $f_m^{\text{equil}} = 0.73$

Remarkably, the spectro-temporal signature of HSWs were found in SCs from systems with large f_m, revealing the involvement of those states in the broadening process. However, the question remains at which part of the process these states occur. Two theories become apparent:

FISSION THEORY During the entire fission process the NIP plays a major role and cannot be neglected. Despite the temporal compression towards the fission point, the NIP is not dominated by the IKP, and sets the phase of the consecutive solitons at fission. The phase of these states might change during further propagation, (i.e., the temporal isolation from other parts of the pulse train), but the NIP dominates over the Kerr phase at all times.

TRANSITION THEORY The temporal compression before the fission point is highly phase-stabilized and enhanced by the NIP, that causes a strong peak power increase up to the fission point. At the fission point, the IKP dominates over the NIP, and the compressed pulse spawns a series of classical solitons. In the temporal window of the compressed pulse, the NIP acts just as a quasi-static offset. During further propagation, the classical solitons experience a temporal delay due to SFS. As soon as a soliton is temporally isolated from other components of the pulse train, and the quasi-static phase offset they cause, this soliton accumulates dynamic NIP caused by its own field, which initiates the transition from a classical soliton to a HSW.

A suitable experimental system might provide further insights into the process. Measurements of SC spectra from LCFs might reveal the impact of a long-lasting response on the soliton dynamics. This is analogous to associating measured SFSs with Raman effects in conventional silica systems. Exposing the dominant impact of NIP gives probable cause for the involvement of HSWs. The next chapter aims to identify suitable laser and fiber systems, which show NIP-dominant SCG, and potentially host HSWs. The spectral observables introduced in this chapter will serve as benchmarks for those systems.

6.1 Supercontinuum measurements in liquid-core fibers

In this chapter, supercontinuum generation will be experimentally demonstrated in multiple LCFs using two pump pulses of distinct width. The results will allow to analyze the measured bandwidth, SC onset energy, and spectral features by means of the observables of dominant NIP introduced in the ch. 5 and GNSE simulations. One experimental system will be identified to host modified soliton dynamics. The shown results are partly published in two journal articles [132, 178].

6.1.1 Experimental details and methodology

The SCG experiments are based on a setup that combines an ultrafast thulium laser source with an optofluidic system (see scheme in Fig. 26). Two custom-made thulium laser systems could be used within the framework of this thesis by courtesy of Prof. Jens Limpert and co-workers of the Institute of Applied Physics in Jena. Since the engineering of the systems was not part of this thesis, their setup shall be described only very briefly. The output parameters of both systems are listed in Fig. 26, and, for more information, the reader is advised to look up the respective references [179, 178].

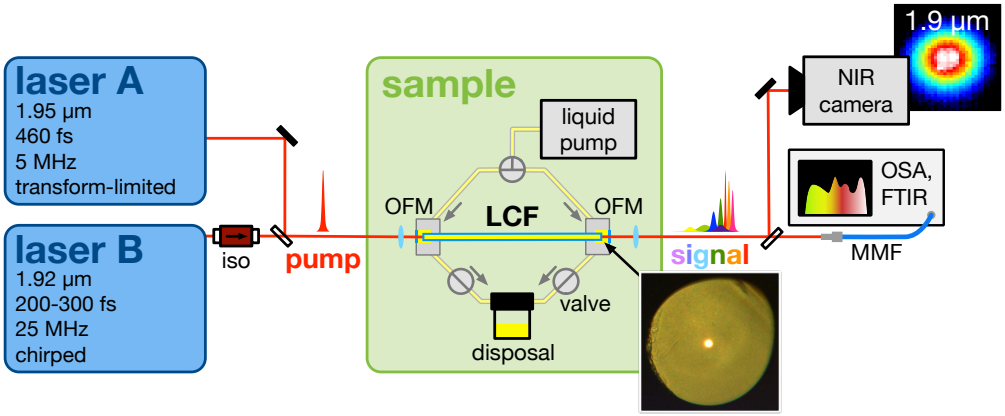

Fig. 26: **Optofluidic supercontinuum setup.** One of two pulsed laser systems pumps a LCF. The spectrum and the auto-correlation of the pump pulse was monitored. Two opto-fluidic mounts (OFMs) mounted the LCF and enabled filling and light coupling. The indicated pump system is optional. The inset shows a transmission microscopy picture of a short CS_2-core LCF. The output signal is characterized with a NIR camera, and a NIR optical spectral analyzer (OSA), or a Fourier-tranform infrared (FTIR) spectrometer. The inset at the camera shows a near-field image of the output fundamental mode at 1.9 µm wavelength.

Laser system A comprised a home-built thulium-based fiber master oscillator whose output was amplified in two successive amplification stages and finally compressed in a grating compressor. The thulium-doped fibers were pumped at 790 nm, and the amplification fibers were constantly water-cooled at a temperature of 20 °C. The grating compressor was used to compensate the second-order phase of the output pulses. An acousto-optical modulator allowed step-wise reduction of the pulse repetition rate starting at 11.6 MHz. The system featured an output spectrum with a 20 dB bandwidth of 26 nm and near-transform-limited optical pulses with a pulse width T_{HP} of 460 fs. The

pulse reconstruction from the Fourier transform of the output spectrum and a third-order phase offset ($D_3 = -0.025\,\mathrm{ps}^3$) matches the recorded auto-correlation very well.

Laser system B consisted of a commercial thulium-based fiber oscillator delivering pulses of 500 fs duration, centered at 1.92 µm, at a repetition rate of 25 MHz. These pulses were stretched in 25 cm anomalous dispersive single-mode fiber (Corning SMF-28) and 4 m normal dispersive ultra-high NA fiber (Thorlabs UHNA4). Before amplification, their polarization was controlled by a combination of a half- and a quarter-wave-plate. Finally, this (seed) signal ($\approx$3 mW average) was coupled to a water-cooled thulium-doped photonic crystal fiber and desirably amplified up to 1 W average power. The initial positive chirp from the oscillator output was partly compensated during nonlinear pulse compression in the anomalous dispersive amplifier fiber. Hence, the pulse duration (i.e., T_{HP}) was adjustable between 200 and 300 fs by decreasing the amplification, and, thus, the nonlinear compression. However, the final output pulse is not transform limited since the last isolator adds a non-negligible chirp. The output pulse shape and spectrum of the laser system were controlled online with two reflexes coupled into an autocorrelator and a spectrometer at any time of the experiments, ensuring stable pulse conditions.

The fabrication of the LCFs can straightforwardly be implemented by mounting each end of a silica capillary in an OFM (i.e., small aluminum tank with sealed sapphire window). The mounts are filled successively with a syringe, while giving enough time in-between that the capillary force can entirely fill the capillary. The fabrication process in described in more detail in appendix C. The properties of the LCFs used for the main data sets are tabulated in Tab. 3. After fabrication in a fume hood, the fiber's OFMs are placed each in front of a fiber coupling stage (i.e. a three-axis translation stage). Light was coupled free-space in and out the fiber using aspheric lenses (e.g., Thorlabs A375, A397, C230) with suitable NA to account for the NA of the LCF and to avoid clipping of the output mode (i.e., $NA_{\mathrm{input}} < NA_{\mathrm{LCF}} < NA_{\mathrm{output}}$). The coupling was optimized at power levels of a few milliwatts, where no significant spectral broadening is observed. Since most LCFs used in the experiments supported few modes, efficient excitation of the fundamental mode was ensured by imaging the output mode patterns with an extended InGaAs camera (Xenics XEVA) or a thermal camera (MCT detector, FLIR SC7000) while optimizing the coupling. Coupling efficiencies up to $\eta = 55\,\%$ were reached estimated using $\eta = P^{\mathrm{out}}_{\mathrm{meas}} / (T^{\mathrm{out}}_{L} T^{\mathrm{out}}_{W} \cdot P^{\mathrm{in}}_{\mathrm{meas}} T^{\mathrm{in}}_{L} T^{\mathrm{in}}_{W} T_{\mathrm{LCF}})$, taking into account modal attenuation (i.e., fiber transmission T_{LCF}) and reflections at lenses (i.e., transmission T_L) and OFM windows (i.e., transmission T_W) each at in- and output side of the LCF. The coupling was stable over several days under atmospheric pressure and even while flushing the opto-fluidic mounts with flow rates up to $10\,\mathrm{ml\,min}^{-1}$.

After coupling optimization, the fiber output was collimated for the pump wavelength and detected with an InF_3 multimode fiber ($\varnothing_{\mathrm{co}} = 100\,\mu\mathrm{m}$) directly placed in the collimated beam and connected to a suitable spectral analyzer (Yokogawa NIR and MIR OSA, Thorlabs FTIR OSA305, Jasco FTIR 6300). The mountings of the LCFs prevented a cut-back of the fibers. Thus, a typical measurement included recording the output spectra

Table 3: **Specifications of the main LCFs measured in this thesis.** Shown are inner diameter ($\varnothing_{co}$), ZDW, the V-parameter at pump wavelength (dependent on the used laser system), fiber length (L), coupling efficiency η, and damage threshold P_{th} measured on the input side. The coupling efficiencies η were calculated assuming 15 % measured reflection and clipping losses at the input lens, 6 % reflection losses at the output lens, 7.3 % reflection loss at each of the two sapphire windows, and lossless propagation in case of CCl_4 and C_2Cl_4 and 14.5 % absorption in case of CS_2, respectively.

ID	core liquid	$\varnothing_{co}$ [µm]	ZDW [µm]	$V(\lambda_0)$	L [cm]	η [%]	P_{th} [mW]	laser system	presented in sec.
#1	CS_2	4.7	1.83	4.55	7	50	170	A	6.2, 7.2.2
#2	CS_2	4.7	1.83	5.04	8	47	150	B	6.2
#3	CS_2	3.3	1.80	3.55	18	30	150	B	7.1.3
#4	10:1 CCl_4:CS_2	4.6	1.64	1.88	25	35	112.5	B	6.2
#5	10:1 CCl_4:CS_2	8.1	1.78	3.31	20	55	112.5	B	6.2
#6	C_2Cl_4	4.6	1.72	2.86	21	50	200	B	6.2
#7	C_2Cl_4	4.9	1.72	3.67	55	42	>200	–	7.3.1
#8	CCl_4	8.2	1.69	1.78	19	~ 30	~ 85	–	7.3.1
#9	6:1 CCl_4:C_2Cl_4	4.9	1.51	1.87	52	50	125	–	7.3.1

for increasing pulse energies, instead of decreasing fiber length, which is analogous to a certain extent (i.e., the nonlinear phase depends on an equal product of pulse power and fiber length). The recorded spectral power evolution is further on called **spectral fingerprint** of a fiber. Input and output power were accurately controlled during all measurements. The pulse energy in each experiment was increased until the transmission efficiency dropped. Thus, the highest pulse energy shown in spectral fingerprints defines the damage threshold of the respective fiber.

Two types of fiber damage were observed in the experiment: (a) mode instabilities and partially reversible transmission drops due to thermal load at high average power (q.v. Tab. 9 in appendix C, row 3), and (b) irreversible transmission drops at high pulse energy (q.v. Tab. 9 in appendix C, row 1). Most probably the thermal damage arises from linear absorption, whereas the other damage is related to nonlinear effects, such as self-focussing. Other groups reported multi-photon absorption as source of transmission drops and bubble formation [67, 68]. However, the output power characteristics of the experiments in this work can be explained entirely with the linear absorption behavior of the LCF (q.v. Fig. 52 in appendix C). Also, nonlinear absorption is typically weak in the NIR.

In sec. 6.2, the SCG results of three different core liquids, CCl_4, CS_2, and C_2Cl_4, are analyzed. Among them, CCl_4 is expected to act the most similar to silica fibers due to its low molecular nonlinearities, which particularly allows to confirm the GNSE solver and the quality of the underlying dispersion model. In case of CS_2 and C_2Cl_4 the noninstantaneous nonlinearity is expected to play a much more dominant role, requiring a careful analysis in sec. 6.3 by means of the theoretical benchmarks and spectral observables introduced in ch. 4 and ch. 5.

6.2 Supercontinuum generation in liquid-core fibers

6.2.1 Carbon tetrachloride (CCl_4)

Supercontinua in CCl_4-core fibers were generated using laser system B (here T_{HP} = 270 fs). A small admixture of 10 vol% CS_2 was necessary to increase the IOR of the core medium and ensure robust wave guiding. As a side effect, f_m was increased from 0.19 (pure CCl_4) to 0.53. Two core diameters were tested. The spectral power evolution of the small-core LCF in Fig. 27a reveals a first breathing cycle of a higher-order soliton until 1 nJ, i.e., a slight spectral broadening until energies of 0.8 nJ followed by spectral narrowing. Above 1 nJ, a spectral red-shift dominates that decomposes the pulse. The maximum soliton number N of the system calculates to 6.6 (i.e., N_{eff} of 4.4). The power dependence of the spectral evolution is well reproduced by the nonlinear simulations based on the dispersive GNSE (cf. Fig. 27a,b). The simulation predicts the emergence of a distant NSR at 1.15 µm which lied outside of the spectral domain of this measurement (cf. red domain in Fig. 27a). The appearance of the NSR after the first spectral breathing cycle is a clear indicator for a higher-order soliton propagation perturbed by third-order dispersion, which initiates the decomposition of the soliton breather [180].

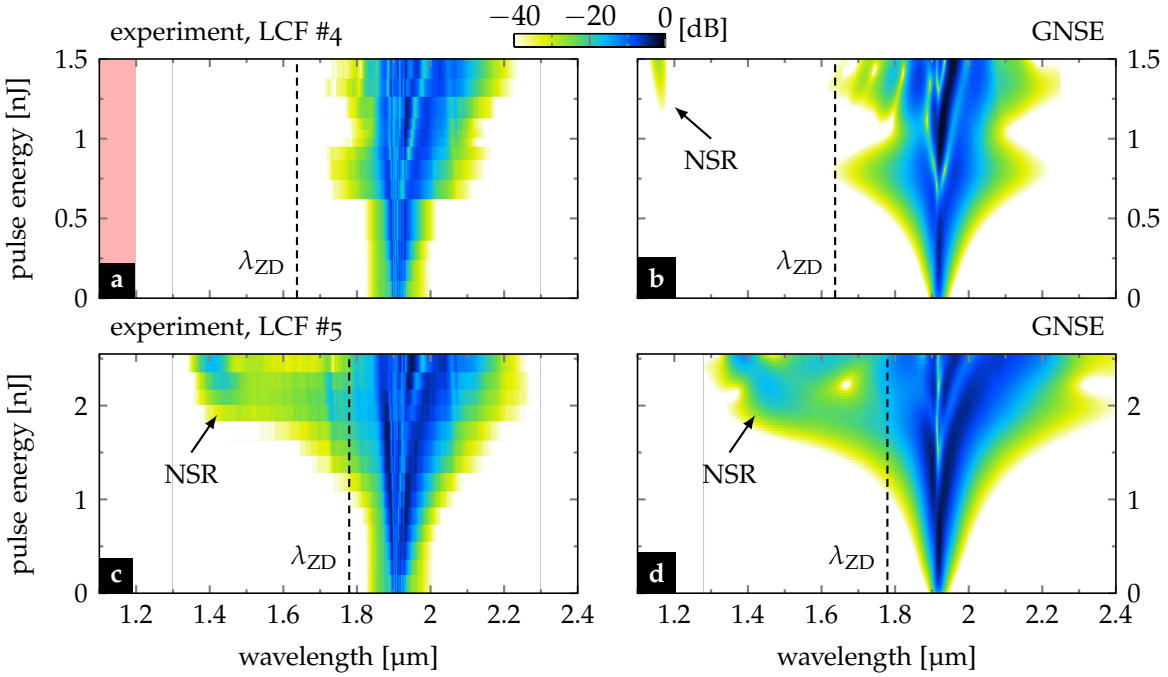

Fig. 27: Spectral fingerprints of fiber #4 and #5. Measured (left) and simulated (right) spectral power evolution of the output spectra generated in two CCl_4-filled LCFs with different core diameter: a, b) $\varnothing_{co}$ 4.6 µm, length 25 cm; c, d) $\varnothing_{co}$ 8.1 µm, length 20 cm. The color scale is the same for all panels and refers to the normalized decadic logarithm of the intensity in dB. Figure reprinted from [178], ©2018, OSA.

The boadening capabilities of the CCl_4-core LCF were improved by increasing the core diameter to 8.1 µm and, thus, shifting the ZDW closer to the pump wavelength, as indicated by the nonlinear design map (q.v. Fig. 15). The corresponding spectral fingerprint in Fig. 27c shows distinct NSR emission at 1.4 µm wavelength starting at 2 nJ pump energy,

as well as a spectral broadening up to 850 nm bandwidth at maximum pulse energy of 2.5 nJ (corresponding to $N = 12$). Both observations are again well described by the GNSE simulations in Fig. 27d. This remarkable match confirms both the applicability of the nonlinear design maps and the quality of the new dispersion models.

The damage threshold of both fibers is comparable when the damage is considered to happen at the fiber input facet, where the highest field intensity is located. The calculated pulse energies before coupling, taking into account the respective coupling efficiencies and highest pulse energies (see Fig. 27), were found to be around 4.5 nJ for both fibers, which corresponds to a peak power limit of approximately 15 kW at 1.92 µm. Peak powers nearly twice that high are achieved during the nonlinear self-compression just before soliton fission, which was measured without stability problems. Therefore, it can be assumed that the observed drop of the transmission is not linked to the injected intensity but rather to accumulated thermal load.

6.2.2 Carbon disulfide (CS_2)

Supercontinua in CS_2-core fibers were measured using both laser systems. The pulses of each laser featured distinct pulse widths and therefore experienced the molecular nonlinearities differently strong. The molecular contributions calculate to $f_m = 0.85$ for laser A ($T_{HP} = 460$ fs), and $f_m = 0.70$ for laser B (here $T_{HP} = 230$ fs). It shall be noted, that the measurements with laser system A were done with a slow Fourier-transform infrared spectrometer reducing the number of consecutive spectral records.

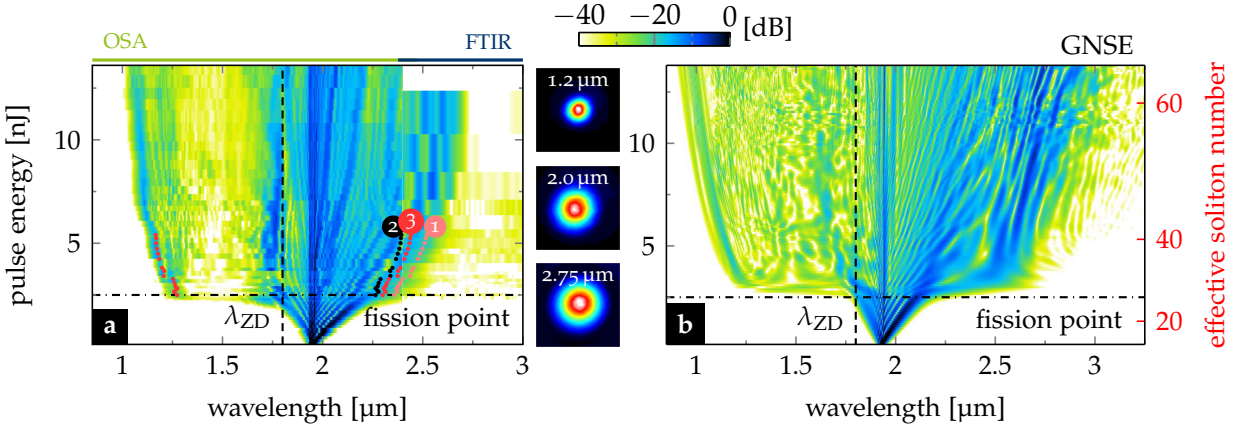

Fig. 28: **Spectral fingerprint of fiber #1 (laser system A).** a) Measured and b) simulated output spectra of the CS_2/silica LCF for increasing pulse energy. Input pulse of the simulation was reconstructed from the measured laser spectrum assuming a residual third-order phase (i.e., $D_3 = -0.025\,\mathrm{ps}^3$) to match the measured pulse auto-correlation. The marks in (a) indicate the measured spectral position of the strongest NSR (red) and the calculated phase-matched wavelengths of the first fundamental solitary wave for the three different nonlinear phase shifts (black, red, light red; numbers correspond to the cases discussed in the main text). The insets show the measured near-field profiles at three selected wavelengths (pulse energy 8 nJ). OSA: optical spectral analyser, FTIR: Fourier transform infrared spectrometer. Figure reprinted from [132] (CC-BY).

Considering the results with laser A, substantial broadening of the output spectrum for increasing input pulse energy was observed, with a maximum spectral extent from 1.1 µm to 2.7 µm, approximately 1.2 octaves, at 14 nJ (q.v. Fig. 28a). Careful alignment ensured energy conversion within the fundamental mode across the entire bandwidth (q.v. mode pictures in Fig. 28a). The low repetition rate of laser system A allowed pumping conditions corresponding to a maximal N_{eff} of 64 (i.e., $N = 165$).

The spectral evolution is characteristic for clean soliton fission: after initial SPM, a sudden increase of the spectral bandwidth is observed at 2.5 nJ pulse energy, with distinct NSR around 1.25 µm neatly repelled from the pump spectrum. This point is identified with the supercontinuum onset, or fission point, respectively. Increasing the pulse energy leads to an increased spectral bandwidth, and more spectral fringes, e.g., on the soliton side at $\lambda > 2$ µm.

The simulation correlates well with the experiment (cf. Fig. 28a,b). In particular, the onset energy and the spectral location of the initial dispersive wave match considerably well, which confirms both an efficient coupling to the fundamental mode and an accurate balance between fiber dispersion and nonlinearity in the simulation. The less spectral extent of the long wavelength side, i.e. beyond 2.7 µm, for higher pump energies might originate from model inaccuracies in the simulation (q.v. error analysis in appendix C) or minor energy loss to parasitic nonlinear effects in the experiment.

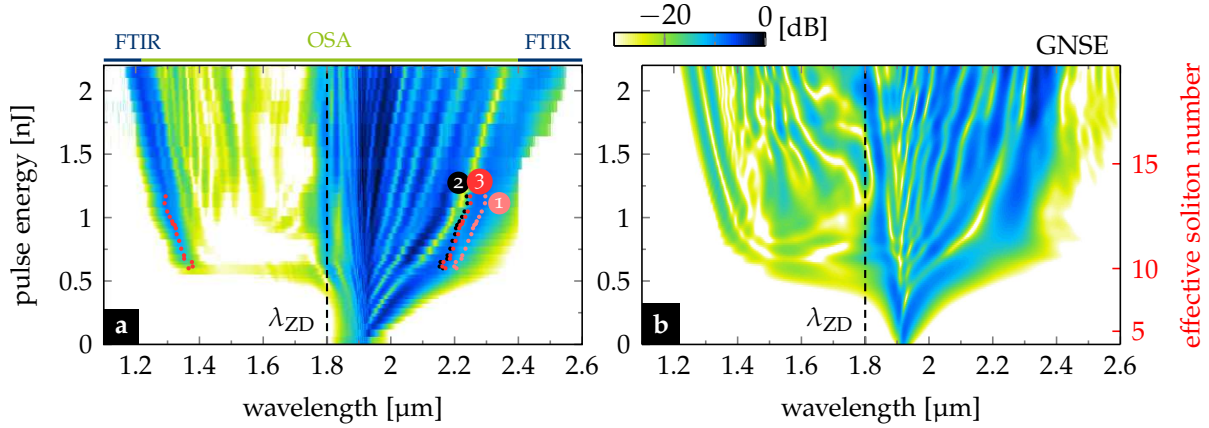

Fig. 29: **Spectral fingerprint of fiber #2 (laser system B).** a) Measured and b) simulated output spectra of the CS_2/silica LCF for increasing pulse energy. The marks in (a) indicate the measured spectral position of the strongest NSR (red) and the calculated phase-matched wavelengths of the first fundamental solitary wave for the three different nonlinear phase shifts (black, red, light red; numbers correspond to the cases discussed in the main text). OSA: optical spectral analyser, FTIR: Fourier transform infrared spectrometer.

The high repetition rate of laser B prevented reaching a similarly large peak power as with laser system A at similar average power damage thresholds. Thus, an effective soliton number of $N_{\text{eff}} = 19$ (i.e., $N = 39$) was reached only. However, the SCG results in Fig. 29a show similar spectral characteristics in the experiment. Compared to system A, halving the pulse width causes a decrease of the SC onset by approximately a factor 5. At the first glance, the results seem to match well again with the simulation results in Fig. 29b, which assume an unchirped 230 fs pulse. Nonetheless, there are

important differences which indicate a lack of information about the input pulse. In particular, the highly asymmetric SPM broadening measured in the experiment for energies below the fission point (i.e. $\mathcal{E}_p < 0.5\,\mathrm{nJ}$) indicates a drastic influence of a pulse chirp, which could not be reproduced in the simulation despite multiple iterations with simple quadratic and third-order phases. The unknown pulse chirp has consequences on the interpretation of the data set via simulations, which limits the significance of theoretical benchmarks.

6.2.3 Tetrachloroethylene (C_2Cl_4)

In case of the C_2Cl_4-core LCF, laser system B (here $T_{HP} = 270\,\mathrm{fs}$) was used to record the spectral fingerprint shown in Fig. 30a. A coherent soliton fission process with a low onset energy of just 0.5 nJ is observed, indicated by the clean shear-off of NSR at 1.35 µm. Increasing the pulse energy increases the spectral bandwidth towards 1 octave at a maximal soliton number of $N_{\mathrm{eff}} = 12$ (i.e., $N = 19$), as well as it creates more spectral features in the *dark valley* between DW and pump suggesting the successive fission of more solitary waves. Moreover, a fine structuring appears in the spectral signatures of both NSR and solitary wave (q.v. highlighted domains in Fig. 30a) caused by the close temporal proximity between different spectral components. The entire spectral power evolution, featuring its slow transition to an octave spanning supercontinuum and its fine spectral fringes, is very well reproduced by the simulations, assuming a chirp-free 270 fs sech^2 input pulse (q.v. Fig. 30b). The match between experiment and simulation is indeed remarkable considering the coarse estimation of the nonlinear model of C_2Cl_4 discussed in appendix A, and clearly confirms the accuracy of the new dispersion model.

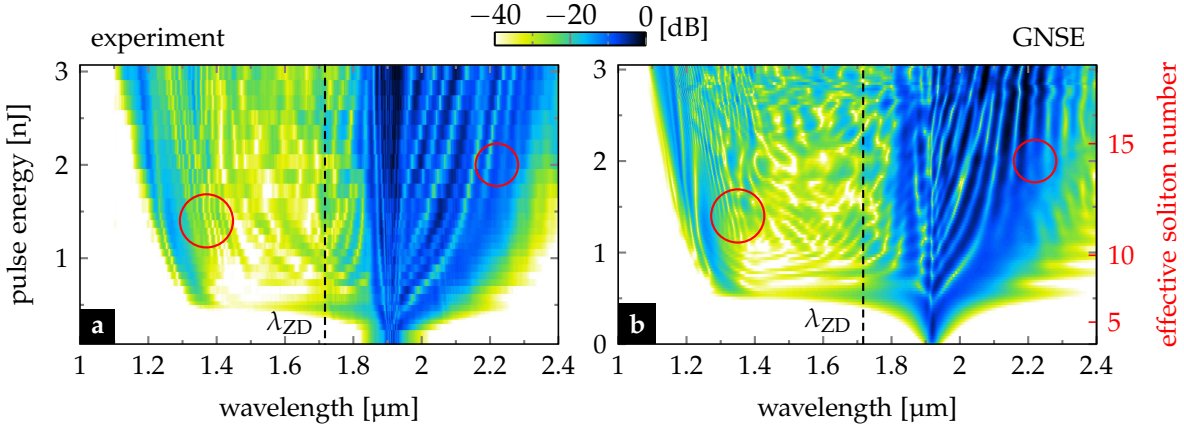

Fig. 30: **Spectral fingerprint of fiber #6.** a) Measured and b) simulated output spectra of a C_2Cl_4/silica LCF for increasing pulse energy. The red circles highlight domains featuring distinct spectral fringes. The location of the domains is the same in (a) and (b). Figure reprinted from [178], ©2018 OSA.

6.3 Indications of hybrid soliton dynamics

6.3.1 *A priori* classification

The measured spectral power evolutions of the CS_2 and C_2Cl_4 samples shown in sec. 6.2 feature very similar spectral characteristics, but underlie quite different nonlinear soliton dynamics. The differences can be brought to light with a careful analysis of bandwidth, onset energy, NSR, and coherence of both measured and simulated SC spectra.

To get a first estimate of the dominant nonlinearity acting on the pulse, the NIP and the IKP of the input pulse as introduced in sec. 4.2.4 can be compared for the individual pulse parameters of the laser systems. Fig. 31 shows the molecular contribution and the NIP relative to the IKP for increasing pulse width. It shall be noted that the input phases φ_{IK} and φ_{NI} from Eq. (65) were put into relation here instead of the corresponding soliton phases as in the definition of f_m^{equil}. In other words, the parameters of the input pulse (i.e., P_0, $\mathcal{E}_p$) were used, not the calculated soliton parameters at fission, to calculate the individual phase contributions.

Both liquids CS_2 and C_2Cl_4 feature an input pulse width, at which the NIP of the pulse exceeds the IKP (cf. red domain in Fig. 31b). Beyond this point, the broadening mechanism can be anticipated to be strongly modified by the noninstantaneous nonlinear response of the liquid. This is different in case of (pure) CCl_4, whose applied NIP is smaller than the IKP at any pulse width. This transition point (i.e., $\varphi_{NI}/\varphi_{IK} = 1$) appears in case of C_2Cl_4 at a much longer pulse widths ($T_{\text{HP}} \approx 600\,\text{fs}$) than in case of CS_2 ($T_{\text{HP}} \approx 210\,\text{fs}$) despite the very high molecular fractions in both cases (cf. marks for CS_2 and C_2Cl_4 in Fig. 31a). This difference is related to the weaker amplitude of the noninstantaneous response of C_2Cl_4 (q.v. Fig. 13) and a three times longer decay time of the molecular reorientation (q.v. Tab. 5 in appendix A).

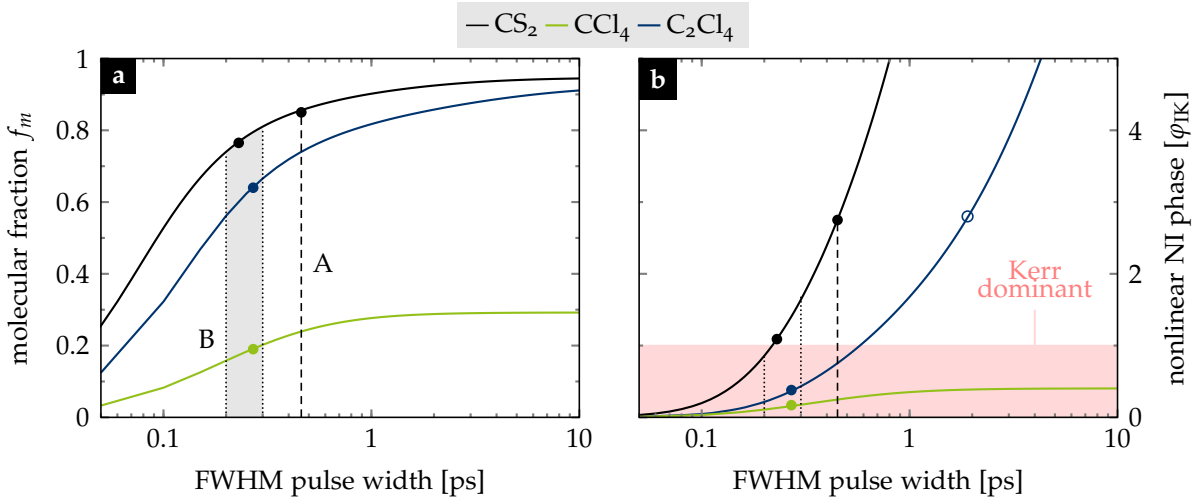

Fig. 31: **Contribution of the noninstantaneous phase.** a) Molecular fraction and b) NIP normalized to the IKP (q.v. Eq. (65)) as function of temporal input pulse width for the three liquids tested in the experiment. Figure reprinted from [178], ©2018 OSA.

The analysis reveals that the CS_2-filled LCFs in the experiment underlie large contributions from the noninstantaneous nonlinearities, although the data gained with laser

system B are close to the threshold. Both fiber systems can now be evaluated in their fission behavior on basis of the equilibrium fraction f_m^{equil}. The equilibrium fraction of fiber system #1 (laser A) is 0.73, which is below the nominal fraction 0.85 of the experiment. On the other hand, for fiber system #2 (laser B) $f_m^{\text{equil}} = 0.85$ is notably larger than the nominal fraction $f_m = 0.76$. Since $f_m > f_m^{\text{equil}}$ is required for a dominant influence of the NIP during the fission process, only fiber system #1 can be anticipated to reveal a distinctly modified soliton dynamics. In the following, this statement will be proven by analyzing the observables identified in sec. 5 in the experimental data.

6.3.2 Bandwidth and fission onset

Bandwidth and onset energy of the measured SCs of fiber #1, #2 and #6 are each compared to the three model systems ①, ②, and ③ as introduced in sec. 5.1. Therefore, Fig. 32 shows the increase of the respective 20 dB bandwidths of each fiber system for increasing pulse energy. In case of fibers #2 and #6 the bandwidth increase is very similar between the conservative case ② and realistic case ③, and coincides remarkably well with the measured bandwidth (q.v. Fig. 32b,c). In case of fiber #1 the differences in the individual simulation results and measurement are significantly stronger (q.v. Fig. 32a). All three fiber systems have in common that the optimistic case ① clearly overestimates the achievable bandwidth and does not allow to estimate the SC onset. Thus, the measurements confirm that the molecular NRI does not contribute to the broadening mechanism in a classical way, which is against the common belief in the literature.

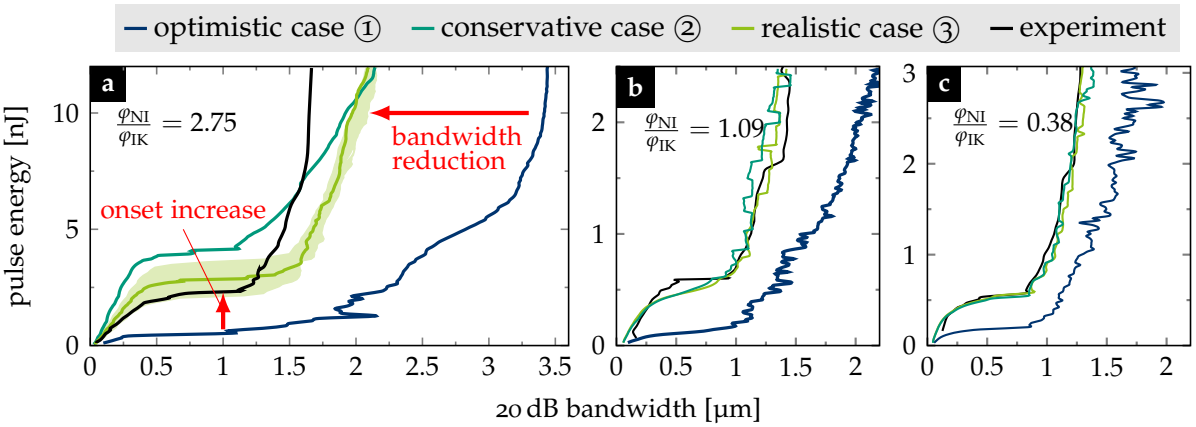

Fig. 32: Bandwidth and onset energy in comparison between experiment and simulations. Measured and simulated bandwidths at 20 dB spectral contrast for a) CS_2 fiber #1 (460 fs pump), b) CS_2 fiber #2 (230 fs pump), and c) C_2Cl_4 fiber #6 (270 fs pump) for increasing input energy. The simulated systems ①-③ are explained in sec. 5.1. The relative strength between NIP and IKP of the input pulse (i.e., not at fission) is labeled. The light green area in (a) denotes simulation results incorporating deviations of the non-instantaneous nonlinear response model and the pulse duration leading to $f_m = 0.85 \pm 0.04$ and $\gamma = 0.28 \pm 0.06$.

Focussing on fiber #1, the fission energy and the slope of the bandwidth increase of the measurements are covered best by the realistic system ③. The green error margins in Fig. 32a give an impression on the susceptibility of the calculated bandwidth against deviations of nonlinear response (based on the error margins of the model parameters

given in [174]) and pulse parameters (based on measurement inaccuracies of the pulse width of about 9%, or ±40 fs, respectively). Most notably, the spectral power characteristics cannot be mimicked by the conservative system ② (cf. turquoise and green curve in Fig. 32a), which is in contrast to the other tested fiber systems (cf. Fig. 32a with b and c). The conservative simulation ② results in a higher onset energy and a lower bandwidth than the realistic system ③ up to energies of 10 nJ in this example, which confirms the empirical findings in sec. 5.3.1. Thus, the strong mismatch in the onset energy and the bandwidth between case ② and ③ are useful indicators for the dominant contribution of noninstantaneous nonlinearities on the fission process. As the measured data correlate with the hybrid nonlinear system ③, modified soliton dynamics can be expected in the experiments.

6.3.3 Non-solitonic radiation

The distinct intensity maxima on the short-wavelength edge of the recorded spectra are associated with NSR, i.e., the phase-matched dispersive radiation of the initially split-off (fundamental) soliton shortly after fission. As introduced in sec. 5.3.2, the phase matching condition depends on the nonlinear phase of the soliton and might be useful to monitor the fission process, and in particular the nature of the emerging solitons, via spectral measurements. It is important to note, that only the spectra right at or slightly beyond the onset energy are meaningful for such an analysis. At those energies, fission appears close to the fiber end (i.e., $L_{\mathrm{fiss}} \approx L_{\mathrm{LCF}}$) and both NSR and the expelled soliton are mainly unaffected in their spectral locations, due to the absence of SFS or NSR-soliton interactions.

The conditions for the systems ① to ③ in Eq. (68) were applied to calculate the expected soliton wavelength (i.e., ω_s) from the measured NSR wavelength (i.e., ω in Eq. (68)) of fiber experiment #1 and #2 (q.v. dotted lines in Fig. 28 and Fig. 29).

Starting with the optimistic case ①, the instantaneous nonlinear phase overestimates the soliton wavelength in both fiber experiments. This is in correlation with the previous findings that the total NRI of the system does not contribute to the classical soliton phase, but a modified phase relation dictates the fission process. Regarding cases ② and ③, notable differences exist between fiber #1 and fiber #2. In case of fiber #2, both models describe the soliton location in the measured spectra equally well, in particular for $\mathcal{E}_p < 0.75\,\mathrm{nJ}$ (q.v. Fig. 29). This confirms, once again, the negligible role of the NIP in this system. The match between calculated and measured spectral location decreases for larger pulse energies, as expected, due to soliton SFS.

In case of fiber #1, however, the calculated wavelength of case ② and case ③ are distinct, which suggests indeed a large contribution of the NIP directly at the fission point. However, the difference between the two cases is moderate, and does not allow an unambiguous allocation of one of the phase terms to the measurement. The seemingly better agreement of the hybrid phase matching condition (case ③) with the measurement above the fission point (i.e., $\mathcal{E}_p \approx 3 \pm 0.5\,\mathrm{nJ}$) cannot be detached from a coincidental overlap

with frequency-shifted solitons in the experiment. It would overstrain the dispersion model and the data base of this experiment to perform a quantitive analysis, e.g., by comparing the measured soliton location with the calculation results.

It seems, that the conservative case ② coincides best with the measured spectral location of the alleged soliton, in particular just above the fission point (i.e., $\mathcal{E}_p \approx 3 \pm 0.5\,\mathrm{nJ}$), but, as the realistic case ③ provided the most accurate match in terms of bandwidth and onset energy, it cannot be excluded here. It would overstrain the dispersion model of this work to perform a more detailed analysis, e.g., by comparing the measured soliton location with the calculation results.

Thus, no definite conclusion regarding the dominant phase contribution at the fission point can be drawn from the NSR analysis. However, NSR proves as interesting tool to indicate dominant noninstantaneous impact. The quantitative application of the phase-matching relation requires both experimental data and model quantities (i.e., dispersion, NRI, power levels) to be known with very high accuracy. This sets a new demand on future material characterization and SCG measurements in liquids.

6.3.4 Coherence

The coherence of the generated supercontinua was not measured directly in the framework of this thesis due to experimental limitations. Coherence measurements in this spectral domain rely on temporally overlapping of either two successive supercontinuum pulse trains [181], or two supercontinuum pulses generated in parallel in two identical fibers [182]. The first method requires either laser sources with GHz repetition rates to keep the length of optical delay lines below 1 m and, thus, minimize diffraction losses, or long lossless fiber delay lines. The current laser and fiber standards put tight limitations on available repetition rates and fiber lengths at the chosen operation wavelength (i.e., $\lambda_0 \approx 2\,\mu\mathrm{m}$). The second method might be possible with the presented setup. However, the use of the overweighted fiber mounts (i.e., OFMs) and short fiber samples inhibited the fabrication of two identical samples within the limited access time to the laser laboratories. Thus, the direct measurement of coherence could not be conducted in the framework of this thesis, and needs to be addressed in the future (q.v. sec. 8.2).

Herein, solely first indications of enhanced coherence in the measured SC spectra shall be discussed. In sec. 5.3.1, symmetric spectral side lobes at the fission onset were identified indicating noise-driven MI as main source for the decay of coherence. Furthermore, the average over noisy SCs far beyond the fission length (or fission energy, respectively) yields flat distributions. Both spectral observables serve as indicator for a decrease in coherence. Amongst the presented data sets only fiber system #1 enters the regime of large effective soliton numbers beyond the deterministic coherence limit, i.e., $N_{\mathrm{eff}} \gg 15$ (q.v. sec. 2.3.4). Once again, the experimental system is compared to the numerical models ② and ③ in Fig. 33b,c, which reveals clear differences in the average spectra and the coherence of each model system.

The individual output spectra of the instantaneous system ② (q.v. Fig. 33c) show strong intensity fluctuations of the order of 30 dB across the entire bandwidth. This high susceptibility to noise removes all fine features from the averaged output spectrum, leading to a flat spectral shape (blue line in Fig. 33c). The realistic system ③, however, features nearly identical output spectra ② for the same pump conditions as in case ②, which results in considerably modulated average spectra, whereas the coherence of the system is close to perfect (q.v. Fig. 33b). Distinct spectral modulations in the measured spectra, thus, indicate a quite moderate coherence.

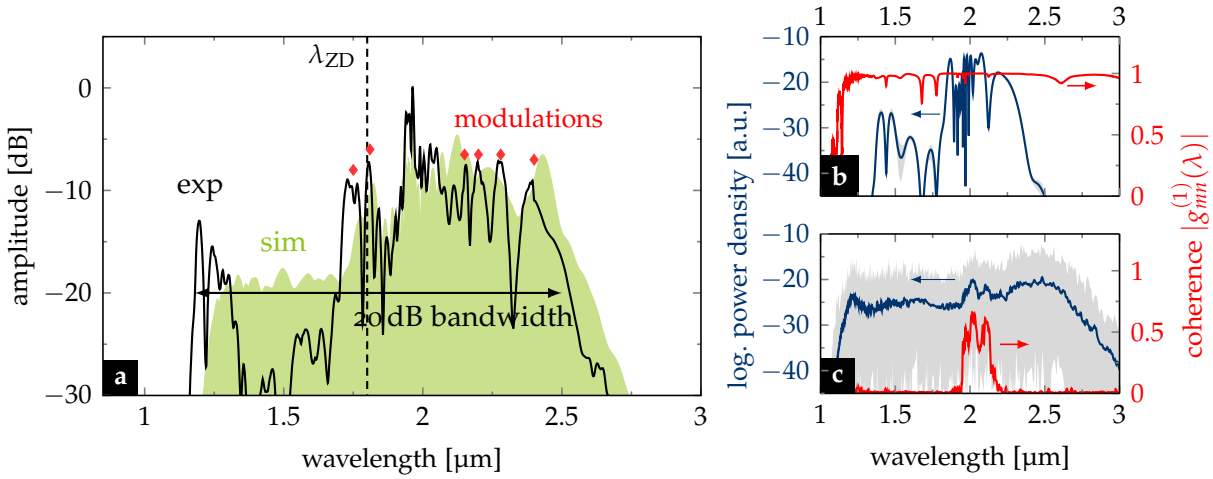

Fig. 33: Coherence indicators in single spectra. a) Measured (exp) and simulated (sim) average output spectra of the CS_2/silica LCF #1 at 3.9 nJ pump energy ($N_{eff} \approx 32$). The red diamonds mark a few locations of distinct spectral fringes indicating a coherent fission process. b-c) Average spectrum (blue) and coherence (red) of 50 individual simulations of (b) the realistic system ③ and (c) the conservative system ②, each after 14 cm propagation and pumped with 1 nJ pump energy ($N_{eff} = 15$). The gray domain represents the maximum spectral fluctuations between single spectra.

The observation of fine spectral fringes between 2.2 µm and 2.7 µm in the measured SC (e.g., red diamonds in Fig. 33a), at effective soliton numbers as large as $N_{eff} \approx 32$ (i.e., $N \approx 81$), indicate a high pulse-to-pulse stability. The modulation contrast of the fringes on the soliton side, in the order of 5 to 10 dB, is even better than in the simulated average spectrum of the LCF. This indicates an overestimation of the input noise in the simulations, which, however, has no consequence on the general relative behavior between the hypothetical systems analyzed in ch. 5. Moreover, clean soliton fission is observed as dominant broadening process in fiber #1, which is clearly indicated by the outbound spectral wing towards the NSR at the fission point (i.e., at $\mathcal{E}_p \approx 2.5$ nJ, and $N_{eff} \approx 25$ in Fig. 28). All evidence allow the prediction of a high first-order coherence in liquid-core systems, which, nonetheless, requires further experimental confirmation in future studies.

6.3.5 Hybrid nonlinear Schrödinger equation

The experimental evidence for the applicability of the theoretical benchmarks introduced in sec. 4 motivates to look for a specialized form of the GNSE to model SCG in hybrid

systems. In fact, the HNSE from Eq. (62) represents such a specialized form. However, the highly non-instantaneous approximation by a static linear potential $\gamma_0 \mathcal{E}_\mathrm{p} h(t)$ causes numerical problems arising from the discontinuity in $t = 0$ due to the in-built Heaviside function. This issue can be solved by replacing $\mathcal{E}_\mathrm{p} h(t)$ with the static initial potential $V_0(t) = \int |A(0;t')|^2 h(t-t')\mathrm{d}t'$, which is the convolution of the NRF with the pulse intensity at the input (i.e., at $z = 0$). This yields the HNSE corrected for arbitrary input pulses

$$\partial_z \tilde{A}(z;\omega) - \mathrm{i}\Delta\beta(\omega)\tilde{A} = \mathrm{i}\bar{\gamma}(\omega)\ \mathcal{F}^{-1}\left\{A\left[(1-f_\mathrm{m})|A(t)|^2 + f_\mathrm{m} V_0(t)\right]\right\}\ , \tag{69}$$

with $\Delta\beta(\omega) = [\beta(\omega) - \beta_0 - \beta_1\Delta\omega]$. The noninstantaneous phase acts as an additional static potential $V_0(t)$ to the nonlinear phase weighted by the molecular fraction f_m. Unlike the GNSE, the convolution between response and intensity has to be calculated only once (i.e., for the initial pulse) and not step-wise, which is numerically much less demanding. Here, all fiber parameters are included with their full dependence on frequency ω, so that its results are comparable to the GNSE simulations.

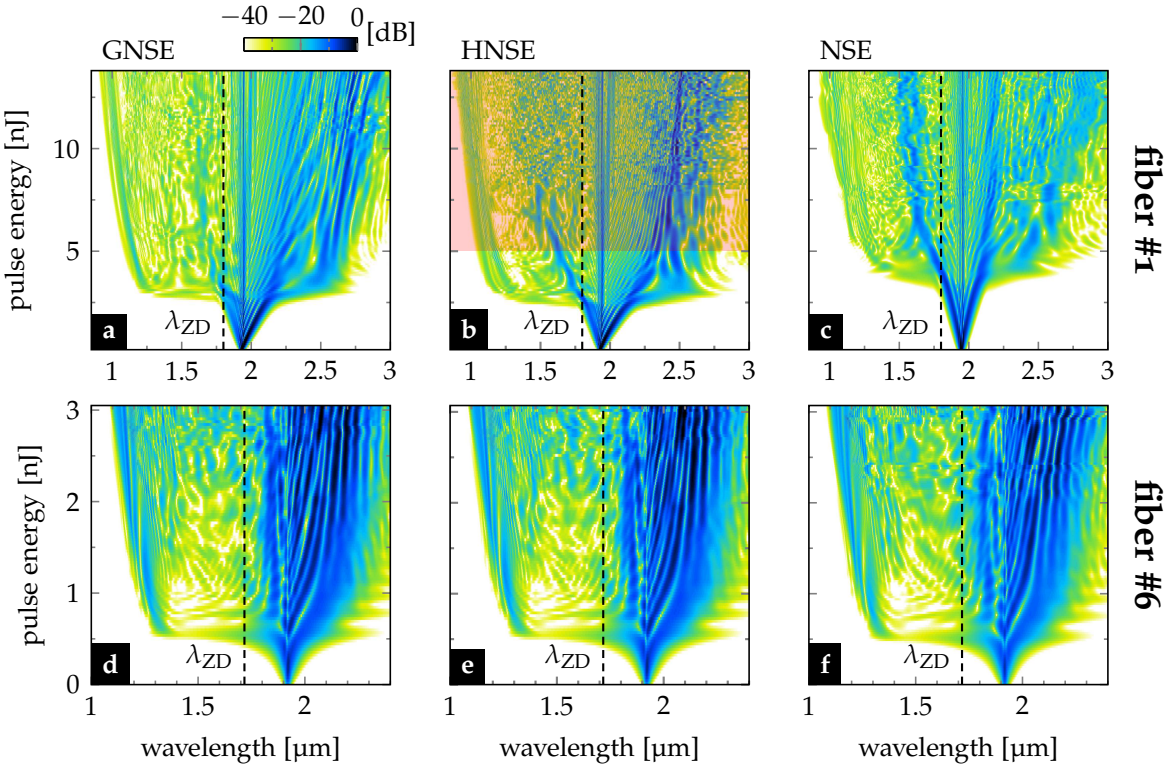

Fig. 34: The hybrid nonlinear Schrödinger equation in direct comparison to GNSE and NSE. Simulated output spectra of (a-c) fiber #1 (CS_2) and (d-f) fiber #6 (C_2Cl_4) for increasing pulse energy each based on solving the (a,d) GNSE (i.e., realistic case ③), (b,e) HNSE, and (c,f) NSE (i.e., conservative case ②). The red-shaded region in (b) marks the domain, where the HNSE becomes presumably inaccurate.

Figure 34 compares the simulated spectral fingerprints resulting from the corrected HNSE with the results of the GNSE (i.e., the realistic case ③), and the NSE (i.e., the conservative case ②), each for the fiber and pulse parameters of the experimental fiber systems #1 and #6. The HNSE describes the spectral characteristics of the GNSE remarkably well

in both fiber systems, especially around the supercontinuum onset (cf. spectra in Fig. 34a,b for $\mathcal{E}_p < 5\,\mathrm{nJ}$, or spectra in Fig. 34d,e). In both systems, the fission point appears at the same energy level, and bandwidth, and spectral features, like NSR, SPM, and the supercontinuum onset behavior on the long wavelength side are very well captured.

For increasing input energies, however, there is an obvious change in the broadening behavior between the HNSE simulations of fiber #1 and #6. This mismatch can be explained by cross-checking the results from the HNSE with the NSE (cf. spectra in Fig. 34b,c, or spectra in Fig. 34e,f). Whereas fiber system #6 is still well covered by the NSE, its results for fiber system #1 differ strongly from the HNSE (and GNSE). Thus, the instantaneous phase term, which is the same in GNSE, NSE and HNSE, dominates the broadening in the C_2Cl_4 fiber #6 making the new noninstantaneous term of the HNSE insignificant. In the CS_2 fiber #1 otherwise, the NIP has a non-negligible impact and the broadening behavior cannot be described solely by the NSE (as found already in the bandwidth analysis in sec. 6.3.2), but it is considerably well covered by the new specialized phase term of the HNSE.

The HNSE from Eq. (69) starts to become inaccurate first for long fiber lengths (i.e. $L \geq L_\mathrm{D}$) and large soliton numbers ($N_\mathrm{eff} > 40$ in Fig. 34b), since strongly delayed wave packets (e.g., NSR, or solitons) temporally shift out of the initial potential $V_0(t)$, whereby the mismatch between fully convolved phase (i.e., GNSE) and approximated phase (i.e., HNSE) becomes inevitable.

Overall, due to the acceptable match between the new hybrid model and the general (realistic) model at the fission point, the specialized HNSE promises to be a quick tool to evaluate hybrid systems in close comparison to the NSE results. It also forms a strong link to the HSW theory and might evolve to become a key tool to further understand hybrid soliton dynamics in future studies.

6.4 Evaluation of significance of the indicators

In the presented methodology, the indicators are not entirely unambiguous without accurate knowledge of the waveguide and pulse parameters. Especially onset energy and bandwidth crucially depend on all kinds of loss, dispersion, nonlinearity, and the individual wavelength dispersion of those quantities (e.g., TOD, mode area dispersion). These dependencies inherently underlie multiple experimental uncertainties such as insufficient knowledge of material dispersion or the nonlinear response of the liquid. Otherwise, phase matching of NSR and temporal coherence have few uncertainties since they rely on a single system property only, such as modal dispersion in case of NSR, or the nonlinear response in case of coherence.

In consequence, a convincing conclusion from the spectral analysis is possible only if the results are analyzed for their vulnerability to model uncertainties. Such an error analysis was performed in case of fiber #1, with regard to fiber dispersion, NRI, losses, and pulse chirp (details can be found in appendix C).

The impact of variations of all tested quantities on the SC spectra is moderate and, most importantly, measurable. The strength of the presented data lies in the accurate modeling of the close-to-perfect step-index LCF geometry chosen for the experiments. In this context, the good match between our GNSE simulations and experiments, without having applied any artificial model adaptions or data corrections, highlights the quality of the experimental data, as well as the material models used in the simulations. Specifically the experiment in CS_2 with moderate noninstantaneous contribution (i.e., fiber #2) confirms the applicability of the models for loss, dispersion and nonlinear parameter, without relying significantly on the nonlinear response model, overall supporting the plausibility of the revealed modified soliton dynamics in fiber #1.

Nonetheless, further studies are desirable to confirm or improve the current material models. In particular, the nonlinear liquid response turns out to be the most vulnerable parameter in the domain $f_m \approx f_m^{\text{equil}}$, and a confirmation of the NRF models would consolidate the significance of the presented findings. Also, material dispersion and losses of highly transparent liquids, (e.g. CS_2, CCl_4, and C_2Cl_4) require more precise measurements and models. However, the residual deviations between GNSE simulations and experiment in fiber #1 (e.g. remaining bandwidth mismatch and the strong residual pump light) are anticipated to originate from parasitic nonlinear processes, such as polarization rotation or energy transfer to higher order modes. The involvement of those effects requires an ingenious multimode treatment of the GNSE [82] in future work.

6.5 Theory of noninstantaneously dominated soliton fission

In conclusion, a single LCF system (i.e., fiber #1) was identified amongst all SCG experiments to be severely influenced by the noninstantaneous nonlinearity of the core liquid. The behavior of spectral benchmarks, such as bandwidth, onset energy, and spectral features both on the NSR and the soliton side, correlate very well with the simulation results of the hybrid nonlinear system ③, and confirm the spectral observables introduced in ch. 5 as useful indicators for modified soliton dynamics. A simplified description of this special experimental system, e.g., using the reduced instantaneous system ②, is not possible, which is in clear contrast to all other LCF systems investigated in the experiment. Instead, the early fission process of the system could be reconstructed notably well by a modified HNSE, which incorporated the NIP as static linear potential. Moreover, a practical soliton-independent phase relation $\varphi_{\text{NI}}/\varphi_{\text{IK}}$ was found to provide a straightforward and general tool to classify the initial conditions of a partly noninstantaneous system, which is different to the phase estimate at the fission point given by f_m^{equil}.

The insights gained by the analysis of the four indicators allow to understand the complicated interplay between IKP and NIP in each of the three stages of the fission process in more detail:

NONLINEAR PULSE COMPRESSION The significantly lower onset energy in the experiment, compared to the conservative case ②, confirms the dominant impact of the NIP to the nonlinear pulse compression (i.e., SPM stage). In particular, the distinct

red-shift of the SPM spectrum leads to a shock-front formation, which boosts the compression process and leads to an earlier fission point (i.e., lower onset energy). The HNSE covers this process very well. Moreover, the dominant NIP leads to an optical phase rectification, which reduces the impact of initial phase noise, and promotes coherent soliton fission. The clean shear-off of NSR at fission and distinct soliton features in the experimental spectra underpin this statement.

SOLITON FISSION In the maximally compressed state, just before soliton fission, the molecular contribution is reduced due to the short pulse form, and the instantaneous phase impact becomes stronger. Nonetheless, the phase-matching analysis of the NSR generation process revealed a non-negligible impact of the NIP at the fission point. This is again confirmed by the HNSE, which reconstructs the spectrum at the fission point remarkably well, while assuming a constantly dominating NIP. Prominent spectral fringes in the measured spectra up to soliton numbers as large as $N_{\mathrm{eff}} = 64$ let assume a uniquely coherent fission dynamic throughout the entire measurement of fiber #1 as a result of the all-time-present NIP. However, despite the notable difference in the phase-matching conditions between both models ② and ③, the data (as well as the current material models) do not allow an unambiguous allocation of any of the two calculated soliton wavelengths to the experiment. Thus, no irrevocable interpretation with regard to the original nature of the solitary wave upon fission can be stated. Nevertheless, the NSR phase-matching relations from Eq. (68) and the HNSE were successfully demonstrated as useful tools to expose the fission dynamics in future work.

POST-FISSION PROPAGATION After fission, the broadening process can still be monitored by the bandwidth increase for increasing pulse energy. The measured bandwidth increase is significantly reduced compared to the fast bandwidth increase of the conservative electronic system ②. Most notably, the bandwidth behavior in the electronic system is not related to soliton SFS, but to the increasingly strong soliton recoil effect. Those results might indicate a hindered soliton repulsion due to a restoring force by the noninstantaneous nonlinear potential. This effect is intrinsically incorporated by the HNSE simulation, too, which reproduces the bandwidth behavior around the SC onset. Despite the gained insights, the correlations do not unambiguously confirm the emergence of HSW in the measurements, but give a proper first support of this hypothesis.

7.1 Temperature tuning

Unraveling the complex soliton dynamics of LCFs might benefit from external control over the soliton formation and radiation. In this chapter, the tuning capabilities of LCFs will be investigated as further potential degree of freedom in terms of soliton control. The phase matching condition of NSR in Eqs. (68) clearly suggests that any change of dispersion has direct consequences on the wavelength of the generated NSR. Hence, a straightforward tuning scheme providing external control over the soliton's exhaust of energy relies on changing the ambient temperature of the respective device. Within fiber optics, however, the thermo-optical coefficients of most glasses and in particular that of silica glasses are rather low (e.g., $8.6 \times 10^{-6}\,\mathrm{K}^{-1}$ for fused silica [183]) and the impact of temperature on modal properties is limited. Liquid-filled fibers overcome this limit and host a great potential for external control over both linear and nonlinear optical properties, based on their miscibility and strong thermodynamic effects. In particular the large thermo-optical response of liquid-infiltrated fibers suggests strong impact on the optical properties, which was utilized for temperature sensing [184, 185], wavelength detuning of microfluidic lasers both on-chip [186, 187] and potentially in-fibre [55], spatial mode coupling [188, 189], and nonlinear signal detuning [190]. Here, the impact of temperature, pressure (i.e., density), and liquid composition on SCG will be investigated in three proof-of-concept experiments using CS_2-core fibers. The fiber design and data analysis successfully involves the thermodynamic Sellmeier model (q.v. Eq. (49)), derived in this work, and the common mixing rule from Eq. (50). It will be shown, that NSR generation is not only potentially suited to monitor modifications of the soliton fission process in LCFs, but also that it paves the way for tunable selective wavelength sources as schematically shown in Fig. 35a. The results of this chapter are partly published in [133].

7.1.1 Device principle and design

The temperature dependence of NSR is exemplarily shown for CS_2 in Fig. 35b. For 40 K temperature increase, the ZDW is shifted towards longer wavelengths causing a redshift of the NSR by few hundreds of nanometers, given a frequency-stable soliton. The spectral tuning domain of the NSR can widely be shifted without exceeding a realistic temperature range between 0 °C (water condensation limit) and 46 °C (boiling point of CS_2) by additionally shifting the initial soliton wavelength (q.v. inset of Fig. 35b). It is important to note that the TOC of silica is about two orders of magnitude smaller than that of CS_2 and is thus negligible for the experiments reported here.

The dispersion design map of step-index CS_2-based LCFs in Fig. 35c reveals that the strongest impact of temperature on ZDW and NSR can be found for core diameters between 2.5 µm and 4 µm in a region omitted by other studies up to date and operateable in the ADD with thulium-doped fiber lasers. LCFs with core diameters larger than

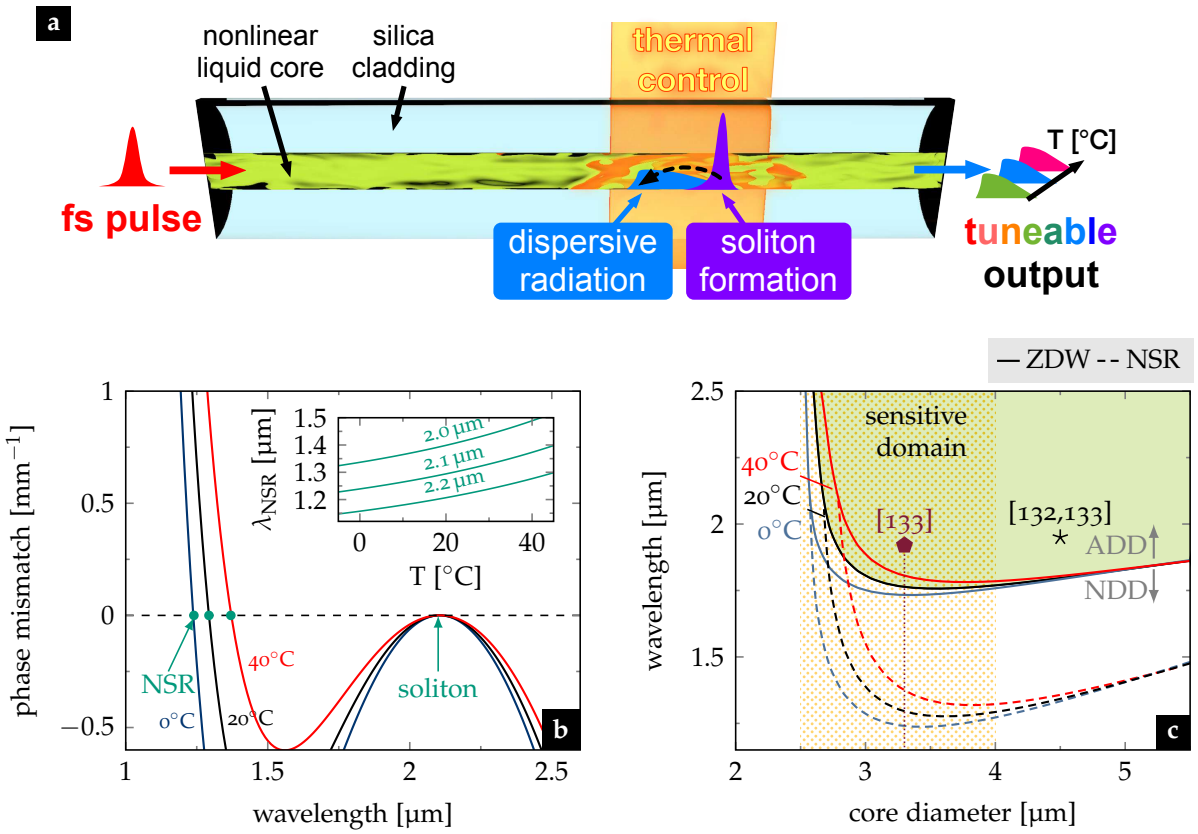

Fig. 35: Thermo-optic effect on dispersive wave generation in liquid-core fiber. a) Device principle: the thermodynamically modified mode dispersion influences the dispersive wave radiated of a solitary pump wave. b) Phase mismatch between NSR and a hypothetical pump soliton at 2.1 µm in a CS_2/silica fiber with $\varnothing_{co} = 3.3\,\mu m$ for three temperatures. The inset shows the temperature dependence of the NSR wavelength exemplarily for three selected pump solitons at 2.0 µm, 2.1 µm, and 2.2 µm. c) ZDW of the fundamental mode (HE_{11}) and NSR of a soliton at 2.1 µm as function of $\varnothing_{co}$ for three temperatures. The marks highlight the parameters used in the previous chapter and the demonstration shown here, which is within the temperature-sensitive domain (dotted orange). Figure reprinted from [133], ©2018 OSA.

6 µm show only a weak dependence on temperature, whereas the interplay of core and cladding dispersion is not as critical.

7.1.2 Experimental modifications

As a proof-of-concept fibers with core diameter of 3.3 µm (i.e., available diameter closest to 3 µm), were experimentally tested, which enables to optically pump the system in the highly temperature sensitive domain in the anomalous dispersion regime close to λ_{ZD} at 1.8 µm with thulium-doped fiber lasers. The experiments were based on laser setup B on fiber #3 as introduced in sec. 6.1.1 (q.v. Fig. 26 and Tab. 3). The setup (q.v. Fig. 36a) was modified by introducing a thermocouple (peltier element, max. power 72 W) placed on an aluminum cooling body, which enabled accurate temperature control between 0 °C and 40 °C over a length of 5 cm. An aluminum plate was placed on top of the LCF and the thermocouple close to the OFM at the output side, which extended the tempered region up to 7 cm (q.v. top plate in Fig. 36c). Thermal conduction paste ensured efficient heat transfer between all mechanical parts. Homogeneous control of the temperature along the entire fiber, including the OFMs and coupling stages, is practically more difficult

to realize, but also not necessary in case of NSR, which is generated within a very small propagation distance. The simulation in Fig. 36b confirms that the temperature influence on the initial NSR process can be made visible solely by heating or cooling the last section of the LCF. Notably, other positions of the thermocouple lead to more sophisticated soliton mechanisms, such as double NSR emission.

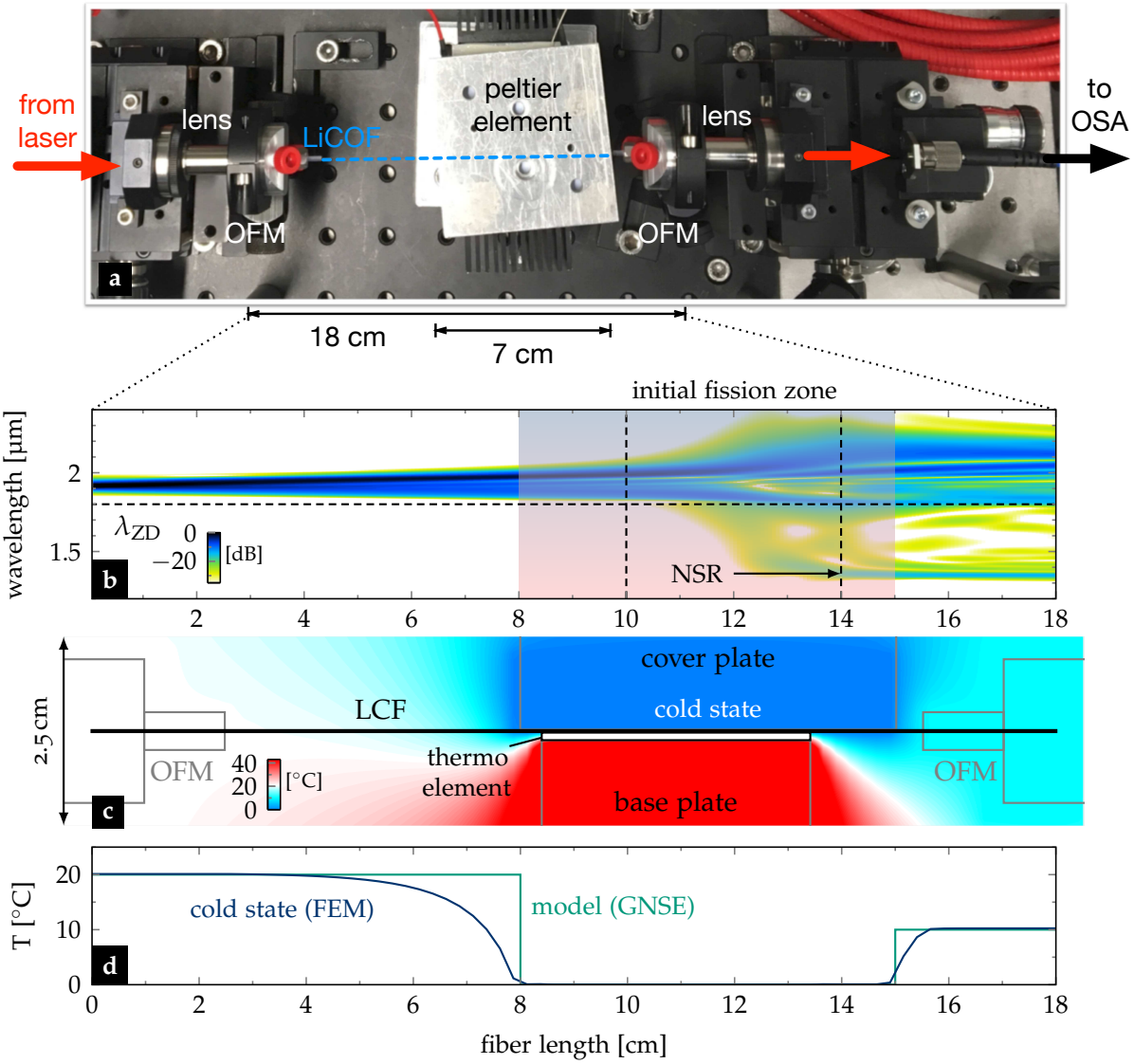

Fig. 36: **Configuration for initial soliton manipulation.** a) Photograph of the temperature tuning setup. b) Individual spectral evolution of a 350 fs pulse with 0.3 nJ pulse energy. The vertical dashed lines highlight the soliton fission area where a temperature element (red-blue shaded zone) has highest impact. c) Simulated heat map of the liquid-core fiber placed on a 5 cm heating element. d) Temperature profile along the fiber core in the cold state (calculated) compared to the temperature distribution assumed in the simulations (GNSE). Figure reprinted from [133], ©2018 OSA.

To cross-check the temperature distribution of the configuration finally used in the experiment, a two-dimensional heat map was calculated based on the finite element solver COMSOL Multiphysics, which promises a constant temperature along the locations where the NSR is generated, in particular along the length of the active cooling region (q.v. Fig. 36d). On the down-side, this simulation reveals that the OFM at the output side acts as a heat sink and hinders the temperature at the fiber output to return to

room temperature. This effect turned out to be required in the simulations, whereby the final temperature was approximated to half of the temperature of the thermocouple.

The reader might note, that the dispersion landscape induced by such a simple temperature treatment typically requires careful tapering in case of glass fibers whereas the resulting dispersion profile is static. Moreover, in the present situation the relative change of the dispersion can even be flipped in sign, i.e., the change of dispersion correlating with heating is the opposite to the case of cooling – an operation which is exceedingly hard to achieve using tapering.

7.1.3 Temperature detuning of non-solitonic radiation

Uncovering the impact of temperature on NSR as clear as possible requires identification of an appropriate power level slightly above the soliton fission energy which needs to be sufficiently low to avoid multiple NSR. To account for that, the spectral fingerprints at low (2 °C) and high (36 °C) temperature were measured first. Compared to the cold state in Fig. 37a the high temperature configuration in Fig. 37b reveals a drastic decrease in onset energy from 360 pJ to 240 pJ (±20 pJ) and a red-shift of the spectral location of the initial NSR. The difference can be primarily explained by the temperature-modified dispersion landscape of the LCF: In the cold state, the dispersion is increased and the ZDW (i.e., λ_{ZD}) is located at a shorter wavelength compared to the high temperature situation. Thus, the phase-matching wavelength λ_{NSR} of the NSR shifts away from the pump λ_0 further into the blue, and the initial pulse needs stronger nonlinear compression to gain the necessary spectral overlap to seed the distant NSR. The necessary compression requires higher pulse energies, which explains the higher fission energy in the cold state. In the hot state, the conditions are exactly reversed: λ_{ZD} and λ_{NSR} are closer to λ_0, thus less compression and less fission energy is required. The impact of temperature on the soliton is less obvious and cannot be deduced from measured spectral power evolution only.

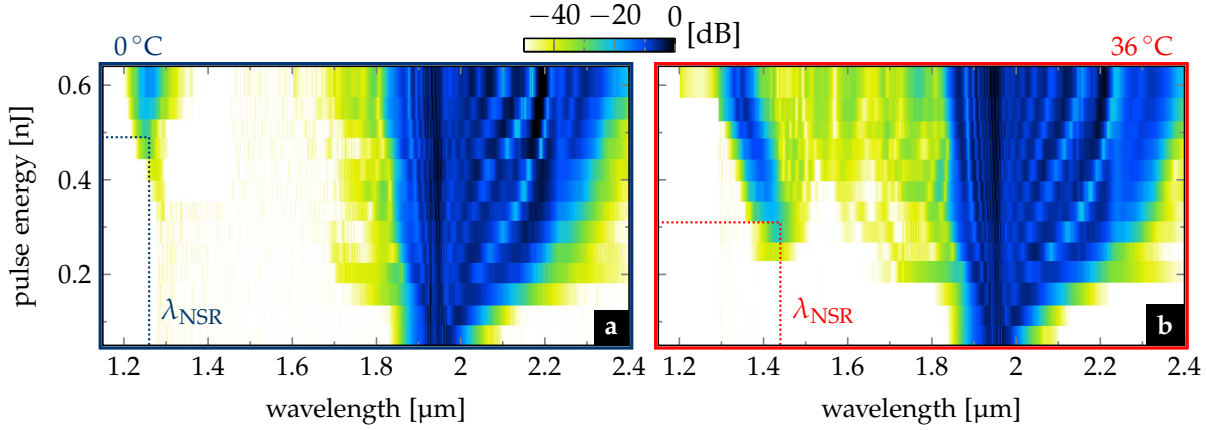

Fig. 37: **Impact of temperature on dispersive wave generation.** a, b) Measured output spectra of the CS_2/silica fiber for increasing input pulse energy in the (a) cold and (b) hot state of a CS_2-based LCF with 7 cm tempered region close to the fiber end. Figure reprinted from [133], ©2018 OSA.

In order to quantify both NSR- and soliton-frequency shift, the output spectra for increasing temperature at constant in-fiber pulse energy of 0.3 nJ were measured. Even though the spectral location of the NSR reacted immediately to a temperature change,

several minutes were conceded to ensure that the system reaches thermal equilibrium before recording the individual spectra. The measurements in Fig. 38a-e reveal a linear red-shift of the NSR of about 140 nm over 40 K temperature increase, corresponding to an average shift of 3.5 nm/K. Furthermore, a continuous increase of the spectral intensity and bandwidth of the NSR with increasing temperature can be noted. The spectral location of the corresponding initial soliton however stays nearly constant at 2.15 µm.

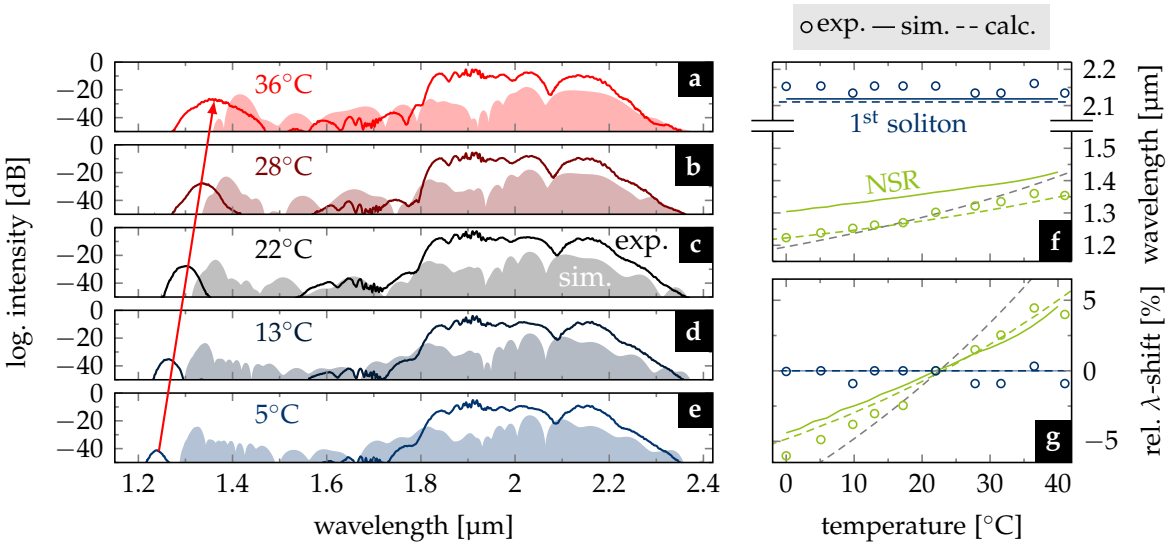

Fig. 38: **Impact of temperature on NSR.** a-e) Measured and simulated output spectra compared for constant input pulse energy of 0.3 nJ and increasing temperature. f-g) Temperature dependence of (f) absolute and (g) relative wavelength shift of the first (most red-shifted) soliton and the strongest NSR as measured, simulated, and calculated from the phase-matching condition. The gray dashed lines show the NSR wavelength using the common linear TOC model as comparison to the new thermodynamic Sellmeier model (green dashed lines) from Eq. (49). Panels (f-g) reprinted from [133], ©2018 OSA.

The modified soliton fission process was modeled by extending the GNSE solver such that it handles successive fiber sections of temperature-modified modal dispersions. The temperature profile was approximated by three fiber sections at constant temperature (q.v. Fig. 36d). The optical pulse used in the simulation was reconstructed from the transform limit of the measured spectrum (corresponding to $T_{HP} = 150$ fs, sech) chirped up to 350 fs with a positive group delay dispersion of $D_2 = 1.7 \times 10^4$ fs^2 to match the measured auto-correlation width. Both adjustments lead to a better match between measured and simulated λ_{NSR}.

The simulated output spectra in Fig. 38a-e qualitatively resemble the measured behavior of NSR and corresponding soliton for all temperatures. Figure 38 f-g allows to compare the measured and simulated spectral locations of initial NSR and soliton at each temperature quantitatively. The solitary wave remains at the same wavelength in both experiment and simulation within the applied temperature range. The measured and simulated NSR, although located at slightly different absolute wavelengths, show an almost identical relative redshift, i.e., from −5 % to +5 % of λ_{NSR} at 22 °C, when increasing the temperature. The small deviation in the absolute wavelength of the measured and simulated NSR might arise from the assumed pulse chirp and temperature profile. Par-

ticularly the assumed constant temperature of the last 3 cm of the fiber turned out to significantly impact the NSR location after fission.

As further benchmark, the NSR wavelength was calculated using the phase-matching condition in Eq. (68) (case ②) assuming that the first soliton is located at around 2.1 µm with peak power $P_s = 2.9\,\mathrm{kW}$ (and $\gamma_s = 62\,\mathrm{W^{-1}km^{-1}}$) at any of the temperatures considered. The obtained phase-matched wavelengths (dashed green lines in Fig. 38f-g) match the measured NSR locations and, thus, resemble the red-shift very well. The small constant offset between the measured and assumed soliton wavelengths (cf. blue dots and dashed lines in Fig. 38f-g) is most probably due to neglecting the soliton recoil effect in the phase-matching calculation. In contrast, the phase-matching wavelength was calculated using the common linear TOC model of Eq. 49 (dashed gray lines in Fig. 38g). The results highlight that the purely linear treatment of the TOC results in an overestimation of the shift.

7.2 Pressure tuning

7.2.1 Experimental modification

Besides the paradigm of incompressibility of liquids, pressure (i.e., density or viscosity modification) has a measurable impact on the dispersive and potentially even on the nonlinear properties of a liquid-core fiber [157, 191]. As proof-of-concept, the supercontinuum onset was investigated in a CS_2-based LCF while applying static pressure to the fluidic inlets of both OFMs using a liquid chromatography pump and high-pressure valves as interconnects of microfluidic tubings (q.v. Fig. 26). Initially, the mounts were subsequently flushed with a delay of a few minutes to wait for the complete filling of the capillary by capillary force.

The output spectra around the NSR onset energy were investigated for atmospheric pressure and static pressure of 100 bar. The coupling efficiencies have been carefully controlled during the pressure build-up to provide identical coupling conditions. The experiments were unintentionally performed with fiber system #1 (here, fiber length 8 cm) and thermodynamic effects influence the mode dispersion much less due to the larger core diameter, i.e., the design does not lie within the thermodynamical sensitive domain shown in Fig. 35c.

7.2.2 Pressure detuning of the fission onset

Under atmospheric pressure the NSR onset was found at 1.64 nJ (±0.03 nJ) energy and 1.3 µm wavelength, whereas at 100 bar the onset energy reduced to 1.51 nJ (±0.03 nJ) with the NSR wavelength remaining at around 1.3 µm. The calculated ZDW, incorporating the thermodynamic model in Eq. (49), reveals only a slight pressure-induced blue-shift of about 10 nm, which is presumably the reason for the slight blue-shift of about 20 nm of the NSR measured directly at fission onset (cf. blue and green curve in Fig. 39c each measured at the lowest energies at which the individual NSR is still distinctly visible).

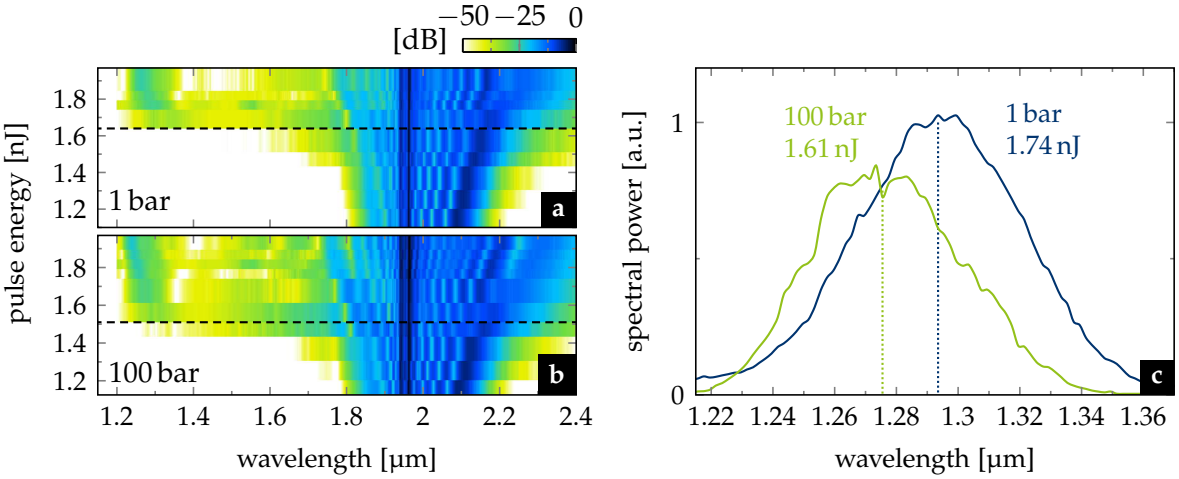

Fig. 39: **Impact of pressure on fission onset.** Measured output spectra as function of input pulse energy for two different applied pressures: (a) atmospheric pressure (1 bar), and (b) 100 bar. The dashed horizontal lines indicate the onset pulse energy of the dispersive wave generation (i.e., the fission energy). (c) Spectral intensity profile of the initial dispersive wave at the two pressure states. The spectra have been selected accordingly to the pulse energy at which the dispersive wave is clearly distinguishable from the solitary background for the first time. The dotted lines mark the positions of the non-solitonic radiation at the onset. Figure reprinted from [133], ©2018 OSA).

The change of the fission energy can be understood from the empirical fission length in Eq. (42), which can be expressed in fission (onset) energy $\mathcal{E}_{p,\mathrm{fiss}}$ and dispersion, i.e., $L_{\mathrm{fiss}} \approx L_{\mathrm{D}}/N \propto (\mathcal{E}_{p,\mathrm{fiss}}|\beta_2|)^{-\frac{1}{2}}$. Thus, if a constant fission length $L_{\mathrm{fiss}} = L_{\mathrm{LCF}}$ is considered at NSR onset for each pressure state, Eq. (42) shows that a decrease in fission energy indicates an increase in group velocity dispersion β_2 when the system changes from low pressure state (L) to high pressure state (H). From $L^L_{\mathrm{fiss}} = L^H_{\mathrm{fiss}}$ follows that $\mathcal{E}^L_{p,\mathrm{fiss}}/\mathcal{E}^H_{p,\mathrm{fiss}} = |\beta^H_2|/|\beta^L_2|$, assuming nonlinearity and input pulse width to be invariant with regard to applied pressure. The measured relative decrease of the onset energies $\mathcal{E}^{\mathrm{atm}}_{p,\mathrm{fiss}}/\mathcal{E}^{\mathrm{100bar}}_{p,\mathrm{fiss}} = 1.086(\pm 0.041)$ is about 10 % when applying 100 bar. The calculated ratio of the group velocity dispersion $|\beta^{\mathrm{100bar}}_2|/|\beta^{\mathrm{atm}}_2| = 1.079$ fits remarkably well into the error margin of this experimental fission energy ratio.

An energy onset difference of 10 % in this thermodynamically insensitive domain (q.v. Fig. 35c) gives reason to expect significant impact of pressure in more optimized fiber designs, which, once again, is non-intuitive for liquid core media. This proof-of-concept promises a further degree of freedom for optical detuning capabilities of LCFs in particular with regard to the extreme pressure domains up to 1000 bar achievable in capillary-like LCF structures, as demonstrated in earlier collaborative work [58].

7.3 Composition control

7.3.1 Dispersion properties of binary liquid mixtures

All discussions presented in this thesis so far, were based on considering thulium lasers and their wavelength domain around 2 µm. As noted, despite the benefits on dispersion and nonlinear losses, most liquids possess large losses in this wavelength domain, inhibiting long propagation lengths and a direct measurement of new soliton features, such as

HSWs. Moreover, diagnostics and lasers in the short-wave infrared are just about to enter the market and are still rather expensive. Thus, shifting the operation domain to the cost-effective and well equipped telecom range (i.e., the erbium emission spectrum between 1.46 and 1.65 µm) is practically highly beneficial. Whereas in case of silica it requires sophisticated fiber designs (i.e., new preforms and draws) to match the dispersion to another laser domain (e.g., W-type fibers can red-shift the ZDW, where micro-structured fibers can blue-shift it), LCFs offer more versatile methods to do so. In particular, the changeability and miscibility of the core liquid opens a new realm in design freedom.

Within the scope of this work, the design and applicability of liquid composite-core fibers was investigated. Here, the discussion shall be limited to the binary composition of low-index CCl_4 and high-index C_2Cl_4. The mixing rule introduced in Eq. (50) implies the variability of the material dispersion solely by adding an admixture to a buffer solution. In addition to the waveguide dispersion, quite a large variety of dispersion landscapes can be formed in simple composite-core silica-cladding fibers, as depicted in the design map in Fig. 40. The design map was calculated for an operation wavelength of $\lambda_0 = 1.56\,\mu m$ being well within the telecom C band. The nonlinear parameter of the binary mixture increases for increasing concentration of C_2Cl_4, whereas the maximum nonlinearity per chosen concentration γ^c_{max} goes closely along with $V(R_{co}, c) = 1.9$.

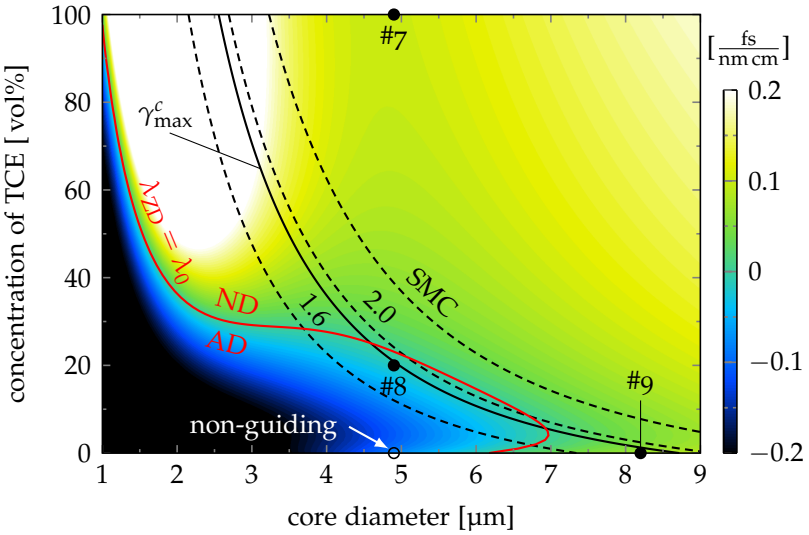

Fig. 40: **Design map for liquid composite-core fibers.** GVD parameter D as function of core diameter and concentration of C_2Cl_4 in CCl_4 (buffer solution) calculated for $\lambda_0 = 1.56\,\mu m$. The color scale is clipped at $0.2\,\frac{fs}{nm\,cm}$ to gain better contrast. The solid red line marks where ZDW equals λ_0, whereas black dashed lines denote discrete values of the V-parameter including the SMC, and the black solid line marks the core diameter of maximum nonlinearity. The labeled dots refer to the fibers tested in the experiment.

Most notably, the mixture opens an ADD in the telecom wavelength domain, while maintaining reliable guidance properties at reasonable core sizes (i.e., $5\,\mu m \leq \varnothing_{co} \leq 7\,\mu m$) and relatively high amounts of the highly nonlinear C_2Cl_4 (i.e., $c \leq 30\,vol\%$). In particular, this favorable domain allows working points with guidance parameters well above the empirically found critical limit i.e., $V > V_{crit} = 1.6$.

7.3.2 Soliton fission in liquid composite-core fibers

To confirm the applicability of the design map, four parameter sets were tested in the experiment (q.v. Fig.40). A mixture with 20 vol% C_2Cl_4 in CCl_4 (8 ml C_2Cl_4 in 40 ml CCl_4, i.e., 5 : 1 ratio) was used as core material for a capillary with $\varnothing_{co} = 4.9\,\mu m$ to get an anomalous dispersive composite LCF (q.v. fiber #8 from Tab. 3). This fiber was opposed to two normal dispersive LCFs with the same $\varnothing_{co}$ but filled with neat CCl_4 and C_2Cl_4 (q.v. fiber #7 from Tab. 3). The neat CCl_4 fiber, however, showed only 6 % transmission due to a low mode confinement in the weak step-index guide, since $V(\lambda_0) = 1.068$. Thus, a larger core size close to maximum nonlinearity (q.v. γ^c_{max} curve in Fig. 40) at $c = 0\,vol\%$) was chosen as nonlinear test system (q.v. fiber #9 from Tab. 3).

An off-the-shelf femtosecond laser with $T_{HP} = 30\,fs$ and $\lambda_0 = 1.56\,\mu m$ (Toptica FemtoPower Pro IRS) was used as pump source. The fiber coupling setup and output diagnostics is as introduced in sec. 6.1.1, whereas an InGaAs camera (ABS Jena, IK1513) was used to monitor the output mode in the C band.

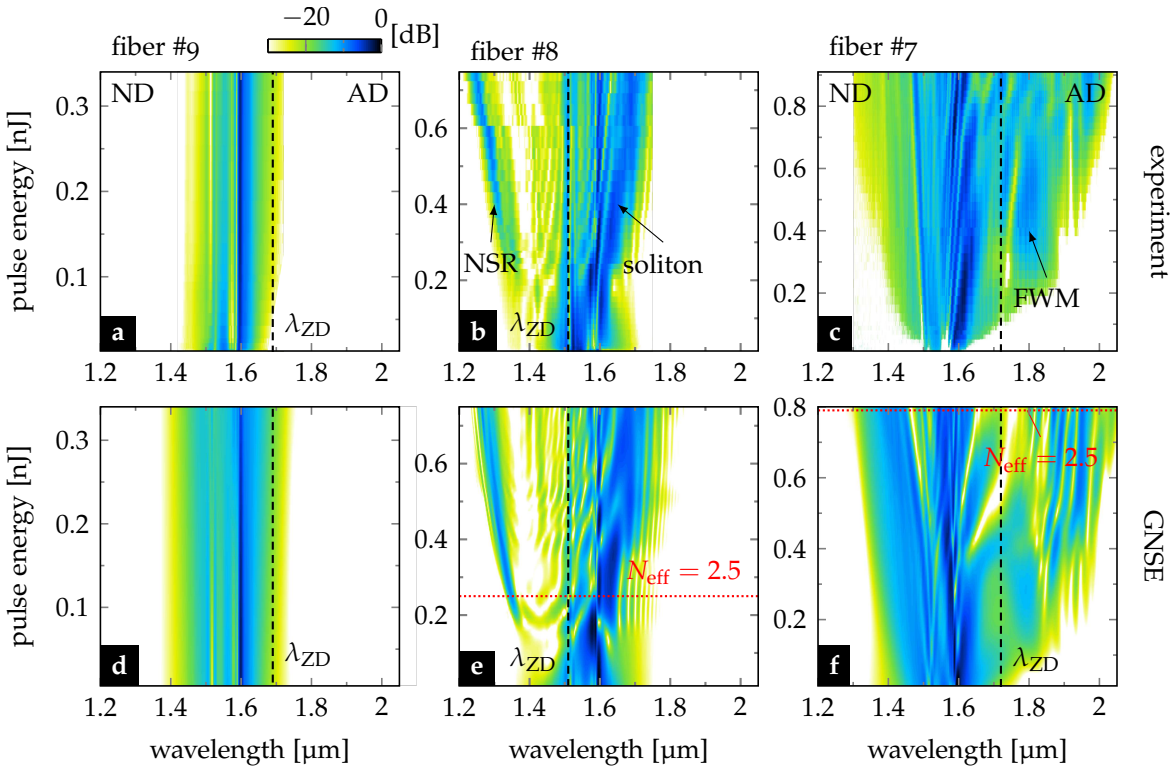

Fig. 41: Spectral fingerprint of fibers #9, #8 (composite LCF) and #7. (a-c) Measured and (d-f) calculated (GNSE) output spectrum for increasing pulse energy for three fibers with (a,d) 8.2 µm neat CCl_4 core (#9), (b, e) 4.9 µm C_2Cl_4:CCl_4 composite core (#8), or (c,f) 4.9 µm neat C_2Cl_4 core (#7). FWM denotes four-wave mixing. The input pulse for the simulations is reconstructed from the measured laser spectrum and propagated through 5 mm silica to emulate the chirp of the coupling lens.

The spectral fingerprints in Fig. 41 are clearly distinguishable from each other. All three systems are remarkably well described by the GNSE simulation, given the uncertainties of the underlying nonlinear models, which allows to unambiguously explain the respective broadening mechanism.

Starting with the CCl_4-based LCF (#9), no spectral broadening is observed (q.v. Fig. 41a,d). The large mode area and the small nonlinearity of CCl_4 result in a relatively small nonlinear parameter (q.v. Tab. 8) and a nonlinear length approximately double the dispersion length for the maximum pulse energy (i.e., $L_D = 3.5\,cm < L_{NL} = 7.5\,cm$). Thus, the pulse propagation is dominated by temporal pulse broadening in the NDD.

Each of the two other fibers exhibits an individual feature-rich broadening process. The composite LCF #8 shows the characteristic spectral features of a split-off soliton on the red side and of NSR on the blue side of the spectrum, confirming operation in the ADD accordingly to the calculated λ_{ZD} in Fig. 41b. The neat C_2Cl_4-filled LCF #7 misses any distinct spectral feature on the short wavelength side, but shows a much further extent towards the infrared despite the lower maximum soliton number of the system (cf. red labels in Fig. 41e,f). The broadening mechanism is an involved combination of SPM, shock-front formation, and four-wave mixing close to the ZDW (i.e., similar to domain 2 in sec. 5.3.4). Without going further into detail, it shall just be mentioned that this mechanism may serve as alternative route to efficiently excite fundamental solitons, as well as to generate highly coherent SC spectra while still operating in the NDD.

To conclude this chapter, the presented proof-of-principle experiments, and their good match to simulations and calculations, prove the applicability of temperature, pressure, and liquid composition for straightforward dispersion adjustment, simultaneously confirming the underlying material models and the nonlinear design maps. In particular, a binary mixture of C_2Cl_4 and CCl_4 straightforwardly infiltrated in a silica capillary opens the ADD for the telecom laser branch. Similar and partly better results could be achieved with deuterated toluene and deuterated nitrobenzene, each mixed in CCl_4, in the master thesis by Walther [192]. This additional dispersion control in LCFs might also be implemented online via concentration- and flow-controlled micro-fluidic circuitry based on commercial liquid-chromatography pumps and valves, similar to the equipment used in sec. 7.2.2 to perform the high pressure experiments. Altogether, the dispersion landscape of an optical soliton propagating in a LCF can be manipulated to a considerable extent, which highlights this fiber type as promising dynamic platform for local and dynamic fission control.

8.1 Conclusion

This work explored the potential of LCFs as platform for novel solitons dynamics and tunable soliton fission. It combined (1) thorough material analysis and fiber design, (2) with semi-analytical and numerical theoretical studies on novel hybrid solitary waves (HSW) and SCG in LCFs, as well as (3) with first experiments on SCG in the HSW regime and external soliton control. The theoretical part consistently links the predictions by Conti *et al.* [70] with the observations to the spectral features in simulated SCs in LCF found by other groups [193], and puts them into a well rounded practical picture. The experimental findings of this work allow the scientific community to catch a first glance on the soliton dynamics in highly noninstantaneous liquid systems, and are in good agreement to the newly elaborated theoretical expectations and benchmarks.

In detail, the new material dispersion dispersion models found in this work proved valuable for accurate LCF design and thermodynamical control of liquid systems (the latter exclusively for CS_2). In particular, high-index heavy organics, such as carbon chlorides and CS_2, were measured to possess formidable transmission and IOR properties for robust light guidance from the VIS to the starting MIR (i.e., proof of hypothesis H1). As a result, unexplored ADDs have been identified in easily producible step-index silica-cladding LCFs filled with CS_2, CCl_4, and C_2Cl_4 with user-friendly core sizes of about 4.5 µm. These operation domains grant access to the soliton domain with state-of-the-art thulium fiber lasers (i.e., proof of H2).

The experimental accessibility to the ADD justified a closer look into the special soliton propagation characteristic of slowly responding nonlinear LCFs. In particular, the linearon hypothesis, introduced by Conti *et al.* in 2010, was revised for the realistic nonlinear response of liquids. Following a semi-analytical eigenmode approach, linearon states were found in form of solutions of a quasi-linear Schrödinger equation. A numerical perturbation analysis, however, exposed the instability of these states over propagation due to violation of the principles of causality in case of realistic nonlinear responses. In detail, the linear states are localized in the minimum of the response potential, distant from the anticipated location at the field-induced origin of the response. This mismatch causes the pulse to adiabatically adapt to a solution of a steadily moving potential, while continuously distributing energy. The observation leads to the falsification of the hypothesis (H3) that linearons may be found in highly noninstantaneous LCFs.

Nonetheless, the here-elaborated theory extended the governing model to a hybrid-nonlinear Schrödinger equation (i.e., the HNSE), which combines the well-known instantaneous NSE with the NISE by Conti *et al.*. The HNSE describes the nonlinear pulse propagation in realistic liquid-core waveguides considerably well within a certain parameter regime. The individual nonlinear phase terms of the HNSE allowed to relate the noninstantaneous phase (i.e., NIP or linearon phase) with the instantaneous Kerr phase (i.e., IKP or soliton phase) and, thus, to identify a critical molecular fraction f_m^{equil}, at

which the NIP equals the IKP. Above this fraction, the pulse propagation in the ADD significantly alters from classical soliton propagation. Most remarkably, under certain conditions, which were found only empirically in this work, the altered solitary wave (i.e., HSW) features a flat phase, indicating true solitary character. Thus, Conti's hypothesis (H3) may be extended to the existence of hybrid soliton states (HSS) in realistic liquid-core media. Those states promise access to so-far unexplored nonlinear regimes being potentially usable for laser engineering, nonlinear light steering, and emulation of unaccessible systems e.g. in physics, math or biochemistry.

The identified experimental regime inhibits the direct observation of fundamental HSW propagation, since the losses at the thulium laser wavelength limit the maximum fiber length to sub-meter lengths, which is below the dispersion length of the required pulses. Hence, this work followed the approach to identify indications of emerging HSW in the spectra resulting from a complex soliton fission process along few ten centimeters of fiber (i.e., SCG). Large parameter studies of SCG in CS_2-core fibers, based on a generalized model (GNSE), revealed NIP-dominant parameter domains featuring unique spectral properties of the SCs in comparison to glass-type systems with same electronic nonlinearity. The iterative study is fully consistent with the theoretically found condition for dominating NIP (i.e., $f_m > f_m^{\text{equil}}$) and identified the spectro-temporal signatures of HSWs in the simulated output spectra of lossless LCF systems. The imposed changes on the SC spectra for increasing molecular fraction f_m can therefore be attributed to the emergence of HSWs (i.e., proof of H4). The impact of the NIP becomes apparent in bandwidth and onset energy of the SC, both in agreement with the empirical findings by Pricking *et al.* [193], but also in the spectral location of the NSR, and the coherence. These numerically found observables correlate with the experimental observations (i.e., proof of H6), and strengthen the hypothesis of emerging HSWs at some point during SCG (H5). Nevertheless, the coherence properties of the SC spectra could only be assessed qualitatively by interpreting distinct spectral features, which do not occur in incoherent broadening schemes, and additional experiments are necessary to further support the findings.

In particular, the observations in the simulations justified the formulation of two soliton fission theories, which differ in the question whether HSWs are created directly at the fission point or shortly after via an adiabatic transformation of classical solitons into a hybrid state. This question might be answered by measuring the phase of the solitary unit created at the fission point. The spectral location of the NSR together with the hybrid nonlinear phase matching condition found in this work provides the ideal tool to access this phase information. However, despite the considerable difference between hybrid solitary phase and conventional solitary phase, the distinction is not large enough in the presented systems to definitely assign one of two solitary states with the measurement. Dispersion tailored micro-structured LCFs may be able to increase the phase difference and provide an answer on the nature of the soliton at the fission point. Yet, none of the both theories can be disproved in this work, but, although the central question of the

origin of HSWs within the fission process (H5) remains open, this study gives profound evidence for their existence.

The external tuneability of the optical properties of the LCFs might become essential to further investigate the origin of HSW, but also to study soliton propagation and dynamics in general. Temperature, pressure, and core composition were shown to notably influence the mode dispersion in a LCF (i.e., proof of H7). The dispersion control allows to accurately steer soliton fission processes, and particularly the frequency and strength of the radiated NSR (i.e., proof of H8). The here-derived thermodynamical models for CS_2 proved quantitatively useful and allow valuable suggestions on bandwidth and coherence improvements of SCG, as shown in the outlook.

Altogether, the presented study contributes to the fundamental understanding of spectral broadening in liquids and the underlying soliton dynamics. It comprehensively demonstrates LCFs as dynamic platform for exploring new solitary states and soliton interactions, as well as for broadband tuneable light generation. LCFs may offer a further playground, next to gas-filled fibers, with many degrees of freedom, which will potentially expand the possibilities of fiber-based emulation systems to study manifold effects of other fields of physics and science. Some anticipated examples are discussed in the following on conclusion of this thesis.

8.2 Future prospects

Light guides for the near- to mid-infrared

The advent of new laser sources for the MIR (e.g., quantum cascade lasers) demands new fiber materials for lossless light transport in this technically important wavelength domain. This work demonstrated halide liquids with a high transparency in the NIR towards the MIR domain as potential alternative to soft-glasses. In particular, the use of halide mixtures, may allow designing **broadband single-mode fibers for the MIR domain**. Preliminary design studies using a 10 mol% C_2Cl_4 in CCl_4 mixture as core material embedded in silica with $\varnothing_{co} = 6\,\mu m$ reveal a robust single-mode guidance domain (with $1.820 < V < 2.405$) from 0.9 to 6.8 µm, i.e., well beyond the transmission limit of fused silica. This result gives confidence for similar waveguide domains when incorporating other cladding materials. Hence, to fully further explore the MIR potential of LCFs, new MIR-friendly glasses (e.g., fluorides) might be investigated as cladding material.

Moreover, there are many **halide and chalcogenide liquids** with moderate toxicity which are unexplored in terms of their promising transparency and nonlinearity. Few examples are $SiCl_4$, $GeCl_4$, $CBrCl_3$, $CHCl_3$, ICl, IF_5, C_6F_{14}, CSe_2, or $AsCl_3$. Accurate measurements on the absorption and dispersion in the MIR of those liquids are required to extend the material models and to make fiber designs possible in future.

Picosecond pulse compression

The superior reduction of the noise impact on nonlinear pulse propagation found in this work might enable the pulse compression of multi-picosecond pulses. In particular C_2Cl_4

with its high transparency and long-lasting response is an ideal candidate to design an **in-fiber pulse compressor**. The device principle becomes clear in Fig. 42a,b, which shows the spectral evolution of a 1.9 ps pulse (here a strongly chirped 270 fs pulse) along lossless propagation each in 2 m C_2Cl_4-core fiber and a comparable glass-type fiber. The glass-type system develops the characteristic spectral modulations originating from MI, triggered by the input phase noise assumed in the simulation. The noninstantaneous C_2Cl_4 system, in contrast, shows clean soliton fission, indicated by the modulation-free symmetrically broadened pedestal and the emission of an intense NSR after 1.5 m propagation in Fig. 42b. Remarkably, the pulse is compressed by two orders of magnitude down to 17 fs (T_{HP}) at the fission point resulting in a peak power enhancement of factor 22 (q.v. inset of Fig. 42b), which is multiple times larger than the maximally achievable peak power in the glass-type system, and most importantly shot-to-shot reproducible.

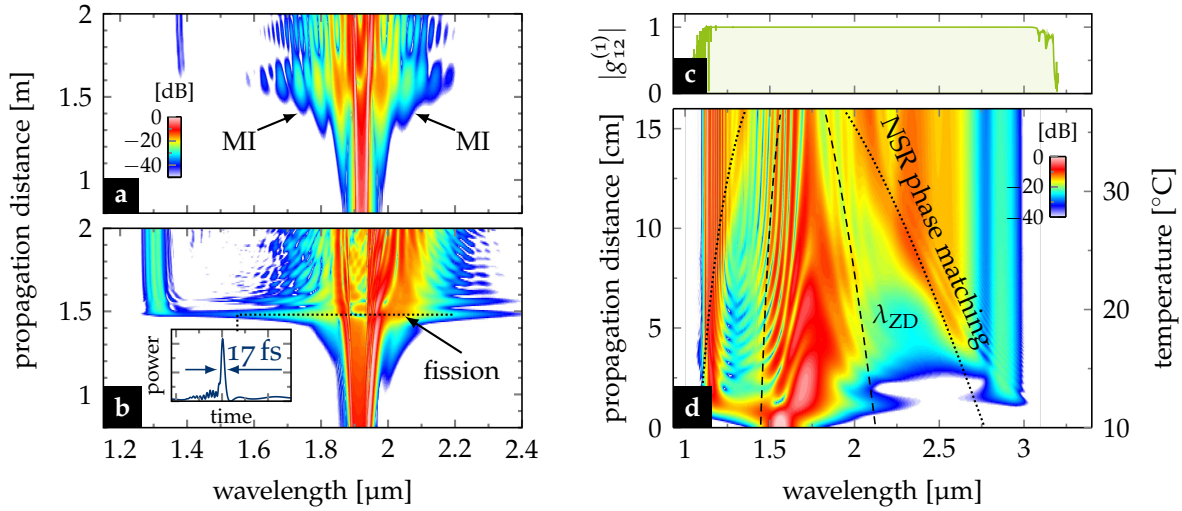

Fig. 42: **Application examples for LCFs.** a-b) Spectral evolution of a strongly chirped 1.9 ps pulse with 500 W peak power numerically calculated using the GNSE (a) without and (b) with NIP. The inset in (b) shows the temporal pulse shape at the fission point. Reprinted from [178], ©2018 OSA. c) Output coherence and d) spectral evolution of a 30 fs pulse (1.56 µm, 6 kW, TM_{01} mode) propagating in a CS_2-core fiber ($\varnothing_{co}$ 3.9 µm) experiencing a linear temperature gradient. The lines indicate the ZDWs and the calculated phase-matched NSR. Reprinted from [133], ©2018 OSA.

Thus, LCFs offer a notable technological potential for enhanced fiber-integrated pulse compression beyond the stability limits of glass fibers, and below the power demands of gas-filled fibers. Particularly picosecond pulse compression may relax the dispersion requirements of laser oscillators and reduce costs and design efforts of fiber laser sources.

Nonlinearity enhancement of liquid-core fibers

There are various strategies to enhance the dispersion and nonlinear properties of anomalously dispersive operating LCFs. One explores **selective-filled micro-structured fibers** to shift the operation wavelength into the technologically well-equiped telecom domain (i.e., 1.4–1.6 µm), as well as to flatten the dispersion landscape and to improve the nonlinear coupling to distance wavelength domains. Such fiber designs were proposed by numerous numerical work (e.g., [194, 195]). They allow to address fundamental soliton

propagation in a much more favorable regime in terms of dispersion and loss. Exciting this regime with sub-picosecond pulses (favourably 400–600 fs) might enable the direct observation of HSW, and prove (or falsify) the above-stated hypothesis of the existence of HSS in liquid-core fibers.

Further, **ionic salt solutions** may be explored as core medium. The nonlinear coupling to ions in a solution were shown to significantly alter the nonlinear behavior of the buffer liquid with interesting consequences on SCG [196]. Also this approach requires substantial material characterization to gain broadband dispersion and loss data, and an estimate for the nonlinearity of the liquid media.

Beside the improvement of the NRI, the nonlinear response can be engineered using **liquid mixtures** as core material. For instance, the combination of CCl_4, $CHCl_3$, and C_2Cl_4 (ordered by increasing response time) might allow the cancelation of the detrimental rise time of the response and to mimic the conditions of the ideal exponential noninstantaneous system, in which Conti *et al.* predicted linearon states.

Techniques for enhancing supercontinuum generation

This work opened multiple promising approaches to explore the bandwidth capabilities of LCFs as nonlinear light source. The large-scale parameter study in sec. 5.3.4 revealed **three operation domains** which feature an improved bandwidth and coherence, compared to glass fibers. All three domains are unique for highly noninstantaneous systems and offer a plethora of research opportunities. In particular, the two unexplored domains in the NDD may host novel nonlinear mechanisms to excite both fundamental solitary states and soliton fission in the ADD across the ZDW. Future experimental and numerical studies in those domains might expose this potential for SCG and oberving HSWs.

Much attention should be paid to the coherence of the output spectra. The simulations predicted an increase of the coherence threshold in highly noninstantaneous LCFs. **Measuring the transition from incoherent to coherent SCG** in a LCF and a comparable instantaneous system would not only support the modified soliton theory elaborated in this work, but also allow to identify the physical origins of the rich nonlinear noise dynamics in high energy systems beyond the simple one-photon-per-mode noise model.

Moreover, the presented study gives a first glance of the great potential of thermodynamic tuning of dispersion properties of LCF using straightforward accessible external controls such as temperature or pressure. From the fundamental science perspective, temperature tuning might become a key tool to dynamically change the fiber dispersion along the propagation direction to directly observe and to control complex soliton dynamics to an extent that is only possible with in dispersion-oscillating micro-structured glass fibers to date [204, 205]. To demonstrate the potential of **thermodynamic tuning**, SCG in a CS_2/silica step-index LCF was simulated for one mode (TM_{01}) which features two ZDWs embracing an interval of anomalous dispersion in the telecom L-band. Launching femtosecond pump pulses with powers easily available from commercial erbium fiber lasers (here: 30 fs, 6 kW, 1.56 µm) into this mode yields a spectrum featuring two pro-

nounced NSR wavelengths (q.v. Fig. 42d). Via the application of an experimentally feasible linear temperature gradient along the LCF, the ZDWs is continuously modified implying a change of the NSR phase matching condition. The dispersion steadily increases along the fiber, which enforces a continuous transfer of energy from the soliton trapped in the ADD to the phase-matched NSR in the NDD. As a consequence, a broadband soliton-based SC between 1 and 3 µm is obtained featuring high spectral flatness and exceptional pulse-to-pulse coherence (q.v. Fig. 42c). Similar spectra could be produced in preliminary experiments utilizing the described system design.

The example demonstrates that the soliton dynamic can be controlled locally in LCFs, providing a unique platform to study optical states and novel light generation schemes. In particular the use of a thermo-couple array might enable complex dispersion landscapes, which can be dynamically changed to alter the generated signal wavelengths. The large set of accessible parameters (i.e., temperature amplitude and profile, pulse widths, and fiber mode) opens much potential to investigate **machine-learning assisted wavelength tuning** and spectral optimization schemes. Also, accessing **other thermodynamic regimes**, such as the supercritical state, surely hosts a multitude of interesting nonlinear effects and observations.

Hybrid soliton states

The empiric approach in this work allowed to predict the existence of a new soliton state, i.e., the HSS, emerging in LCFs. Further theoretical and experimental work is needed to support this hypothesis. **Proofing the existence of HSS** might enable highly noise stable soliton lasers and a novel platform to emulate the soliton physics of other areas in science. A direct measurement of HSSs is challenging but possible. To demonstrate the self-maintaining properties of HSS, pulse form, spectrum and phase of the pulse at the input and the output of a LCF need to be measured. Since sub-picosecond pulses are required to access the highly noninstantaneous regime (i.e., $f_m > f_m^{\mathrm{equil}}$), several meters of optical fiber are needed for a convincing measurement (i.e., $L > L_{\mathrm{D}}$). Hence, operation in a low-loss wavelength domain is mandatory for such a measurement, which makes C_2Cl_4 a good candidate for future experiments.

Most notably, the concept of using **NSR as monitor of the soliton dynamic** demonstrated in this thesis can be expanded in multiple ways. In case of a stably propagating state, the (mean) phase be determined by selectively heating or cooling different locations along the fiber, which may slightly perturb the soliton during its propagation and cause the exhaust of weak NSR. The relative spectral location between NSR and soliton allows to estimate the (mean) phase of the soliton at the position of applied heat via the phase matching condition, as demonstrated in Fig. 38 in sec. 7.1.3. This technique might serve as measure of phase stability along the fiber.

This technique can also serve as powerful tool to identify the character of solitary states at the fission point, as indicated in sec. 6.3.3. Here, an accurate conclusion depends on the discrepancy between the two nonlinear phase terms (i.e., classical soliton

and HSS phase) considered in the phase-matching condition. Large discrepancies can be reached in highly dispersion-sensitive nonlinear systems, such as the one with two ZDWs demonstrated in Fig. 42d. Pumping this system with about 500 fs pulses will cause NSR emission, which is characteristic for classical or hybrid solitons. The measurement of spectral location of the NSR might thus confirm one of the two fission theories introduced in sec. 5.4, finally completing the picture of highly noninstantaneous soliton fission.

High-order bound soliton states and trapped radiation

The large noninstantaneous nonlinear response of liquids may have further unique effects on soliton fission, than observed in the presented experiments. One of those effects, is the formation of **high-order soliton bound states**, or *soliton molecules*. Such states where predicted in the spatial domain for non-local nonlinear media [206] and in the temporal domain in laser cavities [13]. In LCFs similar states can form, too, due to the trapping effect of the nonlinear response potential, as shown in Fig. 43a. Experimental access to such a system might enable emulations of relativistic and chemical processes. However, those states could only be identified so far in simulations with second-order dispersion, non-dispersive γ, and without loss, which is hard to achieve experimentally. However, the emergence of those states is clearly observable in long-period modulations in the output spectra.

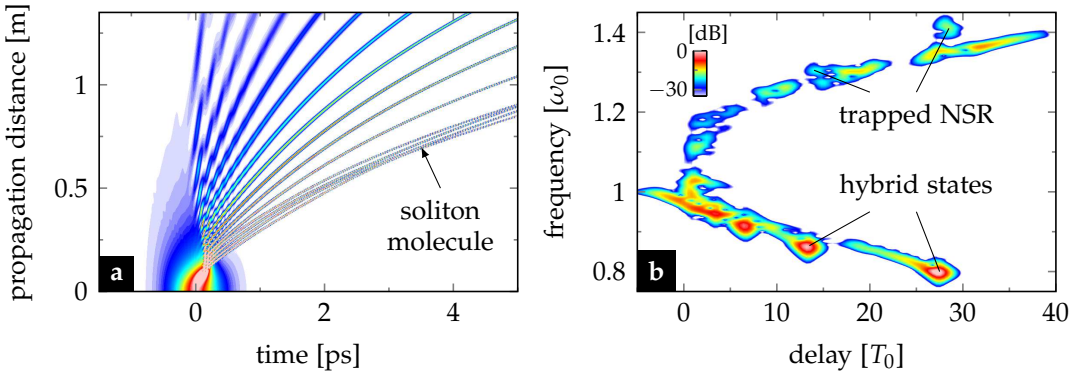

Fig. 43: **Bound states in LCFs.** a) Soliton molecule formation in CS_2-core waveguide with flat GVD. b) Enhanced NSR trapping in a realistic CS_2-core fiber excited with a 450 fs pulse.

A second effect of the noninstantaneous response may be strong trapping of NSR by solitons emerging in SCs of realistic LCF systems (q.v. Fig. 43b). **Radiation trapping** is well known to occur in conventional SCG in silica fibers as an essential mechanism to enlarge the bandwidth of SCs [95, 96]. It can be assumed that the additional impact of the noninstantaneous potential created by the soliton enhances this process and leads to even broader output spectra.

In conclusion, these visions give a first glance at the large diversity of operation domains and optical effects accessible in LCFs, which makes them an unique dynamic platform to study a variety of nonlinear dynamics with much application potential towards tunable and broadband light sources in the infrared.

BIBLIOGRAPHY

[1] E. Fermi, J. Pasta, S. Ulam, and M. Tsingou. Studies of the Nonlinear Problems. I. *Los Alamos Report*, LA-1940:1–20, 1955. (Cited on page 1.)

[2] J. S. Russell. Notice of the reduction of an anomalous fact in hydrodynamics, and of a new law of the resistance of fluids to the motion of floating bodies. *Report British Association*, 4:531–534, 1834. (Cited on page 1.)

[3] C. Kharif and E. Pelinovsky. Physical mechanisms of the rogue wave phenomenon. *European Journal of Mechanics - B/Fluids*, 22(6):603–634, nov 2003. (Cited on page 1.)

[4] Y. Kodama and A. Hasegawa. Nonlinear Pulse Propagation in a Monomode Dielectric Guide. *IEEE Journal of Quantum Electronics*, 23(5):510–524, 1987. (Cited on pages 1, 18, 20, and 24.)

[5] E. Seidel and W. M. Suen. Oscillating soliton stars. *Physical Review Letters*, 66(13):1659–1662, 1991. (Cited on page 1.)

[6] K. E. Strecker, G. B. Partridge, A. G. Truscott, and R. G. Hulet. Formation and propagation of matter-wave soliton trains. *Nature*, 417(6885):150–153, 2002. (Cited on page 1.)

[7] T. Heimburg and A. D. Jackson. On soliton propagation in biomembranes and nerves. *Proceedings of the National Academy of Sciences*, 102(28):9790–9795, 2005. (Cited on page 1.)

[8] A. Hasegawa and F. Tappert. Transmission of stationary nonlinear optical pulses in dispersive dielectric fibers. I. Anomalous dispersion. *Applied Physics Letters*, 23(3):142—144, 1973. (Cited on page 1.)

[9] P. Emplit, J.P. Hamaide, F. Reynaud, C. Froehly, and A. Barthelemy. Picosecond steps and dark pulses through nonlinear single mode fibers. *Optics Communications*, 62(6):374—379, 1987. (Cited on page 2.)

[10] L. F. Mollenauer and K. Smith. Demonstration of soliton transmission over more than 4000 km in fiber with loss periodically compensated by Raman gain. *Optics Letters*, 13(8):675–677, 1988. (Cited on page 2.)

[11] J. M. Arnold. Solitons in Communications. *Electronics & Communication Engineering Journal*, (April):88–96, 1996. (Cited on pages 2 and 22.)

[12] K. Tamura, H. A. Haus, and E. P. Ippen. Self-starting additive pulse mode-locked erbium fibre ring laser. *Electronics Letters*, 28(24):2226, 1992. (Cited on page 2.)

[13] P. Grelu and N. Akhmediev. Dissipative solitons for mode-locked lasers. *Nature Photonics*, 6(2):84–92, 2012. (Cited on pages 2 and 98.)

[14] Y. Tang, L. G Wright, K. Charan, T. Wang, C. Xu, and F. W. Wise. Generation of intense 100 fs solitons tunable from 2 to 4,3 μm in fluoride fiber. *Optica*, 3(9):948–951, 2016. (Cited on pages 2 and 22.)

[15] N. Akhmediev and M. Karlsson. Cherenkov radiation emitted by solitons in optical fibers. *Physical Review A*, 51(3):2602–2607, 1995. (Cited on pages 2, 18, and 21.)

[16] D. R. Solli, C. Ropers, P. Koonath, and B. Jalali. Optical rogue waves. *Nature*, 450(7172):1054–1057, 2007. (Cited on page 2.)

[17] J. M. Dudley, F. Dias, M. Erkintalo, and G. Genty. Instabilities, breathers and rogue waves in optics. *Nature Photonics*, 8(10):755–764, 2014. (Cited on page 2.)

[18] A. Armaroli, C. Conti, and F. Biancalana. Rogue solitons in optical fibers: a dynamical process in a complex energy landscape? *Optica*, 2(5):497, 2015. (Cited on page 2.)

[19] T. G. Philbin, C. Kuklewicz, S. Robertson, S. Hill, F. Konig, and U. Leonhardt. Fiber-Optical Analog of the Event Horizon. *Science*, 319(5868):1367–1370, 2008. (Cited on page 2.)

[20] T. Gottschall, T. Meyer, M. Baumgartl, C. Jauregui, M. Schmitt, J. Popp, J. Limpert, and A. Tünnermann. Fiber-based light sources for biomedical applications of coherent anti-Stokes Raman scattering microscopy. *Laser & Photonics Reviews*, 9(5):435–451, 2015. (Cited on page 2.)

[21] C. F. Kaminski, R. S. Watt, A. D. Elder, J. H. Frank, and J. Hult. Supercontinuum radiation for applications in chemical sensing and microscopy. *Applied Physics B*, 92(3):367–378, 2008. (Cited on page 2.)

[22] J. M. Langridge, T. Laurila, R. S. Watt, R. L. Jones, C. F. Kaminski, and J. Hult. Cavity enhanced absorption spectroscopy of multiple trace gas species using a supercontinuum radiation source. *Optics express*, 16(14):10178–88, 2008. (Cited on page 2.)

[23] A. G. Griffith, R. K. W. Lau, J. Cardenas, Y. Okawachi, A. Mohanty, R. Fain, Y. H. D. Lee, M. Yu, C. T. Phare, C. B. Poitras, A. L. Gaeta, and M. Lipson. Silicon-chip mid-infrared frequency comb generation. *Nature Communications*, 6:6299, 2015. (Cited on page 2.)

[24] T. Udem, R. Holzwarth, and T. W. Hänsch. Optical frequency metrology. *Nature*, 416(6877):233–237, 2002. (Cited on page 2.)

[25] R. Slavík, F. Parmigiani, J. Kakande, C. Lundström, M. Sjödin, P. A. Andrekson, R. Weerasuriya, S. Sygletos, A. D. Ellis, L. Grüner-Nielsen, D. Jakobsen, S. Herstrøm, R. Phelan, J. O'Gorman, A. Bogris, D. Syvridis, S. Dasgupta, P. Petropoulos, and

D. J. Richardson. All-optical phase and amplitude regenerator for next-generation telecommunications systems. *Nature Photonics*, 4(10):690–695, 2010. (Cited on page 2.)

[26] J. Pfeifle, V. Brasch, M. Lauermann, Y. Yu, D. Wegner, T. Herr, K. Hartinger, Ph. Schindler, J. Li, D. Hillerkuss, R. Schmogrow, C. Weimann, R. Holzwarth, W. Freude, J. Leuthold, T. J. Kippenberg, and Ch. Koos. Coherent terabit communications with microresonator Kerr frequency combs. *Nature Photonics*, 8(5):375–380, 2014. (Cited on page 2.)

[27] J. M. Dudley, G. Genty, and S. Coen. Supercontinuum generation in photonic crystal fiber. *Reviews of Modern Physics*, 78(4):1135–1184, 2006. (Cited on pages 2, 17, 23, 24, 25, 26, and 62.)

[28] D. V. Skryabin and A. V. Gorbach. Colloquium : Looking at a soliton through the prism of optical supercontinuum. *Reviews of Modern Physics*, 82(2):1287–1299, 2010. (Cited on pages 2, 18, and 24.)

[29] J. C. Travers. Blue extension of optical fibre supercontinuum generation. *Journal of Optics*, 12(11):113001, 2010. (Cited on pages 2, 24, and 26.)

[30] L. Shen, N. Healy, L. Xu, H. Y. Cheng, T. D. Day, J. H. V. Price, J. V. Badding, and A. C. Peacock. Four-wave mixing and octave-spanning supercontinuum generation in a small core hydrogenated amorphous silicon fiber pumped in the mid-infrared. *Optics Letters*, 39(19):5721, 2014. (Cited on page 2.)

[31] M. A. Schmidt, A. Argyros, and F. Sorin. Hybrid Optical Fibers - An Innovative Platform for In-Fiber Photonic Devices. *Advanced Optical Materials*, 4(1):13–36, 2016. (Cited on page 2.)

[32] Ch. Markos, J. C. Travers, A. Abdolvand, B. J. Eggleton, and O. Bang. Hybrid photonic-crystal fiber. *Reviews of Modern Physics*, 89(4):045003, 2017. (Cited on page 2.)

[33] J. H. V. Price, T. M. Monro, H. Ebendorff-Heidepriem, F. Poletti, P. Horak, V. Finazzi, J. Y. Y. Leong, P. Petropoulos, J. C. Flanagan, G. Brambilla, X. Feng, and D. J. Richardson. Mid-IR Supercontinuum Generation From Nonsilica Microstructured Optical Fibers. *IEEE Journal of Selected Topics in Quantum Electronics*, 13(3):738–749, 2007. (Cited on page 3.)

[34] Ch. Rosenberg Petersen, U. Møller, I. Kubat, B. Zhou, S. Dupont, J. Ramsay, T. Benson, S. Sujecki, N. Abdel-Moneim, Z. Tang, D. Furniss, A. Seddon, and O. Bang. Mid-infrared supercontinuum covering the 1.4–13.3 μm molecular fingerprint region using ultra-high NA chalcogenide step-index fibre. *Nature Photonics*, 8(11):830–834, 2014. (Cited on page 3.)

[35] P. Domachuk, N. A. Wolchover, M. Cronin-Golomb, A. Wang, A. K. George, C. M. B. Cordeiro, J. C. Knight, and F. G. Omenetto. Over 4000 nm bandwidth of mid-IR supercontinuum generation in sub-centimeter segments of highly nonlinear tellurite PCFs. *Optics Express*, 16(10):7161–7168, 2008. (Cited on page 3.)

[36] U. Møller, Y. Yu, I. Kubat, Ch. R. Petersen, X. Gai, L. Brilland, D. Méchin, C. Caillaud, J. Troles, B. Luther-Davies, and O. Bang. Multi-milliwatt mid-infrared supercontinuum generation in a suspended core chalcogenide fiber. *Optics Express*, 23(3):3282, 2015. (Cited on page 3.)

[37] X. Jiang, N. Y. Joly, M. A. Finger, F. Babic, G. K. L. Wong, J. C. Travers, and Ph. St. J. Russell. Deep-ultraviolet to mid-infrared supercontinuum generated in solid-core ZBLAN photonic crystal fibre. *Nature Photonics*, 9(2):133–139, 2015. (Cited on page 3.)

[38] M. F. Saleh and F. Biancalana. Soliton dynamics in gas-filled hollow-core photonic crystal fibers. *Journal of Optics*, 18(1):013002, 2016. (Cited on page 3.)

[39] M. Nisoli, S. Stagira, S. De Silvestri, O. Svelto, S. Sartania, Z. Cheng, M. Lenzner, Ch. Spielmann, and F. Krausz. A novel-high energy pulse compression system: Generation of multigigawatt sub-5-fs pulses. *Applied Physics B: Lasers and Optics*, 65(2):189–196, 1997. (Cited on page 3.)

[40] P. Hölzer, W. Chang, J. C. Travers, A. Nazarkin, J. Nold, N. Y. Joly, M. F. Saleh, F. Biancalana, and P. St. J. Russell. Femtosecond Nonlinear Fiber Optics in the Ionization Regime. *Physical Review Letters*, 107(20):203901, 2011. (Cited on page 3.)

[41] F. Tani, J. C. Travers, and P. St. J. Russell. PHz-wide Supercontinua of Nondispersing Subcycle Pulses Generated by Extreme Modulational Instability. *Physical Review Letters*, 111(3):033902, 2013. (Cited on page 3.)

[42] F. Belli, A. Abdolvand, W. Chang, J. C. Travers, and Ph. St. J. Russell. Vacuum-ultraviolet to infrared supercontinuum in hydrogen-filled photonic crystal fiber. *Optica*, 2(4):292–300, 2015. (Cited on pages 3 and 20.)

[43] R. Sollapur, D. Kartashov, M. Zürch, A. Hoffmann, T. Grigorova, G. Sauer, A. Hartung, A. Schwuchow, J. Bierlich, J. Kobelke, M. Chemnitz, M. A. Schmidt, and Ch. Spielmann. Resonance-enhanced multi-octave supercontinuum generation in antiresonant hollow-core fibers. *Light: Science & Applications*, 6(12):e17124, 2017. (Cited on page 3.)

[44] K. F. Mak, J. C. Travers, P. Holzer, N. Y. Joly, and P. S. Russell. Tunable vacuum-UV to visible ultrafast pulse source based on gas-filled Kagome-PCF. *Optics Express*, 21(9):10942–10953, 2013. (Cited on page 3.)

[45] P. S. J. Russell, P. Hölzer, W. Chang, A. Abdolvand, and J. C. Travers. Hollow-core photonic crystal fibres for gas-based nonlinear optics. *Nature Photonics*, 8(4):278–286, 2014. (Cited on page 3.)

[46] M. F. Saleh, W. Chang, J. C. Travers, P. S. J. Russell, and F. Biancalana. Plasma-induced asymmetric self-phase modulation and modulational instability in gas-filled hollow-core photonic crystal fibers. *Physical Review Letters*, 109(11):1–5, 2012. (Cited on page 3.)

[47] D. Novoa, M. Cassataro, J. C. Travers, and P. S. T. Russell. Photoionization-Induced Emission of Tunable Few-Cycle Midinfrared Dispersive Waves in Gas-Filled Hollow-Core Photonic Crystal Fibers. *Physical Review Letters*, 115(3):1–5, 2015. (Cited on page 3.)

[48] G. J. Ogilvie, R. J. Esdaile, and G. P. Kidd. Transmission loss of tetrachloroethylene-filled liquid-core-fibre light guide. *Electronics Letters*, 8(22):533, 1972. (Cited on page 3.)

[49] J. Stone. Optical transmission loss in liquid-core hollow fibers. *IEEE Journal of Quantum Electronics*, 8(3):386–388, 1972. (Cited on page 3.)

[50] A. Samoc. Dispersion of refractive properties of solvents: Chloroform, toluene, benzene, and carbon disulfide in ultraviolet, visible, and near-infrared. *Journal of Applied Physics*, 94(9):6167–6174, 2003. (Cited on pages 4, 29, 33, 34, 118, and 134.)

[51] S. Kedenburg, M. Vieweg, T. Gissibl, and H. Giessen. Linear refractive index and absorption measurements of nonlinear optical liquids in the visible and near-infrared spectral region. *Optical Materials Express*, 2(11):1588–1611, 2012. (Cited on pages 4, 29, 30, 31, 32, 33, 34, 118, and 134.)

[52] M. Reichert, H. Hu, M. R. Ferdinandus, M. Seidel, P. Zhao, T. R. Ensley, D. Peceli, J. M. Reed, D. A. Fishman, S. Webster, D. J. Hagan, and E. W. Van Stryland. Temporal, spectral, and polarization dependence of the nonlinear optical response of carbon disulfide: erratum. *Optica*, 3(6):657, 2016. (Cited on page 4.)

[53] P. Zhao, M. Reichert, S. Benis, D. J. Hagan, and E. W. Van Stryland. Temporal and polarization dependence of the nonlinear optical response of solvents. *Optica*, 5(5):583, 2018. (Cited on pages 4, 37, 39, 120, and 121.)

[54] D. Lopez-Cortes, O. Tarasenko, and W. Margulis. All-fiber Kerr cell. *Optics Letters*, 37(15):3288–3290, 2012. (Cited on page 4.)

[55] R. M. Gerosa, A. Sudirman, L. de S. Menezes, W. Margulis, and Ch. J. S. de Matos. All-fiber high repetition rate microfluidic dye laser. *Optica*, 2(2):186–193, 2015. (Cited on pages 4 and 82.)

[56] H. W. Lee, M. A. Schmidt, P. Uebel, H. Tyagi, N. Y. Joly, M. Scharrer, and P. St. J. Russell. Optofluidic refractive-index sensor in step-index fiber with parallel hollow micro-channel. *Optics Express*, 19(9):8200–8207, 2011. (Cited on page 4.)

[57] Y. Peng, J. Hou, Y. Zhang, Z. Huang, R. Xiao, and Q. Lu. Temperature sensing using the bandgap-like effect in a selectively liquid-filled photonic crystal fiber. *Optics Letters*, 38(3):263, 2013. (Cited on page 4.)

[58] S. Pumpe, M. Chemnitz, J. Kobelke, and M. A. Schmidt. Monolithic optofluidic mode coupler for broadband thermo- and piezo-optical characterization of liquids. *Optics Express*, 25(19):22932–22946, 2017. (Cited on pages 4, 34, 35, 36, 88, and 118.)

[59] M. Schmidt, A. M. Cubillas, N. Taccardi, T. G. Euser, T. Cremer, F. Maier, H.-P. Steinrück, P. S. J. Russell, P. Wasserscheid, and B. J. M. Etzold. Chemical and (Photo)-Catalytical Transformations in Photonic Crystal Fibers. *ChemCatChem*, 5(3):641–650, 2013. (Cited on page 4.)

[60] D. Yan, J. Popp, M. W. Pletz, and T. Frosch. Highly sensitive broadband Raman sensing of antibiotics in step-index hollow-core photonic crystal fibers. *ACS Photonics*, 4(1):138–145, 2017. (Cited on page 4.)

[61] M. Nissen, B. Doherty, J. Hamperl, J. Kobelke, K. Weber, T. Henkel, and M. A. Schmidt. UV absorption spectroscopy in water-filled antiresonant hollow core fibers for pharmaceutical detection. *Sensors (Switzerland)*, 18(2):1–12, 2018. (Cited on page 4.)

[62] J. Meister, R. Franzen, G. Eyrich, J. Bongartz, N. Gutknecht, and P. Hering. First clinical application of a liquid-core light guide connected to an Er:YAG laser for oral treatment of leukoplakia. *Lasers in Medical Science*, 25(5):669–673, 2010. (Cited on page 4.)

[63] A. R. Chraplyvy and T. J. Bridges. Infrared generation by means of multiple-order stimulated Raman scattering in CCl(4)- and CBrCl(3)-filled hollow silica fibers. *Optics letters*, 6(12):632–633, 1981. (Cited on page 4.)

[64] K. Kieu and L. Schneebeli. Integrated liquid-core optical fibers for ultra-efficient nonlinear liquid photonics. *Optics Express*, 20(7):8148–8154, 2012. (Cited on page 4.)

[65] G. Fanjoux, A. Sudirman, J.-Ch. Beugnot, L. Furfaro, W. Margulis, and T. Sylvestre. Stimulated Raman-Kerr scattering in an integrated nonlinear optofluidic fiber arrangement. *Optics Letters*, 39(18):5407–5410, 2014. (Cited on page 4.)

[66] S. Kedenburg, A. Steinmann, R. Hegenbarth, T. Steinle, and H. Giessen. Nonlinear refractive indices of nonlinear liquids: wavelength dependence and influence of retarded response. *Applied Physics B*, 117(3):803–816, 2014. (Cited on page 4.)

[67] D. Churin, T. N. Nguyen, K. Kieu, R. A. Norwood, and N. Peyghambarian. Mid-IR supercontinuum generation in an integrated liquid-core optical fiber filled with CS_2. *Optical Materials Express*, 3(9):1358–1364, 2013. (Cited on pages 4 and 68.)

[68] S. Kedenburg, T. Gissibl, T. Steinle, A. Steinmann, and H. Giessen. Towards integration of a liquid-filled fiber capillary for supercontinuum generation in the 1.2-2.4μm range. *Optics Express*, 23(7):8281–8289, 2015. (Cited on pages 4 and 68.)

[69] S. Pricking and H. Giessen. Generalized retarded response of nonlinear media and its influence on soliton dynamics. *Optics Express*, 19(4):2895, 2011. (Cited on page 4.)

[70] C. Conti, M. A. Schmidt, P. S. J. Russell, and F. Biancalana. Highly Noninstantaneous Solitons in Liquid-Core Photonic Crystal Fibers. *Physical Review Letters*, 105(26):263902, 2010. (Cited on pages 4, 43, 44, 92, 126, 127, and 129.)

[71] M. Vieweg, T. Gissibl, S. Pricking, B. T. Kuhlmey, D. C. Wu, B. J. Eggleton, and H. Giessen. Ultrafast nonlinear optofluidics in selectively liquid-filled photonic crystal fibers. *Optics Express*, 18(24):25232–25240, 2010. (Cited on page 4.)

[72] A. Bozolan, C.J. de Matos, C. M. Cordeiro, E. M. Dos Santos, and J. Travers. Supercontinuum generation in a water-core photonic crystal fiber. *Optics Express*, 16(13):9671–9676, 2008. (Cited on page 4.)

[73] J. Bethge, A. Husakou, F. Mitschke, F. Noack, U. Griebner, G. Steinmeyer, and J. Herrmann. Two-octave supercontinuum generation in a water-filled photonic crystal fiber. *Optics Express*, 18(6):6230–6240, 2010. (Cited on page 4.)

[74] B. E. A. Saleh and M. C. Teich. Electromagnetic Optics. In *Fundamentals of Photonics*, chapter 5, pages 157–192. John Wiley & Sons, Inc., New York, Chichester, Brisbane, Toronto, Singapore, 1991. (Cited on pages 7 and 35.)

[75] A. W. Snyder and J. D. Love. Waveguides with exact solutions. In *Optical Waveguide Theory*, chapter 12, pages 238–279. Chapman and Hall, London, New York, 1983. (Cited on pages 8, 9, and 124.)

[76] C. Yeh and F. I. Shimabukuro. Circular dielectric waveguides. In *The Essence of Dielectric Waveguides*, chapter 5, pages 137–177. Springer, New York, 2008. (Cited on pages 8 and 9.)

[77] R. W. Hellwarth. Third-order optical susceptibilities of liquids and solids. *Progress in Quantum Electronics*, 5:1–68, 1979. (Cited on pages 11, 29, and 126.)

[78] R. W. Boyd. The intensity-dependent refractive index. In *Nonlinear Optics*, chapter 4, pages 207–252. Academic Press, 3rd edition, 2007. (Cited on pages 11, 119, 125, and 126.)

[79] G. P. Agrawal. Nonlinear Pulse Propagation. In *Nonlinear Fiber Optics*, chapter 2, pages 27–56. Academic Press, Boston, 5th edition, 2013. (Cited on pages 11, 12, 13, 14, 125, and 126.)

[80] A. Couairon, E. Brambilla, T. Corti, D. Majus, O. de J. Ramírez-Góngora, and M. Kolesik. Practitioner's guide to laser pulse propagation models and simulation. *The European Physical Journal Special Topics*, 199(1):5–76, 2011. (Cited on page 12.)

[81] P. V. Mamyshev and S. V. Chernikov. Ultrashort-pulse propagation in optical fibers. *Optics Letters*, 15(19):1076, 1990. (Cited on pages 12, 13, and 126.)

[82] M. Kolesik and J. V. Moloney. Nonlinear optical pulse propagation simulation: From Maxwell's to unidirectional equations. *Physical Review E*, 2004. (Cited on pages 12 and 80.)

[83] J. Laegsgaard. Mode profile dispersion in the generalized nonlinear Schrödinger equation. *Optics Express*, 15(24):16110–16123, 2007. (Cited on pages 13 and 14.)

[84] M. Chemnitz and M. A. Schmidt. Single mode criterion - a benchmark figure to optimize the performance of nonlinear fibers. *Optics Express*, 24(14):16191–16205, 2016. (Cited on pages 14, 15, 42, 43, and 124.)

[85] S. Afshar V. and T. M. Monro. A full vectorial model for pulse propagation in emerging waveguides with subwavelength structures part I: Kerr nonlinearity. *Optics Express*, 17(4):2298–2318, 2009. (Cited on page 14.)

[86] M. Artiglia and G. Coppa. Mode field diameter measurements in single-mode optical fibers. *Journal of Lightwave Technology*, 7(8):1139–1152, 1989. (Cited on page 15.)

[87] V. E. Zakharovand and A. B. Shabat. Exact Theory of Two-Dimensional Self-Focusing and One- Dimensional Self-Modulation of Waves in Nonlinear Media. *Zh. Eksp. Teor. Fiz*, 34(61):118–134, 1972. (Cited on page 15.)

[88] Y. Kodama. Optical solitons in a monomode fiber. *Journal of Statistical Physics*, 39(5-6):597–614, 1985. (Cited on page 18.)

[89] J. P. Gordon. Theory of the soliton self-frequency shift. *Optics Letters*, 11(10):662, 1986. (Cited on pages 18 and 22.)

[90] J. P. Gordon. Dispersive perturbations of solitons of the nonlinear Schrödinger equation. *J. Opt. Soc. Am. B*, 9(1):91–97, 1992. (Cited on pages 18 and 21.)

[91] J. N. Elgin. Soliton propagation in an optical fiber with third-order dispersion. *Optics Letters*, 17(20):1409, 1992. (Cited on page 18.)

[92] D. V. Skryabin. Soliton Self-Frequency Shift Cancellation in Photonic Crystal Fibers. *Science*, 301(5640):1705–1708, 2003. (Cited on page 18.)

[93] F. Biancalana, D. V. Skryabin, and A. V. Yulin. Theory of the soliton self-frequency shift compensation by the resonant radiation in photonic crystal fibers. *Physical Review E - Statistical, Nonlinear, and Soft Matter Physics*, 70(1 2):1–9, 2004. (Cited on pages 18, 21, and 22.)

[94] A. V Gorbach, D. V. Skryabin, J. M. Stone, and J. C. Knight. Four-wave mixing of solitons with radiation and quasi-nondispersive wave packets at the short-wavelength edge of a supercontinuum. *Optics Express*, 14(21):9854–9863, 2006. (Cited on page 18.)

[95] A. V. Gorbach and D. V. Skryabin. Light trapping in gravity-like potentials and expansion of supercontinuum spectra in photonic-crystal fibres. *Nature Photonics*, 1(11):653–657, 2007. (Cited on pages 18, 21, 24, and 98.)

[96] A. V. Gorbach and D. V. Skryabin. Theory of radiation trapping by the accelerating solitons in optical fibers. *Physical Review A - Atomic, Molecular, and Optical Physics*, 76(5), 2007. (Cited on pages 18, 24, and 98.)

[97] G. P. Agrawal. Optical Solitons. In *Nonlinear Fiber Optics*, chapter 5, pages 129–191. Academic Press, Boston, 5th edition, 2013. (Cited on page 18.)

[98] N. Akhmediev and A. Ankiewicz. *Solitons: Non-linear pulses and beams*. Chapman and Hall, London, Weinheim, New York, Tokyo, Melbourne, Madras, 1st edition, 1997. (Cited on pages 18 and 19.)

[99] P. K. A. Wai, C. R. Menyuk, Y. C. Lee, and H. H. Chen. Nonlinear pulse propagation in the neighborhood of the zero-dispersion wavelength of monomode optical fibers. *Optics Letters*, 11(7):464, 1986. (Cited on page 20.)

[100] P. K. A. Wai, C. R. Menyuk, H. H. Chen, and Y. C. Lee. Soliton at the zero-group-dispersion wavelength of a single-model fiber. *Optics letters*, 12(8):628–630, 1987. (Cited on page 20.)

[101] J. N. Elgin, T. Brabec, and S. M.J. Kelly. A perturbative theory of soliton propagation in the presence of third order dispersion. *Optics Communications*, 114(3-4):321–328, 1995. (Cited on page 20.)

[102] A. V. Husakou and J. Herrmann. Supercontinuum generation, four-wave mixing, and fission of higher-order solitons in photonic-crystal fiber. *Journal Of The Optical Society Of America B Optical Physics*, 19(9):2171–2182, 2002. (Cited on pages 20 and 24.)

[103] S. Roy, S. K. Bhadra, and G. P. Agrawal. Dispersive waves emitted by solitons perturbed by third-order dispersion inside optical fibers. *Physical Review A*, 79(2):023824, 2009. (Cited on page 20.)

[104] R. Driben, A. V. Yulin, and A. Efimov. Resonant radiation from oscillating higher order solitons. *Optics Express*, 23(15):19112, 2015. (Cited on page 20.)

[105] I. Cristiani, R. Tediosi, L. Tartara, and V. Degiorgio. Dispersive wave generation by solitons in microstructured optical fibers. *Optics express*, 12(1):124–135, 2004. (Cited on page 20.)

[106] N. Granzow, M. A. Schmidt, W. Chang, L. Wang, Q. Coulombier, J. Troles, P. Toupin, I. Hartl, K. F. Lee, M. E. Fermann, L. Wondraczek, and P. S.J. Russell. Mid-infrared supercontinuum generation in As_2S_3-silica "nano-spike" step-index waveguide. *Optics Express*, 21(9):10969, 2013. (Cited on page 20.)

[107] M. Chemnitz, J. Wei, C. Jain, B. P. Rodrigues, T. Wieduwilt, J. Kobelke, L. Wondraczek, and M. A. Schmidt. Octave-spanning supercontinuum generation in hybrid silver metaphosphate/silica step-index fibers. *Optics Letters*, 41(15):3519, 2016. (Cited on page 20.)

[108] F. Leo, J. Safioui, B. Kuyken, G. Roelkens, and S.-P. Gorza. Generation of coherent supercontinuum in a-Si:H waveguides: experiment and modeling based on measured dispersion profile. *Optics Express*, 22(23):28997–29007, 2014. (Cited on page 20.)

[109] V. Brasch, T. Herr, M. Geiselmann, G. Lihachev, M. H. P. Pfeiffer, M. L. Gorodetsky, and T. J. Kippenberg. Photonic chip-based optical frequency comb using soliton Cherenkov radiation. *Science*, 351(6271):357–360, 2016. (Cited on page 20.)

[110] D. Grassani, E. Tagkoudi, H. Guo, C. Herkommer, T. J. Kippenberg, and C.-S. Brès. Highly efficient 4 micron light generation through fs-fiber laser driven supercontinuum in Si_3N_4 waveguides. *arXiv*:1806.06633, 1–9, 2018. (Cited on page 20.)

[111] J. Herrmann, U. Griebner, N. Zhavoronkov, A. Husakou, D. Nickel, J. C. Knight, W. J. Wadsworth, P. S. J. Russell, and G. Korn. Experimental evidence for supercontinuum generation by fission of higher-order solitons in photonic fibers. *Physical Review Letters*, 88(17):173901, 2002. (Cited on page 21.)

[112] A. Efimov, A. V. Yulin, D. V. Skryabin, J. C. Knight, N. Joly, F. G. Omenetto, A. J. Taylor, and P. Russell. Interaction of an Optical Soliton with a Dispersive Wave. *Physical Review Letters*, 95(21):1–4, 2005. (Cited on page 21.)

[113] A.. V Yulin, D. V. Skryabin, and P. S. J. Russell. Four-wave mixing of linear waves and solitons in fibers with higher-order dispersion. *Optics Letters*, 29(20):2411–2413, 2004. (Cited on page 21.)

[114] D. V. Skryabin and A. V. Yulin. Theory of generation of new frequencies by mixing of solitons and dispersive waves in optical fibers. *Physical Review E - Statistical, Nonlinear, and Soft Matter Physics*, 72(016619):1–10, 2005. (Cited on page 21.)

[115] H. Guo, S. Wang, X. Zeng, and M. Bache. Understanding soliton spectral tunneling as a spectral coupling effect. *IEEE Photonics Technology Letters*, 25(19):1928–1931, 2013. (Cited on page 21.)

[116] K. E. Webb, M. Erkintalo, Y. Xu, N. G. R. Broderick, J. M. Dudley, G. Genty, and S. G. Murdoch. Nonlinear optics of fibre event horizons. *Nature Communications*, 5:4969, 2014. (Cited on page 21.)

[117] R. H. Stolen, W. J. Tomlinson, H. A. Haus, and J. P. Gordon. Raman response function of silica-core fibers. *Journal of the Optical Society of America B*, 6(6):1159, 1989. (Cited on page 21.)

[118] D. Hollenbeck and C. D. Cantrell. Multiple-vibrational-mode model for fiber-optic Raman gain spectrum and response function. *Journal of the Optical Society of America B*, 19(12):2886–2892, 2002. (Cited on pages 21, 24, and 120.)

[119] Q. Lin and G. P. Agrawal. Raman response function for silica fibers. *Optics Letters*, 31(21):3086, 2006. (Cited on page 21.)

[120] K. Porsezian and K. Nakkeeran. Optical solitons in presence of Kerr dispersion and self-frequency shift. *Physical Review Letters*, 76(21):3955–3958, 1996. (Cited on page 22.)

[121] F. M. Mitschke, L. F. Mollenauer, and J. P. Gordon. Discovery of the soliton self-frequency shift. *Physics Today*, 26(10):26–26, 1987. (Cited on page 22.)

[122] G. Genty, M. Surakka, J. Turunen, and A. T. Friberg. Complete characterization of supercontinuum coherence. *Journal of the Optical Society of America B*, 28(9):2301, 2011. (Cited on page 23.)

[123] I. Zeylikovich, V. Kartazaev, and R. R. Alfano. Spectral, temporal, and coherence properties of supercontinuum generation in microstructure fiber. *Journal of the Optical Society of America B*, 22(7):1453, 2005. (Cited on page 23.)

[124] M. Erkintalo, G. Genty, B. Wetzel, and J. M. Dudley. Limitations of the linear Raman gain approximation in modeling broadband nonlinear propagation in optical fibers. *Optics Express*, 18(24):25449–60, 2010. (Cited on page 23.)

[125] S. Dupont, Z. Qu, S. S. Kiwanuka, L. E. Hooper, J. C. Knight, S. R. Keiding, and C. F. Kaminski. Ultra-high repetition rate absorption spectroscopy with low noise supercontinuum radiation generated in an all-normal dispersion fibre. *Laser Physics Letters*, 11(7):1–8, 2014. (Cited on page 23.)

[126] A. M. Heidt, J. S. Feehan, J. H. V. Price, and T. Feurer. Limits of coherent supercontinuum generation in normal dispersion fibers. *Journal of the Optical Society of America B*, 34(4):764, 2017. (Cited on page 23.)

[127] A. M. Heidt, J. Rothhardt, A. Hartung, H. Bartelt, E. G. Rohwer, J. Limpert, and A. Tünnermann. High quality sub-two cycle pulses from compression of supercontinuum generated in all-normal dispersion photonic crystal fiber. *Optics Express*, 19(15):13873–13879, 2011. (Cited on page 23.)

[128] A. V. Husakou and J. Herrmann. Supercontinuum Generation of Higher-Order Solitons by Fission in Photonic Crystal Fibers. *Physical Review Letters*, 87(20):203901, 2001. (Cited on page 24.)

[129] G. Genty, S. Coen, and J. M. Dudley. Fiber supercontinuum sources (Invited). *Journal of the Optical Society of America B*, 24(8):1771, 2007. (Cited on pages 24 and 62.)

[130] N. Karasawa and K. Tada. Optical Solitons from a Photonic Crystal Fiber and Their Applications. In *Photonic Crystals*, chapter 10, pages 201–224. IntechOpen, Rijeka, 2007. (Cited on page 24.)

[131] H. Zhang, S. Yu, J. Zhang, and W. Gu. Effect of frequency chirp on supercontinuum generation in photonic crystal fibers with two zero-dispersion wavelengths. *Optics express*, 15(3):1147–1154, 2007. (Cited on pages 24 and 135.)

[132] M. Chemnitz, M. Gebhardt, C. Gaida, F. Stutzki, J. Kobelke, J. Limpert, A. Tünnermann, and M. A. Schmidt. Hybrid soliton dynamics in liquid-core fibres. *Nature Communications*, 8(1):42, 2017. (Cited on pages 27, 55, 66, and 70.)

[133] M. Chemnitz, R. Scheibinger, Ch. Gaida, M. Gebhardt, F. Stutzki, S. Pumpe, J. Kobelke, A. Tünnermann, J. Limpert, and M. A. Schmidt. Thermodynamic control of soliton dynamics in liquid-core fibers. *Optica*, 5(6):695, 2018. (Cited on pages 27, 35, 82, 83, 84, 85, 86, 88, and 95.)

[134] C.-S. Laboratories Inc. Cargille Microscope Immersion Oils, 2018. (Cited on page 27.)

[135] J. D. Jackson. Frequency Dispersion Characteristics of Dielectrics, Conductors, and Plasmas. In John David Jackson, editor, *Classical Electrodynamics*, chapter 7.5, pages 309–316. John Wiley & Sons, Inc., Berkeley, 3rd edition, 1999. (Cited on page 29.)

[136] W. v. Sellmeier. Zur Erklärung der abnormen Farbenfolge im Spectrum einiger Substanzen. *Annalen der Physik und Chemie*, 219(6):272–282, 1871. (Cited on page 29.)

[137] J. W. Fleming. Dispersion in GeO2-SiO2 glasses. *Applied Optics*, 23(24):4486–4493, 1984. (Cited on page 29.)

[138] K. Moutzouris, M. Papamichael, S. C. Betsis, I. Stavrakas, G. Hloupis, and D. Triantis. Refractive, dispersive and thermo-optic properties of twelve organic solvents in the visible and near-infrared. *Applied Physics B*, 116(3):617–622, 2013. (Cited on pages 29 and 35.)

[139] T. M. Monro and H. Ebendorff-Heidepriem. Progress in Microstructured Optical Fibers. *Annual Review of Materials Research*, 36(1):467–495, 2006. (Cited on pages 30 and 31.)

[140] B. D. Mistry. *A Handbook of Spectroscopic Data Chemistry*. Oxford Book Company, Jaipur, 2009. (Cited on pages 30 and 31.)

[141] M. Plidschun, M. Chemnitz, and M. A. Schmidt. Low-loss deuterated organic solvents for visible and near-infrared photonics. *Optical Materials Express*, 7(4):1122–1130, 2017. (Cited on pages 30, 31, and 32.)

[142] F. Théberge, P. Mathieu, N. Thiré, J.-F. Daigle, B. E. Schmidt, J. Fortin, R. Vallée, Y. Messaddeq, and F. Légaré. Mid-infrared nonlinear absorption in As_2S_3 chalcogenide glass. *Optics Express*, 24(21):24600, 2016. (Cited on page 31.)

[143] NIST Mass Spec Data Center. Infrared Spectra. In W.G. Mallard and P.J. Linstrom, editors, *NIST Chemistry WebBook*. National Institute of Standards and Technology, Gaithersburg MD, nist stand edition. (Cited on pages 31 and 131.)

[144] E. K. Plyler and C. J. Humphreys. Infrared absorption spectrum of carbon disulfide. *Journal of research of the National Bureau of Standards*, 39(1):59–65, 1947. (Cited on page 31.)

[145] D. E. Mann, N. Acquista, and E. K. Plyler. Vibrational spectra of tetrafluoroethylene and tetrachloroethylene. *Journal of Research of the National Bureau of Standards*, 52(2):67–72, 1954. (Cited on page 31.)

[146] D. P. Shelton. Refractive index measured by laser beam displacement at λ=1064nm for solvents and deuterated solvents. *Applied Optics*, 50(21):4091, 2011. (Cited on page 32.)

[147] A. H. Pfund. The Dispersion of CS_2 and CCl_2 in the Infrared. *Journal of the Optical Society of America*, 25(11):351–354, 1935. (Cited on pages 33, 34, and 118.)

[148] R. E. Kagarise. Infrared Dispersion of Some Organic Liquids. *Journal of the Optical Society of America*, 50(1):36–39, 1960. (Cited on pages 33, 34, and 118.)

[149] B. Wilhelmi. Über die Anwendung von Dispersionsrelationen zur Bestimmung optischer Konstanten. *Annalen der Physik*, 474(5-6):244–252, 1967. (Cited on pages 33 and 118.)

[150] S. Ghosal, J. L. Ebert, and S. A. Self. The infrared refractive indices of CHBr3, CCl4 and CS2. *Infrared Physics*, 34(6):621–628, 1993. (Cited on pages 33 and 118.)

[151] S. Valkai, J. Liszi, and I. Szalai. Temperature dependence of the refractive index for three chloromethane liquids at 514.5 nm and 632.8 nm wavelengths. *The Journal of Chemical Thermodynamics*, 30(7):825–832, 1998. (Cited on page 34.)

[152] M. J. Weber. Liquids. In *Handbook of Optical Materials*, chapter 5, pages 383–445. CRC Press, Boca Raton, London, New York, Washington, D.C., 2003. (Cited on pages 34 and 118.)

[153] J. Vincent-Geisse. Dispersion de quelques liquides organiques dans l'infrarouge. détermination des intensités de bandes et des polarisations. *Journal de Physique*, 26(6):289–296, 1965. (Cited on pages 34 and 118.)

[154] J. Yarwood and W. J. Orville-Thomas. Infra-red dispersion studies. Part 7 Band intensities and atomic polarizations of CX_2= CCl_2(X = H, F, Cl) molecules. *Transactions of the Faraday Society*, 62(1):3294–3309, 1966. (Cited on pages 34 and 118.)

[155] J. Matsuoka, N. Kitamura, S. Fujinaga, T. Kitaoka, and H. Tamashita. Temperature dependence of refractive index of SiO_2 glass. *Journal of Non-Crystaline Solids*, 135:86–89, 1991. (Cited on page 35.)

[156] G. Ghosh, M. Endo, and T. Iwasaki. Temperature-Dependent sellmeier Coefficients and Chromatic Dispersions for Some Optical fiber glasses. *Journal of Lightwave Technology*, 12(8):1338–1342, 1994. (Cited on page 35.)

[157] E. Reisler, H. Eisenberg, and A. P. Minton. Temperature and density dependence of the refractive index of pure liquids. *Journal of the Chemical Society, Faraday Transactions 2*, 68:1001, 1972. (Cited on pages 35 and 87.)

[158] C. D. Keefe and S. Mac Innis. Temperature dependence of the optical properties of liquid toluene between 4000 and 400cm-1 from 30 to 105°C. *Journal of Molecular Structure*, 737(2-3):207–219, 2005. (Cited on page 35.)

[159] H. El-Kashef. Study of the refractive properties of laser dye solvents: Toluene, carbon disulphide, chloroform, and benzene. *Optical Materials*, 20(2):81–86, 2002. (Cited on page 35.)

[160] W. Hauf and U. Grigull. Optical methods in heat transfer. In James P. Hartnett and Thomas F. Irvine, editors, *Advances in Heat Transfer*, chapter 2, pages 133–366. Academic Press, 1970. (Cited on page 35.)

[161] E. W. Washburn. *International Critical Tables of Numerical Data, Physics, Chemistry and Technology, Vol. VII*. McGraw-Hill, New York, 1st edition, 1930. (Cited on page 35.)

[162] H. El-Kashef. Optical and electrical properties of materials. *Review of Scientific Instruments*, 65(6):2056–2061, 1994. (Cited on page 35.)

[163] H. El-Kashef. Thermo-optical and dielectric constants of laser dye solvents. *Review of Scientific Instruments*, 69(3):1243–1245, 1998. (Cited on page 35.)

[164] D. J. Coumou, E. L. Mackor, and J. Hijmans. Isotropic light-scattering in pure liquids. *Transactions of the Faraday Society*, 60(0):1539–1547, 1964. (Cited on page 35.)

[165] J. C. R. Reis, I. M. S. Lampreia, Â. F. S. Santos, M. Luísa C. J. Moita, and G. Douhéret. Refractive Index of Liquid Mixtures: Theory and Experiment. *ChemPhysChem*, 11(17):3722–3733, 2010. (Cited on page 36.)

[166] N. An, B. Zhuang, M. Li, Y. Lu, and Z.-G. Wang. Combined Theoretical and Experimental Study of Refractive Indices of Water-Acetonitrile-Salt Systems. *The Journal of Physical Chemistry B*, 119(33):10701–10709, 2015. (Cited on pages 36 and 37.)

[167] L. Lorenz. Ueber die Refractionsconstante. *Annalen der Physik*, 247(9):70–103, 1880. (Cited on page 37.)

[168] H. A. Lorentz. *Theory of Electrons*. Teubner, Leipzig, Berlin, 2nd edition, 1916. (Cited on page 37.)

[169] G. Baranovič. Refractive Index Mixing Rules and Excess Infrared Spectra of Binary Mixtures. *Applied Spectroscopy*, 71(5):1039–1049, 2017. (Cited on page 37.)

[170] R. W. Hellwarth, A. Owyoung, and N. George. Origin of the Nonlinear Refractive Index of Liquid C Cl 4. *Physical Review A*, pages 5–10, 1971. (Cited on page 37.)

[171] P. P. Ho and R. R. Alfano. Optical Kerr effect in liquids. *Physical Review A*, 20:2170–2187, 1979. (Cited on page 37.)

[172] D. McMorrow, W.T. Lotshaw, and G.A. Kenney-Wallace. Femtosecond optical Kerr studies on the origin of the nonlinear responses in simple liquids. *IEEE Journal of Quantum Electronics*, 24(2):443–454, 1988. (Cited on page 37.)

[173] W. T. Lotshaw, D. McMorrow, N. Thantu, J. S. Melinger, and R. Kitchenham. Intermolecular vibrational coherence in molecular liquids. *Journal of Raman Spectroscopy*, 26(7):571–583, 1995. (Cited on page 37.)

[174] M. Reichert, H. Hu, M. R. Ferdinandus, M. Seidel, P. Zhao, T. R Ensley, D. Peceli, J. M. Reed, D. A. Fishman, S. Webster, D. J. Hagan, and E. W. Van Stryland. Temporal, spectral, and polarization dependence of the nonlinear optical response of carbon disulfide. *Optica*, 1(6):436–445, 2014. (Cited on pages 37, 38, and 75.)

[175] M. L. Miguez, T. G. B. De Souza, E. C. Barbano, S. C. Zilio, and L. Misoguti. Measurement of third-order nonlinearities in selected solvents as a function of the pulse width. *Optics Express*, 25(4):3553, 2017. (Cited on pages 37, 39, and 120.)

[176] P. Zhao, M. Reichert, T. R. Ensley, W. M. Shensky, A. G. Mott, D. J. Hagan, and E. W. Van Stryland. Nonlinear refraction dynamics of solvents and gases. *Nonlinear Frequency Generation and Conversion: Materials, Devices, and Applications XV*, 9731:97310F, 2016. (Cited on pages 39 and 122.)

[177] N. Thantu and R. S. Schley. Ultrafast third-order nonlinear optical spectroscopy of chlorinated hydrocarbons. *Vibrational Spectroscopy*, 32(2):215–223, 2003. (Cited on pages 40 and 122.)

[178] M. Chemnitz, Ch. Gaida, M. Gebhardt, F. Stutzki, J. Kobelke, A. Tünnermann, J. Limpert, and M. A. Schmidt. Carbon chloride-core fibers for soliton mediated supercontinuum generation. *Optics Express*, 26(3):3221–3235, 2018. (Cited on pages 66, 69, 72, 73, and 95.)

[179] M. Gebhardt, C. Gaida, S. Hädrich, F. Stutzki, C. Jauregui, J. Limpert, and A. Tünnermann. Nonlinear compression of an ultrashort-pulse thulium-based fiber laser to sub-70 fs in Kagome photonic crystal fiber. *Optics Letters*, 40(12):2770, 2015. (Cited on page 66.)

[180] G. P. Agrawal. Novel Nonlinear Phenomena. In *Nonlinear Fiber Optics*, chapter 12, pages 497–551. Academic Press, Boston, 5th edition, 2013. (Cited on page 69.)

[181] M. Klimczak, G. Soboń, R. Kasztelanic, K. M. Abramski, and R. Buczyński. Direct comparison of shot-to-shot noise performance of all normal dispersion and anomalous dispersion supercontinuum pumped with sub-picosecond pulse fiber-based laser. *Scientific Reports*, 6:19284, 2016. (Cited on page 76.)

[182] X. Gu, M. Kimmel, A. Shreenath, R. Trebino, J. Dudley, S. Coen, and R. Windeler. Experimental studies of the coherence of microstructure-fiber supercontinuum. *Optics Express*, 11(21):2697–2703, 2003. (Cited on page 76.)

[183] G. Ghosh. Model for the thermo-optic coefficients of some standard optical glasses. *Journal of Non-Crystalline Solids*, 189(1-2):191–196, 1995. (Cited on page 82.)

[184] H. W. Lee, M. A. Schmidt, P. Uebel, H. Tyagi, N. Y. Joly, M. Scharrer, and P. St. J. Russell. Optofluidic refractive-index sensor in step-index fiber with parallel hollow micro-channel. *Optics Express*, 19(9):8200–8207, 2011. (Cited on page 82.)

[185] Y. Xu, X. Chen, and Y. Zhu. High Sensitive Temperature Sensor Using a Liquid-core Optical Fiber with Small Refractive Index Difference Between Core and Cladding Materials. *Sensors*, 8(3):1872–1878, 2008. (Cited on page 82.)

[186] Z. Li and D. Psaltis. Optofluidic dye lasers. *Microfluidics and Nanofluidics*, 4(1-2):145–158, 2008. (Cited on page 82.)

[187] X. Fan and S.-H. Yun. The potential of optofluidic biolasers. *Nature Methods*, 11(2):141–147, 2014. (Cited on page 82.)

[188] M. Vieweg, S. Pricking, T. Gissibl, Y. Kartashov, L. Torner, and H. Giessen. Tunable ultrafast nonlinear optofluidic coupler. *Optics Letters*, 37(6):1058–1060, 2012. (Cited on page 82.)

[189] B. T. Kuhlmey, B. J. Eggleton, and D. K. C. Wu. Fluid-Filled Solid-Core Photonic Bandgap Fibers. *Journal of Lightwave Technology*, 27(11):1617–1630, 2009. (Cited on page 82.)

[190] L. Velázquez-Ibarra, A. Díez, E. Silvestre, and M. V. Andrés. Wideband tuning of four-wave mixing in solid-core liquid-filled photonic crystal fibers. *Optics Letters*, 41(11):2600–2603, 2016. (Cited on page 82.)

[191] R. W. Boyd and G. L. Fischer. Nonlinear Optical Materials. *Encyclopedia of Materials: Science and Technology*, 2nd edition, 6237–6244, 2001. (Cited on page 87.)

[192] N. Walther. *Dispersion design of liquid composite-core fibers for the generation of supercontinua*. Master thesis, Friedrich-Schiller University Jena, 2018. (Cited on page 91.)

[193] S. Pricking, M. Vieweg, and H. Giessen. Influence of the retarded response on an ultrafast nonlinear optofluidic fiber coupler. *Optics Express*, 19(22):21673, 2011. (Cited on pages 92 and 93.)

[194] R. Zhang, J. Teipel, and H. Giessen. Theoretical design of a liquid-core photonic crystal fiber for supercontinuum generation. *Optics Express*, 14(15):6800–6812, 2006. (Cited on page 95.)

[195] R. Raei. Supercontinuum generation in organic liquid-liquid core-cladding photonic crystal fiber in visible and near-infrared regions. *Journal of the Optical Society of America B*, 35(2):323–330, 2018. (Cited on page 95.)

[196] T. Jimbo, V. L. Caplan, Q. X. Li, Q. Z. Wang, P. P. Ho, and R. R. Alfano. Enhancement of ultrafast supercontinuum generation in water by the addition of Znˆ2+ and Kˆ+ cations. *Optics Letters*, 12(7):477, 1987. (Cited on page 96.)

[197] A. Idrissi, M. Ricci, P. Bartolini, and R. Righini. Optical Kerr-effect investigation of the reorientational dynamics of CS2 in CCl4 solutions. *Journal of Chemical Physics*, 111(1999):4148–4152, 1999.

[198] J. E. Bertie and Z. Lan. The refractive index of colorless liquids in the visible and infrared: Contributions from the absorption of infrared and ultraviolet radiation and the electronic molar polarizability below 20 500 cm1. *The Journal of Chemical Physics*, 103(23):10152, 1995.

[199] G. S. He. *Nonlinear Optics and Photonics*. Oxford University Press, 1st edition, 2015. (Cited on page 119.)

[200] N. Tang and R. L. Sutherland. Time-domain theory for pump-probe experiments with chirped pulses. *Journal of the Optical Society of America B*, 14(12):3412–3423, 1997. (Cited on page 125.)

[201] A. Martínez-Rios, A. N. Starodumov, Y. O. Barmenkov, V. N. Filippov, and I. Torres-Gomez. Influence of the symmetry rules for Raman susceptibility on the accuracy of nonlinear index measurements in optical fibers. *Journal of the Optical Society of America B*, 18(6):794, 2001. (Cited on pages 125 and 126.)

[202] C. Conti, M. Schmidt, P. St. J. Russell, and F. Biancalana. Linearons: highly non-instantaneous solitons in liquid-core photonic crystal fibers. arXiv:1010.0331, 2010. (Cited on page 128.)

[203] J. Hult. A Fourth-Order Runge-Kutta in the Interaction Picture Method for Simulating Supercontinuum Generation in Optical Fibers. *Journal of Lightwave Technology*, 25(12):3770–3775, 2007. (Cited on page 131.)

[204] A. Bendahmane, F. Braud, M. Conforti, B. Barviau, A. Mussot, and A. Kudlinski. Dynamics of cascaded resonant radiations in a dispersion-varying optical fiber. *Optica*, 1(4):243-–249, 2014. (Cited on page 96.)

[205] A. Mussot, M. Conforti, S. Trillo, F. Copie, and A. Kudlinski. Modulation instability in dispersion oscillating fibers. *Advances in Optics and Photonics*, 10(1):1–42, 2018. (Cited on page 96.)

[206] A. W. Snyder and D. J. Mitchell. Accessible Solitons. *Science*, 276(5318):1538—1541, 1997. (Cited on page 98.)

Absorption measurements of highly transparent solvents

As described in sec. 3.2.1, linear optical absorption can be expressed either in terms of the imaginary part κ of the general IOR $\bar{n}(\omega)$, or in terms of the absorption coefficient α. An accurate determination of α usually requires measuring the output spectrum $I_{i,\text{out}}$ for multiple sample lengths L_i of the same material composition. Thereby, the absorption coefficient α is extracted from a linear regression $\log(I_{i,\text{out}}) = -\alpha L_i/10 + \log(I_{i,\text{in}})$ in the linear domains of $I_{i,\text{out}}(L_i)$.

In fiber optics this methodology is used in the so-called *cut-back measurement* where the fiber is successively shortened by defined length intervals after each transmission measurement. The strength of this techniques relies on the static optical coupling into the sample fiber, which remains unchanged for each *cut-back* measurement (i.e., $I_{in} = const.$). Unfortunately, this successful scheme is hard to transfer to LCFs since the liquid's menisci hinder reliable coupling in and out of the LCF.

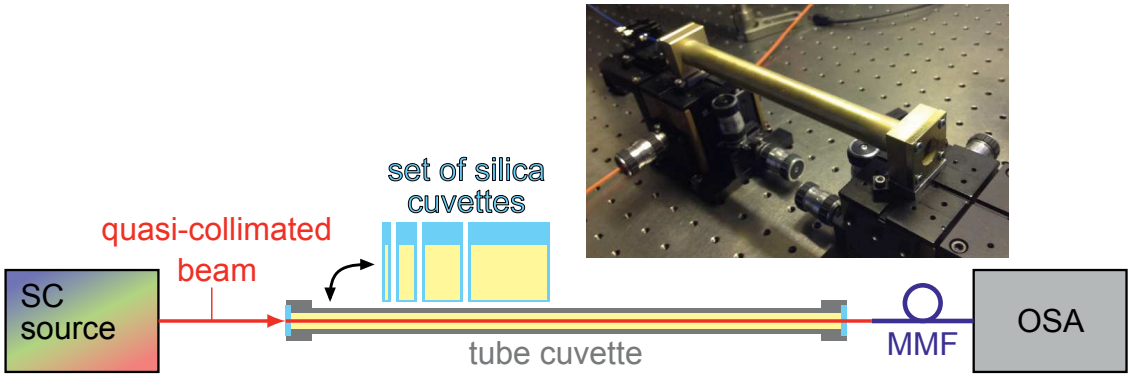

Fig. 44: **Scheme of the transmission setup** used to measure highly transparent solvents. The photograph exemplarily shows the 200 mm long custom-made cuvette.

Thus, liquid bulk measurements were performed in standard and customized cuvettes with lengths of 1 to 1000 mm (see Fig. 44). The customized cuvettes were built in the workshop of the IPHT and each consist of a brass tube with a certain length (i.e., 100, 200, 500, 1000 mm) and brass mounts on each side. The brass mounts were finely milled such that they could be welded on top of the tube ends in a rectangular angle. Each brass mount features a 25 mm wide frame for a sealing ring and a 1 mm thick sapphire window, which were pressed onto each other by a brass rim. Two types of measurements were performed:

1. In case of CH-based molecular liquids with higher absorption a measurement involved the record of one broadband transmission spectrum I_{out} for multiple cuvettes with different length with the spectrometer delivery fiber at a fixed position. Thus, the transmission spectrum I_{out} is known for multiple absorption lengths L, which justified the extraction of the absorption coefficient α by linear regression.

2. In case of highly transparent liquids such as C_2Cl_4 and CS_2 just the transmission spectrum (i.e., I_{out}) behind the 1000 mm cuvette showed absorption peaks and was

used to deduce a guess of the absorption coefficient based on a reference spectrum (i.e., I_{in}) of the SC laser source without cuvette.

Refractive index model parameters of CS_2, CCl_4, C_2Cl_4, and $CHCl_3$

Tab. 4 shows the best-fit parameter of the multi-parameter Sellmeier fit applied on the IOR data of various sources (cf. citations in the caption). The fits were based on the nonlinear least squares method and the inbuilt *Trust-Region* algorithm of Mathwork's programming environment MATLAB. The goodness of the fit is expresses by means of the R-squared value R^2 in the same table. All R^2 values are very close to 1 confirming a high quality of the fits.

Table 4: **Sellmeier coefficients and goodness of fit** (i.e., coefficient of determination R^2) of carbon disulfide and few liquid halogens. Additionally the TOC values are given for each liquid at 25 °C and 633 nm (taken from [152, 58]).

	CS_2	$CHCl_3$	CCl_4	C_2Cl_4
B_1	1.499426	1.04988049	1.09278717	1.21446261
B_2	0.089531	0.00495926	0.10628401	0.03501211
B_3	–	0.08854569	–	0.00792664
C_1 [µm]	0.178763	0.10737192	0.10937681	0.12071436
C_2 [µm]	6.591946	8.19132820	12.79529912	11.09560501
C_3 [µm]	–	13.11783889	–	13.21814444
R^2	0.9994	0.9989	0.9947	0.9951
Refs. used	[147, 149, 150, 50, 51]	[148, 50, 51]	[147, 51, 152]	[148, 153, 154]
TOC [$10^{-4}K^{-1}$]	−7.96	−5.98	−5.98	−6.23

Review of the nonlinear response model for liquids by Reichert *et al.*

In the following the three individual molecular responses are introduced and explained in detail. The response functions $r_k(t)$ defined in Eq. (52) are each incorporated in the total response function of the material, that is used in Eq. (51) to calculate the pulse-width dependent $n_{2,\text{eff}}$.

Molecular reorientation

A dominant part of the nuclear nonlinearity of CS_2 arises from molecular reorientation, also known as diffusive reorientation. Due to its linear shape the molecule features an anisotropic polarizability $\alpha = \alpha_\perp + \alpha_\parallel$ indicated by an ellipsoid in the pictograms in Fig. 12. Thus, despite its zero permanent dipole moment, an incident electric field causes an induced dipole moment along the molecule orientation being in general not parallel to the field polarization. The dipole moment couples to the electric field and leads to a torque on the molecule and, hence, to a reorientation of the versatile molecule towards the polarization of the field. In an ensemble of molecules this process can be seen as induced anisotropy counteracting the diffusive randomization of the molecule's orientation dictated by the second law of thermodynamics. The strength of the induced anisotropy is intensity dependent and thus by definition nonlinear. The induced torque is strong

enough that the reorientation continues for a certain time even though the field is absent until thermal diffusion overwhelms again. The decay time of the molecular reorientation is in the range of picoseconds [78, 199] and depends on the viscosity of the molecule ensemble.

For mathematical description Reichert *et al.* used the model of an overdamped oscillator

$$r_{\mathrm{re}}(t) = C_{\mathrm{re}}(1 - \mathrm{e}^{-t/\tau_{\mathrm{r}}})\mathrm{e}^{-t/\tau_{\mathrm{d,re}}}\,\Theta(t)\;, \tag{70}$$

which accounts for the rise time τ_{r} and decay time $\tau_{\mathrm{d,re}}$ of the reorientation, with the Heaviside function $\Theta(t)$ ensuring causality, and the normalization constant C_{re}. The rise time τ_{r} is usually approximated with 100 fs since the temporal resolution of common pump-probe setups is limited to 50–100 fs. However, it shall be noted that it is this rise time which significantly influences the impact of the molecular nonlinearities caused by ultrafast laser pulse with pulse durations of 100 fs and below. The long decay time of 1.6 ps makes it the most noninstantaneous processes of all considered nonlinear terms as visible in Fig. 12(a).

Libration

Another large contribution to the total nonlinearity of prolate molecules such as CS_2 originates from librational motions. The anisotropic polarizability of such molecules implies that the induced dipole moment is not parallel to the symmetry axis of the molecule. If we consider the ideal case of parallel alignment between dipole moment and electric field, the molecule is still free to rotate around this axis causing a torque with a characteristic frequency similar to the Larmor precession of an induced magnetic dipole moment in a magnetic field used in magnet resonance tomography. A resonant excitation of librations in a molecule ensemble causes an intensity-dependent index change hindered by collisional dephasing in the thermal environment. Mathematically this mechanism is described by an underdamped oscillator

$$r_{\mathrm{l}}(t) = C_{\mathrm{l}}\mathrm{e}^{-t/\tau_{\mathrm{d,l}}}\,\Theta(t)\int_0^\infty \frac{\sin(\omega t)}{\omega} g(\omega)\,\mathrm{d}\omega \tag{71}$$

with decay time $\tau_{\mathrm{d,l}}$ and normalization constant C_{l}. As suggested by Reichert *et al.* the spectral resonance of this process can be fit by an anti-symmetric Gaussian distribution $g(\omega) = \exp\left(-(\omega-\Omega)^2/(2\sigma^2)\right) - \exp\left(-(\omega+\Omega)^2/(2\sigma^2)\right)$ (central frequency Ω, spectral width σ). The resulting spectral distribution is clearly visible in the response spectrum $\tilde{R}(\nu)$, as exemplarily shown for CS_2 in Fig. 12, and, thus, becomes also visible in Raman spectra, as shown later.

Dipole-dipole interactions

A nonlinear mechanism which is not limited to prolate molecules is the collision-induced change of the molecular polarizability. In this process dipole moments initially induced

by an light field radiate an own electric field and induce dipole moments in neighboring molecules in close proximity, which can also be seen as a collective momentum transfer between colliding molecules. Energy dissipation might attenuate the build-up of such dipole clusters and leads to the decay of this induced nonlinearity. This mechanism is commonly resampled by an overdamped oscillation analogously to Eq. (70)

$$r_c(t) = C_c(1 - e^{-t/\tau_r})e^{-t/\tau_{d,c}}\,\Theta(t)\ , \tag{72}$$

with an individual decay time $\tau_{d,c}$ (index c for *collision*).

Raman-active vibrational modes

Recent research in ultrafast nonlinear processes focus on applying the above model to other liquids [175, 53]. However, those studies do not discuss the impact of coherently excited vibrational modes (i.e., Raman modes) because of the lack of temporal resolution of their pump-probe experiments. For some liquids with Raman bands beyond 10 THz, such as CS_2, neglecting the Raman response is a reasonable assumption. For example, the convolution of a 60 fs pulse with the CS_2 response function (incl. Raman) in Fig. 12b shows no fast oscillations, that would indicate coherent Raman scattering. Respectively, the Fourier transform of the convolution signal in Fig. 12b does not overlap with the Raman signal at 20 THz.

Nevertheless, other liquids, such as CCl_4, have strong Raman lines around 10 THz and below, and Raman can become reasonably strong for pulse widths of 100 fs or below. Therefore, in this work, the model by Reichert *et al.* was extended by the vibrational response (i.e., Raman response, with index $k = v$) due to its relevance for soliton dynamics. This was done by straightforwardly extending Eq. (52) by the normalized inverse Fourier transform of the measured Raman spectrum $S(\omega)$ in form of

$$r_v(t) = \mathrm{Im}(\mathcal{F}^{-1}\{S(\omega)\})\Theta(t)\ , \tag{73}$$

where r_v is normalized such that $\int r_v(t)\mathrm{d}t = 1$. The Raman spectra of selected liquids are shown in Fig. 45. A high-pass filter at 5 THz was applied to isolate the Raman signal from the residual spectral components of the slower noninstantaneous processes.

The specific NRIs $n_{2,v}$ were estimated from the linear Raman spectrum of each liquid normalized to a silica reference. The method was as follows: (1) The linear Raman spectrum of each liquid and a fused silica sample (Hereaus Suprasil300) were measured by Dr. Radu (IPHT Jena) under identical measurement conditions (i.e., using the same pump power, same sample lengths). (2) The maximum Raman signal of fused silica (i.e., the maximum signal of the Raman spectrum) was referenced to the maximum Raman gain using the quantitative model of silica [118]. (3) Due to the identical measurement conditions, the ratio between the Raman peak signal of silica and the Raman peak signal of each liquid spectrum was used to normalize the individual liquid spectrum to the units of a Raman gain spectrum $\tilde{g}_R(\omega)$. (4) Finally, the NRI $n_{2,v}$ of each liquid was de-

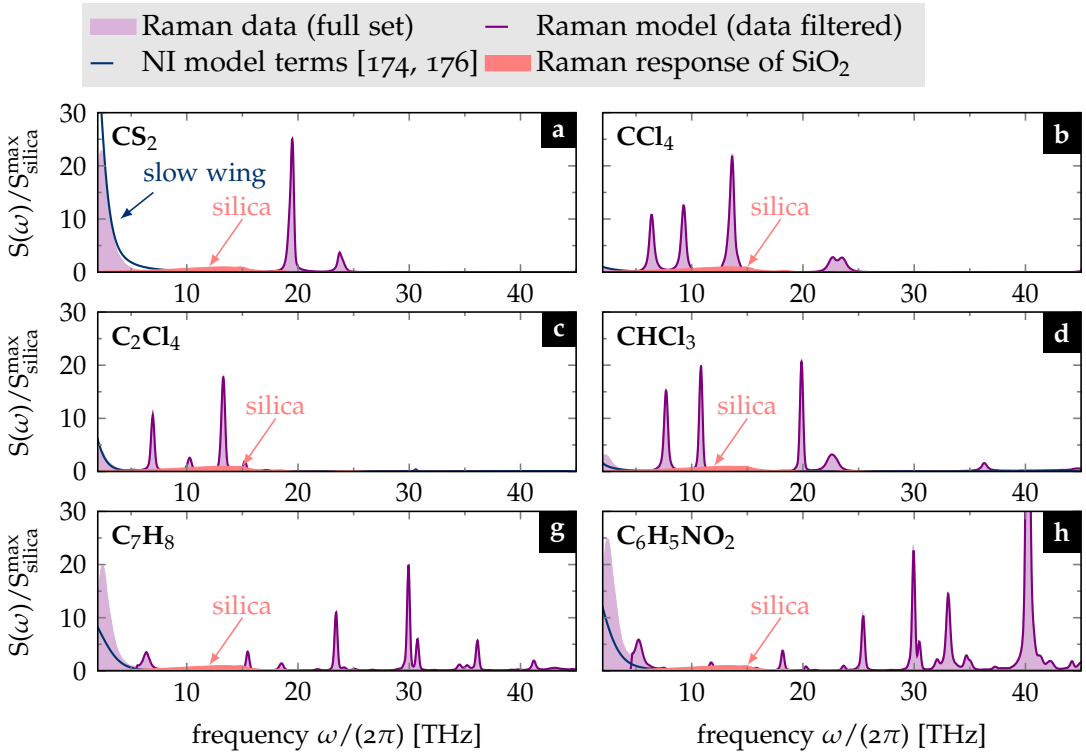

Fig. 45: Measured Raman spectra of selected liquids in comparison to their noninstantaneous response. Each panel shows the measured Raman spectrum of a liquid (filled light-purple curves) compared to the spectrum of the noninstantaneous NRFs without Raman (dark blue curves), each normalized to the maximum of the Raman spectrum of fused silica. The solid (non-filled) purple curves are the filtered Raman spectra which provide the spectrum $S(\omega)$ to be included in the model function in Eq. (73).

termined by normalizing the imaginary part of the response model function in Eq. (73) (i.e., $\Im\{\mathcal{F}\{n_{2,\mathrm{v}} r_{\mathrm{v}}(t)\}\}$) to the Raman gain spectrum $\tilde{g}_R(\omega)$. The estimated model parameters are listed in Tab. 5 in appendix A. The resulting temporal response is exemplarily shown for CS_2 in Fig. 12a.

The operability of the normalization can be tested by comparing the full normalized Raman spectra with the spectrum of the quantitatively known NRF model of each liquid. The low frequency components in the measured Raman spectra originate from the slower noninstantaneous processes, which are covered by the NRF. As shown in Fig. 45, the decaying wing of the measured spectra at frequencies below 5 THz match well to the spectral contribution of the noninstantaneous mechanisms (labeled as *slow wing* in Fig. 45a), in particular for the liquids CS_2, CCl_4, and C_2Cl_4. Since, the low frequencies are not used for the normalization of the Raman spectra, the good match between measurement and NRF model is not implied by the method, but indicates a well selected amplitude of the Raman gain.

Model parameters for selected liquids

Table 5 lists the NRF model parameters taken from [53] and the model fit for C_2Cl_4 elaborated in this work.

Table 5: **NRF model parameters for selected liquids.** References are given in the table. All NRIs (i.e., all $n_{2,i}$) are given in units of $10^{-20}\mathrm{m^2W^{-1}}$. The electronic NRI is considered to be wavelength dependent accordingly to Eq. (19) and given here for the wavelength 1.55 µm.

	CS_2	$CHCl_3$	CCl_4	C_2Cl_4	C_7H_8	$C_6H_5NO_2$
$n_{2,\mathrm{el}}$	15.1	4.1	4.8	5.5	6.1	6.1
$n_{2,\mathrm{d}}$	180.0	7.5	0.0	50.1	30.0	50.0
$\tau_{\mathrm{d,d}}$ [ps]	1.61	1.8	–	4.5	2.1	3.5
$n_{2,\mathrm{l}}$	76.0	4.0	0.0	20.8	12.0	17.0
$\tau_{\mathrm{d,l}}$ [ps]	0.45	0.25	–	0.78	0.35	0.4
Ω [THz]	8.5	5.0	–	4.0	11.0	5.0
σ [THz]	5.0	2.0	–	6.3	8.0	9.0
$n_{2,\mathrm{c}}$	10.0	0.8	2.0	3.1	1.2	3.5
$\tau_{\mathrm{d,c}}$ [ps]	0.14	0.1	0.15	2.98	0.2	0.1
$n_{2,\mathrm{v}}$	0.41	1.42	1.59	0.89	0.91	2.09

Retrieval of the nonlinear model for C_2Cl_4

In the scope of this work, C_2Cl_4 was identified as further promising liquid candidate for infrared softphotonics due its broadband transmission properties. Prior this work, no model existed for the linear dispersion or the nonlinear response. The latter could be found by fitting the NRF model by Reichert *et al.* to the experimental pump-probe data of trichloroethylene by Thantu and Schley [177]. Their data were published in a digital image format which allowed to read out the data points electronically.

The fit to retrieve a nonlinear model for C_2Cl_4 is based on two sets of data and Eq. (51) in the following form

$$n_{2,\mathrm{eff}}(t) = \frac{1}{\int I^2(t)\mathrm{d}t}\int I(t)\left(n_{2,\mathrm{el}} + \int R(t-\tau)I(\tau)\mathrm{d}\tau\right)\mathrm{d}t \tag{74}$$

$$= \int \frac{I(t)}{\int I(t)\mathrm{d}t}\int \frac{I(\tau)}{\int I(t)\mathrm{d}t}\left(n_{2,\mathrm{el}}\delta(\tau) + \sum_k n_{2,k}r_k(t-\tau)\right)\mathrm{d}\tau\mathrm{d}t \tag{75}$$

$$= n_{2,\mathrm{el}}\int G_s(t)\int G_p(\tau)\left(\delta(\tau) + \frac{n_{2,\mathrm{re}}}{n_{2,\mathrm{el}}}\sum_k \frac{n_{2,k}}{n_{2,\mathrm{re}}}r_k(t-\tau)\right)\mathrm{d}\tau\mathrm{d}t\,. \tag{76}$$

In a first step, the well resolved temporal and spectral response data by Thantu & Schley [177] and their measured decay times were used to estimate the amplitude ratios between reorientation, libration, and collision term (i.e. the ratios $n_{2,\mathrm{l}}/n_{2,\mathrm{re}}$, and $n_{2,\mathrm{c}}/n_{2,\mathrm{re}}$ in Eq. (76)). In a second step, a pump-probe data set measured by Dr. Christian Karras was used to estimate the electronic nonlinear index $n_{2,\mathrm{el}}$ and the ratio $n_{2,\mathrm{re}}/n_{2,\mathrm{el}}$.

The methodology of first step was as follows:

(1) Fixing response and decay times to reduce fit complexity: The rise times of the diffusive reorientation and the collision mechanism were both set to 100 fs, which is a common assumption when the temporal data resolution does not allow an accurate estimation [176]. For the decay times of the reorientation and libration mechanisms the values by Thantu & Schley were taken (i.e., 4.5 ps and 0.78 ps, respectively).

(2) Fit the response with the longest decay time: The main contribution to the nonlinear response at long decay times arise from reorientation. Thus, the data points of the pump-probe measurement for delay times larger than 1 ps are used to fit the normalized convolution of a 60 fs Gaussian probe pulse with Eq. (70) to find the first amplitude coefficient a_{re}.

(3) Fit the librational resonance: The spectral response data by Thantu & Schley (without contribution from reorientation) offered a good data base to fit a Gaussian spectral distribution (with bandwidth σ and resonance frequency Ω) according to Eq. (71). The final fit shown in Fig. 46 matches the given data set very well. The residual peaks between 5 and 15 THz belong to Raman resonances, which are not included in the model fit. The amplitude coefficient a_l was determined by fitting the model term to the temporal data subtracted by the reorientation term.

(4) Fit the residual data with the collision term: Finally, the data set shown in Fig. 46(a) was subtracted by the reorientation and libration term and the residual data set was used to fit Eq. (72) with regard to the decay time $\tau_{d,c}$ and the amplitude coefficient a_c. The contribution of the term is also rather small and plays a negligible role in this model.

(5) Calculate the amplitude ratios: Now that all terms are set, the amplitude ratios a_l/a_{re} and a_c/a_{re} define the ration of the respective NRIs $n_{2,l}/n_{2,re}$ and $n_{2,c}/n_{2,re}$. Thus, the number of model parameters could be effectively reduced to two, which is the electronic NRI and the ratio $n_{2,re}/n_{2,el}$.

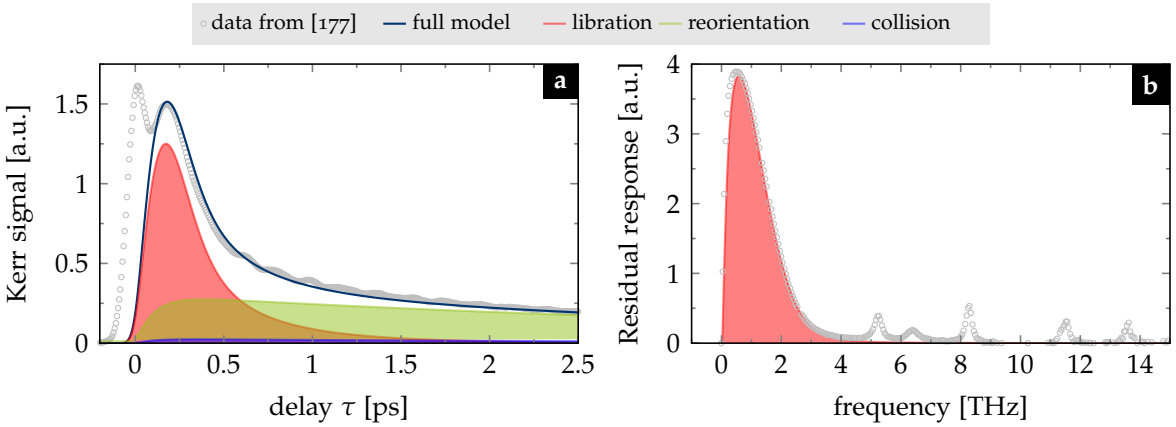

Fig. 46: **Model fit of the nonlinear response of C_2Cl_4.** a) Measured and modeled Kerr probe signal. b) The residual response spectrum of the Kerr signal in (a) without reorientation.

The electronic NRI and the molecular fraction f_m were not measured by Thantu & Schley. Therefore, estimates of those values needed to be found with an own pump-probe data set, which was measured by Dr. Christian Karras in the IPHT. The setup he used was a standard z-scan polarization Kerr gate, which shall not further be described here. The gained value is corrected for the nonlinearity of the cuvette walls resulting in $n_{2,el} = \Delta n - n_{2,SiO_2} \approx 5.5 \times 10^{-20}\,m^2/W$. The ratio $n_{2,re}/n_{2,el}$ was estimated by iteratively reconstructing the the measured Kerr signal. Our fitting procedure results in the model parameters listed in Tab. 5.

Power flow of step-index fiber modes

The power flow, or intensity, of an optical mode in a fiber is given by the z-component of the Poynting vector $S_z(\mathbf{r}) = \langle \boldsymbol{\mathcal{E}}(\mathbf{r},t) \times \boldsymbol{\mathcal{H}}^*(\mathbf{r},t) \rangle \mathbf{e}_z$ (the operator $\langle \cdot \rangle$ denotes for the temporal average). This quantity is of high relevance for the calculation of the effective mode area in nonlinear quantities as introduced in sec. 2.2.3. The Poynting vector for step-index fiber modes can be expressed in the following generalized form [75, 84]

$$S_z = C_1\, G_{m-1}^2(r) \;+\; C_2\, G_{m+1}^2(r) + \; C_3\, G_{m-1}(r) G_{m+1}(r) \cos(2m\varphi). \tag{77}$$

In the core domain, the argument r becomes $r = p\varrho$ and the general spheric functionals G_m have to be replaced with the Bessel functions J_m. In the cladding the functionals G_m have to be replaced by Bessel functions K_m with the argument $r = q\varrho$. The constants C_i are different for both regions, as listed in Tab. 6.

Table 6: **Locally dependent functions and constants.** The nomenclature is based on a book by Snyder and Love [75]. The required constants are listed in Tab. 7.

	core	cladding
$G_m(q)$	$J_m(q)$	$K_m(q)$
q	$r(k_{co}^2 - \beta^2)^{\frac{1}{2}}$	$r(\beta^2 - k_{cl}^2)^{\frac{1}{2}}$
HE, EH		
C_1	$\frac{p}{4} \cdot (F_1 - 1)(F_2 - 1)$	$\frac{p}{4} \cdot (F_2 - 1)(F_1 - 1 + 2\Delta)$
C_2	$\frac{p}{4} \cdot (F_1 + 1)(F_2 + 1)$	$\frac{p}{4} \cdot (F_2 + 1)(F_1 + 1 - 2\Delta)$
C_3	$(-1)^m \frac{p}{2} \cdot (1 - F_1 F_2)$	$(-1)^{m+1} \frac{p}{2} \cdot (1 - 2\delta - F_1 F_2)$
p	$\alpha / J_m^2(U)$	$\alpha / K_m^2(W) \cdot U^2/W^2$
TE		
C_1, C_3	0	0
C_2	$\alpha / J_1^2(U) \cdot \beta^2/(k_0 n_{co})^2$	$\alpha / K_1^2(W) \cdot \beta^2/(k_0 n_{co})^2$
TM		
C_1, C_3	0	0
C_2	$\alpha / J_1^2(U)$	$1/(1-2\Delta) \cdot \alpha / K_1^2(W)$

Table 7: **Locally independent constants.** A_m - modal amplitudes, R - core radius, $n_{\mathrm{co,cl}}$ - refractive core/cladding index, β - propagation constant.

α	$\lvert A_m \rvert^2 k_0 n_{\mathrm{co}}^2 / (2c_0\mu_0\beta)$		
F_1	$\left(\frac{UW}{V}\right)^2 (b_1 + (1-2\Delta)b_2)/m$	F_2	$\left(\frac{V}{UW}\right)^2 m/(b_1 + b_2)$
b_1	$\frac{1}{2U}\left(\frac{J_{m-1}(U)}{J_m(U)} - \frac{J_{m+1}(U)}{J_m(U)}\right)$	b_2	$-\frac{1}{2W}\left(\frac{K_{m-1}(U)}{K_m(W)} + \frac{K_{m+1}(W)}{K_m(W)}\right)$
Δ	$\frac{1}{2}\left(1 - n_{cl}^2/n_{co}^2\right)$	V	$R(k_{co}^2 - k_{cl}^2)^{\frac{1}{2}}$
U	$R(k_{co}^2 - \beta^2)^{\frac{1}{2}}$	W	$R(\beta^2 - k_{cl}^2)^{\frac{1}{2}}$

Nonlinear response of noninstantaneous materials

A practical description of the nonlinear pulse propagation requires strong assumptions on the optical fields and induced polarizations (q.v. Eq. (6)). In the following, these

assumptions are introduced and applied to deduce a practical form of the nonlinear polarization for partly noninstantaneous nonlinear media (e.g. Raman media).

The third-order nonlinear contribution to the total polarization in Eq. (6) can be written in the most general vectorial form in the frequency domain [78]

$$\tilde{\mathcal{P}}_{i,\mathrm{NL}}(\omega) = \varepsilon_0 C^{(3)} \sum_{jkl} \chi^{(3)}_{ijkl}(\omega;\omega',\omega'',\omega''')\tilde{\mathcal{E}}_j(\omega')\tilde{\mathcal{E}}_k(\omega'')\tilde{\mathcal{E}}_l(\omega''') \,, \tag{78}$$

with the permutation factor $C^{(3)}$. The sum over the polarization components j,k,l will not be written in the following according to the Einstein summation convention.

Fourier-transforming Eq. (78) leads to the general temporal expression of the third-order nonlinear polarization [79, 78]

$$\mathcal{P}_{i,\mathrm{NL}}(t) = \varepsilon_0 \int_{-\infty}^{t} \mathrm{d}\tau_1 \int_{-\infty}^{t} \mathrm{d}\tau_2 \int_{-\infty}^{t} \mathrm{d}\tau_3 R_{ijkl}(t-\tau_1, t-\tau_2, t-\tau_3)\mathcal{E}_j(\tau_1)\mathcal{E}_k(\tau_2)\mathcal{E}_l(\tau_3) \tag{79}$$

with the nonlinear response function R_{ijkl} being the Fourier transform of the third-order susceptibility

$$\begin{aligned} R_{ijkl}(\tau_1,\tau_2,\tau_3) = C^{(3)} \int_{-\infty}^{\infty} \mathrm{d}\omega' \int_{-\infty}^{\infty} \mathrm{d}\omega'' \int_{-\infty}^{\infty} \mathrm{d}\omega''' \chi^{(3)}_{ijkl}(\omega;\omega',\omega'',\omega''') \\ \times \mathrm{e}^{-\mathrm{i}\omega'\tau_1}\mathrm{e}^{-\mathrm{i}\omega''\tau_2}\mathrm{e}^{-\mathrm{i}\omega'''\tau_3} \,. \end{aligned} \tag{80}$$

The integration limits in Eq. (79) are chosen such, that the response term fulfills the principles of causality, i.e., it is zero for all negative times. The response function can be a linear combination of different nonlinear contributions, such as instantaneous electronic motions and noninstantaneous nuclear effects (e.g., stimulated Raman scattering), i.e., $R_{ijkl} = R^{\mathrm{el}}_{ijkl} + R^{\mathrm{mol}}_{ijkl}$. In case of electronic effects, R^{el}_{ijkl} can be expressed as product of Kronecker delta functions [200, 201]: $R^{\mathrm{el}}_{ijkl} = 3\chi^{\mathrm{el}}_{ijkl}\delta(\tau_1)\delta(\tau_2)\delta(\tau_3)$. The reader should note, that the factor 3 is the permutation factor for the optical Kerr effect. Thus, only the terms for $P_{NL}(\omega = \omega + \omega - \omega) \propto \tilde{\mathcal{E}}\tilde{\mathcal{E}}\tilde{\mathcal{E}}^*$ are considered in the following accordingly to [78].

In case of noninstantaneous effects, the response function is known in the following symmetric form [200, 201]

$$\begin{aligned} R^{\mathrm{mol}}_{ijkl}(\tau_1,\tau_2,\tau_3) = \chi^{\mathrm{mol}}_{ijkl}[R(\tau_1)\delta(\tau_2)\delta(\tau_3-\tau_1) + \delta(\tau_1-\tau_2)R(\tau_2)\delta(\tau_3) \\ + \delta(\tau_1)\delta(\tau_2-\tau_3)R(\tau_3)] \,, \end{aligned} \tag{81}$$

whereas $R(t)$ includes the *Heaviside* function to ensure causality, and is normalized to $\int R(t)\mathrm{d}t = 1$. Physically, e.g., the term $\delta(\tau_1-\tau_2)R(\tau_2)\delta(\tau_3)$ means that the distortion is created by the fields 1 and 2 at the moment τ_2 before field 3 arrives at the later time τ_3 to

experience the nonlinearity [201]. Inserting Eq. (81) in the nonlinear polarization in Eq. (79) yields the well-known Raman-Kerr expression [79]

$$\mathcal{P}_{i,\mathrm{NL}}(t) = 3\varepsilon_0 \chi^{\mathrm{mol}}_{ijkl} \left[\int_{-\infty}^{\infty} \mathrm{d}\tau \; R(t-\tau) \mathcal{E}_j(\tau) \mathcal{E}_k^{(*)}(\tau) \right] \mathcal{E}_l(t) \; . \tag{82}$$

For the derivation of nonlinear pulse propagation equations, the frequency representation of Eq. (82) is useful, which is [81]

$$\tilde{\mathcal{P}}_{i,\mathrm{NL}}(\omega) = 3\varepsilon_0 \int_{-\infty}^{\infty} \mathrm{d}\omega' \int_{-\infty}^{\infty} \mathrm{d}\omega'' \chi^{(3)}_{ijkl}(\omega-\omega') \tilde{\mathcal{E}}_j(\omega'') \tilde{\mathcal{E}}_l^*(\omega'+\omega''-\omega) \tilde{\mathcal{E}}_k(\omega') \; . \tag{83}$$

Eq. 83 can incorporate both electronic and molecular nonlinearities in a linear combination of the response terms, i.e., $\chi^{(3)}_{ijkl}(\omega) = \mathcal{F}\{\chi^{\mathrm{el}}_{ijkl}\delta(t) + \chi^{\mathrm{mol}}_{ijkl} R(t)\}$.

The general polarization in Eq. (83) is still rather complicated, and further assumption are needed to simplify this term. In general (i.e., materials with triclinic symmetry), the third-order susceptibility tensor $\hat{\chi}^{(3)}$ has 81 nonzero and independent elements, which, however, can be drastically reduced to 21 nonzero elements, of which only three are independent, when assuming isotropic (or weakly anisotropic) nonlinear materials [77, 78]. These three components can be further reduced to a single independent component assuming non-resonant nonlinear processes (i.e., lossless materials) and linearly polarized intrapulse wave mixing (i.e., self-induced nonlinear refraction with $\omega = \omega + \omega - \omega$ and identical polarization of all involved fields, i.e., $\tilde{\boldsymbol{\mathcal{E}}}/|\tilde{\boldsymbol{\mathcal{E}}}| = \tilde{\boldsymbol{\mathcal{P}}}_{\mathrm{NL}}/|\tilde{\boldsymbol{\mathcal{P}}}_{\mathrm{NL}}|$). This relevant single element is straightforwardly denoted as $\chi^{(3)}_{\mathrm{eff}} = \chi^{(3)}_{xxxx}$ in the common literature (e.g., [79]). Under those assumptions, it is valid to simplify Eq. (83) to

$$\tilde{\mathcal{P}}_{\mathrm{NL}}(\omega) = 3\varepsilon_0 \chi^{(3)}_{\mathrm{eff}}(\omega) \tilde{\mathcal{E}}(\omega) \tilde{\mathcal{E}}^*(\omega) \tilde{\mathcal{E}}(\omega) \; , \tag{84}$$

exemplarily for an instantaneous nonlinear medium.

Review of the semi-analytic solution of the noninstantaneous Schrödinger equation

The inhomogeneous linear differential equation Eq. (57) can be expressed as eigenvalue equation. Therefore, the ansatz $a(Z,T) = a(T)\exp(\imath\beta Z)$ was used to find the normalized Conti eigenvalue equation [70]

$$\beta a + \tfrac{1}{2}\mathrm{sgn}(\beta_2)\partial_T^2 a = \mathcal{E}_a H(T) a(Z,T) \; , \tag{85}$$

with normalized propagation constant β.

Equation (85) is an inhomogeneous eigenvalue equation and can be solved for very special noninstantaneous cases analytically. In the analytical example by Conti *et al.* the authors assumed a single exponential response function $H(T) = \Theta(T)\exp(-T)$ to ap-

proximate the noninstantaneous response of liquids. They found a set of linear solutions of the mathematical form [70]

$$a_m(T) = \mathcal{N} \begin{cases} \exp\left(\sqrt{2\beta_m}T\right) & \text{for } T < 0 \\ J_\nu\left(\sqrt{8\mathcal{E}_a}\exp(-T/2)\right) / J_\nu\left(\sqrt{8\mathcal{E}_a}\right) & \text{for } T > 0 \end{cases} \tag{86}$$

with the bessel functions of the first kind J_ν with the order $\nu = \sqrt{8\beta_m}$, and the normalization constant $\mathcal{N}$, which can be found by imposing $\int_{-\infty}^{\infty} a(T)\mathrm{d}T \equiv \mathcal{E}_a/N_R^2$. The eigenvalues β_m are implicitly given by $\sum_{n=0}^{\infty}(-2\mathcal{E}_a)^n/n!(\sqrt{8\beta_m})_n \equiv 0$, where $(x)_n = \Gamma(x+n)/\Gamma(x)$ is the rising factorial. This provides a dispersion relation $\beta(\mathcal{E}_a)$ and can be solved numerically for a healthy parameter set, i.e., for small orders ν of the Bessel function. The chosen normalization to the response time T_R reduces the parameter space to a single dimension, i.e., the normalized pulse energy $\mathcal{E}_a$ only, whereas it was possible to discuss the general set of solutions by solely varying this parameter.

The first four modes of the solution set are exemplarily depicted for $\mathcal{E}_a = 300$ in Fig. 47(a). They may be classified by counting the number of nodes m (cf. labels in Fig. 47a), whereas higher mode numbers have smaller propagation constants, or eigenvalues, respectively.

Fig. 47(b) shows the propagation constant β and the $1/e^2$ pulse width T_{e^2} of all four modes for pulse energies easily addressable by low- to medium-power lasers (i.e., $\mathcal{E}_p = 0.1\,\mathrm{pJ}\ldots100\,\mathrm{nJ}$ for CS_2 with $T_R = 1.26\,\mathrm{ps}$ and $\gamma_0 L_R = 0.125$). The propagation constants of all modes converge towards an upper limit (q.v. red curve in Fig. 47(b)). This limit can be found by pushing the noninstantaneous approximation even further to approximate the field amplitude of the fundamental mode by $a_0(T) = \sqrt{\mathcal{E}_a}\delta(T - T_c)$, whereas the time T_c marks the pulse center. Thus, the noninstantaneous term becomes $\mathcal{E}_a^{3/2}R(T)\delta(T - T_c)$ and with a transition of Eq. (85) to frequency space the condition is found

$$\beta = \frac{1}{2}\omega_s^2 + \mathcal{E}_a R(T_c) \xrightarrow{\mathcal{E}_a\to\infty} \mathcal{E}_a R_0\,, \tag{87}$$

where $R_0 = \max(R(T))$. The last asymptotic step is justified, since in the high-energy limit the pulse center T_c tends into the minimum of the response potential. Thus, for large energies the pulse underlies a maximum phase shift of $R_0\mathcal{E}_a$, which is in accordance to the theoretical prediction by Conti *et al.* besides a factor of $(2/\pi)^2$.

The phase discrimination of the individual modes decreases drastically for increasing pulse energy, i.e., above $\mathcal{E}_a = 10^3$ the modes are nearly indistinguishable which can be understood as an increasing density of states to a continuum with increasing potential depth (i.e., $\mathcal{E}_a$). Necessary conditions for the excitation of linearons are given by the validity of the noninstantaneous approximation being dependent on the pulse width (i.e., $T_R/T_0 \gg 1$). The pulse width of the states decreases from $T_0 \gtrsim T_R$ low energy to $T_0 < T_R$. Thus, the solutions justify the noninstantaneous approximation increasingly more for higher energies. The pulse energy $\mathcal{E}_a$ has to be chosen such that the calculated states fulfill the noninstantaneous conditions (i.e., pulse width $T_0 \ll$ response time T_R).

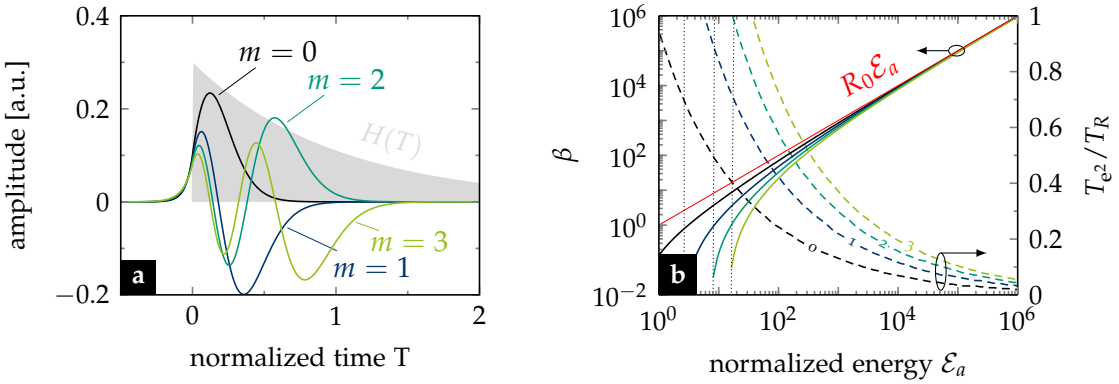

Fig. 47: **Linearon states of an exponential response** a) Modes for a system with $\mathcal{E}_a = 300$. The eigenvalues are $\beta_0 = 233.6$, $\beta_1 = 182.6$, $\beta_2 = 145.7$, $\beta_3 = 116.7$ and agree with the example shown by Conti *et al.* considering the renormalization. b) Phase constant and $1/e^2$ pulse width of the first four mode solutions of Eq. (57) as function of the energy parameter. The $1/e^2$-width of the pulse intensity was chosen to avoid discontinuities arising from the varying amplitudes of the modulations of higher order modes (i.e., $m > 0$). The dotted lines indicate the mode cutoffs.

Conti *et al.* called the general set of linear states given by Eq. (86) ***noninstantaneous solitons***, or ***linearons*** (accordingly to the arXiv version by Conti *et al.* [202]), since they are propagation-invariant eigenfunctions of this special nonlinear system. However, note that Conti *et al.* further revealed essential properties of linearon states which are shared with classical solitons, such as high noise stability, dispersive resonant radiation (in case of TOD) and soliton self-frequency shift. In the following, a practical extension of Conti's theory will be discussed incorporating the natural response function of liquid CS_2.

Recursive solution of the noninstantaneous Schrödinger equation

Noninstantaneous nonlinearities act accumulative, i.e. longer pulses experience a much stronger nonlinear phase. This implies that the noninstantaneous NRI depends on pulse shape and width, which can be expressed quantitatively by the integration rule given in Eq. (51). This implication has consequences for the existence of a linearon state calculated with Eq. (85) and the given NRI (or γ_0, respectively) assumed to remain constant. A recalculation of the NRI using the found linearon solution might change the NRI – a dependency that would normally lead to a nonlinear problem again. However, since the NRI is limited in its codomain, a recursive solution from an iterative procedure is possible.

In Fig. 48(a) an implemented instance of an iterative procedure is shown. The recursive kernel consists of the eigenvalue solver that gives a solution for a given potential $H(T)$, pulse energy $\mathcal{E}_p$, and dispersion β_2, whereas this solution is used to calculate a new noninstantaneous NRI based on Eq. (51) being fed back via γ_0 into the solver. Thus, γ_0 is not a free parameter anymore, but set by the width and shape of the eigensolution and the response of the material.

The algorithm may be started by giving an initial field $a_0(T)$. This process converges as soon as a_0 is well conditioned (e.g., $T_0 < T_R$) and the noninstantaneous NRI is limited,

i.e. cannot become infinitive. Fig. 48b shows exemplarily the convergence over only 10 iterations of pulse width T_{e^2}, peak power P_0 and molecular NRI (each in relative units) for two fields with largely different pulse energies of $\mathcal{E}_a = 1$ and $\mathcal{E}_a = 10^5$, respectively.

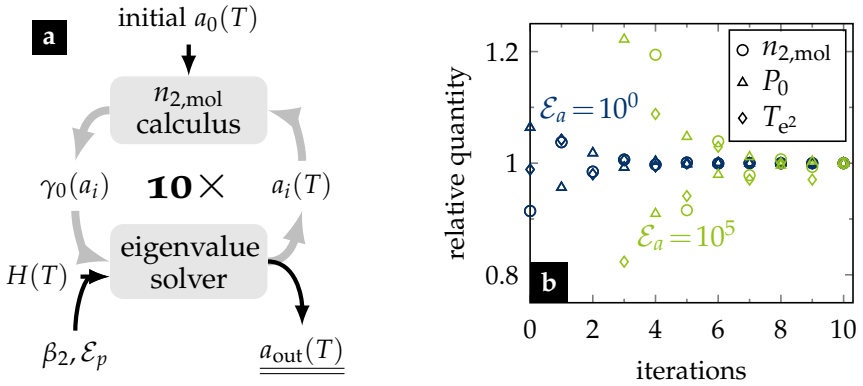

Fig. 48: **Iteration scheme.** a) Scheme of the implemented recursive solver to account for the dependency of the noninstantaneous NRI on pulse shape. The quantities are explained in the previous sections. b) Pulse width T_{e^2}, peak power P_0 and caused molecular NRI (all in relative units) of the fundamental linearon state at each iteration step for two largely different pulse energies.

Goodness of the solution of the NISE

As obvious from Fig. 16c, the pulse width of the solution may get close to the response time of the nonlinear medium, which violates the noninstantaneous approximation. Thus, further evaluation parameters are necessary to estimate the set of reasonable solutions. Conti *et al.* introduced three conditions, which allow to restrict the set of solutions *a posteriori*: $T_0/T_R \ll 1$, $\beta \gg 1/2$, $\mathcal{E}_a \gg \pi^2/8$ [70]. Those conditions give very rough estimates of the validity range of *ideal* solutions (i.e., in case of the exponential model). Unfortunately, their validity for other (*non-ideal*) noninstantaneous systems is unclear.

For practical purposes, it is possible to define an empirical ***goodness parameter*** $\mathcal{G}$, which is based on the mismatch between the actual noninstantaneous phase and the ideal phase assumed for the NISE. Mathematically this mismatch can be expressed by the error integral

$$\mathcal{G}^{-1} = \int_{-\infty}^{\infty} \left| \frac{N_R^2}{\mathcal{E}_a} \int_{-\infty}^{\infty} H(T-\tau)|a(\tau)|^2 \mathrm{d}\tau - H(T) \right| \mathrm{d}T = \int_{-\infty}^{\infty} \left| \frac{V_0(T)}{\mathcal{E}_a} - H(T) \right| \mathrm{d}T \,. \quad (88)$$

The operation compares the accurate noninstantaneous potential $V_0(T)$, i.e. the general convolution of the solution $a(T)$ with the nonlinear response function $H(T)$, with the approximated potential of the NISE $H(T)$. Conflicting solutions cause a strong mismatch between the potentials, leading to small values of $\mathcal{G}$. Large values of $\mathcal{G}$ indicate a good solution. The acceptable limit of $\mathcal{G}$ may be set to 5, since *ideal* solutions with $\mathcal{G} = 5$ feature $10T_0 \approx T_R$ being the least acceptable limit of the noninstantaneous approximation.

The goodness parameter does not enable to narrow down the validity domains *a priori* or any better than the three Conti parameters. However, the benefit of this quantity is that

it allows to judge the solutions of systems with arbitrary noninstantaneous potentials by just a single test.

Figure 49 shows an example for critical (cf. Fig. 49a) and reasonable conditions (cf. Fig. 49b) for the solution in a medium with an exponential response. The improvement of the goodness between those two solutions can graphically be seen in the improving overlap between the exponential potential $H(T)$ and the convolved phase $V_0(T)$. The goodness improves for higher energy $\mathcal{E}_a$ (q.v. Fig. 49d) confirming that the increasing potential depth leads to narrower states increasingly justifying the noninstantaneous approximation (i.e., $T_0 \ll T_R$).

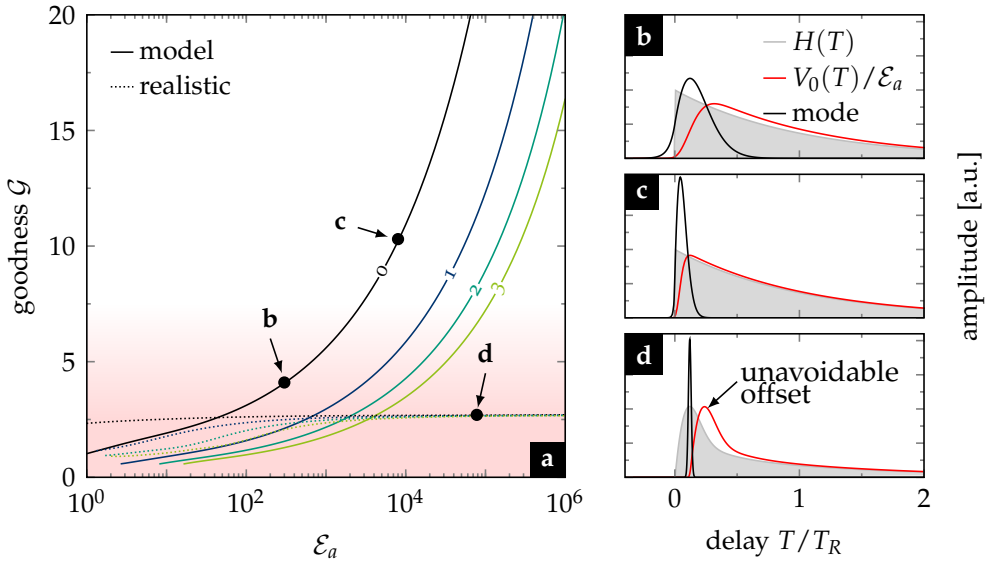

Fig. 49: **Comparison of the accurate and approximated nonlinear potential** Noninstantaneous potential $H(T)$, the fundamental mode, and the convolution potential $V_0(T)$ caused by this mode for a) ideal exponential response with $\mathcal{E}_a = 300$, b) ideal exponential response with $\mathcal{E}_a = 7500$, and realistic response with $\mathcal{E}_a = 77800$. d) Goodness $\mathcal{G}$ of the solution for both models as function of energy parameter $\mathcal{E}_a$.

This is not necessarily the case for more realistic potentials. Although these solutions also have a subset of parameters that fulfills all three Conti conditions (cf. Fig. 16c) that can be found in Fig. 49d, the goodness of the solutions from a realistic potential never exceeds the acceptable limit (i.e., $\mathcal{G} < 5$), instead it stagnates. This is mainly due to the unavoidable offset of the maximum between ideal and convoluted potential (cf. red and gray curve in Fig. 49c), which is caused by the finitely rising edge of the response.

These findings imply that linearon states only exists in media with zero rise time and infinitive response time. Thus, any state propagating through a realistic (*non-ideal*) non-instantaneous medium will disperse assuming endless propagation. However, if the propagation length in which the state remains in shape, i.e., the quasi-invariant length, exceeds the absorption length of the medium, which is always an intrinsic property of realistic media, too, the state can be considered to be a *quasi-linearon* state in the same manner as perturbed solitary waves measured in glass fibers are consider as solitons.

Simulation details

The stability of the algorithms depends significantly on the solver that is used to solve the integration over z in the nonlinear step [203]. The *split-step* algorithm implemented in this work uses a 4^{th}*-order Runge-Kutta integrator*, which very robust and straightforward to implement following these operations (in the time domain)

$$
\begin{aligned}
A(z+h) &= A(z) + \tfrac{1}{3}\left(\tfrac{1}{2}K_1 + K_2 + K_3 + \tfrac{1}{2}K_4\right) \qquad (89)\\
\text{with } K_1 &= h\hat{N}(A(z), z)\\
K_2 &= h\hat{N}(A(z) + \tfrac{1}{2}K_1, z + \tfrac{h}{2})\\
K_3 &= h\hat{N}(A(z) + \tfrac{1}{2}K_2, z + \tfrac{h}{2})\\
K_4 &= h\hat{N}(A(z) + K_3, z + h)\ .
\end{aligned}
$$

To further reduce computation time, the convolution integral in the nonlinear operator was solved using the Fourier theorem, i.e., $R * |A|^2 = \mathcal{F}^{-1}\{\mathcal{F}\{R\} \cdot \mathcal{F}\{|A|^2\}\}$. Hence, each of the four K coefficients of the integrator compute two additional Fourier transforms per step (i.e., number of operations: $2N \log N$; note that $\mathcal{F}\{R\}$ is invariant). Nevertheless, the Fourier-assisted convolution becomes increasingly more efficient than the direct convolution (number of operations: N^2) with an increasing number of grid points. Table 8 shows the parameters of all simulations shown in the main text. Since dispersion and nonlinear parameter were calculated over a large bandwidth using the semi-analytical models for step-index fibers, the Taylor-expansion parameters for β and γ give only a coarse estimate of both properties.

In case of CS_2, a coarse absorption model was used in the simulations associated with the experiments. The model is shown in Fig. 50 and accounts for the increasing losses in the near- to mid-infrared given in [143].

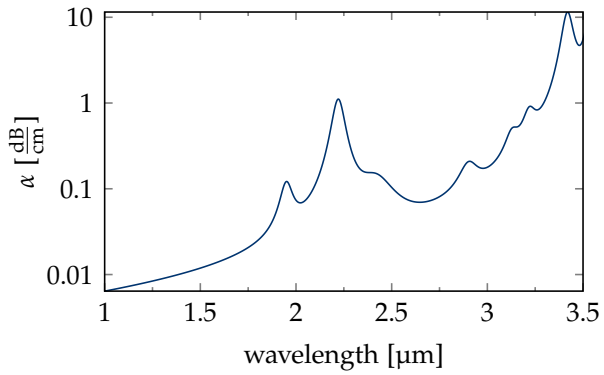

Fig. 50: **Absorption model of CS_2.** The model was applied in SC simulations whenever loss is indicated in Tab. 8.

Table 8: **Simulation parameters for the data presented in main sections.** *) reconstructed from measured spectrum, var.: varying

Fig.	eq. type	T_{HP} [fs]	P_0 [kW]	λ_0 [µm]	shape	noise	$\varnothing_{co}$ [µm]	α_0 [$\frac{1}{m}$]	β_2 [$\frac{fs^2}{mm}$]	β_3 [$\frac{fs^3}{mm}$]	β_4 [$\frac{fs^4}{mm}$]	β_5 [$\frac{fs^5}{mm}$]	β_6 [$\frac{fs^6}{mm}$]	γ_0 [$\frac{1}{Wm}$]	γ_1 [$\frac{fs}{Wm}$]	f_m	N_{eff}	resp. model
4 a-c	NSE	50	5.5	1.4	sech	no	8.1	0	8.36	0	0	0	0	0	0	0	0	–
4 d-f	NSE	50	5.5	1.4	sech	no	8.1	0	0	0	0	0	0	0.002	0	0	∞	–
4 g-i	NSE	50	5.5	1.4	sech	no	8.1	0	−8.30	0	0	0	0	0.002	0	0	1	–
4 j-l	NSE	50	21	1.4	sech	no	8.1	0	−8.30	89.75	0	0	0	0.002	0	0	2	–
4 m-o	GNSE	50	21	1.4	sech	no	8.1	0	−8.30	89.75	0	0	0	0.002	0	0.18	1.8	SiO_2
5 a-c	GNSE	50	250	1.35	sech	yes	8.1	0.005	−4.17	79.72	−88.2	53.75	−10.31	0.0021	0.003	0.18	9.2	SiO_2
5 d-f	GNSE	300	250	1.35	sech	yes	8.1	0.005	−4.17	79.72	−88.2	53.75	−10.31	0.0021	0.003	0.18	55	SiO_2
21 a-b	GNSE	450	10	1.95	sech	no	4.7	0	−21.1	385.55	−845.89	1092.76	−484.96	0.2741	0.3943	0	91.7	–
21 c-d	GNSE	450	10	1.95	sech	no	4.7	0	−21.1	385.55	−845.89	1092.76	−484.96	0.2741	0.3943	0.85	35.5	–
21 e-f	GNSE	450	10	1.95	sech	no	4.7	0	−21.1	385.55	−845.89	1092.76	−484.96	0.2741	0.3943	0.85	35.5	CS_2
21 g-h	GNSE	450	10	1.95	sech	no	4.7	0	−21.1	385.55	−845.89	1092.76	−484.96	0.2741	0.3943	1	0	CS_2
22 a	GNSE	450	10	1.95	sech	no	4.7	0	−21.1	385.55	−845.89	1092.76	−484.96	0.0411	0.0591	0	35.6	–
22 b	GNSE	450	10	1.95	sech	no	4.7	0	−21.1	385.55	−845.89	1092.76	−484.96	0.2742	0.3943	0.85	35.6	CS_2
24 a	GNSE	460	2.5	1.95	sech	yes	4.7	0	−25.58	384.09	−429.74	284.22	−54.37	0.0412	0.0585	0	16.5	CS_2
24 d	GNSE	460	2.5	1.95	sech	yes	4.7	0	−25.58	384.09	−429.74	284.22	−54.37	0.2742	0.3943	0.85	16.5	CS_2
28b	GNSE	461.5	var.	1.95	exp*	no	4.7	0.143	−20.65	384.13	−741.46	824.86	−303.17	0.2618	0.3823	0.85	var.	CS_2
29b	GNSE	230	var.	1.92	sech	no	4.7	0.141	−15.68	366.86	−395.7	262.7	−49.43	0.1789	0.2526	0.76	19.1	CS_2
30b	GNSE	270	11.5	1.92	sech	no	4.6	0	−19	207.41	−248.61	167.26	−34.33	0.032	0.0557	0.65	12.5	C_2Cl_4
32a	NSE	461.5	var.	1.95	exp*	no	4.7	0.143	−20.65	384.13	−741.46	824.86	−303.17	0.0413	0.0593	0	var.	–
32a	NSE	461.5	var.	1.95	exp*	no	4.7	0.143	−20.65	384.13	−741.46	824.86	−303.17	0.2618	0.3823	0	var.	–
32b	NSE	230	var.	1.92	sech	no	4.7	0.141	−15.68	366.86	−395.7	262.7	−49.43	0.0427	0.0603	0	var.	–
32b	NSE	230	var.	1.92	sech	no	4.7	0.141	−15.68	366.86	−395.7	262.7	−49.43	0.1789	0.2526	0	var.	–
32c	NSE	270	var.	1.92	sech	no	4.6	0	−19	207.41	−248.61	167.26	−34.33	0.0111	0.0193	0	var.	–
32c	NSE	270	var.	1.92	sech	no	4.6	0	−19	207.41	−248.61	167.26	−34.33	0.0303	0.0526	0	var.	–
33a	GNSE	459.0	7	1.95	exp*	yes	4.5	0.143	−22.88	383.85	−733.2	811.94	−297.76	0.3053	0.446	0.85	31.7	CS_2
34a	GNSE	461.5	var.	1.95	exp*	no	4.7	0.143	−20.65	384.13	−741.46	824.86	−303.17	0.2618	0.3823	0.85	var.	CS_2
34b	HNSE	461.5	var.	1.95	exp*	no	4.7	0.143	−20.65	384.13	−741.46	824.86	−303.17	0.2618	0.3823	0.85	var.	CS_2
34c	NSE	461.5	var.	1.95	exp*	no	4.7	0.143	−20.65	384.13	−741.46	824.86	−303.17	0.0413	0.0593	0	var.	CS_2
34d	GNSE	270	var.	1.92	sech	no	4.6	0	−19	207.41	−248.61	167.26	−34.33	0.032	0.0557	0.65	var.	C_2Cl_4
34e	HNSE	270	var.	1.92	sech	no	4.6	0	−19	207.41	−248.61	167.26	−34.33	0.032	0.0557	0.65	var.	C_2Cl_4
34f	NSE	270	var.	1.92	sech	no	4.6	0	−19	207.41	−248.61	167.26	−34.33	0.0111	0.0193	0	var.	C_2Cl_4
38c	GNSE	351.6	0.83	1.92	exp*	no	3.3	0.141	−22.65	291.04	−266.17	166.53	−29.16	0.3256	0.5456	0.78	9.5	CS_2
41d	GNSE	31.7	var.	1.56	exp*	no	8.2	0	9.39	87.44	−83.4	94.28	−27.08	0.002	−0.0008	0.04	var.	CCl_4
41e	GNSE	31.7	var.	1.56	exp*	no	5	0	−4.22	132.48	−159.24	98.75	−19.09	0.0061	0.0089	0.16	var.	mix
41f	GNSE	31.7	var.	1.56	exp*	no	4.9	0	12.9	96.54	−84.9	55.28	−10.66	0.0174	0.022	0.17	var.	C_2Cl_4

Liquid-core fiber fabrication and usage

A liquid-core step-index fibre can straightforwardly be fabricated by filling a capillary with the solvent solely using capillary forces, substantially reducing the fabrication effort compared to selectively filled photonic crystal fibres. The capillaries used in this work were fabricated in the IPHT Jena. To enable secure filling of and optical coupling into the capillaries a series of OFMs were designed within the scope of this thesis, and fabricated by the IPHT-internal workshop. The mounts feature two fluidic side ports (inlet and outlet) and one central fiber port facing a sealed Sapphire window (q.v. Fig. 51 a). The capillary and tubings were mounted in the OFMs by micro-fluidic connectors (Upchurch *finger-tights* and ferrule nuts). The OFMs were successively filled using either a syringe and fluoropolymer port blocks to seal the side ports (static operation), or a liquid pump connected via a micro-fluidic tubing and high-pressure valve system with the mounts enabling a controlled liquid flow (dynamic operation). Filling happened under the fume hood, or, in very rare cases, directly in the lab. After flushing the first holder, the capillary forces start to fill the capillary. The filled length over time can be calculated using the Washburn equation $L = \sqrt{\sigma \cdot \varnothing_{co} \cdot \cos\phi \cdot t/(4\eta)}$, which depends on the core diameter $\varnothing_{co}$, the contact angle ϕ, the surface tension σ, and the liquid viscosity η.

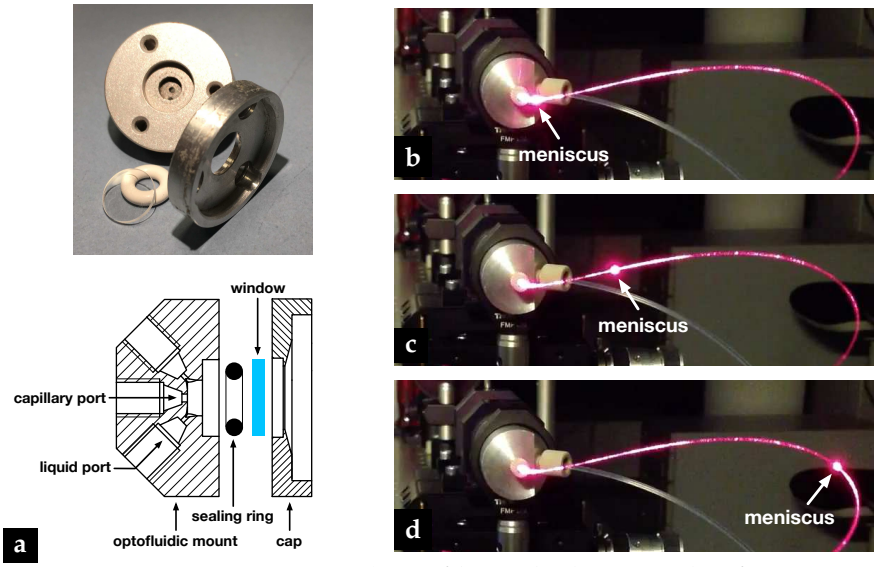

Fig. 51: **Fabrication of step-index LCFs.** a) Profile and photograph of an OFM. b-d) Snapshots capturing the filling process of a 10 µm core capillary with toluene. The meniscus is indicated by the strong scattering of a red diode coupled into the capillary mounted in the OFM.

Fig. 51 b shows the filling of 10 µm capillary with toluene. Red light was coupled into the hollow core of the capillary before filling to make the traveling meniscus visible. After the filling was complete, the second holder was flushed. In static operation, all side ports were closed and the opto-mechanical system remained under the hood for a few hours to ensure evaporation of possible leakage.

Power damage threshold of CS_2

Table 9 summarizes the damage thresholds observed while working with the repetition rate adjustable laser in fiber system #1.

Table 9: **Damage thresholds of the CS_2/silica fiber #1.** Estimated laser parameters in the focus of the coupling side when a transmission drop was detected for three individual LCF samples with comparable core diameters between 4.4 and 4.8 µm. f_{rep}: pulse repetition rate; $\bar{P}$: average power; $\mathcal{E}_p$: pulse energy; P_0: pulse peak power; I_0: pulse peak intensity. Underlined quantities mark common values between the measurements.

f_{rep} [MHz]	$\bar{P}$ [mW]	$\mathcal{E}_p$ [nJ]	P_0 [kW]	I_0 [TW/cm^2]
2.50	80.0	27.7	52.5	0.882
5.62	152.2	27.1	51.3	1.295
11.24	$\gtrsim$ 152.2	13.6	26.9	0.649

Figure 52 shows the measured and simulated transmission data of fiber system #1. The simulation thereby uses the coarse absorption model shown in Fig. 50. Two linear absorption regimes can be identified. The correlation between simulation and experiment confirms the absence of nonlinear losses in the experiment. The transition from regime 1 to regime 2 is at the fission point.

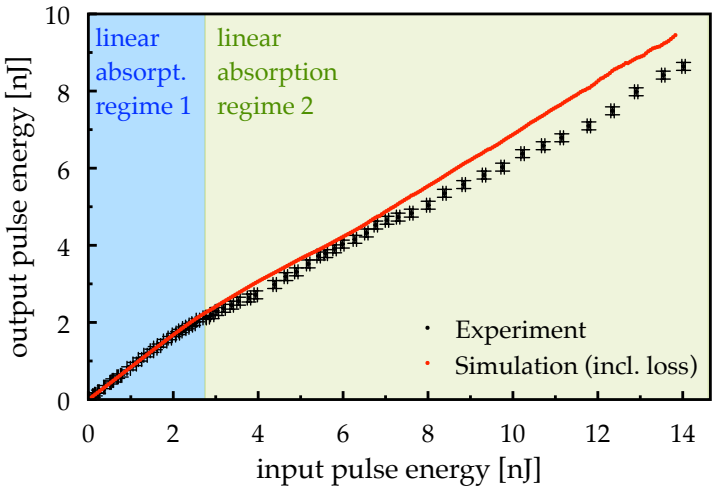

Fig. 52: Transmission characteristic of fiber #1. Measured and simulated output power over input power. Two linear absorption regimes become apparent (colored blue and green).

Error analysis of the SCG simulation results

FIBER DISPERSION The impact of the fiber dispersion on the SC spectra was investigated by performing simulations for identical pump conditions and (1) either fix LCF geometry, but different dispersion models of CS_2, (2) or fix material disperison, but slightly different core sizes. In the first case, the single-term Sellmeier dispersion models [50, 51], were tested against the double oscillator model of this work (q.v. sec. (3.2.3)). All three models show coherent soliton fission. However, the single-term models moderately overestimate bandwidth and required onset energy by up to ca. 10%. The two-term Sellmeier equation results in the best-match scenario to the experiment, emphasizing the quality of the model in the near- to mid-infrared.

The second test was performed for three distinctly different core diameters close to the experimental one (4.4 µm, 4.7 µm, 5.0 µm). Whereas the bandwidth shows up to be relatively independent on variation of the core size, the onset energy changes moderately in the order of 5% per 300 nm in this example. However, this uncertainty was minimized in this work by using electron microscopes to measure the core diameter with tens of nanometer precision.

NONLINEAR REFRACTIVE INDEX The most recent model of the nonlinear refractive index of CS_2 has been included in the presented work (q.v. sec. 3.3.1), whereas the model parameters were given with rather large error margins. Only small deviations of the response function influence the NRI and, thus, the molecular fraction f_m, with a strong influence on bandwidth, fission length, and noise characteristics of the SCs, especially for $f_\mathrm{m} \approx f_m^{\mathrm{equil}}$. For instance, Fig. 32 a shows the deviation of the bandwidth evolution within the error margins of the CS_2 model. Whereas the influence on the maximum bandwidth is minor, a drastic variation of the onset energy becomes apparent, which highlights the required accuracy of the response model for presented SCG studies.

UNKNOWN LOSSES Further reductions in bandwidth and onset energy are possible due to additional linear losses at mid-infrared wavelengths or nonlinear losses, whereas the latter become particularly dominant at lower wavelengths. The numerical solvers applied here include only a very coarse numerical fit model for the linear absorption of CS_2. However, a direct comparison of the input-to-output power characteristics of fiber #1 (q.v. Fig. 52) shows an acceptable match between measurements and simulations, and no evidence for an unknown dominant source of loss in the experiment. Thus, a rough estimation of the system loss appears to be sufficient to get the correct correlation between bandwidth and onset energy. These findings also justify to neglect nonlinear losses in the propagation models.

PULSE CHIRP Adding a quadratic spectral phase to the pump pulse at constant input bandwidth (i.e., second-order chirp) impacts the SC bandwidth and onset energy, whereas the bandwidth reaches maximum for a certain non-zero chirp [131]. Thus, knowing and, in the best case, controlling the input chirp in the experiment is necessary to obtain a reasonable match between measurements and simulations. In this work, the pulse from laser system A can be assumed free from second-order chirp due the phase compensation by the grating compressor. The residual third-order phase of the pulse was included in the simulations and had a negligible influence on the broadening process. The pulses from laser system B, however, accumulated a relatively strong second-order phase from the last isolator. However, assuming a chirp-free pulse with a pulse width corresponding to the measured auto-correlation resulted in the best match between simulation and experiment, in particular in case of fibers #4, #5, and #6. Thus, measuring the auto-correlation of the input pulse is the bare minimum for relevant simulation results.

ACKNOWLEDGEMENTS

I thank Prof. Dr. Markus Schmidt for his excellent scientific support and dedicated mentoring throughout my entire PhD time.

I thank Prof. Dr. Limpert and his co-workers Dr. Fabian Stutzki, Martin Gebhardt, and Christian Gaida for their scientific input and the opportunity to work with their world-leading thulium fiber lasers.

I acknowledge the support by Dr. Falk Eilenberger, who introduced me to the numerical methods to efficiently solve nonlinear propagation equations.

I acknowledge fruitful discussions with Prof. Dr. Claudio Conti and Prof. Dr. Fabio Biancalana about theoretical concepts and methods.

I am grateful for the theoretical hints by Prof. Dr. Ulf Peschel, that made me think more carefully about claiming new soliton states.

I thank Prof. Dr. Christopher G. Poulton for many helpful discussions and particularly for helping me to solve the linear eigenvalue problem presented in this work.

I thank Prof. Dr. John Travers for pointing out an inaccuracy in my simulation model.

I thank Dr. Christian Karras and Dr. Andreaa Radu for measuring nonlinear refractive indices and Raman spectra of selected liquids.

I thank Dr. Alessandro Tuniz for personal support and the continuous improvement of my English writing.

I thank my students Malte Plidschun, Sebastian Pumpe, Nico Walter, Gregor Sauer, and Ramona Scheibinger for acquiring a wider knowledge base about liquids and liquid-core fibers with their excellent work.

I acknowledge the many discussions with Kay Schaarschmidt that helped to reconsider some aspects of my work.

I thank all my former and recent colleagues for the great time in the Fiber Photonics group.

Finally, I thank all my friends and family for the long-term support during my PhD, and in particular my life partner Margarethe for backing me up many times in those years.

Journal articles

1. M. Baumgartl, **M. Chemnitz**, C. Jauregui, T. Meyer, B. Dietzek, J. Popp, J. Limpert, and A. Tünnermann, "All-fiber laser source for CARS microscopy based on fiber optical parametric frequency conversion," Optics Express 20, 4484-4493 (**2012**).

2. **M. Chemnitz**, M. Baumgartl, T. Meyer, C. Jauregui, B. Dietzek, J. Popp, J. Limpert, and A. Tünnermann, "Widely tuneable fiber optical parametric amplifier for coherent anti-Stokes Raman scattering microscopy," Optics Express 20, 26583-26595 (**2012**).

3. T. Meyer, **M. Chemnitz**, M. Baumgartl, T. Gottschall, T. Pascher, C. Matthäus, B. F. M. Romeike, B. R. Brehm, J. Limpert, A. Tünnermann, M. Schmitt, B. Dietzek, and J. Popp, "Expanding multimodal microscopy by high spectral resolution coherent anti-Stokes Raman scattering imaging for clinical disease diagnostics.," Analytical Chemistry 85, 6703–6715 (**2013**).

4. **M. Chemnitz** and M. A. Schmidt, "Single mode criterion - a benchmark figure to optimize the performance of nonlinear fibers," Optics Express 24, 16191–16205 (**2016**).

5. T. Wieduwilt, M. Zeisberger, M. Thiele, B. Doherty, **M. Chemnitz**, A. Csaki, W. Fritzsche, and M. A. Schmidt, "Gold-reinforced silver nanoprisms on optical fiber tapers—A new base for high precision sensing," APL Photonics 1, 066102 (**2016**).

6. **M. Chemnitz**, J. Wei, C. Jain, B. P. Rodrigues, T. Wieduwilt, J. Kobelke, L. Wondraczek, and M. A. Schmidt, "Octave-spanning supercontinuum generation in hybrid silver metaphosphate/silica step-index fibers," Optics Letters 41, 3519-3522 (**2016**).

7. S. C. Warren-Smith, J. Wie, **M. Chemnitz**, R. Kostecki, H. Ebendorff-Heidepriem, T. M. Monro, and M. A. Schmidt, "Third harmonic generation in exposed-core microstructured optical fibers," Optics Express 24, 17860-17867 (**2016**).

8. **M. Chemnitz**, G. Schmidl, A. Schwuchow, M. Zeisberger, U. Hübner, K. Weber, and M. A. Schmidt, "Enhanced sensitivity in single-mode silicon nitride stadium resonators at visible wavelengths," Optics Letters 41, 5377-5380 (**2016**).

9. S. Pumpe, **M. Chemnitz**, J. Kobelke, and M. A. Schmidt, "Monolithic optofluidic mode coupler for broadband thermo- and piezo-optical characterization of liquids," Optics Express 25, 22932-22946 (**2017**).

10. **M. Chemnitz**, M. Zeisberger, and M. A. Schmidt, "Performance limits of single nano-object detection with optical fiber tapers," Journal of the Optical Society of America B 34, 1833-1841 (**2017**).

11. **M. Chemnitz**, M. Gebhardt, C. Gaida, F. Stutzki, J. Kobelke, J. Limpert, A. Tünnermann, and M. A. Schmidt, "Hybrid soliton dynamics in liquid-core fibres," Nature Communications 8, 42 (**2017**).

12. S. C. Warren-Smith, **M. Chemnitz**, H. Schneidewind, R. Kostecki, H. Ebendorff-Heidepriem, T. M. Monro, and M. A. Schmidt, "Nanofilm-induced spectral tuning of third harmonic generation," Optics Letters 42, 1812-1815 (**2017**).

13. A. Tuniz, **M. Chemnitz**, J. Dellith, S. Weidlich, and M. A. Schmidt, "Hybrid-Mode-Assisted Long-Distance Excitation of Short-Range Surface Plasmons in a Nanotip-Enhanced Step-Index Fiber," Nano Letters 17, 631-637 (**2017**).

14. R. Sollapur, D. Kartashov, M. Zürch, A. Hoffmann, T. Grigorova, G. Sauer, A. Hartung, A. Schwuchow, J. Bierlich, J. Kobelke, **M. Chemnitz**, M. A. Schmidt, and C. Spielmann, "Resonance-enhanced multi-octave supercontinuum generation in antiresonant hollow-core fibers," Light: Science & Applications 6, e17124 (**2017**).

15. M. Plidschun, **M. Chemnitz**, and M. A. Schmidt, "Low-loss deuterated organic solvents for visible and near-infrared photonics," Optical Materials Express 7, 1122-1130 (**2017**).

16. **M. Chemnitz**, J. Wei, C. Jain, B. P. Rodrigues, L. Wondraczek, and M. Schmidt, "Externally tunable fibers for tailored nonlinear light sources," SPIE Newsroom 2–4 (**2017**).

17. **M. Chemnitz**, R. Scheibinger, C. Gaida, M. Gebhardt, F. Stutzki, S. Pumpe, J. Kobelke, A. Tünnermann, J. Limpert, and M. A. Schmidt, "Thermodynamic control of soliton dynamics in liquid-core fibers," Optica 5, 695-703 (**2018**).

18. **M. Chemnitz**, C. Gaida, M. Gebhardt, F. Stutzki, J. Kobelke, A. Tünnermann, J. Limpert, and M. A. Schmidt, "Carbon chloride-core fibers for soliton mediated supercontinuum generation," Optics Express 26, 3221-3235 (**2018**).

Conference proceedings

1. **M. Chemnitz**, M. Baumgartl, C. M. Jauregui, J. Limpert, and A. Tünnermann, "Justagefreie ps-Faserlaserquelle auf Basis von Vierwellenmischung für kohärente Raman-Mikroskopie," in 75. Jahrestagung Der DPG Und DPG Frühjahrstagung (Deutsche Physikalische Gesellschaft, **2011**), p. Q 63.2.

2. M. Baumgartl, **M. Chemnitz**, C. Jauregui, T. Gottschall, T. Meyer, B. Dietzek, J. Popp, J. Limpert, and A. Tünnermann, "Fiber Optical Parametric Frequency Conversion: Alignment and Maintenance Free All-fiber Laser Concept for CARS Microscopy," in Conference on Lasers and Electro-Optics 2012 (OSA, **2012**), p. CF1B.4.

3. M. Baumgartl, **M. Chemnitz**, C. Jauregui, T. Meyer, B. Dietzek, J. Popp, J. Limpert, and A. Tünnermann, "Alignment and maintenance free all-fiber laser source for CARS microscopy based on frequency conversion by four-wave-mixing," in Proc. SPIE 8247, A. Heisterkamp, M. Meunier, and S. Nolte, eds. (**2012**), p. 82470F–7.

4. M. Baumgartl, **M. Chemnitz**, C. Jauregui, T. Meyer, B. Dietzek, J. Popp, J. Limpert, and A. Tunnermann, "Fiber optical parametric frequency conversion: Alignment and maintenance free all-fiber laser concept for CARS microscopy," in 2012 Conference on Lasers and Electro-Optics, CLEO 2012 (**2012**).

5. T. Gottschall, M. Baumgartl, **M. Chemnitz**, J. Abreu-Afonso, T. Meyer, B. Dietzek, J. Popp, J. Limpert, and A. Tunnermann, "All-fiber laser source for CARS-microscopy," in 2013 Conference on Lasers & Electro-Optics Europe & International Quantum Electronics Conference CLEO EUROPE/IQEC (IEEE, **2013**), pp. 1–1.

6. **M. Chemnitz**, Z. Qu, S. Dupont, S. R. Keiding, and C. F. Kaminski, "Supercontinuum generation in an all-normal dispersion fiber for broadband MHz absorption spectroscopy," in Doctoral Conference on Optics DoKDoK (**2013**), pp. 32–33.

7. A. Tuniz, **M. Chemnitz**, J. Dellith, S. Weidlich, and M. A. Schmidt, "Deep subwavelength and broadband light delivery using an all-fiber plasmonic nanotip-enhanced near-field probe," in Frontiers in Optics 2016 (OSA, **2016**), FW3E.4.

8. **M. Chemnitz**, C. Gaida, M. Gebhardt, F. Stutzki, J. Limpert, and M. Schmidt, "Temperature-based wavelength tuning of non-solitonic radiation in liquid-core fibers," in 2017 European Conference on Lasers and Electro-Optics and European Quantum Electronics Conference (**2015**), Vol. 7, p. 10953.

9. **M. Chemnitz** and M. A. Schmidt, "The wet journey towards widely tunable MIR light sources : highly nonlinear liquid-core fibers," in Doctoral Conference on Optics DoKDoK (**2015**), p. 20–21.

10. **M. Chemnitz**, M. Gebhardt, C. Gaida, F. Stutzki, J. Limpert, and M. A. Schmidt, "Soliton-based MIR generation until 2.4µm in a CS_2-core step-index fiber," in Frontiers in Optics 2015 (OSA, **2015**), p. FW5F.2.

11. **M. Chemnitz**, C. Jain, and M. A. Schmidt, "Transformable material fibers - A new route for tunable broadband light sources," in Doctoral Conference on Optics DoKDoK (**2016**), pp. 48–49.

12. **M. Chemnitz**, M. Gebhardt, C. Gaida, F. Stutzki, J. Limpert, and M. A. Schmidt, "Indications of new solitonic states within mid-IR supercontinuum generated in highly non-instantaneous fiber," in Conference on Lasers and Electro-Optics (OSA, **2016**), p. FF1M.4.

13. S. C. Warren-Smith, J. Wei, **M. Chemnitz**, R. Kostecki, H. Ebendorff-Heidepriem, T. M. Monro, and M. A. Schmidt, "Wavelength shifted third harmonic generation in an exposed-core microstructured optical fiber," in 2017 Opto-Electronics and Communications Conference, OECC 2017 and Photonics Global Conference, PGC 2017 (**2017**).

EHRENWÖRTLICHE ERKLÄRUNG

Ich erkläre hiermit ehrenwörtlich, dass ich die vorliegende Arbeit selbstständig, ohne unzulässige Hilfe Dritter und ohne Benutzung anderer als der angegebenen Hilfsmittel und Literatur angefertigt habe. Die aus anderen Quellen direkt oder indirekt übernommenen Daten und Konzepte sind unter Angabe der Quelle gekennzeichnet.

Bei der Auswahl und Auswertung folgenden Materials haben mir die nachstehend aufgeführten Personen in der jeweils beschriebenen Weise unentgeltlich geholfen:

1. Dr. Christian Karras mit der Bereitstellung von Messdaten zu dem nichtlinearen Verhalten von Flüssigkeiten.
2. Dr. Andreea-Ioana Radu mit der Bereitstellung von gemessenen Raman-Spektren von Flüssigkeiten.
3. Malte Plidschun mit der Bereitstellung von gemessenen Transmissionspektren von einigen Flüssigkeiten.

Weitere Personen waren an der inhaltlich-materiellen Erstellung der vorliegenden Arbeit nicht beteiligt. Insbesondere habe ich hierfür nicht die entgeltliche Hilfe von Vermittlungs- bzw. Beratungsdiensten (Promotionsberater oder andere Personen) in Anspruch genommen. Niemand hat von mir unmittelbar oder mittelbar geldwerte Leistungen für Arbeiten erhalten, die im Zusammenhang mit dem Inhalt der vorgelegten Dissertation stehen.

Die Arbeit wurde bisher weder im In- noch Ausland in gleicher oder ähnlicher Form einer anderen Prüfungsbehörde vorgelegt.

Die geltende Promotionsordnung der Physikalisch-Astronomischen Fakultät ist mir bekannt. Ich versichere ehrenwörtlich, dass ich nach bestem Wissen die reine Wahrheit gesagt und nichts verschwiegen habe.

Jena, 9th November 2018

Mario Chemnitz